Comfort-Oriented Thermal Modeling and Operational Strategies for Shared Office Spaces

Vorgelegt von

Janine Günther

geboren in München

Vorwort

Die vorliegende Arbeit entstand im Rahmen meiner Tätigkeit als wissenschaftlicher Mitarbeiter am Institut für Systemdynamik der Universität Stuttgart in enger Zusammenarbeit mit der Robert Bosch (South East Asia) Pte Ltd in Singapur.

An dieser Stelle möchte ich allen Menschen danken, die mich in dieser interessanten, aber auch herausfordernden Zeit begleitet, unterstützt und ermutigt haben. Ich danke daher dem Institutsdirektor, Herrn Prof. Dr.-Ing. Dr. h.c. Oliver Sawodny, für die Ermöglichung dieser Arbeit sowie das entgegengebrachte Vertrauen. Weiterhin gilt mein Dank Prof. Dr.-Ing. habil. Rudibert King für die freundliche Übernahme des Mitberichts und die angenehme Kommunikation.

Die mit meinem Projekt einhergehende Zusammenarbeit mit der Forschungsabteilung in Singapur bot mir eine einzigartige Chance meine Arbeit mit wertvollen interkulturellen Erfahrungen zu verbinden. Daher geht ein großes Dankeschön an Falco Sengebusch, Dr.-Ing. Kai Oertel und Dr.-Ing. Markus Kneifel, die diese Kooperation möglich gemacht haben.

Insbesonders möchte ich allen Kolleginnen und -kollegen danken, durch die die Zeit am Institut und in Singapur zu einer einzigartigen Erfahrung wurde. Vielen Dank für die vielen lustigen Momente und Erlebnisse und vor allem für die anregenden Diskussionen. Ich freue mich, dass mir neben den unvergesslichen Erinnerungen auch wunderbare Freundschaften erhalten bleiben.

Ganz besonderer Dank gilt außerdem meinen Korrekturlesern für das wertvolle Feedback, meinen Bürokolleginnen und -kollegen für den guten Austausch und das stets vertrauensvolle Verhältnis sowie allen Diskussionspartnern, die mir besonders auf der Zielgeraden mit Rat und Tat zur Seite standen.

Auch meiner Familie danke ich für das uneingeschränkte Vertrauen, den beständigen Rückhalt und ihre Unterstützung. Besonders dankbar bin ich Martin, der mich in jederlei Hinsicht bestärkt und ermutigt hat. Vielen Dank für dein Verständnis und die Bereitschaft dieses Abenteuer mit mir zu bestreiten.

Leinfelden, Juli 2020   Janine Günther

Abstract

People spend up to 90 % of their lifetime in buildings. The design and operation of buildings therefore have a significant impact on our quality of life. Thermal indoor conditions are particularly important in order to create a pleasant atmosphere, which makes air-conditioning to the central objective of building operation also referred to as building control. Two main questions arise from this objective: What does thermal comfort mean and how can it be achieved by appropriate control strategies? Common control approaches address these questions by the use of standardized temperature set-points for the whole building. The compliance with this target temperature is usually monitored by few sensors, where one measurement value represents the conditions of a large thermal zone. In reality, this control strategy often entails discomfort due to notable but unconsidered spatial temperature differences, e. g. by means of solar loads, as well as the very subjective thermal expectations. Consequently, this thesis forms the basis for an optimized building control strategy that aims for an improved comfort level to the satisfaction of all users that is able to quantify and evaluate spatial conditions based on the air-conditioning operation and at the same time accounts for the comfort requirements of individual occupants.

The spatial thermal conditions are the result of complex flow effects which are mainly driven by the air-conditioning system, the position and size of the windows as well as internal loads. Accurate representations of these effects by means of computational fluid dynamics simulations are computationally expensive and therefore not suited for control design. Hence, simplified data-driven models for the prediction of the stationary temperature field are developed in the first part of this thesis. A key difficulty for the selection of a suitable modeling approach is the limited data base. The available input parameters are restricted to commonly accessible sensor data consisting of discrete temperature measurements and the operational mode of the air-conditioning system. Under these prerequisites, a Gaussian Process regression model is derived which improves the prediction of the temperature field by up to 60 % compared to the standard assumption of well-mixed conditions. The predictive ability is even further improved by an optimized sensor setup. Two optimal placement approaches are compared which either focus on the reduction of the prediction error or the variance of the model. Compared to other modeling approaches with a similar degree of detail, the derived data-driven approach provides more detailed information about the spatial thermal conditions with significantly smaller computational or implementation effort which makes it applicable to real-time control concepts. Moreover, this data-

based approach enables an online model adaptation to constantly changing conditions commonly occurring in office buildings, for example changes of the floor plan.

The second part of this thesis focuses on the definition of individual thermal comfort. Although well-established models exist for the design and operation of building air-conditioning systems, most of them are not suitable for predicting the personal comfort sensation. Comparing these models with the collected user feedback results in an unsatisfactory individual predictability. Therefore, alternative models are investigated and derived which lead to a better accordance. The main challenge originates from the high uncertainty of the user data that are collected during the daily working routine. The low system excitation of the everyday operation limits the data quality so that the developed comfort model structure and the identification process must ensure physically feasible prediction models. Polynomial basis functions serve as easily interpretable trial functions which are reduced using combinational feature selection and LASSO regression to avoid overfitting. The resulting well generalizing model characteristic is particularly important for the subsequent integration in optimization-based control concepts. The best model structure for the considered test group is a linear basis function in combination with a Gaussian process model which depends on the parameters air temperature, fan level, humidity, outside temperature, and daytime. This personalized approach improves the individual prediction accuracy by over 50 % compared to standard models.

Based on the personal comfort models, control strategies are deduced for optimizing the individual thermal comfort. Apart from temperature control, additional ceiling fans are installed for the local actuation of air movement. In a first approach, the comfort models are used to define an optimal combination of temperature and air velocity for the entire user group. The personalized models are constantly adapted during the operation to account for individual and group-related changes. Thus, modifications are always included in the comfort optimization. The complementary cooling effect by increased air velocities incorporates an energy saving potential of approx. 20 % while enhancing the individual comfort. Since changing occupancy causes dynamical variations of the comfort requirements, concepts for a reasonable consideration of these variations are devised. The proposed concept demonstrates an improvement of the average comfort level by additional 6 %. Eventually, all results are combined to extend the temperature and air velocity optimization to a model predictive control strategy that makes use of the underlying room dynamic. This allows to account for coupling effects between the comfort factors in the control concept which yields a further improvement of the overall thermal comfort.

Kurzfassung

Menschen verbringen bis zu 90 % ihrer Lebenszeit in geschlossenen Räumen. Dementsprechend haben die Auslegung, das Design und der Betrieb von Gebäuden einen entscheidenden Einfluss auf unsere Lebensqualität. Insbesondere die thermischen Raumbedingungen tragen entscheidend zu einer angenehmen Atmosphäre bei, sodass eine komfortable Klimatisierung zum zentralen Ziel der Gebäuderegelung wird. Aus diesem Ziel ergeben sich vor allem zwei Fragestellungen: Was bedeutet thermischer Komfort für den Einzelnen und wie kann dieser durch geeignete Regelungskonzepte sichergestellt werden? Üblicherweise angewandte Regelstrategien adressieren diese Fragen, indem sie gebäudeübergreifend standardisierte Temperaturvorgaben zugrunde legen. Die Einhaltung dieser Vorgaben wird dann über wenige Sensoren überwacht, wobei ein Messwert meist eine verhältnismäßig große thermische Zone repräsentiert. Diese Regelstrategie führt allerdings häufig zu Diskomfort, da die tatsächlichen, örtlich verteilten Bedingungen stark vom gemessenen Referenzwert abweichen können, z. B. durch solare Einflüsse, und auch die subjektive thermische Wahrnehmung der Nutzer große Unterschiede aufweist. Daher wird in dieser Arbeit die Basis für eine komfortoptimierte Regelstrategie gelegt, die zum einen in der Lage ist, die örtlich verteilten Einflüsse des Klimasystems miteinzubeziehen und zum anderen individuelle Komfortanforderungen berücksichtigt.

Die örtlich verteilten thermischen Bedingungen im Raum sind das Resultat komplexer Strömungseffekte, die hauptsächlich durch das Belüftungssystem, die Lage und Größe der Fenster aber auch interne Lasten beeinflusst werden. Da die Simulation dieser Effekte sehr rechenaufwendig ist, werden im ersten Teil der Arbeit Modelle entwickelt, die eine vereinfachte Prädiktion der stationären Temperaturverteilung ermöglichen. Eine der wesentlichen Herausforderungen bei der Auswahl eines passenden Modellansatzes liegt in der limitierten Datenbasis, da sich die verfügbaren Eingangsparameter auf üblicherweise verfügbare Sensormessungen beschränken, d.h. diskrete Temperaturwerte sowie der Betriebszustand des Belüftungssystems. Unter diesen Voraussetzungen wird ein Gaußprozessmodell entwickelt, welches die Prädiktion der örtlich verteilten Temperatur um bis zu 60 % verbessert gegenüber der Standardannahme einer homogenen Temperaturverteilung. Durch eine optimierte Sensorplatzierung kann der Prädiktionsfehler weiter reduziert werden, wofür zwei Ansätze untersucht werden, die sich auf Fehler- bzw. Varianzminimierung fokussieren. Im Vergleich zu Modellen mit ähnlichem Detaillierungsgrad erlaubt der vorgestellte datengetriebene Ansatz detailliertere Informationen über die verteilten thermischen Bedingungen im Raum zu erhalten jedoch mit deutlich geringerem Implementierungs- und Instandhaltungsaufwand. Außerdem

ermöglicht die datenbasierte Herangehensweise eine Adaption des Modells während der Betriebszeit, da Änderungen der Raumaufteilung oder Ausstattung besonders in Bürogebäuden keine Seltenheit sind.

Der zweite Teil der Arbeit konzentriert sich auf die Definition von individuellem thermischen Komfort. Auch wenn es bereits etablierte Komfortmodelle für die Auslegung und den Betrieb der Gebäudeklimatisierung gibt, sind diese für die Bestimmung der persönlichen Bedürfnisse meist ungeeignet. Der Abgleich dieser Modelle mit den vorliegenden Nutzerdaten ergibt eine unzureichende individuelle Prädizierbarkeit. Daher werden alternative Modellierungsansätze untersucht und abgeleitet, die zu einer besseren Übereinstimmung führen. Die größte Herausforderung ergibt sich dabei aus der hohen Unsicherheit der unter alltäglichen Arbeitsbedingungen gesammelten Nutzerdaten. Die geringe Systemanregung im Tagesbetrieb limitiert die Datenqualität, weshalb die Komfortmodellstruktur und der Identifikationsprozess mit dem Ziel entwickelt werden robuste Komfortvorhersagen zu treffen. Als Ansatzfunktionen werden verschiedene leicht interpretierbare Polynomansätze verglichen, die mit Hilfe von kombinatorischer Merkmalsauswahl sowie LASSO-Regression reduziert werden um Überanpassung zu vermeiden, sodass sich nur physikalisch sinnvolle Schätzmodelle ergeben. Die daraus resultierende, gut generalisierende Modellcharakteristik ist besonders relevant für die spätere Integration in optimierungsbasierte Regelungskonzepte. Als beste Ansatzstruktur ergibt sich für die betrachteten Nutzerdaten eine lineare Basisfunktion in Kombination mit einem Gaußprozessmodell, welches von den Parametern Lufttemperatur, Ventilatorstufe, Feuchtigkeit, Außentemperatur und Tageszeit abhängt. Dieser personalisierte Ansatz verbessert die individuelle Vorhersagegenauigkeit gegenüber einem Standardansatz um über 50 %.

Basierend auf den personalisierten Komfortmodellen werden anschließend Regelungsstrategien abgeleitet, die den individuellen Komfort optimieren. Dabei werden, neben der Temperaturregelung, Deckenventilatoren eingesetzt, die einen lokalen Einfluss auf die Luftgeschwindigkeit haben. In einem ersten Ansatz werden die Komfortmodelle genutzt um eine optimale Kombination aus Temperatur und Luftgeschwindigkeit für die gesamte Nutzergruppe zu bestimmen. Die personalisierten Nutzermodelle werden während der Laufzeit adaptiert, sodass personen- sowie gruppenbezogene Veränderungen stets für die Komfortoptimierung berücksichtigt werden. Der zusätzliche Kühlungseffekt durch erhöhte Luftgeschwindigkeiten ermöglicht eine Energieeinsparung von ca. 20 % bei verbessertem individuellem Komfort. Da wechselnde Belegungsprofile eine dynamische Veränderung der Komfortanforderungen verursachen, werden zudem Konzepte entwickelt, die eine sinnvolle Berücksichtigung dieser ermöglichen, wodurch das durchschnittliche Komfortlevel um weitere 6 % gesteigert werden kann. Abschließend wird die Optimierung der Lufttemperatur und -geschwindigkeit auf ein modellprädiktives Regelungskonzept erweitert, welches auch die Raumdynamik mitberücksichtigt. Dadurch können Kopplungseffekte zwischen den Komfortfaktoren in die Regelstrategie miteinbezogen werden, wodurch eine zusätzliche Verbesserung des thermischen Komforts erreicht wird.

Contents

1 Introduction

The main goal for building operation is the occupants' health and comfort. In particular, since the major part of our lives - impressive 90 % [63] - takes place in buildings, comfortable indoor conditions play a major role for the quality of life. Furthermore in commercial and office buildings, the well-being of the occupants is directly related to their productivity and work performance [69]. Therefore, the main interest of the building owner or manager is the improvement of comfort. Consequently, it is no surprise that the control of Heating Ventilation and Air Conditioning (HVAC) systems is an extensively discussed research topic, e. g. [1, 18, 75]. Apart from the comfort target on the *lower level*, the *high-level* requirement is given by reducing the energy consumption of a building. With about 35 %, the building sector has the largest share in final energy consumption, thus incorporates a great potential for improvement to accomplish the intended climate targets [54]. In addition to occupant awareness, insulation, more efficient HVAC components and integration of renewable energies, intelligent control strategies are promising approaches for a sustainable development [7]. The growing energy demand is mainly driven by the developing Asian economies and an increasing demand for space cooling [54]. Satisfying the different stakeholders requires the development of building operation strategies that combine the specifications motivated by the global climate targets as well as guaranteeing the work performance and health of the occupants. Although contrary requirements can arise from energy reduction and comfort improvement, the two objectives are not necessarily mutually exclusive [65]. Hence, the challenge is to develop sustainable control concepts which are able to jointly fulfill comfort and energy requirements.

A holistic understanding of the system is a necessary prerequisite to allow for intelligent building control. This further involves system models that provide a valid representation of the real conditions. Multiple methods are investigated, reaching from white over gray to black box models, to map the indoor conditions and the interaction between the HVAC components [7]. Most approaches focus on the components and assume uniform conditions within the controlled zone. Nevertheless, external and internal disturbances can affect the indoor conditions locally [41]. Furthermore, thermal comfort is usually addressed by standardized comfort assumptions which provide a fixed design/target temperature or admissible temperature range. However, individual thermal sensation can vary significantly from these standard conditions [42]. Therefore, the following guiding questions arise:

1. How can indoor conditions be represented on the room level with a complexity that is suitable for control design?

2. How can personal thermal comfort be defined and integrated in the control strategy?

Answering the first question aims to get a more detailed understanding how the HVAC system affects the room locally. The second question tackles the limited validity of standard models to represent the diverse individual perception [42]. Both aspects are important steps towards a comprehensive system understanding and hence comfort-based control approaches including the target of energy efficiency.

1.1 State of the Art

Building automation encompasses multiple domains including the control of the HVAC system, energy management, fault detection, security and access control as well as life safety and fire detection. While all aspects aim for the occupants' well-being and satisfaction, their thermal comfort is mainly a result of the HVAC operation. Due to the great amount of involved devices, this is one of the most complex tasks and thus commonly designed in a hierarchical manner as outlined in Figure 1.1. The lowest layer is represented by the field devices such as sensors, valves, switches and other local actuators. These devices are controlled by unitary controllers whose operation is usually independent from each other. The next level are the supervisory controllers that adapt the central building components or unitary controller set-points based on schedules, weather conditions or occupancy. The server applications build the top layer where all data are collected and processed for reasons of monitoring and possibly optimization [99]. Most often the control approach for the supervisory layer is rule-based due to its simple implementation of best practices. The main problem in this context are poorly tuned unitary controllers and the great variety of buildings which require diverse operational strategies [76]. Therefore, rule-based controllers always lead to a suboptimal operation. Due to the increased interest in energy efficiency, the advances in recent years focused on predictive control approaches. Particularly, Model Predictive Control (MPC) dominates the building applications [1] because of its ability to handle input and output constraints which are a decisive limitation for building systems [7]. These approaches incorporate a significant energy saving potential, e. g. [23, 77, 93], but always require a valid building model. The available modeling approaches can be classified in three categories: white box, data-driven and hybrid modeling methods [7]. White box models rely on physical relations and properties where the complex heat and flow equations are solved based on Finite Volume Methods (FVMs) or Finite Element Methods (FEMs). The data-driven approaches do not require a physical system model but use input-output data to identify the building characteristics. System identification methods, such as Autoregressive-Moving Average (ARMA), state-space models, or Machine Learning (ML) techniques, like Artificial Neural Networks
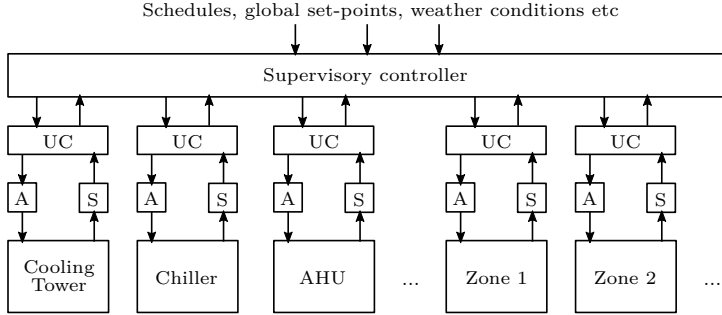
Figure 1.1: Hierarchical control architecture for a common HVAC system with unitary controllers (UC) for the local actuators (A) using the sensor signals (S), inspired by [75].

(ANNs) and Support Vector Machines (SVMs), are used for the modeling task in this case. Hybrid approaches are often gray box methods which combine physical and data-driven concepts. Lumped parameter or Resistance-Capacitance (RC) models are common examples.

The white box models mostly result in a high complexity and require detailed knowledge about the building properties and boundary conditions. While simulation software, like EnergyPlus, TrnSys or Modelica, provides a useful tool for system design or demand estimation, the underlying models are most often too complex for a direct application to controller design. Therefore, simplified gray box approaches are preferred for control-oriented modeling [7]. The most common method is the RC network approach due to its good physical interpretability where an analogy between electrical and thermal systems is established. The deduced general heat transfer equation

$$\dot{Q} = \frac{T_i - T_j}{R} \tag{1.1}$$

allows to rewrite the conductive, convective, radiation and advective heat transfer respectively:

$$\dot{Q}_{\text{cond}} = \alpha_{\text{cond}} A (T_i - T_j) \qquad \rightarrow \qquad R_{\text{cond}} = \frac{1}{\alpha_{\text{cond}} A} \tag{1.2a}$$

$$\dot{Q}_{\text{conv}} = \alpha_{\text{conv}} A (T_i - T_j) \qquad \rightarrow \qquad R_{\text{conv}} = \frac{1}{\alpha_{\text{conv}} A} \tag{1.2b}$$

$$\dot{Q}_{\text{rad}} = \alpha_{\text{rad}} A (T_i - T_j) \qquad \rightarrow \qquad R_{\text{rad}} = \frac{1}{\alpha_{\text{rad}} A} \tag{1.2c}$$

$$\dot{Q}_{\text{adv}} = c_p \dot{m} (T_i - T_j) \qquad \rightarrow \qquad R_{\text{adv}} = \frac{1}{c_p \dot{m}} \tag{1.2d}$$

where A denotes the cross-sectional area of the body perpendicular to the heat transfer direction, α_{cond} and α_{conv} are the conductive and convectional heat transfer coefficient respectively, $\dot{m}$ the mass flow and α_{rad} the linearized radiation heat transfer coefficient. The temperatures T_i and T_j either represent the temperatures of the involved fluid or solid. The thermal capacitance of a component is defined by the specific heat coefficient c_p, its volume V and density ρ

$$C = c_p \rho V. \tag{1.3}$$

Refer to [7, 53] for more detailed explanations. Finally, the dynamical heat transfer equation for an arbitrary thermal node with N neighboring nodes results in

$$C\dot{T} = \sum_{i=1}^{N} \frac{T_i - T}{R_i}. \tag{1.4}$$

The number of thermal nodes and resistors defines the accuracy of the model. The model parameters can either be identified based on measurements or computed using (1.2) and (1.3). Exclusively using the physical properties of the materials to define the parameter values results in a white box approach. However, detailed knowledge about the exact construction properties is mostly not available such that system identification must be used to specify the unknown parameters. This, on the other hand, requires measurement data with a sufficient frequency content. Hence, a combination of both is often applied to obtain a reasonable compromise between the model's complexity and the requirements on the measurement data. Additionally, the physical interpretation helps to evaluate the identified values.

Although the RC network approach is suitable for control design and enables various levels of detail, it only uses at most one node to represent the air conditions of a zone. This common approach for modeling the zone conditions relies on the assumption that the room air is well mixed so that the temperature (and humidity) differences within the zone can be neglected [99]. For small zones without significant local loads, this assumption is a valid approximation. Considering large open-plan offices, on the other hand, entails a higher risk of violating this simplification. Local disturbance impacts, e.g. due to solar loads or very distinct occupancy, can lead to significant temperature differences accompanied by thermal discomfort. An unfavorably placed sensor for monitoring the overall room conditions can further impair the situation by supplying a non-representative measurement to the HVAC controller or for the system identification process. As a result, a better representation of the room conditions must be found to fully answer the first guiding question of Chapter 1.
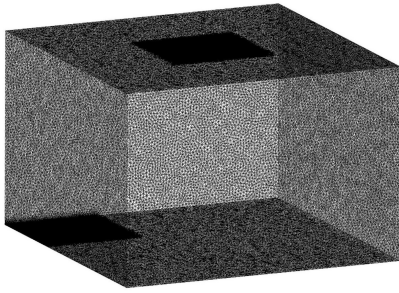
1.1.1 Modeling of the Room Conditions

Generally, room models can be divided into three groups: well-mixed, zonal and Computational Fluid Dynamics (CFD) models. The most detailed resolution of the room conditions is attained by CFD simulations. The temperature field and the spatial flow conditions are represented by the Navier-Stokes equations

$$\frac{\partial \rho}{\partial t} + \nabla \cdot (\rho \boldsymbol{v}) = 0 \tag{1.5a}$$

$$\frac{\partial \rho \boldsymbol{v}}{\partial t} + \nabla \cdot \left(\rho \boldsymbol{v} \boldsymbol{v}^{\mathrm{T}} + p\boldsymbol{I} - \boldsymbol{\tau} \right) = \rho \boldsymbol{g} \tag{1.5b}$$

$$\frac{\partial}{\partial t} \left(\rho \left(e + \frac{1}{2} \boldsymbol{v}^2 \right) \right) + \nabla \cdot \left(\rho \boldsymbol{v} \left(h + \frac{1}{2} \boldsymbol{v}^2 \right) - \boldsymbol{\tau} \cdot \boldsymbol{v} - \lambda \nabla T \right) = \rho \boldsymbol{g} \cdot \boldsymbol{v} \tag{1.5c}$$

which describe the conservation of mass (1.5a), momentum (1.5b) and energy (1.5c) [70], where $\boldsymbol{v}$ denotes the velocity vector, p the fluid pressure, $\boldsymbol{I}$ the unit matrix, $\boldsymbol{\tau}$ the stress tensor, e the specific internal energy, h the specific enthalpy and λ the thermal conductivity. For solving these nonlinear partial differential equations 12 additional equations are required: one thermal and two caloric equations of state as well as 9 equations for the normal and shear stress terms. An analytical solution can only be found for very few special cases but not for the general 3-dimensional case with arbitrary boundary conditions as it occurs in buildings. Therefore, only numerical solutions can be obtained for the considered application which are usually implemented using the FVM. In particular directly solving (1.5) for turbulent flows entails a high computational effort because the volume elements of the mesh must be very small for being able to resolve the smallest turbulences. Most often this results in unreasonable computing times for technical applications [70]. Therefore, CFD simulation software commonly solves the Reynolds-averaged Navier-Stokes (RANS) equations where the velocities are separated in a low- and a high-frequency component at which the high-frequency share, thus the small turbulences, are mapped by turbulence models. Although this simplification allows to solve flow processes within a reasonable time period, real-time applications are unattainable yet. Achieving a consistent, stable and converging solution still requires a fine discretization, as exemplary sketched in Figure 1.2a, and consequently involves a great implementation effort as well as computation time. Another challenge regarding the application of CFD simulations in the context of building control is the generally limited knowledge of the exact boundary conditions during the daily operation. Extensive measurements would be required to allow for a quantitative accordance between the CFD simulation results and the real world conditions. In summary, the high complexity and missing real-time capability makes this approach unsuitable for an application in building control. However, the detailed simulation output regarding the local flow effects and the consequent impact on the temperature field provides a useful reference for the evaluation of alternate modeling approaches and is therefore used accordingly in the following.

(a) Exemplary mesh for a CFD simulation of a simple room.
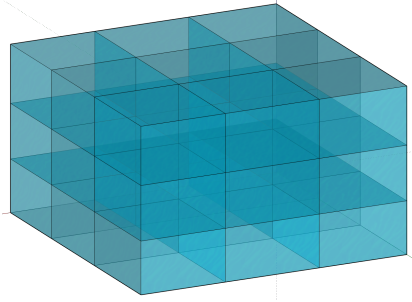
(b) Separation into sub-zones for a zonal modeling approach.

Figure 1.2: Examples for a more detailed resolution of the room conditions.

The high computational effort of CFD simulations is mainly due to the need for very fine grids (Figure 1.2a). Coarser partitioning reduces the computing time significantly but requires alternative formulations of the flow equations. For this reason, different zonal models were developed which separate the zone in multiple sub-zones and define the laws for the air exchange between the adjacent zones. An exemplary partitioning for a zonal approach is depicted in Figure 1.2b. The power law model

$$\dot{m}_{ij} = -\rho A_{ij} \psi \, \text{sign}\left(\left|\frac{\Delta p_{ij}}{\rho} + g\Delta z_{ij}\right|\right) \sqrt{2\left|\frac{\Delta p_{ij}}{\rho} + g\Delta z_{ij}\right|} \tag{1.6}$$

is a commonly used approach to define the air mass flow between the sub-zones, e. g. [11, 46, 52], where g denotes the gravitational acceleration, ρ the density of air and ψ the discharge coefficient. It is based on the Bernoulli equation and uses the height difference Δz_{ij}, the pressure difference Δp_{ij} and the common area A_{ij} between two zones i and j to calculate the mass exchange. Due to the dissipation of the air flow within the zones, alternate zone formulations for driving air flows [80, 86], like jets or plumes, are necessary and require prior knowledge of the airflow pattern. Another approach uses the momentum equation to avoid the inclusion of the prior knowledge of the flow conditions [40, 102] by introducing the air velocity as a zone property. A similar approach is pursued by the velocity propagating zonal model (VEPZO) model [81], where a viscous loss model is proposed as representation of the air flow. Although the computation time and complexity is significantly reduced by these approaches, the models still require thoughtful calibration by measurements and are sensitive to a change of the room layout. However, particularly commercial buildings are commonly exposed to changes of the floor plan due to a rearrangement of offices or furniture. Adapting these models to a new setup involves a great effort and expert knowledge which is usually an exclusion criteria for large-scale applications.

The limited applicability of physically motivated approaches and the trend towards digitization afford an opportunity for data-based models. Instead of using a (purely) physically motivated structure, an arbitrary mapping function $f(\cdot)$ can be selected that is able to reflect the general system behavior. For the identification of the unknown model parameters, sufficient training data are required. These data usually come from distributed sensor measurements or simulation results of more complex models. The simplest example would be a linear regression between the distributed sensor values. However, for mapping the impact of varying inputs, e. g. different ventilation conditions, a suitable relation must be chosen to define the effect of different model inputs. Since flow conditions and resulting room temperatures are a result of a highly nonlinear process, ML techniques proved to be a useful tool in this context. Previous research explored the practicability of an ANN [74] and Gaussian Process (GP) regression [29, 66, 79] to estimate the temperature distribution. The latter approach is most commonly used due to good interpretability, the possibility to directly consider measurement noise and the additional output information about the uncertainty of the prediction. Therefore, the data-based modeling approach based on GP regression is adopted for the temperature field prediction in this work, whereby the focus is set on mapping the interaction between the indoor conditions and the HVAC system.

1.1.2 Thermal Comfort Modeling

More detailed room models allow to develop advanced control concepts that ensure comfortable conditions over the entire space. However, they also need a target conditions. This arises the question of how to set the indoor conditions that thermal comfort is achieved. Generally, comfort standards, such as DIN EN ISO 7730 [26] or ANSI/ASHRAE Standard 55 [2], are used to assess the comfort requirements. These standards target to reflect an averaged comfort level based on empirical studies. Although these models are physically motivated by the human's heat balance, the validity for the individual is very limited due to the very subjective perception [42, 51]. It can also be observed that the personal preferences are even more distinct than usually occurring temperature differences within an open space due to deficient HVAC control and unconsidered disturbance effects. As a result, a reliable representation of the desired conditions is a crucial step towards the improvement of thermal comfort.

The most commonly used approach is the Predicted Mean Vote (PMV) introduced by Fanger [30]. The popularity of this approach originates from its embedding in the mentioned comfort standards [2, 26] and the great data base for validation. The interaction between the human body and the environment is modeled by its stationary heat balance and takes into account convective and evaporative heat losses, heat loss via the skin and by respiration as well as metabolism. The different heat flows are defined by a combination of physical and empirical equations and require

detailed knowledge about a specific person regarding height, weight, surface area etc. Therefore, standardized values were derived for a generalized estimation of comfort and multiple extensions of this approach were proposed to improve its validity in real-world applications [24, 51].

More detailed modeling approaches extend the description of the human body to multiple nodes or segments. The two node model, for example, differentiates between a core and a skin compartment and incorporates increased metabolism due to shivering [36]. Even more detailed models, distinguish multiple body zones to map the influence of non-uniform conditions (displacement ventilation, floor heating, radiative heating cooling etc.) [33]. Although these models extend the PMV and allow for a more accurate representation of the thermal interaction of a human being, the main challenge for an application in real buildings is the limited sensor data. The more detailed the model describes the human body, the more prior knowledge about the specific user must be available. For an application based on commonly accessible data, the usage of these models is very confined.

Most mentioned comfort modeling approaches target to find a universal representation of the human's thermal sensation so that the proposed models map the average perception of a large user group. While these standardized models are very useful for system design, their application to individualized comfort-optimizing control is bounded due to the high complexity that goes along with an individualization and the limited validity. Therefore, data-based modeling approaches are explored in more recent developments. They start with a personalized parameter estimation of standard models like the PMV [42, 105] and apply different ML techniques, such as GP [32, 42] regression, SVMs, Random Forests (RFs) [31, 61] and ANNs [56]. The data base that is used for predicting thermal comfort corresponds mainly to the physically motivated models and is adjusted according to the respective system prerequisites. The training is then performed based on measurements and user feedback. These data-based approaches are particularly popular for personal comfort modeling and thus revisited in this work.

1.1.3 Comfort-Based Control

Numerous research can be found regarding the control of HVAC systems. As mentioned above, the main focus in this context is generally on energy consumption and thermal comfort. While energy consumption is mainly examined on building level without the inclusion of detailed room models, all thermal comfort-oriented control approaches face two challenges: Limited knowledge about the actual physical and psychological state of the occupant and underactuation of the occupied building areas.

The most common approach to address the first challenge is the use of standardized assumptions on unknown parameter values. This leads for instance to PMV-based control strategies where the standard model is applied to define a comfortable range for

the operation whereby the energy consumption is reduced within this range, e. g. [34, 62]. However, optimal control concepts based on standardized comfort models do not lead to individual thermal comfort [42]. Therefore, the second method targets a better understanding of the occupant's preferences for example by the use of wearable sensor devices which provide more detailed information about the actual user state. This allows for a better representation of the individual and thus improved target conditions [71]. Nevertheless, in most cases the building operation system does not have access to occupant-related sensor data so that a control concept that is easily applicable to arbitrary buildings can only use usually available measurements of the environmental conditions. As a consequence, control approaches based on user feedback mostly only consider the relation between temperature and thermal sensation but neglect the coupling to further comfort-influencing factors. The agent-based [57] or fuzzy logic [55] control approaches are examples for this kind of personalized control strategy.

The reduction of thermal comfort to a common optimal temperature level is explained by the second challenge, namely underactuation. Most buildings are designed to maintain one temperature level in all zones and local differences cannot be realized due to a low number of actuators and dominant mixing effects. Therefore, ongoing research investigates local actuation regarding its potential for better individualization. Thermally adjustable chairs are one example for so called Personal Comfort Systems (PCSs) [59]. While these systems have the potential to improve the individual comfort significantly, they require a great investment in retrofitting. An alternative approach is given by locally elevated air movement to enable additional cooling effects and thus personalized indoor conditions. Since this idea is adopted in the present thesis, a more detailed discussion of the associated effects is provided below.

1.1.4 Elevated Air Velocities

Mechanical ventilation provides another locally effective actuation method which can be retrofitted with a relatively low expenditure. The increased convective heat transfer between the human body and the environment for a higher air velocity is also known as wind chill and can be used to adjust the thermal sensation without changing the air temperature. Since energy efficiency is highly related to the required cooling power in hot climates, elevated air movement incorporates not only the possibility of local and individualized actuation but has also a significant energy saving potential. These prospects explain the great interest in capturing the actual effect of air velocity on thermal comfort. Although the PMV and most other comfort models include this effect, they are often proven to overestimate the real impact [73, 94]. Particularly in hot and humid environments, the acceptability of increased air movement is significantly higher than suggested by European studies. However, dominant differences were determined between the individuals. Figure 1.3 emphasizes the different identified
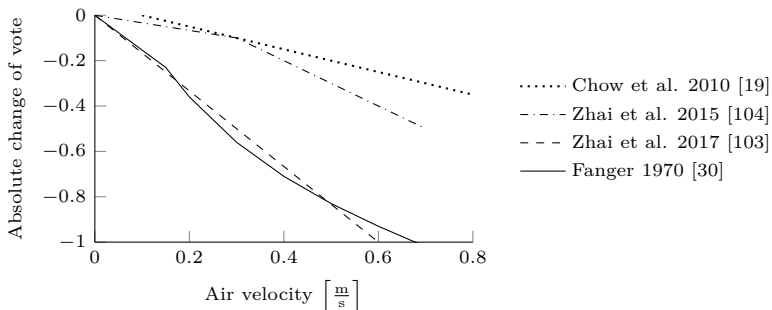
Figure 1.3: Comparison of different literature results that investigate how the air velocity changes the thermal sensation vote.

sensitivities of the thermal sensation vote as a function of air velocity based on selected literature. Chow et al. (2010) [19] investigated the perception of subjects from Hong Kong, Zhai et al. analyzed the sensation of a Chinese group in [104] and regarded international subjects in [103]. While the results from the international test group [103] are similar to Fanger's PMV model, the field studies with Chinese subjects lead to significantly lower sensitivities. Although air speed variations can have a very distinct effect on the individual user [91], it provides additional cooling and thus allows for local actuation, especially under the assumption of well mixed conditions with a common temperature set-point. This property is therefore applied for individualization of the room conditions.

1.2 Objective and Outline

This thesis targets to lay a foundation for control approaches that allow for individualized thermal comfort in shared office spaces. This requires a suitable representation how the HVAC system affects the spatial room conditions as well as a valid prediction model for personal thermal comfort. As discussed above, most available approaches either rely on inaccessible sensor data or require expensive equipment such that an application to existing buildings is almost impossible. Therefore, three crucial aspects are addressed in this work to pave the way towards individual thermal comfort in office buildings:

- ✓ A data-based modeling approach for a more detailed representation of the spatial room conditions to enable the possibility of localized temperature control without the need for exact knowledge about the boundary conditions and expensive CFD simulations.

✓ A methodology for the derivation of well predicting personal thermal comfort models is developed based on real world voting data. A scalable modeling approach is derived that can be used in the context of optimal control.

✓ Optimization-based control approaches are devised for improving the individual thermal comfort in a shared office space by the use of multiple ceiling fans.

Chapter 2 covers the first aspect. Multiple CFD scenarios with various ventilation conditions are used as ground truth for the spatially heterogeneous room conditions of a large open-plan office. A GP regression model is derived to represent the impact of different HVAC operation modes on the stationary temperature profile based on a sensor network. Since the sensor configuration has a direct impact on the model's quality, optimal sensor placement strategies are derived and transferred to general placement rules.

Chapter 3 addresses the second objective where a better understanding of individual comfort is obtained. Commonly applied standard models are investigated according to their ability to map the subjective thermal sensation. To cope with the revealed disadvantages of existing models, a generalizable structure is defined and different feature selection algorithms are applied to specify a commonly optimal approach.

The previously derived models are then adopted in Chapter 4.2 to find the best compromise between all occupants. A trajectory planning algorithm is developed based on the individual comfort models. It incorporates the ability to learn the occupants thermal preferences online and adapts new input from ongoing user feedback. The trajectory generation as well as the modeling process are designed under the premise to ensure robust and physically feasible solutions based on limited knowledge of the occupants' physical and psychological state. Furthermore, the building dynamics are considered as a black-box where only measurements serve as an interface to the room conditions. Therefore, the trajectory planning algorithm can be considered as a retrofit solution that is nearly independent from the building system.

Chapter 4.3 combines the comfort model with a physical room model so that the trajectory generation is replaced by an MPC approach. This allows for a coupled consideration of the system dynamics and the personal comfort. Since the system as well as the comfort prediction models are nonlinear and complicate the MPC algorithm, a linearization is performed for an application of simpler, linear concepts. Subsequently, the performance of the nonlinear and linear MPC approach are compared to the results from the trajectory planning approach.

Chapter 5 summarizes all results and provides some perspectives about potential development opportunities.

2 Temperature Field Prediction

For the control of the thermal conditions in commercial buildings, the building is commonly separated in multiple zones. Most often one room corresponds to one zone and the room air is assumed to be well-mixed which leads to a uniform temperature distribution within this zone. However, influences like changing occupancy, solar radiation or internal loads from computers and other devices affect the room temperature locally and can lead to diverse conditions within one zone. Moreover, unfavorable setup of partitions and desks or adverse location and operation of the Air Conditioning (AC) system can further exacerbate the heterogeneity of the indoor conditions. While these effects are commonly neglected in building operation, they can have a significant impact on the occupants' satisfaction. A more detailed representation of the room conditions can be either achieved by physically motivated models representing the fluid dynamics or by additional sensing. The high complexity, implementation and computation effort as well as the limited validity are still an exclusion criterion of physical models for user-friendly, large-scale applications in commercial buildings [7]. The trend towards the Internet of Things (IoT), on the other hand, opens up opportunities for the deployment of more sensors that can be used to reconstruct the indoor conditions. Data-based models are the logical consequence to this development. The great advantage of this approach over physical models is the inherent adaptivity to system changes. The physical approach needs detailed knowledge about the boundary conditions and the geometric information. However, the former is difficult to obtain due to limited measurements (particularly of dynamic disturbances, e.g. occupancy, open doors etc.) and the latter is often subject to changes during the lifetime of a building. The data-based approach can be updated continuously based on the current measurements so that system changes and disturbance patterns are adapted online. This idea builds the basis for the following modeling approach. The model is derived and evaluated based on CFD simulations that provide very detailed information about the spatial room conditions.

In the following, the terms inlet and supply refer to the opening at the system boundary of the room where conditioned air enters the space and are used equivalently. Similarly outlet and exhaust are used equipollent. Furthermore, parts of the consecutive results are published in [41] and [44].

2.1 CFD Simulation Setup

A CFD simulation of a large open-plan office serves as a reference for the data-based modeling of the temperature field. All CFD results are taken from [8] where more detailed descriptions about the exact simulation settings (solver, meshing etc.) can be found. Figure 2.1 illustrates the simulation setup and an exemplary temperature field. It represents a typical shared office space with numerous desks, occupants and a partition. The downward facing side is a window facade as indicated in Figure 2.1a. The internal heat sources are given by the 16 occupants, 24 light modules and computers placed in front of each occupant. The conditioned air is introduced by 14 ceiling swirl diffuser inlets and discharged by 3 outlets, as depicted in Figure 2.1a. The mass flows collected in the vector $\dot{\boldsymbol{m}}_{\mathrm{sup}}$ are varied to excite the room in multiple ways. The corresponding supply temperatures $\boldsymbol{T}_{\mathrm{sup}}$ are set to $17\,^{\circ}\mathrm{C}$ when $\dot{\boldsymbol{m}}_{\mathrm{sup}} > 0$ and otherwise represent the local room temperature. The exhaust conditions, given by $\boldsymbol{T}_{\mathrm{exh}}$ and $\dot{\boldsymbol{m}}_{\mathrm{exh}}$, are a results of the supplied mass flows to satisfy the conservation equations for mass, momentum and energy (1.5).

For defining the various AC operational scenarios, the office is divided in three similarly sized zones and each zone is operated with different Air Changes per Hour (ACH) as described in Figure 2.2. Zone 1 and 2 are separated by a partition. Each zone has multiple inlets and one outlet. In most cases, the middle zone 2 is operated with an air change rate of 3 ACH. Simultaneously, the air change rate of the outer zones is gradually increased from 1 to 5 ACH. Each operational mode is combined with one out of three outlet setups where either the outlet in zone 1 or 2 is closed. Additionally, one extreme operational mode is added where the air change rate in zone 2 is reduced to 1 ACH and the outer zones are operated with the maximum mass flow of 5 ACH. This inlet condition is also combined with the three different outlet setups. Figure 2.2 illustrates how inlet and outlet conditions are combined for the simulations. Furthermore, four unidirectional ventilation conditions are investigated where the outer zones are operated dominantly and either the supplies or the exhaust of a zone are activated. ANSYS Fluent is used to simulate the steady-state temperature and flow conditions of the $N_{\mathrm{cfd}} = 18$ different ventilation scenarios which serve as a reference for the following model derivation.

Only the supply and exhaust conditions are varied in the different simulation setups while all other boundary conditions, such as occupancy, lights, computers and outside conditions are maintained. Since the simulated office space is surrounded by other offices all internal walls are assumed to be adiabatic except for the window facade. The external boundary conditions correspond to an exemplary sunny day in Stuttgart at the end of March. Solar radiation enters the office through the window front and is computed for a sun position around noon. The resulting solar influences are calculated based on Fluent's solar ray tracing algorithm [5]. The outside temperature is $15\,^{\circ}\mathrm{C}$. These boundary conditions in combination with the different ventilation setups of Figure 2.2 lead to average room temperatures that vary between $23.2\,^{\circ}\mathrm{C}$ and
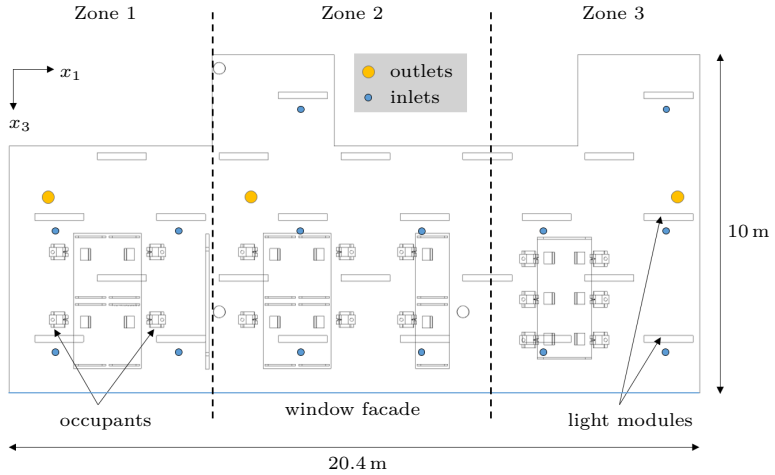
(a) Top view of CFD simulation setup.
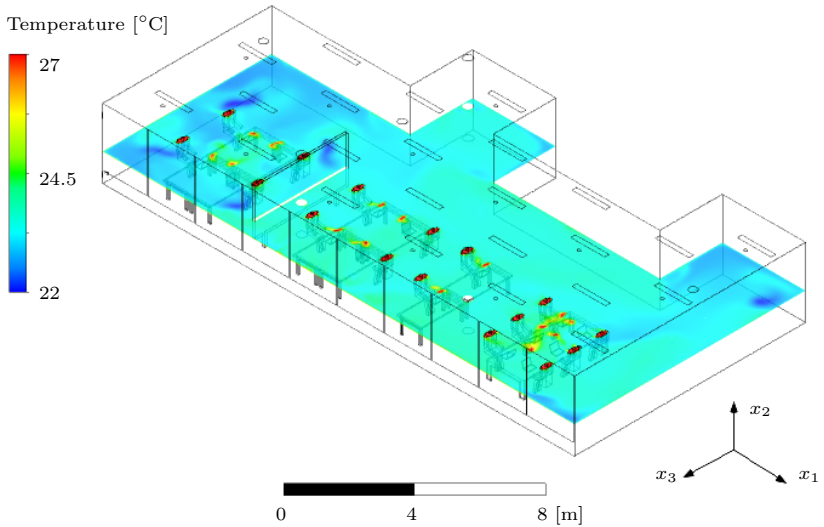
(b) Exemplary result for the temperature distribution where zone 1 and 3 are operated with 4 ACH and the outlet of zone 2 is closed [41].

Figure 2.1: CFD simulation of open-plan office used as reference for data-based modeling.

Inlet conditions

Zone 1	Zone 2	Zone 3
1 ACH	3 ACH	1 ACH
3 ACH	3 ACH	3 ACH
4 ACH	3 ACH	4 ACH
5 ACH	3 ACH	5 ACH
5 ACH	1 ACH	5 ACH
0 ACH	0 ACH	3 ACH
0 ACH	0 ACH	8 ACH
5 ACH	0 ACH	5 ACH
9 ACH	$\frac{3}{2}$ ACH	0 ACH

Position of outlet

Zone 2 and 3

Zone 1 and 3

All zones

Zone 1

Zone 2

Zone 3
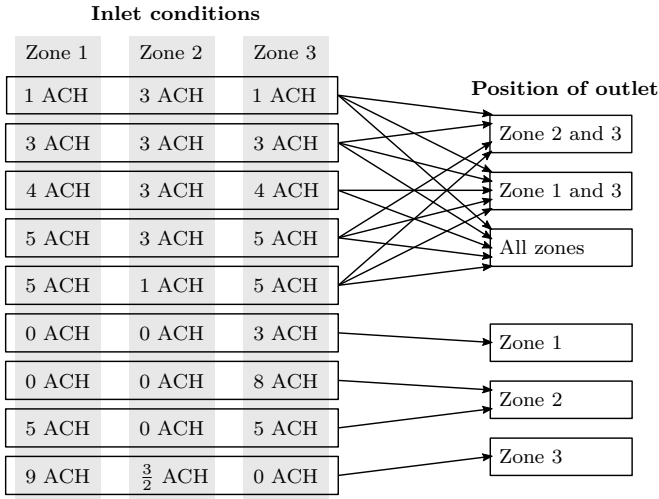
Figure 2.2: Combination of inlet and outlet conditions for the different ventilation scenarios.

31.6 °C depending on the applied air change rate. A more detailed description of the ventilation setups and the corresponding room conditions is provided in Appendix A.2.

One exemplary simulation output for the temperature distribution is shown in Figure 2.1b. The pictured temperature field corresponds to the ventilation condition where zone 1 and 3 are operated with an air change rate of 4 ACH and zone 2 with 3 ACH whereas the outlet in zone 2 is closed. As a result, the outer zones with a higher ventilation rates have lower temperatures, especially in zone 1 where the partition partially blocks the air exchange.

2.2 Data-Based Modeling of Temperature Field

CFD simulations give a very detailed representation of the room conditions but are computationally expensive and require a high implementation effort. Furthermore, the knowledge of the exact room geometries, materials or boundary conditions are often unknown, not to mention disturbances by moving occupants, changing weather conditions and varying usage of devices. This disqualifies the application of CFD on building level for most control approaches. Zonal models, as presented in [81] and [102], can provide a higher resolution of the room conditions but require careful calibration including detailed measurements and a high expert knowledge for implementation.

Both, zonal models and CFD, are very sensitive to changes in the room layout, such as restructuring of work stations, desks and partitions what can happen regularly in office buildings. This introduces a high complexity for large-scale commercial buildings and the need for monitoring the exact room setup throughout the operational life. Besides the high computational effort and complexity, disproportionate many sensors and advanced monitoring systems would be necessary to provide all required information for an application of these approaches for building control. However, the available measurements on room level are commonly limited to air temperatures T_air and inlet or outlet conditions. Consequently, the room temperature is commonly assumed to be uniformly distributed so that one or the average of multiple sensor measurements serves as representative temperature value for further control actions. Certainly, an increasing number of sensors improves the knowledge about the spatial room conditions but enhanced control methods also require information how to interpolate between the discrete measurements and how changing AC operation affects the local conditions. To overcome the challenges of the described physics-based models, a purely data-based room model is designed which only uses available measurements instead of requiring universal knowledge about the building geometry, materials, operation and usage. The local temperature measurements can be considered as samples of a specific probability distribution and estimating the hidden spatial process - here the temperature field - refers to sampling from this distribution. Due to its beneficial properties, a commonly applied distribution is the multivariate Gaussian distribution

$$P(\boldsymbol{T}) = (2\pi)^{-\frac{n}{2}} |\boldsymbol{K}_\mathcal{D}|^{-\frac{1}{2}} \exp\left(-\frac{1}{2}(\boldsymbol{T}-\boldsymbol{\mu})^\text{T} \boldsymbol{K}_\mathcal{D}^{-1}(\boldsymbol{T}-\boldsymbol{\mu})\right) \tag{2.1}$$

where $\boldsymbol{T}$ represents the vector of temperature samples and $\mathcal{D}$ indexes the n dimensional set of all considered observations. Using the multivariate Gaussian distribution allows for a concise formulation based on the mean vector $\boldsymbol{\mu}$ and the covariance matrix $\boldsymbol{K}_\mathcal{D}$ as well as efficient interference to define conditional distributions [66]. The GP regression approach provides the framework to specify $\boldsymbol{\mu}$ and $\boldsymbol{K}_\mathcal{D}$ based on a finite set of observations. It further enables to incorporate prior assumptions on smoothness or other known process characteristics and thus is especially useful for an estimation based on uncertain or limited data. This describes also the main advantage over other ML methods, for example ANN. The GP method provides a better understanding how the predictions work, thus leads to well-interpretable results. Moreover, measurement noise can be taken into account and each prediction value is inherently associated with a variance information. This explains why GP regression was successfully applied earlier for predicting spatial temperature distributions [29, 66]. Therefore, this method is adapted in the following and extended for mapping the influence of inlet and outlet conditions while only easily accessible environmental measurements are used [41]. Since the sensor amount and location directly define the available training data, intelligent sensor placement strategies are developed subsequently. Different strategies are compared and evaluated according to their predictive qualities.
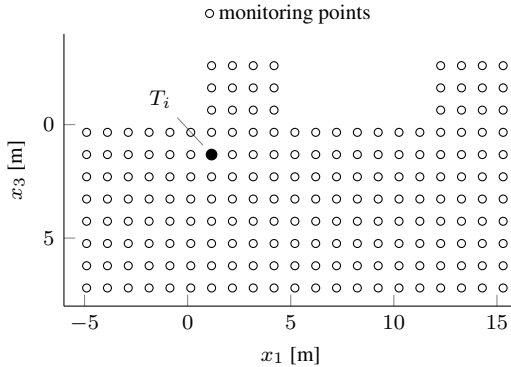
Figure 2.3: Monitoring points and possible sensor locations for the office space placed in the height of $x_2 = 1.2\,\text{m}$ [41].

2.2.1 Gaussian Process Model

The steady-state temperature field based on a specific ventilation setup is a location-dependent variable $T(\boldsymbol{\chi})$, where $\boldsymbol{\chi} = \begin{bmatrix} x_1 & x_2 & x_3 \end{bmatrix}^{\text{T}}$ denotes the Cartesian coordinates. Generally, the area of interest for the AC task is limited to the occupied zone which corresponds to the lower part of the room. For simplicity and due to mostly small vertical temperature differences within this zone, the 3 D temperature distribution is represented by the 2 D plane in the height of $x_2 = 1.2\,\text{m}$ according to the colored surface in Figure 2.1b. Consequently, the location vector can be reduced to $\boldsymbol{\chi} = \begin{bmatrix} x_1 & x_3 \end{bmatrix}^{\text{T}}$ for the following analysis. Furthermore, the temperature is monitored by multiple sensors distributed over the space. It is assumed that these sensors are located within the occupied zone. Figure 2.3 illustrates the $N_\text{m} = 192$ considered monitoring points in the x_1-x_3-plane which represent all possible sensor locations.

Modeling the effect of different ventilation scenarios requires additional knowledge about the varied boundary conditions. The actual temperature is consequently a function of the location as well as the supply and exhaust conditions, occupancy, internal heat sources, weather conditions and possible other disturbance effects. Thus, modeling the temperature field aims to find a mapping function[a]

$$T = f(\boldsymbol{z}) \tag{2.2}$$

[a]Generally, GP regression includes the Gaussian noise term $\epsilon \sim \mathcal{N}(0, \sigma_n)$ so that $T = f(\boldsymbol{z}) + \epsilon$. However, since all *measurement* data are extracted from CFD simulations, they can be considered as noise-free and ϵ is neglected hereinafter.

where all influencing factors are collected in the vector $\boldsymbol{z}$. Assuming every finite collection of local temperature measurements $T_i = T(\boldsymbol{z}_i)$ is normally distributed, the latent function $f(\boldsymbol{z})$ can be defined using GP regression [66].

The observation probability density of the temperature $P(T|f(\boldsymbol{z}))$ given by the prior of the GP can be conditioned on a set of observations $\mathcal{D} = \{(\boldsymbol{z}_i, T_i)\,|\,i = 1,\ldots,n\}$ [84]. The observed temperatures T_i are collected in the vector $\boldsymbol{T} = \begin{bmatrix} T_1 & \ldots & T_n \end{bmatrix}^{\mathrm{T}}$ and the corresponding inputs $\boldsymbol{z}_i$ (referred to as regression or feature vectors) in the matrix of observations $\boldsymbol{Z} = \begin{bmatrix} \boldsymbol{z}_1 & \ldots & \boldsymbol{z}_n \end{bmatrix}^{\mathrm{T}}$. Since a GP is used as a prior on f, the joint distribution of the function values $\boldsymbol{f} = \begin{bmatrix} f(\boldsymbol{z}_1) & \ldots & f(\boldsymbol{z}_n) \end{bmatrix}^{\mathrm{T}}$ is multivariate Gaussian

$$P(\boldsymbol{f}|\mathcal{D}) = \mathcal{N}(\boldsymbol{\mu}, \boldsymbol{K}) \tag{2.3}$$

with mean $\boldsymbol{\mu}$ and covariance matrix $\boldsymbol{K}$ [67]. The mean

$$\boldsymbol{\mu} = \boldsymbol{\mu}(\boldsymbol{Z}) = [\mu(\boldsymbol{z}_1)\ldots\mu(\boldsymbol{z}_n)]^{\mathrm{T}} \tag{2.4}$$

and the covariance function $\kappa(\boldsymbol{z}_i, \boldsymbol{z}_j)$ that specifies the matrix

$$\boldsymbol{K} = \boldsymbol{K}(\boldsymbol{Z}, \boldsymbol{Z}) = \begin{bmatrix} \kappa(\boldsymbol{z}_1, \boldsymbol{z}_1) & \ldots & \kappa(\boldsymbol{z}_1, \boldsymbol{z}_n) \\ \vdots & \ddots & \vdots \\ \kappa(\boldsymbol{z}_n, \boldsymbol{z}_1) & \ldots & \kappa(\boldsymbol{z}_n, \boldsymbol{z}_n) \end{bmatrix}, \tag{2.5}$$

provide multiple degrees of freedom for the modeling. For the temperature prediction task, a deterministic mean $\boldsymbol{\mu}$ is assumed which can either be prespecified as an overall average of the room temperatures or identified during the model training based on the available measurements. Both approaches are applied and compared in Section 2.2.3. The selection of the covariance function $\kappa(\boldsymbol{z}_i, \boldsymbol{z}_j)$ is a structural decision that defines the process properties. It can be interpreted as a similarity measure that defines the degree of correlation between the outputs based on the distance of the inputs. Five commonly applied candidates for the covariance function [84], as listed in Table 2.1, are considered and compared according their ability to adequately represent the spatial temperature field. Each kernel depends on the hyperparameters $\boldsymbol{\theta}$ which control its properties and provide a further degree of freedom. The hyperparameters $\boldsymbol{\theta}$ encompass the characteristic length scale σ_l, the signal standard deviation σ_f and the scale-mixture parameter ζ. These parameters are defined by maximizing the log likelihood function of the GP regression model [10]

$$\ln P(\boldsymbol{T}|\boldsymbol{\theta}) = -\frac{1}{2}\ln|\boldsymbol{K}| - \frac{1}{2}(\boldsymbol{T} - \boldsymbol{\mu})^{\mathrm{T}}\boldsymbol{K}^{-1}(\boldsymbol{T} - \boldsymbol{\mu}) - \frac{n}{2}\ln(2\pi). \tag{2.6}$$

The hyperparameters $\boldsymbol{\theta}$ are a structural model decision which is why the full knowledge about the room conditions is used for identifying $\boldsymbol{\theta}$ of each kernel candidate. Thus, the complete set of available observations is applied so that all N_{m} monitoring points are

Table 2.1: Kernel function candidates $\kappa(\boldsymbol{z}_i, \boldsymbol{z}_j)$ for the temperature prediction model, where $\left|\left|\Delta \boldsymbol{z}_{ij}\right|\right|_2 = \sqrt{\left(\boldsymbol{z}_i - \boldsymbol{z}_j\right)^{\mathrm{T}} \left(\boldsymbol{z}_i - \boldsymbol{z}_j\right)}$.

Kernel function	Definition for $\kappa(\boldsymbol{z}_i, \boldsymbol{z}_j)$
Squared Exponential Kernel	$\sigma_f^2 e^{-\frac{\|\Delta \boldsymbol{z}_{ij}\|_2^2}{2\sigma_l^2}}$
Rational Quadratic Kernel	$\sigma_f^2 \left(1 + \frac{\|\Delta \boldsymbol{z}_{ij}\|_2^2}{2\zeta\sigma_l^2}\right)^{-\zeta}$
Exponential Kernel	$\sigma_f^2 e^{-\frac{\|\Delta \boldsymbol{z}_{ij}\|_2}{\sigma_l}}$
Matérn 3/2	$\sigma_f^2 \left(1 + \frac{\sqrt{3}\|\Delta \boldsymbol{z}_{ij}\|_2}{\sigma_l}\right) e^{-\frac{\sqrt{3}\|\Delta \boldsymbol{z}_{ij}\|_2}{\sigma_l}}$
Matérn 5/2	$\sigma_f^2 \left(1 + \frac{\sqrt{5}\|\Delta \boldsymbol{z}_{ij}\|_2}{\sigma_l} + \frac{5\|\Delta \boldsymbol{z}_{ij}\|_2^2}{3\sigma_l^2}\right) e^{-\frac{\sqrt{5}\|\Delta \boldsymbol{z}_{ij}\|_2}{\sigma_l}}$

considered. Note that (2.6) can also be evaluated based on a subset of observations which will be the case for a real-world application where the available number of measurements is limited. However, full knowledge is used for the kernel selection to separate this step from the sensor placement problem. Since the evaluation of different kernels can only be performed when the model input $\boldsymbol{z}$ is selected, a comparison of the covariance function candidates is conducted in combination with the feature selection in the following section.

The GP modeling approach enables predictions of an unknown output temperature T_{pre} by considering the joint Gaussian distribution

$$\begin{bmatrix} \boldsymbol{T} \\ T_{\mathrm{pre}} \end{bmatrix} \sim \mathcal{N}\left(\begin{bmatrix} \boldsymbol{\mu}(\boldsymbol{Z}) \\ \mu(\boldsymbol{z}_{\mathrm{pre}}) \end{bmatrix}, \begin{bmatrix} \boldsymbol{K} & \kappa(\boldsymbol{Z}, \boldsymbol{z}_{\mathrm{pre}}) \\ \kappa(\boldsymbol{z}_{\mathrm{pre}}, \boldsymbol{Z}) & \kappa(\boldsymbol{z}_{\mathrm{pre}}, \boldsymbol{z}_{\mathrm{pre}}) \end{bmatrix}\right). \tag{2.7}$$

The sought estimate of T_{pre} at a test point $\boldsymbol{z}_{\mathrm{pre}}$ is then given by the posterior mean and variance

$$\mu_{\mathrm{pre}} = \mu(\boldsymbol{z}_{\mathrm{pre}}) + \kappa(\boldsymbol{z}_{\mathrm{pre}}, \boldsymbol{Z})\boldsymbol{K}^{-1}(\boldsymbol{T} - \boldsymbol{\mu}(\boldsymbol{Z})) \tag{2.8a}$$

$$\sigma_{\mathrm{pre}}^2 = \kappa(\boldsymbol{z}_{\mathrm{pre}}, \boldsymbol{z}_{\mathrm{pre}}) - \kappa(\boldsymbol{z}_{\mathrm{pre}}, \boldsymbol{Z})\boldsymbol{K}^{-1}\kappa(\boldsymbol{Z}, \boldsymbol{z}_{\mathrm{pre}}) \tag{2.8b}$$

which is derived in Appendix A.1.

2.2.2 Selection of Kernel Function and Model Input Definition

The input vector $\boldsymbol{z} \in \mathbb{R}^{N_z}$ for the GP model can be chosen in different ways. The definition of the optimal input combination (feature selection) is an important part of the modeling process and a crucial impact factor for the predictive model capabilities [47]. The more data are available the better the trained prediction model. However, using the wrong (irrelevant) data can lead to overfitting and poorly generalizing models. Hence, the relevance and composition of potential model inputs is considered in addition to the structural decision regarding mean value μ and covariance function κ. For the following analysis, the temperature prediction task is divided into two levels of complexity:

1. Spatial temperature prediction with fixed HVAC operation (mapping function for one CFD scenario),

2. Spatial temperature prediction with varying HVAC operation (mapping function for all CFD scenarios).

The model's input selection for the first task is trivial because the steady-state temperature T_{ir} resulting from the ventilation scenario r only depends on the location $\boldsymbol{\chi}_i$ when all other boundary conditions are constant. In this case, the set of N_{sens} sensors distributed over the room for monitoring the local temperature provides the training data $\mathcal{T}_r = \{(\boldsymbol{\chi}_i, T_{ir}) | i = 1, \ldots, N_{\text{sens}}\}$ and the GP model has the form

$$T_{ir} = f_r(\boldsymbol{\chi}_i).$$

Predicting the local temperature based on varying HVAC operation, on the other hand, requires additional knowledge about the boundary conditions. Instead of training separate models f_r for each ventilation scenario r, the target model ought to map the temperature profile for an arbitrary HVAC mode. Thus, the observed temperature

$$T_{ir} = f(\boldsymbol{z}_{ir})$$

also depends on the supply conditions and occurring disturbances, where disturbances refer to occupancy, boundary and weather conditions as well as internal loads. Measurements of the inlet and outlet conditions are commonly monitored in commercial buildings and thus can be included in the list of potential model inputs. Although internal and external disturbances have a significant impact on the temperature profile of a real-world office space, they are not varied over the considered CFD simulation setups and therefore neglected for the following analysis. Nevertheless, the modeling approach and corresponding analysis can be easily extended by additional inputs for mapping the influence of further parameters.

In a first analysis, each ventilation scenario is considered separately. This corresponds to the task of mapping one of the simulation setups outlined in Figure 2.2. Hence, the GP model only needs to represent the steady-state profile due to one specific supply

Table 2.2: Comparison of different kernel functions $\kappa(\boldsymbol{z}_i, \boldsymbol{z}_j)$ for the setup-specific temperature prediction model based on the prediction error of over 140 random sensor placements.

GP model	MSE	Squared Exp.	Rational Quadratic	Exp.	Matérn 3/2	Matérn 5/2	$\bar{T}_{\mathrm{sens}}$
	ave.	0.300	0.285	0.291	0.286	0.288	0.354
$f_r(\boldsymbol{\chi}_i)$	min.	0.235	0.229	0.233	0.231	0.232	0.339
	max.	0.457	0.338	0.431	0.395	0.423	0.394

and exhaust condition. Since all boundary conditions are constant and the HVAC system is operated in a fixed mode, the only necessary input information is given by the location $\boldsymbol{\chi}_i$ and the model input is set to $\boldsymbol{z}_i = \boldsymbol{\chi}_i$. With this input definition, all kernels of Table 2.1 are applied and compared according to their predictive performance. After identifying the setup-specific hyperparameters $\boldsymbol{\theta}_r$ and prior mean μ_r based on (2.6) using the full data set $\mathcal{D}_r = \{(\boldsymbol{\chi}_i, T_{ir}) | i = 1, \ldots, N_{\mathrm{m}}\}$, the prediction accuracy of the different kernel functions is compared for multiple random sensor placements. The GP model is trained with the tuples of the sensor location and the corresponding output temperature $\mathcal{T}_r = \{(\boldsymbol{\chi}_i, T_{ir}) | i = 1, \ldots, N_{\mathrm{sens}}\}$ and then used to predict the remaining room temperatures based on (2.8a). Figure 2.4 illustrates the model training process when further sensors are added to the setup and provide supplementary observations, thus improve the prediction of the spatial room conditions. The GP prediction $T_{\mathrm{GP},ir} = f_r(\boldsymbol{\chi}_i)$ is compared to the ground truth $T_{\mathrm{CFD},ir}$ by evaluating the average Mean Squared Error (MSE)

$$\mathrm{MSE} = \frac{1}{N_{\mathrm{cfd}}} \sum_{r=1}^{N_{\mathrm{cfd}}} \frac{1}{N_{\mathrm{m}}} \sum_{i=1}^{N_{\mathrm{m}}} (T_{\mathrm{CFD},ir} - T_{\mathrm{GP},ir})^2. \tag{2.9}$$

As described above, the training data $\mathcal{T}_r$ comprise the N_{sens} sensor measurements. This means that each sensor setup j results in a different training set $\mathcal{T}_{rj}$ which is represented by a particular matrix of observations $\boldsymbol{Z}_{rj}$ and corresponding vector of outputs $\boldsymbol{T}_{rj}$. Consequently, the sensor setup inevitably influences the prediction accuracy, as illustrated in Figure 2.4, and can also lead to a different ranking of the kernel candidates. Therefore, more than 140 random sensor configurations of 5 to 10 sensors are evaluated and the average prediction error of all configurations is used for the selection of the kernel function. Note that using more sensors generally leads to lower prediction errors. The random configurations are chosen based on 5 to 10 sensors because particularly the performance for realistically sized sensor networks is of interest for a later application of this method. Table 2.2 lists the average, minimum and maximum MSE for the applied sensor setups. The range between the minimum

2 sensors (MSE=1.01 K^2)

(a) GP model prediction trained with two sensors.

5 sensors (MSE=0.38 K^2)

(b) GP model prediction trained with five sensors.

10 sensors (MSE=0.28 K^2)

T_{CFD} (ground truth)

T_{GP}

95 % confidence interval

• Sensors

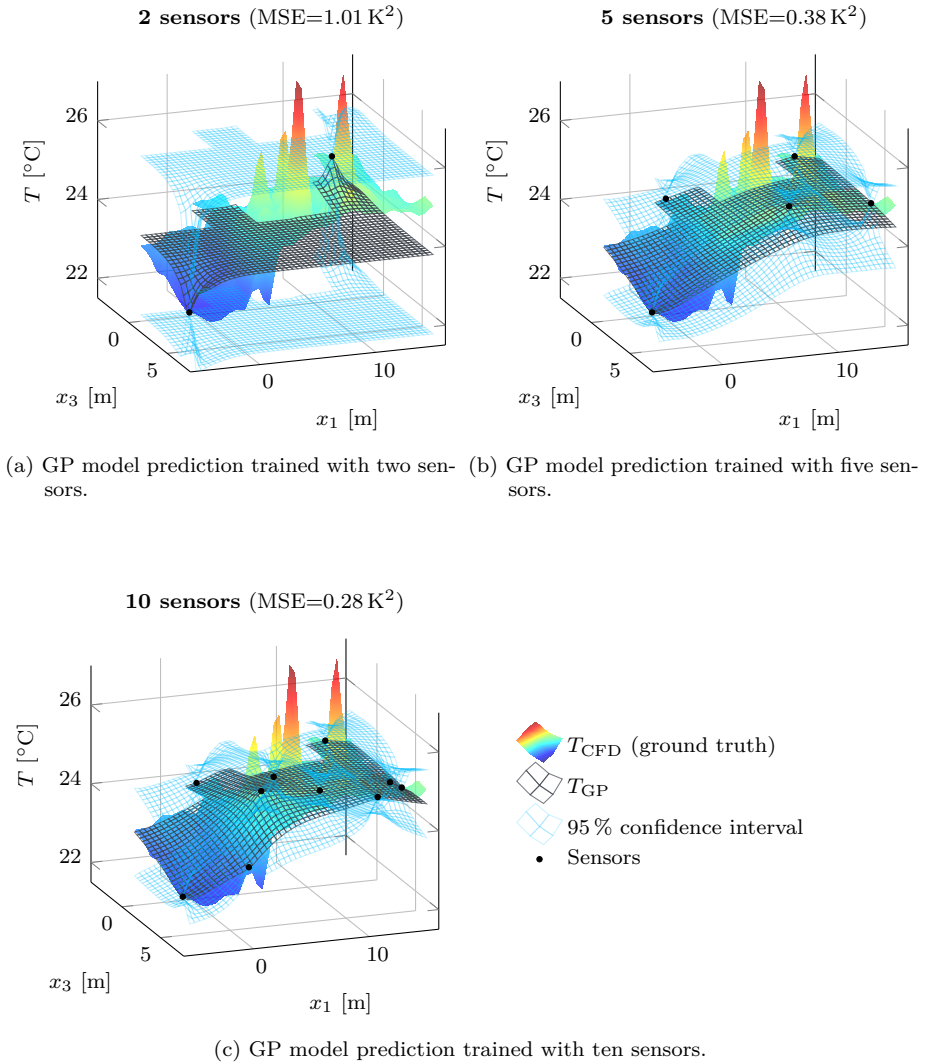(c) GP model prediction trained with ten sensors.

Figure 2.4: Visualization of the training process while increasing the number of sensors using the Rational Quadratic Kernel and Setup 18 (see Appendix A.2).

and maximum MSE clearly demonstrates the importance of the sensor locations and emphasizes that unfavorably placed sensors provide a poor data base for the corresponding model. However, unfavorably selected sensor positions also affect the performance of the benchmark assumption of well-mixed conditions where the average sensor temperature

$$\bar{T}_{\text{sens},r} = \frac{1}{N_{\text{sens}}} \sum_{i=1}^{N_{\text{sens}}} T_{\text{sens},ir} \tag{2.10}$$

serves as the best guess for a uniform temperature field. According to Table 2.2, all GP models outperform this standard approach regarding the average MSE. Furthermore, the achievable prediction accuracy is comparable for all applied kernels. Only the maximum error, which is related to the worst sensor placement, reveals some differences. Here, the Rational Quadratic Kernel shows the most beneficial properties by leading to lower predictions errors even for unfavorable sensor setups. In summary, this kernel yields the best results regarding the average, best and worst case performance and is therefore chosen for the following analysis. The suitability of this covariance function, can also be explained by the expected characteristic of the temperature profile: The Rational Quadratic Kernel is equivalent to an infinite sum of Squared Exponential Kernels with varying length scales σ_l and hence suitable for functions that vary smoothly across different length scales. The scale-mixture ζ defines the weighting of the different length scales at which a small value allows for mapping local variations while larger scale trends can be still captured by σ_l. For $\zeta \to \infty$, the Rational Quadratic Kernel equals the Squared Exponential Kernel. Similarly to the described kernel characteristics, temperature is expected to vary smoothly over the room due to relatively high mixing effects what suggests a large length scale. However, local heat sources, like electrical devices, occupants or supplies, influence the temperature distribution selectively as it can be observed in Figure 2.4. These effects can be incorporated by a smaller value ζ.

A comparison between the GP model prediction T_{GP} and the average sensor temperature $\bar{T}_{\text{sens}}$ by means of one exemplary setup is depicted in Figure 2.5. The partition at approximately $x_1 = 0$ reduces the mixing effects and produces a significant temperature gradient within the office space. As a consequence, the assumption of well-mixed conditions does not provide a good representation of the room conditions. The GP regression approach interpolates between the sensor measurements and improves the prediction by over 60 % so that the overall temperature profile is mapped appropriately. Only the temperature peaks at local heat sources cannot be captured yet due to the limited number of measurement samples. Mapping these effects would require additional sensors at the corresponding locations.

Another benefit of the GP regression approach originates from the associated prediction variance (2.8b). This can be interpreted as an indicator for the certainty of the prediction. Hence, a high variance points to a high risk of an incorrect estimate.
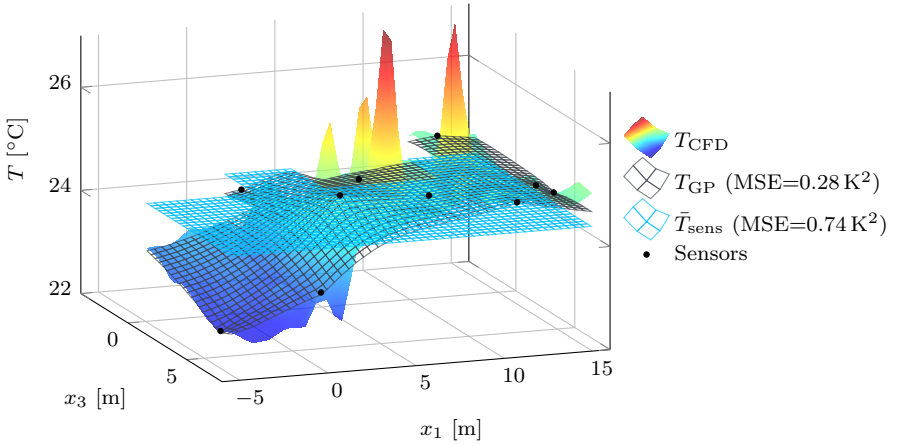
Figure 2.5: Comparison of the GP model prediction T_{GP} and the average sensor temperature $\bar{T}_{\text{sens}}$ for estimating the ground truth T_{CFD} of Setup 18.

The 95% confidence interval $(\pm 2\sigma(\boldsymbol{\chi}))$, shown in Figure 2.4, highlights the higher uncertainty for few sensors and the narrowing bounds while the training set is extended by additional observations. Consequently, the variance of the GP prediction does not only indicate the prediction quality but also points towards good or bad sensor configurations which is revisited for the optimization of sensor locations in the consecutive section.

The previous results show the general validity of the regression method and allow for spatial temperature predictions based on a specific ventilation condition. However, intelligent control approaches require a mapping how the operation mode influences the temperature profile. In contrast to the previous evaluation, the final model should be able to map the temperature distribution resulting from various ventilation conditions. Hence, the temperature does not only depend on the location but also on the supply and exhaust setup. Therefore, the model input is extended by the supply and exhaust conditions given in terms of the corresponding vector of inlet and outlet temperatures, $\boldsymbol{T}_{\text{sup}}$ and $\boldsymbol{T}_{\text{exh}}$, as well as the mass flows, $\dot{\boldsymbol{m}}_{\text{sup}}$ and $\dot{\boldsymbol{m}}_{\text{exh}}$:

$$\boldsymbol{z}_{\boldsymbol{\chi}} = \begin{bmatrix} \boldsymbol{\chi}^{\text{T}} & \boldsymbol{T}_{\text{sup}}^{\text{T}} & \dot{\boldsymbol{m}}_{\text{sup}}^{\text{T}} & \boldsymbol{T}_{\text{exh}}^{\text{T}} & \dot{\boldsymbol{m}}_{\text{exh}}^{\text{T}} \end{bmatrix}^{\text{T}}. \tag{2.11a}$$

Furthermore, a second approach for the input definition is considered. Instead of using the Cartesian coordinates $\boldsymbol{\chi} = \begin{bmatrix} x_1 & x_3 \end{bmatrix}^{\text{T}}$, the location can be alternatively defined based on distances to the corresponding inlets and outlets. This relative definition of the location is outlined in Figure 2.6. The motivation for this alternative representation is based on the assumption that the impact of an actuator or a disturbance source is
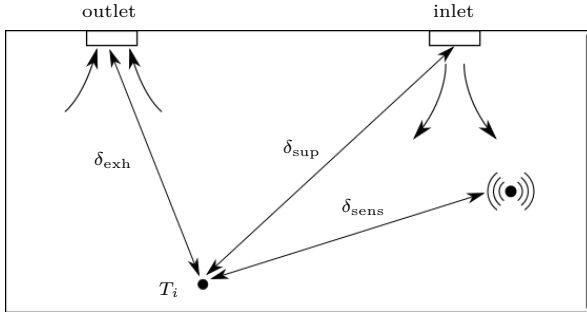
Figure 2.6: Distance-based model generation for predicting T_i [41].

connected to the distance between the point of interest and the source. Consequently, a second input vector is taken into account for the GP regression model:

$$z_\delta = \begin{bmatrix} \boldsymbol{\delta}_{\text{sup}}^{\text{T}} & \boldsymbol{T}_{\text{sup}}^{\text{T}} & \dot{\boldsymbol{m}}_{\text{sup}}^{\text{T}} & \boldsymbol{\delta}_{\text{exh}}^{\text{T}} & \boldsymbol{T}_{\text{exh}}^{\text{T}} & \dot{\boldsymbol{m}}_{\text{exh}}^{\text{T}} \end{bmatrix}^{\text{T}} \tag{2.11b}$$

where $\boldsymbol{\delta}_{\text{sup}}$ contains the distances to all supplies and $\boldsymbol{\delta}_{\text{exh}}$ to the exhausts. Equivalently to the previous separate setup consideration, the five different stationary kernels presented in Table 2.1, are again compared regarding their ability of mapping the temperature profile but now including various ventilation conditions. Hence in this case, the training set encompasses the input and output data from all ventilation scenarios $\mathcal{T} = \{(z_{ir}, T_{ir}) | i = 1, \dots, N_{\text{sens}}, r = 1, \dots, N_{\text{cfd}}\}$. Since the input vector elements of z_{ir} do not have the same unit/scale, the columns of the corresponding matrix of observations $\boldsymbol{Z}$ are standardized to ensure an equivalent impact on the Euclidean norm $\left\|\Delta z_{ij}\right\|_2$ in the kernel function $\kappa(z_i, z_j)$. The previously considered > 140 sensor configurations are applied and evaluated for the various kernel functions. Table 2.3 lists the resulting average MSE for the two input vector definitions (2.11). Comparing the results of the approaches $T_{ir} = f(z_{(\cdot),ir})$ to the previous separate approach $T_{ir} = f_r(\boldsymbol{\chi}_i)$ (according to Table 2.2) shows that the prediction error is lower for the scenario-specific models. The reason for this result is the higher complexity of the second modeling goal. Finding one model that describes the spatial relations for various boundary conditions is more difficult than only mapping one fixed temperature profile. The differences between the different kernels are again relatively small but remarkable deviations are visible for the maximum prediction errors. Regarding the average, minimum and maximum MSE for both, the location- and distance-based input combinations, the Rational Quadratic Kernel leads once more to the best performance and is consequently retained for the following analysis where the two approaches are evaluated in more detail.

A comparison of the MSE values in Table 2.3 supports that the selected elements

Table 2.3: Comparison of different kernel functions $\kappa(\boldsymbol{z}_i, \boldsymbol{z}_j)$ for the temperature prediction models based on the prediction error of over 140 random sensor placements.

GP model	MSE	Squared Exp.	Rational Quadratic	Exp.	Matérn 3/2	Matérn 5/2	$\bar{T}_{\text{sens}}$
	ave.	0.485	0.273	0.314	0.331	0.372	0.354
$f(\boldsymbol{z}_{\boldsymbol{\chi},ir})$	min.	0.257	0.229	0.240	0.235	0.242	0.339
	max.	1.276	0.386	0.578	0.827	0.925	0.394
	ave.	5.058	0.301	0.312	0.309	0.320	0.354
$f(\boldsymbol{z}_{\delta,ir})$	min.	4.951	0.240	0.246	0.243	0.245	0.339
	max.	5.222	0.423	0.586	0.769	0.620	0.394

of the input vector $\boldsymbol{z}$ have a significant impact on the prediction quality. To define the best feature vector, not only the two vectors (2.11) are considered but also their condensed forms

$$\boldsymbol{z}_{\boldsymbol{\chi}}^{\text{sup}} = \begin{bmatrix} \boldsymbol{\chi}^{\text{T}} & \boldsymbol{T}_{\text{sup}}^{\text{T}} & \dot{\boldsymbol{m}}_{\text{sup}}^{\text{T}} \end{bmatrix}^{\text{T}} \tag{2.12a}$$

$$\boldsymbol{z}_{\delta}^{\text{sup}} = \begin{bmatrix} \boldsymbol{\delta}_{\text{sup}}^{\text{T}} & \boldsymbol{T}_{\text{sup}}^{\text{T}} & \dot{\boldsymbol{m}}_{\text{sup}}^{\text{T}} \end{bmatrix}^{\text{T}} \tag{2.12b}$$

where the exhaust conditions are neglected. Accordingly, four different input combinations are compared regarding their influence on the prediction accuracy of the resulting GP model:

$$T_{\boldsymbol{\chi}}^{\text{sup}} = f(\boldsymbol{z}_{\boldsymbol{\chi}}^{\text{sup}}), \qquad T_{\boldsymbol{\chi}} = f(\boldsymbol{z}_{\boldsymbol{\chi}}), \qquad T_{\delta}^{\text{sup}} = f(\boldsymbol{z}_{\delta}^{\text{sup}}) \qquad \text{and} \qquad T_{\delta} = f(\boldsymbol{z}_{\delta}).$$

The evaluation is again conducted based on the performance of the > 140 sensor setups to obtain a representative result. Since the optimal hyperparameters $\boldsymbol{\theta}$ depend on the applied input vector, $\boldsymbol{\theta}$ is identified separately for each modeling approach where the input $\boldsymbol{z}_{ir}$ is replaced by the model-specific representation. The training data are provided by the monitored outputs of the assumed sensor configuration, thus $\mathcal{T} = \{(\boldsymbol{z}_{ir}, T_{ir}) | i = 1, \ldots, N_{\text{sens}}, r = 1, \ldots, N_{\text{cfd}}\}$. Subsequently, the trained models are utilized to predict the temperature at every points of interest for all ventilation scenarios and the MSE (2.9) serves as indicator for the model performance. Each prediction is further associated with a variance, according to (2.8b), to indicate the general prediction certainty. Therefore, the average prediction variance

$$\bar{\sigma}^2 = \frac{1}{N_{\text{cfd}}} \sum_{r=1}^{N_{\text{cfd}}} \frac{1}{N_{\text{m}}} \sum_{i=1}^{N_{\text{m}}} \sigma^2(\boldsymbol{z}_{ir}) \tag{2.13}$$
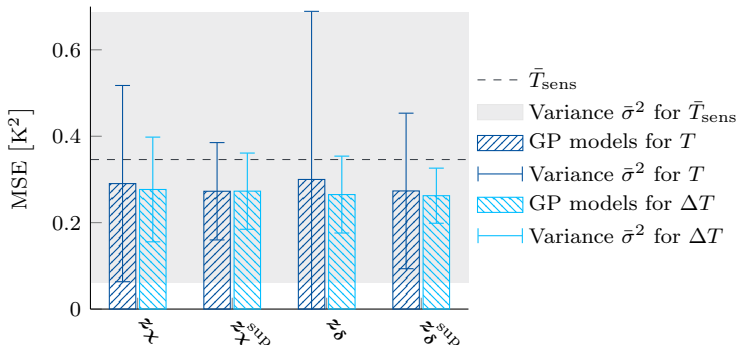
Figure 2.7: Comparison of location- and distance-based GP model approaches and different definitions of the mean. The MSE and variance are averaged over all monitoring points and ventilation scenarios.

is introduced as additional measure for the model quality. The dark blue bars of Figure 2.7 show the average mean and variance values over all monitoring points and ventilation scenarios according to (2.9) and (2.13) respectively. Similarly to the outcome of Table 2.3, it can be observed that all GP approaches (2.11) and (2.12) improve the temperature profile estimation compared to $\bar{T}_{\text{sens}}$. However, the resulting MSE is also similar for all feature vector candidates. The actual benefit becomes obvious when the model variance $\bar{\sigma}^2$ is considered. Comparing the variance of the average sensor temperature $\bar{T}_{\text{sens}}$ with the GP model results reveals the significant improvement of certainty. Furthermore, the model variance using the larger feature vectors (2.11) is higher than for (2.12) where $\boldsymbol{T}_{\text{exh}}$ and $\dot{\boldsymbol{m}}_{\text{exh}}$ are neglected. Consequently, the inlet conditions are not only important but also sufficient for the temperature field estimation. The outlet conditions do not provide significant information content that outweighs the uncertainty of the higher dimensional input combination. The higher number of features introduces a risk of overfitting which increases the variance of the predictions [47]. This effect is also visible when the location- and distance-based models are compared. The greater number of model parameters for the distance-based approaches, (2.11b) and (2.12b), results in a higher variance although the average prediction accuracy is almost identical.

The achievable prediction accuracy is related to the present ventilation condition. The individual results for each CFD simulation scenario $r \in \{1, \dots, N_{\text{cfd}}\}$ are depicted in Figure 2.8. It contrasts the MSE for the different GP models with the average sensor temperature $\bar{T}_{\text{sens}}$. In most cases, the GP models perform better but occasional outliers occur, e. g. due to inadequate model extrapolation when sensors are placed unfortunately. The data-based GP model only learns the effects that are part of the
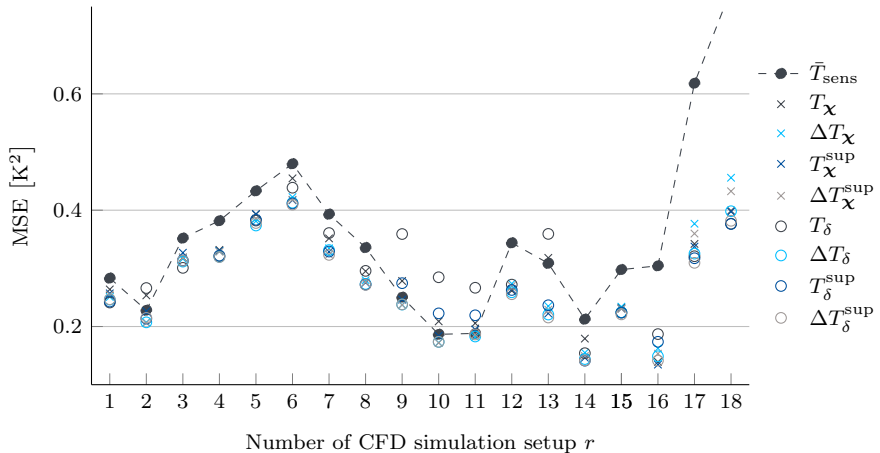
Figure 2.8: Comparison of different GP models for the N_{cfd} considered ventilation scenarios.

training data. Therefore, the small number of sensors limits the information content captured by the observations such that low system excitation at the sensor positions can occur for some of the simulated ventilation scenarios and sensor setups. For measuring the actual benefit of the GP model compared to the benchmark $\bar{T}_{\text{sens}}$, the reduction of the average MSE

$$D_r = \frac{\text{MSE}(\bar{T}_{\text{sens},r}) - \text{MSE}(T_{\text{GP},r})}{\text{MSE}(\bar{T}_{\text{sens},r})} \cdot 100\,\% \tag{2.14}$$

is examined. The first half of Table 2.4 lists the corresponding average, minimum and maximum values of D_r. Although the difference between the averaged MSE for the GP model and $\bar{T}_{\text{sens}}$ (see Figure 2.7) is relatively small, the estimation error for a specific ventilation scenario can be reduced by up to 56\,% using the model $T_{\boldsymbol{\chi}}^{\text{sup}}$. Moreover, this value is based on the average MSE of > 140 sensor configurations and even includes the impact of unfortunate setups. On the other hand, the worst case scenario introduces a deterioration of up to $-51\,\%$ for the model T_δ. In this case, the training data do not include enough information that the high dimensional, distance-based GP model allows for valid interpolation between the sensor measurements for the considered ventilation condition. Combining the observed results suggests that the model $T_{\boldsymbol{\chi}}^{\text{sup}}$ is the best compromise between accuracy, variance and worst case assessment. This approach provides the best average prediction accuracy and the lowest variance. Furthermore, it incorporates the highest improvement compared to the average sensor temperature $\bar{T}_{\text{sens}}$. Although this model already yields an

Table 2.4: Minimum and maximum improvement D_r (2.14) for all GP model approaches compared to the sensor average.

		$T_{\boldsymbol{\chi}}$	$T_{\boldsymbol{\chi}}^{\text{sup}}$	T_{δ}	T_{δ}^{sup}	$\Delta T_{\boldsymbol{\chi}}$	$\Delta T_{\boldsymbol{\chi}}^{\text{sup}}$	ΔT_{δ}	$\Delta T_{\delta}^{\text{sup}}$
$\frac{1}{N_{\text{cfd}}}\sum_{r}^{N_{\text{cfd}}} D_r$	[%]	12.7	19.0	7.0	17.4	18.7	19.6	21.3	21.8
$\min_{r}(D_r)$	[%]	-10.6	-3.2	-50.9	-19.3	3.2	1.1	1.0	2.8
$\max_{r}(D_r)$	[%]	54.3	55.8	51.6	51.7	46.7	49.6	51.1	53.5

average improvement of 19 %, some outliers still degrade the predominant advantages. Figure 2.8 reveals that the prediction error of the GP model is similar and even worse than the benchmark $\bar{T}_{\text{sens}}$ for the ventilation setups 9 to 11. Referring to the corresponding temperature profiles depicted in Figure A.1 exposes that these scenarios result in generally higher temperatures due to the lower ACHs. Furthermore, the local temperature differences are small such that $\bar{T}_{\text{sens}}$ already results in a valid estimation and the actual potential of improvement is relatively small. Additionally, the prior mean of the GP model, which is based on all ventilation scenarios, is not a good presumption for these setups. This entails the problem that the GP prediction seeks towards the prior mean where no training data are available. Thus, the estimated temperature for locations far away from the observation samples differs from the actual temperature level. Therefore, a modified assumption on the prior mean is examined for further improvement.

2.2.3 Analysis of Different GP Mean Definitions

So far, it is assumed that the mean of the GP model is constant and fixed for all ventilation scenarios. As observed in Figure 2.8, this is only a good assumption if the target room temperature is always set to a similar value. However, the target value can vary depending on seasons or comfort requirements [3]. In particular, the average room temperature for the simulated cases varies between 23.2 °C and 31.6 °C. Therefore, it is meaningful to imply the available knowledge of the average room temperature by setting the prior GP mean to $\mu = \bar{T}_{\text{sens}}$ instead of one fixed value for any air conditioning mode. This corresponds to the modeling approach

$$T_{ir} = \bar{T}_{\text{sens}} + \Delta T(\boldsymbol{z}_{ir}) \tag{2.15}$$

where only the temperature deviations $\Delta T(\boldsymbol{z}_i)$ must be mapped by the GP model. Hence, $\Delta T(\boldsymbol{z}_i)$ can be modeled by a GP with zero mean:

$$P(\Delta \boldsymbol{T} = \boldsymbol{f} | \boldsymbol{Z}, \boldsymbol{\theta}) = \mathcal{N}(\boldsymbol{0}, \boldsymbol{K}).$$

Figure 2.7 shows that using the prior knowledge about the general temperature level allows for additional 5 to 10 % reduction of the MSE. Furthermore, the variance is notably reduced, particularly for the distance-based approaches what makes them competitive to the location-based model. Table 2.4 reveals the substantial benefit of including a scenario dependent mean, thus modeling temperature deviations instead of the absolute temperatures. The worst case, namely $\min_r(D_r)$, is improved significantly and extrapolation errors are reduced to a great extent. Now, the GP models outperform the benchmark $\bar{T}_{\mathrm{sens}}$ for all ventilation setups as indicated by the positive minimum improvement. The best input combination for mapping the temperature deviation is given by z_δ^{sup}. This approach leads to the lowest MSE and $\bar{\sigma}^2$ as well as to the greatest improvement D_r compared to the benchmark. Thus, it is preferred over the model $T_{\boldsymbol{\chi}}^{\mathrm{sup}}$ and serves as modeling assumption for further investigations.

The previous analysis was performed based on multiple random sensor placements to prove the applicability and superiority of the GP approach even for little thought out sensor setups. Therefore, the evaluation also includes sensor configurations that are disadvantageous and thus increase the average prediction error. Revisiting the values for the minimum MSE in Table 2.3 shows the true potential of the GP model. Although none of the applied sensor configurations is optimal, an average improvement over all ventilation scenarios of more than 30 % can be observed for the best sensor setup. To exploit the full potential of the GP modeling approach, optimal sensor placement strategies are derived in the next section.

2.3 Optimal Sensor Placement

The sensor locations are crucial for the prediction accuracy because they are the only source for training data. This can be illustrated by the scenario where all sensors are located close to heat sources such that an overestimation of the room temperature is very likely. Defining the best sensor configuration requires a combinational analysis incorporating $\binom{N_{\mathrm{m}}}{N_{\mathrm{sens}}}$ evaluations. This can only be evaluated for a low amount of sensors or a small set of possible sensor locations. For example in the present case, over one million setup evaluations are necessary for placing three sensors whereas placing five sensors already encompasses over two billion possible combinations. To circumvent the infeasible computational effort, greedy optimization algorithms provide a useful alternative to solve such kind of optimization problems [47]. In this context, forward or backward stepwise optimization are commonly applied algorithms to find the most suitable set. More detailed information about their functional principle can be found in Appendix A.3.

In the following, three different optimization approaches are applied and compared for the optimal sensor placement task:

   - Stepwise forward selection (Algorithm A.1)

- Stepwise backward selection (Algorithm A.2)

- Differential Evolution (DE) [92].

DE is a population-based genetic algorithm for global optimization [12, 14] and serves as comparative reference for the quality of the greedy optimization results. The DE optimization is initialized with the results from the greedy algorithm and the iteration is limited to 1000.

Still unanswered is the question how to define the objective cost to evaluate a specific sensor setup. Generally, the information content that is observed by the sensors must be maximized. This can be done by optimizing the training data so that either the prediction error or the uncertainty about the prediction is minimized. Therefore, two approaches are applied in the following and subsequently compared regarding their placement results.

2.3.1 Optimal Sensor Placement based on MSE

The most intuitive choice as measure for optimal placement targets to minimize the MSE of the temperature estimation based on a specific sensor setup s. Using the MSE as placement criterion, the vector of optimal locations is given by

$$s_{\mathrm{MSE}}^* = \operatorname*{arg\,min}_{s \in \mathcal{M}} \mathrm{MSE}(s) = \operatorname*{arg\,min}_{s \in \mathcal{M}} \frac{1}{N_{\mathrm{cfd}}} \sum_{r=1}^{N_{\mathrm{cfd}}} \frac{1}{N_{\mathrm{m}}} \sum_{i=1}^{N_{\mathrm{m}}} (T_{\mathrm{CFD},ir} - T_{\mathrm{GP},ir}(s))^2 \quad (2.16)$$

where $T_{\mathrm{GP},ir}(s) = T_{\mathrm{GP}}(z_{ir}, Z(s))$ refers to the predicted temperature which is a result of the available training data coming from the sensor measurements $Z(s)$ and the considered actual input z_{ir}. $\mathcal{M}$ defines the set of all N_{m} possible sensor locations, thus monitoring points as shown in Figure 2.3. The best locations for a uniform temperature assumption, for example, results in a sensor setup where the average sensor temperature matches the mean room temperature as closely as possible for all considered ventilation scenarios.

The optimization problem (2.16) is solved using the three introduced algorithms. Figure 2.9 shows the average MSE and the variance of the GP predictions for optimized placements. As expected, the prediction accuracy increases when more sensors are placed within the room. Increasing the amount of sensors from 1 to 20 reduces the MSE from 0.4 to $0.1\,\mathrm{K}^2$. A comparison of the forward and backward greedy results reveals that the backward selection outperforms the forward selection for large sensor networks but is less suitable for a low number of sensors (<7). The global optimum refers to the evaluation of the complete combinatorics and is computed for the placement of up to three sensors. A comparison to the DE algorithm shows that the genetic algorithm results in the same or at least a competitive solution to the global optimum. The placement of the first 14 sensors surpasses the greedy algorithms
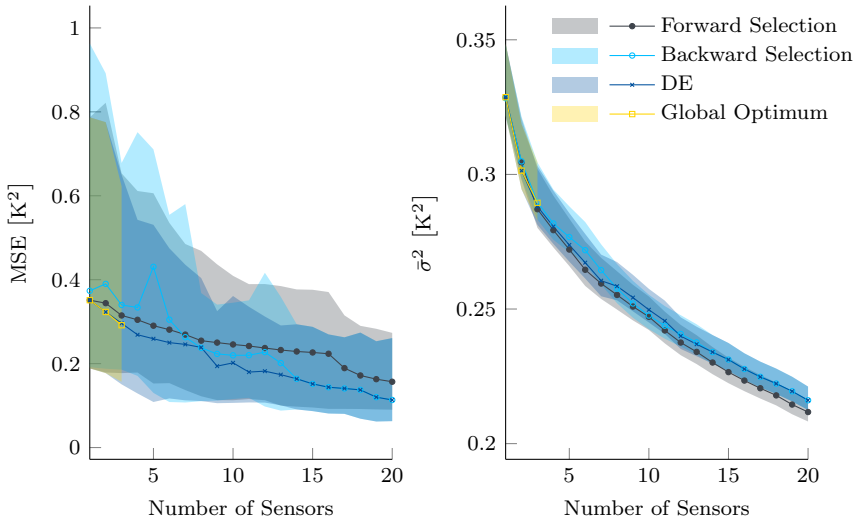
Figure 2.9: Average MSE and standard deviation for optimized sensor positions based on the different optimization methods. The shaded area indicates maximum and minimum values over all ventilation scenarios.

but matches the outcome of the backward selection for a larger amount of sensors. Consequently, no better locations can be found within the defined iteration limit of the DE.

The corresponding model variance decreases monotonically when sensors are added to the network. However, the percentage of improvement is highest for placing the second sensor. Adding more sensors still reduces the variance but with lower associated benefit. Although the forward selection leads to a slightly lower variance compared to the other algorithms, the applied optimization method does not impact the model uncertainty remarkably.

The superiority of the combinational optimization or the DE becomes obvious when the results for the first optimal location are compared. Since the first evaluation of the forward selection is identical to the combinational analysis and the number of iterations for the DE are sufficient, placing one sensor leads to the same (and optimal) position for all approaches except for the backward selection as shown in Figure 2.10. This location corresponds to the spot where the temperature is closest to the average temperature for all ventilation scenarios. The backward selection method has deficits for a small amount of sensors since useful locations are already excluded in previous steps and cannot contribute anymore. The disadvantage of the stepwise
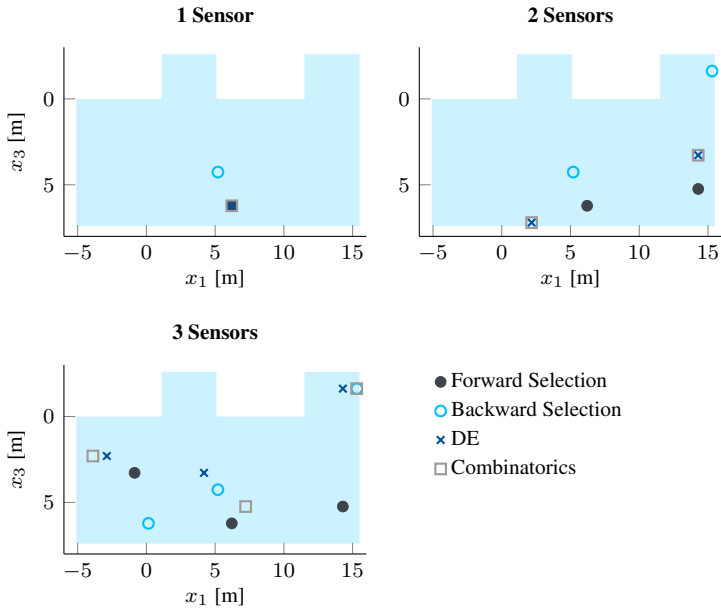
Figure 2.10: Optimized sensor positions for minimizing the MSE based on four different optimization algorithms.

forward greedy algorithm opposed to the global optimum is explained by the fixed first position such that the additional degree of freedom of placing two sensors cannot be used in full extent. While the global optimum requires replacing the first optimal sensor, the forward algorithm must proceed based on the previous setup and thus leads to suboptimal placement. Nevertheless, similarities can be observed for all results. The first sensor is placed centralized within the occupied zone and close to the window. Due to its proximity to the internal heat sources, this sensor incorporates a great amount of information how the heat transfer is affected by the ventilation condition. Furthermore, the central location is a good representative for the overall room condition because the middle zone is mainly operated moderately while the outer zones are exposed to more extreme conditions. Subsequently, additional sensors are added to the unexplored corners and result in a uniformly distributed sensor network. Before a more detailed evaluation of general placement strategies is performed, another definition of optimality for sensor positioning is introduced in the following.

2.3.2 Maximizing Mutual Information

One major drawback of the MSE-based sensor placement optimization is the need for detailed ground truth data. The evaluation of (2.16) requires reference measurements with a high resolution of the actual spatial temperature profile. Therefore, a direct application of this method to large commercial buildings is usually not practicable unless general placement strategies can be derived from the MSE-based approach. However, the structural properties of the GP model allow for an alternative consideration which uses entropy as measure for the information content. Given the random variables $X_1, X_2, ..., X_n$, the joint entropy of a multivariate Gaussian distribution is given by [20]

$$\mathcal{H}(X_1, X_2, ..., X_n) = \frac{1}{2} \log \left((2\pi e)^n |\boldsymbol{K}| \right), \quad |\boldsymbol{K}| = \det \boldsymbol{K} \tag{2.17}$$

and thus fully defined by the covariance matrix $\boldsymbol{K}$. In the GP regression framework $\boldsymbol{K}$ only depends on the matrix of observations $\boldsymbol{Z}$ and can be evaluated for arbitrary inputs without the knowledge of the actual output. Subsequently, the entropy of the GP model can be computed for all potential sensor configurations although the output temperatures are unknown. An optimal sensor setup maximizes the information content that is captured by the sensor measurements. This information content can be quantified in terms of Mutual Information (MI), e.g. proposed by Krause (2008) [66]. MI defines the reduction of uncertainty about a random variable X when another random variable Y is known. It can be expressed by the marginal entropies $\mathcal{H}(X)$, and $\mathcal{H}(Y)$ and the conditional entropies $\mathcal{H}(X|Y)$, and $\mathcal{H}(Y|X)$ as

$$\text{MI}(X;Y) = \mathcal{H}(X) - \mathcal{H}(X|Y) = \mathcal{H}(Y) - \mathcal{H}(Y|X). \tag{2.18}$$

Assuming $N_{\text{sens}} < N_{\text{m}}$ sensors are placed on a subset $\mathcal{S} \subset \mathcal{M}$, the covariance matrix of the room can be decomposed into

$$\boldsymbol{K}_{\mathcal{M}} = \begin{bmatrix} \boldsymbol{K}_{\mathcal{S}} & \boldsymbol{K}_{\mathcal{S},\mathcal{M}\setminus\mathcal{S}} \\ \boldsymbol{K}_{\mathcal{M}\setminus\mathcal{S},\mathcal{S}} & \boldsymbol{K}_{\mathcal{M}\setminus\mathcal{S}} \end{bmatrix} \tag{2.19}$$

where $\boldsymbol{K}_{\mathcal{S}}$ contains the covariances associated with the sensor locations, $\boldsymbol{K}_{\mathcal{M}\setminus\mathcal{S}}$ the covariances of the remaining unmonitored points, and $\boldsymbol{K}_{\mathcal{S},\mathcal{M}\setminus\mathcal{S}}$ or $\boldsymbol{K}_{\mathcal{M}\setminus\mathcal{S},\mathcal{S}}$ the coupled covariances. Using (2.18) to (2.19) allows to rewrite the expression for MI of

the sensor and remaining room data:

$$
\begin{aligned}
\mathrm{MI}(X_{\mathcal{S}}; X_{\mathcal{M}\setminus\mathcal{S}}) =\;& \mathcal{H}(X_{\mathcal{S}}) - \mathcal{H}(X_{\mathcal{S}|\mathcal{M}\setminus\mathcal{S}}) \\
=\;& \frac{1}{2}\log\left((2\pi e)^{N_{\mathrm{sens}}}|\boldsymbol{K}_{\mathcal{S}}|\right) - \frac{1}{2}\log\left((2\pi e)^{N_{\mathrm{sens}}}|\boldsymbol{K}_{\mathcal{S}|\mathcal{M}\setminus\mathcal{S}}|\right) \\
=\;& -\frac{1}{2}\log\left(\left|\boldsymbol{K}_{\mathcal{S}}^{-1}\boldsymbol{K}_{\mathcal{S}|\mathcal{M}\setminus\mathcal{S}}\right|\right) \\
=\;& -\frac{1}{2}\log\left(\left|\boldsymbol{K}_{\mathcal{S}}^{-1}\left(\boldsymbol{K}_{\mathcal{S}} - \boldsymbol{K}_{\mathcal{S},\mathcal{M}\setminus\mathcal{S}}\boldsymbol{K}_{\mathcal{M}\setminus\mathcal{S}}^{-1}\boldsymbol{K}_{\mathcal{M}\setminus\mathcal{S},\mathcal{S}}\right)\right|\right) \\
=\;& -\frac{1}{2}\log\left(\left|\boldsymbol{I} - \boldsymbol{K}_{\mathcal{S}}^{-1}\boldsymbol{K}_{\mathcal{S},\mathcal{M}\setminus\mathcal{S}}\boldsymbol{K}_{\mathcal{M}\setminus\mathcal{S}}^{-1}\boldsymbol{K}_{\mathcal{M}\setminus\mathcal{S},\mathcal{S}}\right|\right).
\end{aligned} \tag{2.20}
$$

In general, (2.18) permits two ways to compute MI. Choosing $\mathcal{H}(X_{\mathcal{S}}) - \mathcal{H}(X_{\mathcal{S}|\mathcal{M}\setminus\mathcal{S}})$ over $\mathcal{H}(X_{\mathcal{M}\setminus\mathcal{S}}) - \mathcal{H}(X_{\mathcal{M}\setminus\mathcal{S}|\mathcal{S}})$ is beneficial for this application because it results in a lower dimensional matrix for the calculation of the determinant in (2.20) due to the generally valid relation $N_{\mathrm{sens}} < N_{\mathrm{m}} - N_{\mathrm{sens}}$.

An optimal sensor setup achieves the highest reduction of uncertainty and therefore maximizes (2.20). The optimal sensor locations are obtained by

$$
\boldsymbol{s}_{\mathrm{MI}}^{*} = \operatorname*{arg\,max}_{\boldsymbol{s}\in\mathcal{M}} \mathrm{MI}(\boldsymbol{s}) = \operatorname*{arg\,min}_{\boldsymbol{s}\in\mathcal{M}} |\boldsymbol{I} - \boldsymbol{K}_{\mathcal{S}}^{-1}\boldsymbol{K}_{\mathcal{S},\mathcal{M}\setminus\mathcal{S}}\boldsymbol{K}_{\mathcal{M}\setminus\mathcal{S}}^{-1}\boldsymbol{K}_{\mathcal{M}\setminus\mathcal{S},\mathcal{S}}|. \tag{2.21}
$$

As already mentioned above, this placement method has a crucial advantage over the previously applied MSE criterion. The computation of MI only requires the covariance matrix $\boldsymbol{K}$ of the GP model. Since $\boldsymbol{K}$ is fully defined by the hyperparameters $\boldsymbol{\theta}$ and the matrix of observations $\boldsymbol{Z}$, the sensor placement assessment can be performed as soon as the hyperparameters are determined, e. g. based on a known process characteristic. A possible implementation of this method for a real office space is depicted in Figure 2.11. An arbitrary initial sensor setup $\boldsymbol{s}_0$ can be deployed for the collection of training data $\mathcal{T}_0$. Based on this first data set, the hyperparameters $\boldsymbol{\theta}$ are identified by maximizing the log marginal likelihood (2.6). Note that these two steps could be skipped if a valid first guess of the hyperparameters is already available, for example due to prior measurements in office spaces with a similar layout. Extending the matrix of observation $\boldsymbol{Z}$ with all input vectors that correspond to a potential sensor position allows to compute the optimal sensor configuration $\boldsymbol{s}_{\mathrm{MI}}^{*}$ using (2.21). The sensor setup is then rearranged accordingly to improve the quality of the new observation data. After collecting additional training data, the first guess or computation of the hyperparameters can be revised or verified based on the increasing data set. If necessary, the GP model is adjusted and the sensor setup recomputed with the improved model structure. As soon as the monitored data provide a good basis for the identification of $\boldsymbol{\theta}$ no further model update is needed and the final optimal setup $\boldsymbol{s}_{\mathrm{MI}}^{*}$ is obtained. Hence, defining the optimal sensor setup does not require extensive measurements for collecting reference values as required for evaluating (2.16). One update of the sensor configuration can already lead to satisfying results.
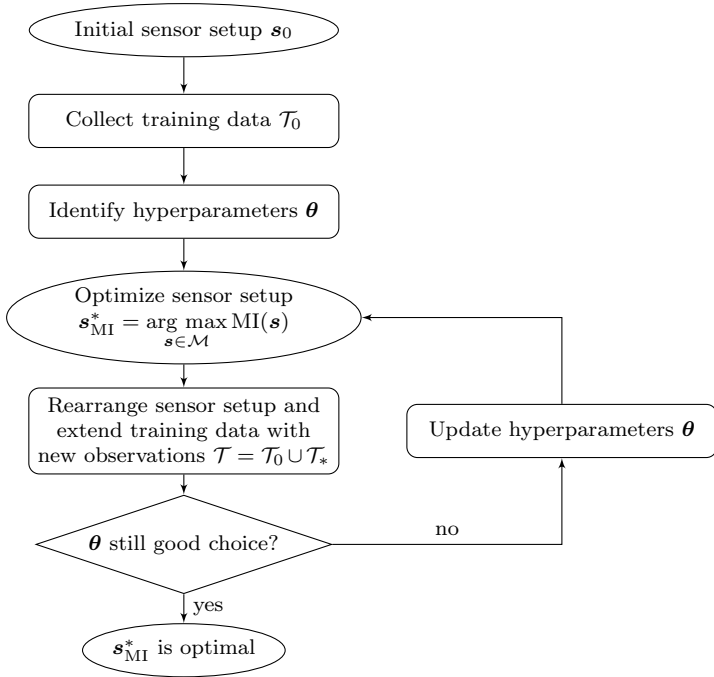
Figure 2.11: Application strategy for the optimal sensor placement based on maximizing MI.

Excursus: Greedy Optimization based on Mutual Information

Before comparing the optimal sensor setups for MSE- and MI-based placement, an important property of the greedy MI-optimization is highlighted. Due to the equality (2.18), the stepwise forward and stepwise backward algorithm solve the equivalent but inverse optimization problem. This can be pictured by exchanging $\mathcal{M} \setminus \mathcal{S}$ with $\mathcal{S}$ which results in an equality of the forward selection of $\mathcal{S}$ and the backward selection of $\mathcal{M} \setminus \mathcal{S}$ and vice versa. The equality is emphasized by Figure 2.12. The resulting values for MI are equivalent when one result is flipped vertically around $N_{\mathrm{sens}}/2 = 96$ sensors. Furthermore, a problem arises when applying the forward stepwise algorithm: Since training data are only provided from active sensors, the number of observations is given by $N_{\mathrm{cfd}} \cdot N_{\mathrm{sens}}$. The number of features, thus the dimension of $\boldsymbol{z}$, is $N_z = N_{\mathrm{sup}}(2 + N_{\mathrm{sens}})$. Therefore, the matrix of observations $\boldsymbol{Z}$ has fewer rows than columns for $N_{\mathrm{sens}} < \frac{2N_{\mathrm{sup}}}{N_{\mathrm{cfd}} - N_{\mathrm{sup}}} = 7$ such that the influence of different features
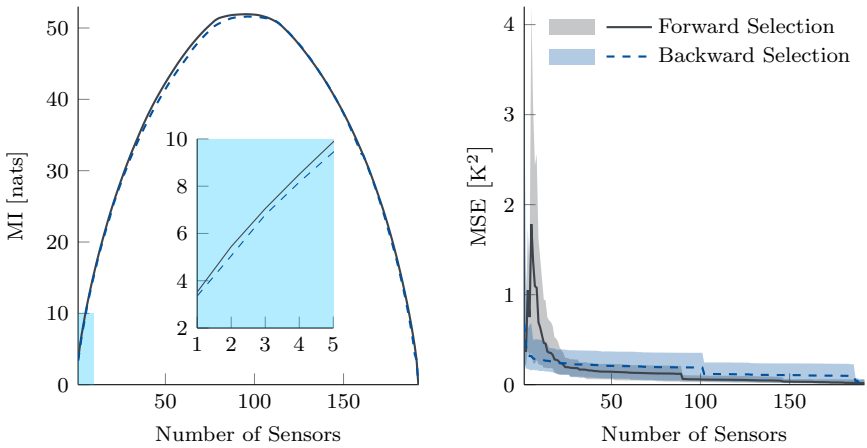
Figure 2.12: Comparison of forward and backward sensor selection for maximizing MI based on (2.21).

cannot be distinguished due to missing observations. As a consequence, the optimum is not unique and supposedly optimal locations result in high prediction errors as depicted in Figure 2.12. Moreover, as soon as a sensor location is selected, its position is fixed and unfavorable locations are carried along while the forward selection process is continued. The backward selection, on the other hand, ensures meaningful positions for a low number of sensors because the resulting configuration already incorporates knowledge about the overall system by definition. The algorithm starts with full system knowledge and excludes positions with low information content. This avoids the problem of unknown cause-and-effect relationships. Since the MI values for forward and backward selection are comparable and the prediction quality is significantly better with backward selection for the relevant amount of sensors, only the latter is used for the following comparison of MSE- and MI-based optimization.

2.3.3 Comparison of MSE and MI criterion

The predictive quality of the MI-optimized models is compared to the MSE-based results. Figure 2.13a depicts the prediction error, variance and corresponding MI for both approaches. The error made by the assumption of a uniform temperature, thus averaging the sensor measurements, is also shown to highlight the benefit of a higher resolving temperature model. It can be observed that the average prediction accuracy of the maximized MI solution is lower than the achievable accuracy given by minimizing the MSE, although the difference is relatively small for 2 to 8 sensors. While

the gap between the prediction errors of the two methods increases with additional sensors, the process variance of the MI solution undercuts the MSE approach. This property highlights the fundamental idea of MI, reduction of uncertainty, and is further demonstrated by the difference in mutual information for more than 7 sensors.

A more detailed analysis of the sensor positions reveals additional differences between the two methods. These considerations allow to derive general relations for optimal placement strategies that can be applied when a detailed computational evaluation is not possible. To get a general idea of where sensors should be located, the monitored temperature ranges of optimally placed sensors are further investigated. Therefore, the normalized deviations from the present average temperature level depending on the sensor amount are evaluated. The normalized temperature deviation for a ventilation scenario r is defined as

$$\Delta T_r(s) = \frac{T_{\mathrm{CFD},r}(s) - \bar{T}_r}{T_r^{\mathrm{max}} - T_r^{\mathrm{min}}} \tag{2.22}$$

where $\qquad \bar{T}_r = \frac{1}{N_{\mathrm{m}}} \sum_{i=1}^{N_{\mathrm{m}}} T_{\mathrm{CFD},ir}, \quad T_r^{\mathrm{min}} = \min_{i \in \mathcal{M}} T_{\mathrm{CFD},ir}, \quad T_r^{\mathrm{max}} = \max_{i \in \mathcal{M}} T_{\mathrm{CFD},ir}.$

The normalized temperature ranges at the optimized sensor locations are evaluated according to (2.22) and visualized in Figure 2.13b. The marks represent the average normalized sensor temperature deviation over all CFD results:

$$\Delta \bar{T} = \frac{1}{N_{\mathrm{cfd}}} \sum_{r=1}^{N_{\mathrm{cfd}}} \frac{1}{n_{\mathrm{sens}}} \sum_{j=1}^{n_{\mathrm{sens}}} \Delta T_r(s_j). \tag{2.23}$$

The shaded area shows the range between averaged minimum and maximum sensor temperatures:

$$\Delta \bar{T}_{\mathrm{min}} = \frac{1}{N_{\mathrm{cfd}}} \sum_{r=1}^{N_{\mathrm{cfd}}} \min_{s \in \mathcal{S}} \Delta T_r(s) \tag{2.24}$$

$$\Delta \bar{T}_{\mathrm{max}} = \frac{1}{N_{\mathrm{cfd}}} \sum_{r=1}^{N_{\mathrm{cfd}}} \max_{s \in \mathcal{S}} \Delta T_r(s). \tag{2.25}$$

A value close to zero of $\Delta \bar{T}$ suggests sensor positions close to the average room temperature whereas a high range advises to choose sensor locations that cover a large range of occurring temperatures. A normalized temperature of ± 1 refers to a sensor location at the global extreme values. Figure 2.13b compares the placement characteristics for both approaches and illustrates their main difference. High precision of the predictions requires a sensor network that monitors a large range of the present temperatures. Reduction of uncertainty, on the other hand, is based on locations that are within the region of average conditions. The corresponding optimized sensor
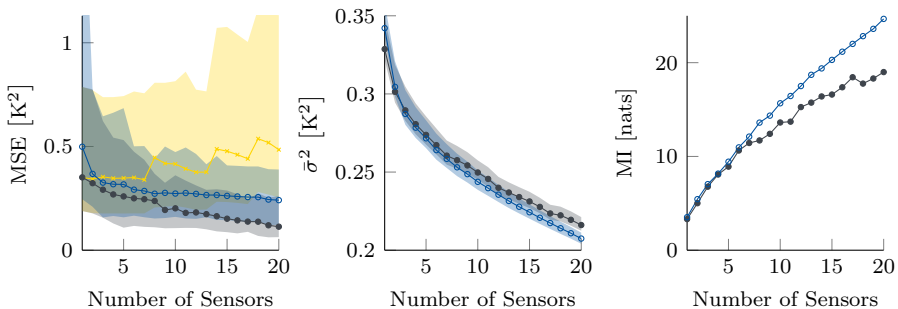
(a) Comparison of prediction quality. The shaded area indicates the range between the minimum and the maximum value over all CFD scenarios.
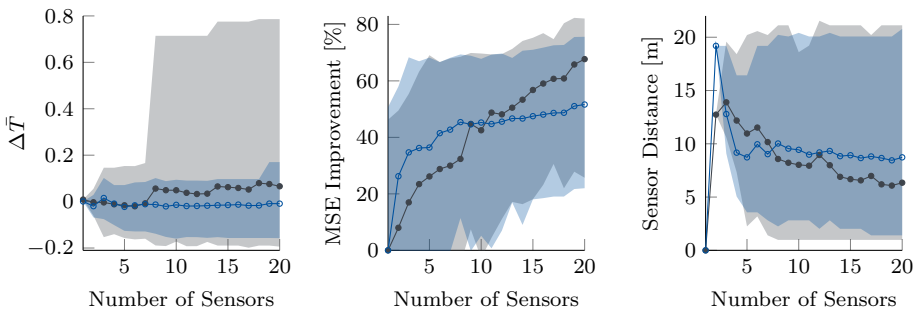
(b) Normalized optimized sensor temperatures. The shaded area indicates the range between $\Delta \bar{T}_{\min}$ and $\Delta \bar{T}_{\max}$.

(c) Percentage of MSE reduction compared to using one sensor.

(d) Average distance between sensor locations. The shaded area indicates minimum and maximum distances.
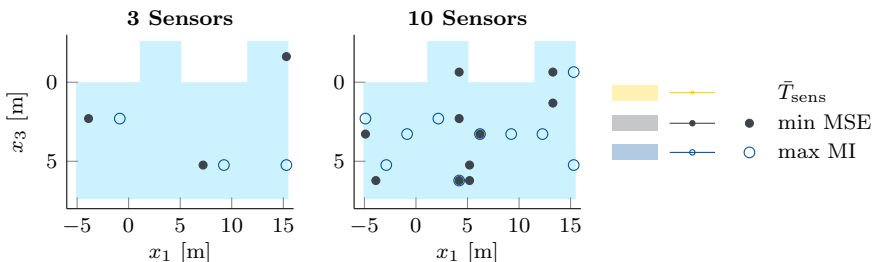
(e) Optimized sensor positions for MSE-based and MI-based optimization.

Figure 2.13: Comparison of MSE-based and MI-based optimization [44].

locations are given in Figure 2.13e for three and ten sensors. The positions of the three sensors are uniformly distributed and similar for both methods. This matches the resemblance regarding prediction accuracy (Figure 2.13a) and covered temperature range (Figure 2.13b). However, placing ten sensors reveals the impact of the different objectives. While MI-based positioning continues with a uniform sensor distribution that minimizes the uncertainty, MSE-based optimization concentrates additional sensors around areas with high temperature gradients and leads to sensor clusters. This effect is also visible in Figure 2.13d and results in lower average distances between the sensors for an increasing sensor amount. Adding more sensors to locations with higher gradients improves the predictive quality of the GP's posterior mean but does not reduce the uncertainty about the holistic room conditions in an analogous extent. Moreover, the clustering and biased average sensor temperature explains the increasing error of the average sensor temperature estimate $\bar{T}_{\mathrm{sens}}$ depicted in Figure 2.13a.

The question of how many sensors are required for temperature sensing, cannot be answered universally. The decision is always based on accuracy as well as cost requirements. However, Figure 2.13c provides an indication about a meaningful amount. It shows the percentage of the MSE improvement when another sensor is added to the network in relation to using only one sensor. The highest improvement is achieved by the first three to four sensors. In particular for the MI criterion, using more than six sensors does not lead to a significant improvement. Note that a network of more than 20 sensors certainly improves the predictive properties (also for the MI-based placement) but a trade-off between required precision and the cost related to additional sensors must be chosen. Moreover, a larger number of sensors is not (yet) realistic for an office environment. The presented analysis leads to different suggestions for different system requirements. If only a low number of sensors is available, the placement strategy should rely on the identification of locations that represent average conditions and hence have a sufficient distance from supplies, internal heat or other disturbance sources. For the considered office space, already 4 sensors are able to provide a reliable temperature field prediction for various ventilation scenarios and reduce the maximum error significantly compared to the uniform temperature assumption. In the case that a larger amount of sensors can be distributed, two possible strategies are proposed depending on the required outcome. A good representation of the overall room conditions can be achieved by uniformly distributed sensors. An optimization based on MI can even be performed without extensive measurements but only identifying feasible hyperparameters. If a higher accuracy is desired while accepting an increased uncertainty about the validity of the prediction, the sensors can be separated into two sets. The first set should be distributed uniformly to form a well predicting basis, whereas the second set should be focused on areas where disturbance effects occur.

2.4 Conclusion

The discussed modeling approach enables a more detailed mapping of room conditions in large open spaces. It allows for an evaluation of the spatial effects due to room geometries and HVAC system operation and provides an easily implementable alternative to physically motivated models. The GP model copes with the majority of problems which physical models cannot overcome. The main challenges encompass the limited knowledge of the room geometry, furniture and boundary conditions as well as non-measurable disturbances and layout changes during the lifetime. The possibilities to include these effects in physical models are limited and/or involve a significant implementation effort. Moreover, the high computation time disqualifies them mainly for real-time applications.

The data-based GP modeling approach closes the gap between complex CFD simulations and the often invalid simplification of uniform room conditions. The relation between the HVAC mode and temperature profile can be learned online during the daily operation based on a relatively low number of sensors while only accessible sensor data are used. No exact knowledge of room geometry is required apart from sensor locations and the HVAC actuator setup. A connected sensor network, that is able to exchange information about its location and affiliation (component type), even enables an automated setup initialization. Consequently, no additional expert knowledge is necessary to commission the prediction model.

Since sensor measurements are the only data source for the training of the GP model, a favorable sensor configuration is a crucial design decision. The presented placement algorithms lead to different placement strategies which can be integrated during the system design. However, solving the optimization problem for a real-world application is only possible for the MI-based approach because the MSE cannot be evaluated due to missing knowledge about the true reference values. Therefore, the MI criterion provides a useful tool to optimize the sensor positions for arbitrary rooms but should be checked against the general placement strategy that was derived from the MSE approach. This avoids choosing disadvantageous locations originating from the smoothing character of the GP model.

The error made by the standard assumption of a uniform room temperature can be reduced significantly by the GP approach and allows for a more reliable representation of the indoor conditions. This asset can be used to improve the thermal comfort of the occupants locally. However, it also leads to the question which conditions generate thermal comfort. Although standardized conditions are given by comfort standards such as DIN EN ISO 7730 [26] or ASHRAE 55 [2], the individual perception can vary significantly. Consequently, a profound analysis of thermal comfort is performed to clarify the requirements and to pave the way for personalized comfort control.

3 Personal Thermal Comfort Modeling

The analysis of Chapter 2 showed how the spatial temperature profile can be mapped by a data-based GP regression model. Making use of this additional knowledge requires the definition of target conditions, where generally two main goals drive the design of HVAC systems: energy efficiency and thermal comfort. The former objective is mainly motivated by environmental goals to combat climate change and cope with the increasing demand for infrastructure and buildings [96]. Since the building sector is one of the largest consumers with a share of about 40 % of the world's energy consumption [83], governments continuously exacerbate the building code related laws to push the industry. The building owner or operator, on the other side, is rather interested in the well-being of the occupants because cost savings due to a reduced energy demand is generally incommensurable with the costs related to the users' salary. Thus in particular in existing office buildings, the focus lies on thermal comfort to ensure productivity and health of the employees [69, 98]. While temperature differences within one thermal zone are often relatively small ($< 1\,^{\circ}$C), the individual perception of thermal comfort can vary significantly regarding gender, cultural background, physical or even psychological conditions [15]. Comfort standards, such as the ISO 7730 norm [26] and the ASHRAE Standard 55 [2], try to find a compromise between the individual modes of perception. They define guidelines which represent an averaged user sensation so that the majority of users is satisfied. The basis for these comfort models is provided by Fanger (1970) [30] where he presents the comfort measure called Predicted Mean Vote (PMV) in combination with the Predicted Percentage of Dissatisfied (PPD). His approach is based on the heat balance of the human body and is one of the best validated and reviewed comfort models. The 7-point thermal sensation scale, as shown in Table 3.1, is used for the quantification of thermal comfort. However, significant deviation between model and field data were identified by many consecutive studies [51]. In some cases, the neutral temperature[a] can deviate by more than $3.6\,^{\circ}$C from the actual thermal perception. Furthermore, better prediction accuracy was identified in stationary air conditioned environments than in naturally ventilated buildings [82]. Moreover, a direct model transfer to tropical areas led to a poor validity because the model was developed based on data from subjects of temperate climates [101]. To improve the poor predictive ability, adaptive adjustments of the PMV were proposed, such as an adjustment based on outdoor conditions [25] or introducing a bias [51]. However, the high variance over

---

[a]Temperature that corresponds to a zero vote and thus represents comfortable conditions.

Table 3.1: 7-point thermal sensation scale used for comfort evaluation in the test-bed.

Vote ν	Perceived Comfort
3	Much too warm
2	Too warm
1	Comfortably warm
0	Comfortable
−1	Comfortably cool
−2	Too cool
−3	Much too cool

different comfort studies suggests a prior analysis of the applicability of the PMV to the considered test bed.

To enable the application of control concepts that focus on personal thermal comfort, a model for the individual sensation is derived in the following chapter. Due to the diverse results found in literature, existing comfort modeling approaches are investigated firstly if and to what extend they can be used as measure for personal comfort. Individualized versions of the PMV are compared to alternative regression-based formulations according to their ability of mapping the personal thermal sensation. In this context a thorough feature selection is performed to identify the most important comfort-influencing factors. The modeling procedure is designed to ensure resilient comfort predictions based on voting data that are collected under daily working conditions. Since physical or psychological states are not measurable, the derived model identification process must rely on environmental data which comprise limited system excitation as well as non-measurable subjective influences.

The following results and presented methods are partly published in [42, 43] but based on a different data set.

3.1 Test-Bed

The regarded test environment consists of two mid-sized open-plan offices ($\sim 65\,\mathrm{m}^2$ each) located in Singapore. Each office is occupied by 7-10 employees and equipped with four additional ceiling fans. The fans serve as a supplementary degree of freedom for individualized comfort conditions. Most systems are designed to actuate the room holistically such that personalized conditions cannot be realized due to substantial mixing effects of the air and underactuation. Commonly, only the state of the supplied
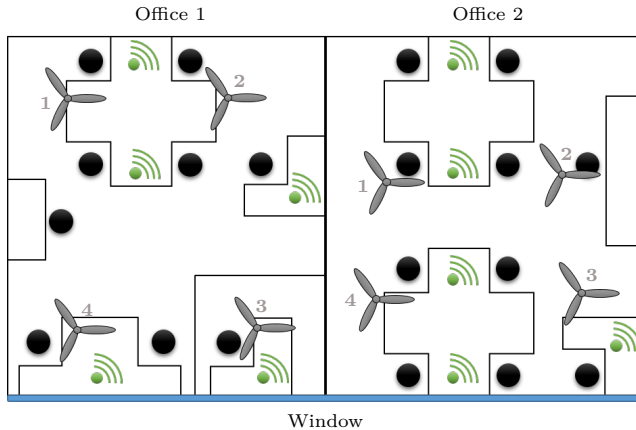
Figure 3.1: Test-bed layout with seating positions represented by black circles, locations of indoor air quality sensors shown in green and positioning of ceiling fans indicated in gray.

air can be manipulated for thermal actuation and limits the capabilities for comfort-oriented building control. In order to address this challenge, the system is extended by locally controlled air movement by means of ceiling fans. Moreover, using the cooling effect of mechanical ventilation establishes energy saving potential [6] by allowing an increased temperature set-point [78]. Additionally, elevated air velocities can improve the perceived comfort [104] and consequently achieve a higher self-reported productivity [73]. As depicted in Figure 3.1, each ceiling fan is shared by 2-3 employees. Ten Libelium sensors [72] (five in each office) monitor the indoor conditions. The Sensirion temperature and humidity sensors [90] measure air and mean radiant temperatures, T_{air} and T_{mr} respectively, as well as relative humidity RH. A weather station on the considered building records the local outdoor conditions, such as outside temperature T_{out}, humidity RH_{out} and solar radiation I_{sol}. More detailed specifications of the sensor setup can be found in Appendix B.1.

The thermal comfort of the occupants is monitored by a desktop application as shown in Figure 3.2. The personal comfort level is measured on a 7-point sensation scale in accordance with the common comfort standards [2, 26] and similar to the PMV. The user feedback is collected every 20-60 min during the daily working routine. The comfort study was conducted over six month from September until February with training periods of various temperature and fan levels during the everyday working hours. The number of occupants in the offices varied over the period due to leaving employees and interns or new entrants. The voting feedback of 16 employees is
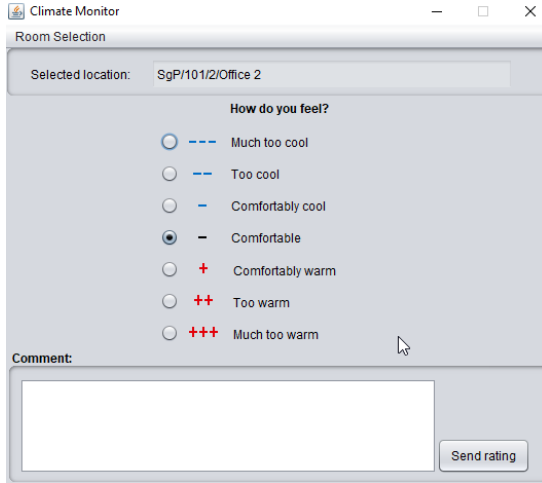
Figure 3.2: Voting application for thermal comfort evaluation.

considered in the following analysis and consists on average of 237 votes per user. However, due to various attendance times, the individual sample size varies between 50 and 551 observations. Appendix B.2 provides further insights about the content of the collected voting data. To ensure acceptance of the employees during the test phase, the system excitation had to be limited to tolerable room conditions.

3.2 PMV Calculation

Many physical and psychological factors influence the heat transfer between the human body and its surroundings, thus the perceived thermal comfort. The interaction between the body and the environment is sketched in Figure 3.3. The body's heat production is given by the metabolic rate M less the accomplished mechanical work W. The heat is transferred to the environment through the skin surface and by respiration, q_{sk} and q_{res} respectively. Moreover, stored heat q_{sto} changes the body temperature. This leads to the heat balance of the human body [3]

$$M - W = \underbrace{q_{\mathrm{sk}}^{\mathrm{conv}} + q_{\mathrm{sk}}^{\mathrm{rad}} + q_{\mathrm{sk}}^{\mathrm{eva}}}_{q_{\mathrm{sk}}} + \underbrace{q_{\mathrm{res}}^{\mathrm{conv}} + q_{\mathrm{res}}^{\mathrm{eva}}}_{q_{\mathrm{res}}} + \underbrace{q_{\mathrm{sto}}^{\mathrm{sk}} + q_{\mathrm{sto}}^{\mathrm{core}}}_{q_{\mathrm{sto}}}. \tag{3.1}$$

As illustrated in Figure 3.3, the heat transfer over the skin q_{sk} can be separated in convective $q_{\mathrm{sk}}^{\mathrm{conv}}$, radiation $q_{\mathrm{sk}}^{\mathrm{rad}}$ and evaporative $q_{\mathrm{sk}}^{\mathrm{eva}}$ losses. Similarly, the heat transfer through the respiratory tract q_{res} encompasses the evaporative $q_{\mathrm{res}}^{\mathrm{eva}}$ and
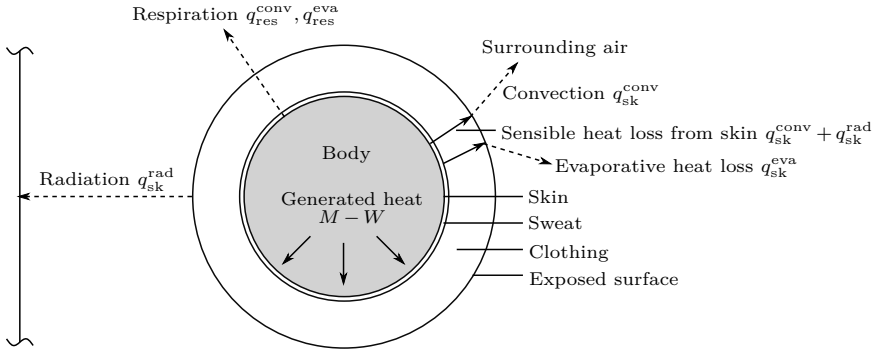
Figure 3.3: Interaction between the human body and the environment, inspired by [3].

convective $q_{\text{res}}^{\text{conv}}$ losses. Furthermore, the heat storage rate is either assigned to the skin $q_{\text{sto}}^{\text{sk}}$ or the core $q_{\text{sto}}^{\text{core}}$ compartment.

The PMV generalizes the comfort prediction based on the human's sensible and latent heat balance and introduces empirical expressions for the different heat exchange rates [3]. According to Fanger [30], thermal comfort can be expressed in terms of an imbalance between the actual heat exchange of the body with the environment and the required heat flow for a neutral sensation at a given metabolism rate M. This imbalance is represented by the thermal load L which defines the difference between the actual heat flow $M - W$ and the required heat flow that produces thermal comfort. Section B.3 states the equations for computing L. In conclusion, only six comfort factors remain for the computation of the imbalance L: metabolism M, clothing insulation I_{cl}, air temperature T_{air}, radiation temperature T_{mr}, air velocity v_{air} and humidity RH_{air} [2]. Finally, Fanger relates the comfort vote to the thermal load L and the current activity level M according to

$$\text{PMV} = \left(0.303 e^{-0.036M} + 0.028 \right) L. \tag{3.2}$$

The relation (3.2) predicts the average comfort vote of occupants under steady-state conditions based on the voting scale of Table 3.1. A more detailed description how the various terms for the PMV calculation are formed is provided in [3].

Since the PMV is still the most popular comfort model, a validation with the collected test data is performed to evaluate its validity and applicability for the considered test group.

Table 3.2: Standard parameter values for office work and light business clothing [26].

Parameter		Standard Value	Unit
Metabolic rate	M	70	$\mathrm{W/m^2}$
Clothing level	I_{cl}	0.09	$\mathrm{m^2\,K/W}$
Air velocity	v_{air}	$v_0 + c_{\mathrm{fan}} \cdot l_{\mathrm{fan}}$	$\mathrm{m/s}$

3.3 Evaluation of PMV Calculation

The six PMV comfort factors can be separated in personal and environmental parameters. Clothing insulation I_{cl} and metabolism M are characteristics of the occupants and can vary over time and between the individuals. Assuming rather stationary conditions and similar work tasks, these parameters are commonly set to constant values based on look-up tables provided by the comfort standards [2, 26]. The standardized values for office work and light business clothes are given in Table 3.2. The metabolic rate usually varies between 55 and $80\,\mathrm{W/m^2}$ for office activities [3]. Here, the value is set to $70\,\mathrm{W/m^2}$ because most occupants make use of height-adjustable tables so that a variation between seated and standing work positions is assumed. The remaining environmental factors are measured by the indoor air quality sensors.

One exception is the measurement of air velocity. The application of distributed air velocity measurements is usually not realizable in large office buildings due to the associated sensor costs. Nevertheless, the cooling effect of increased air velocities received closer attention in multiple studies during the last years, particularly in comfort analyses for tropical environments [21, 88] due to its energy saving potential. The actual air velocity varies significantly depending on the fan type, the distance to the fan and blockages by furniture. For quantifying the effect of the ceiling fan operation on the perceived comfort, a relation between the measurable fan level l_{fan} and the resulting average air velocity v_{air} is identified at each seating position in the regarded offices. Local air velocity measurements are used to approximate the desk-specific fan-velocity relations. Figure 3.4 shows the measurement results in a box plot for all seating positions and fan levels. The relation between the fan level and the measured air velocity is dominantly linear. Hence, it can be approximated by

$$v_{\mathrm{air}} \approx v_0 + c_{\mathrm{fan}} \cdot l_{\mathrm{fan}}. \tag{3.3}$$

The large range of the velocity measurements highlights the variance of the actual location-dependent air speed which is particularly increasing for higher fan levels. The zero crossing v_0 denotes the mean air velocity based on natural and forced convection
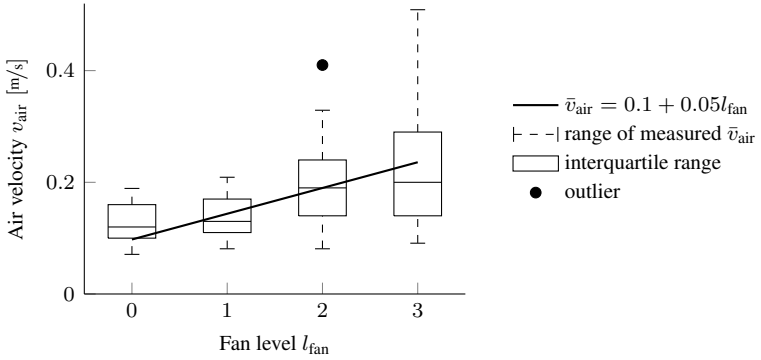
Figure 3.4: Identified relation between fan level and air velocity.

during the normal air conditioning operation. The solid line in Figure 3.4 indicates the linear regression result

$$\bar{v}_{\text{air}} = 0.1 + 0.05 l_{\text{fan}} \tag{3.4}$$

combining all measurements, thus defining an average relation for all desks. The identified coefficients in (3.4) provide an idea about the general impact of the ceiling fans. However, the approximation $\bar{v}_{\text{air}}$ does not provide a suitable representation for all seating positions as emphasized by the wide ranges in Figure 3.4. Therefore, the desk-specific measurements are used to fit the coefficient c_{fan} for each seat separately whereas the base air velocity v_0 is set to 0.1 according to the overall average for deactivated fans. The individual approximations are then used to calculate an air velocity equivalent for each user based on his seating position and the monitored fan level. The PMV can now be evaluated based on environmental measurements and the office-related standard parameters of Table 3.2. The following analysis is performed similarly to [42] but uses a different voting data set.

The collected voting data set of each user $j \in \{1, \ldots, N_{\text{occ}}\}$ with n_j observations is used to compute the PMV prediction accuracy based on the Root Mean Squared Error (RMSE)

$$\text{RMSE}_j = \sqrt{\frac{1}{n_j} \sum_{i=1}^{n_j} (\text{PMV}_{ij} - \nu_{ij})^2}, \tag{3.5}$$

where ν_{ij} denotes the recorded vote of user j corresponding to the observation $i \in \{1, \ldots, n_j\}$. The standard PMV, denoted as PMV_{std}, is calculated using the indoor air quality measurements of T_{air}, T_{mr} and RH, the standardized values for M and

I_{cl}, and the individually identified fan coefficients c_{fan}. The achieved accuracy over all users is depicted by the first box plot of Figure 3.5a and results in an average error of 1.4 steps on the voting scale. Two users even show an offset of over 2.7 such that supposedly comfortable conditions lead to an unacceptable true sensation on the far end of the thermal comfort scale. The distribution of the identified fan coefficients is shown in Figure 3.5b which vary between 0.002 and 0.14 depending on the seating position.

Obviously, using standardized values is not a realistic assumption for the representation of personal comfort. User-specific activity levels and clothing styles can result in significant deviations from the standard values of Table 3.2. Moreover, the perception of increased air velocities is very subjective and varying sensitivity can be found within different test groups, e.g based on diverse cultural backgrounds [103, 104]. Therefore, in a second analysis, the PMV parameters are identified and adjusted individually based on the following optimization problem

$$
\min_{c_{fan,j}, M_j, I_{cl,j}} \quad \sum_{i=1}^{n_j} (\mathrm{PMV}_{ij}(c_{fan,j}, M_j, I_{cl,j}) - \nu_{ij})^2
$$
$$
\text{s.t.} \quad \begin{aligned} c_{fan,j} &\in [0, 0.2] \\ M_j &\in [46, 110] \\ I_{cl,j} &\in [0.05, 0.11]. \end{aligned} \tag{3.6}
$$

The constraints are added to define physically feasible ranges according to [26] and the subjective sensation of increased air movement is captured by a personalized fan coefficient c_{fan}. The second box plot of Figure 3.5a visualizes the prediction error of the customized vote prediction $\mathrm{PMV}_{ij}(c_{fan,j}, M_j, I_{cl,j})$. Compared to the standard PMV, the average RMSE is reduced by 22 % to 1.1. The distribution of the associated individualized parameters is visualized in Figure 3.5b. Although the average values for metabolic rate and clothing level show only a small bias compared to the standard assumption, the personally optimized values cover almost the complete permissible range. Furthermore, the impact of the fan level is almost tripled compared to the experimental measurement results. A possible explanation for the increased cooling effect is given by strong turbulences [35] whereas the measured average air velocity is relatively low [17]. However, the higher than expected influence of the fan level can more likely be traced back to a general offset of the PMV model for the considered user group and the climatic conditions [51]. Previous research often identified biased PMV predictions such that the increased effect of the fan potentially compensates for a generally overestimated PMV [39]. Therefore, this assumption is adapted and included as additional user-related offset parameter b_j to the evaluation. Consequently,

the biased standard PMV is investigated according to

$$\min_{b_j} \quad \sum_{i=1}^{n_j} \big(\underbrace{\text{PMV}_{\text{std},ij} + b_j}_{\text{PMV}_{\text{std},b,ij}(b_j)} - \nu_{ij}\big)^2, \tag{3.7}$$

where $\text{PMV}_{\text{std},b,ij}(b_j)$ represents an individually biased standard PMV using the assumptions of Table 3.2. The corresponding prediction error is given by the third box plot of Figure 3.5a. Interestingly, the introduced bias achieves a similar accuracy compared to the personalized parameter identification and hence supports previous findings. The associated bias is depicted in Figure 3.5b and varies between 0.2 and -1.4. The user average of -0.7 clarifies that the standard PMV over-predicts the actual vote for most of the occupants.

A best predictive quality is attained by the individualization of all four parameters c_{fan}, M, I_{cl} and b_j. This leads to the extended objective

$$\min_{b_j, c_{\text{fan},j}, M_j, I_{\text{cl},j}} \quad \sum_{i=1}^{n_j} \big(\underbrace{\text{PMV}_{ij}(c_{\text{fan},j}, M_j, I_{\text{cl},j}) + b_j}_{\text{PMV}_{b,ij}(b_j, c_{\text{fan},j}, M_j, I_{\text{cl},j})} - \nu_{ij}\big)^2$$

$$\text{s.t.} \quad \begin{aligned} b_j &\in \mathbb{R} \\ c_{\text{fan},j} &\in [0, 0.2] \\ M_j &\in [46, 110] \\ I_{\text{cl},j} &\in [0.05, 0.11] \end{aligned} \tag{3.8}$$

and yields a RMSE reduction of 27% in relation to using standard parameters. The last box plots of Figure 3.5 describe the error and parameter distributions for the considered user group. Although this approach stands for the highest individualization, the mean error is still greater than 0.8 and thus only a moderate representation for personal thermal comfort. Analyzing the corresponding parameters reveals a high variance over the test subjects. The average metabolic rate, clothing insulation and fan impact are all higher than the expected value but cover the complete permitted range. Consequently, the bias also shows a greater scattering than for (3.8) although its mean stays on an identical level. The previous observations lead to two conclusions:

▶ The individual perception and comfort parameters vary in a wide range that standardized values are a bad assumption for personal vote prediction.

▶ Fanger's PMV model is not able to capture the complexity of individual thermal comfort in a real-world environment.

Besides the bad individualization of the PMV, the average values of the previous analysis still support the standardized parameters so that average comfort requirements can be mapped appropriately, particularly when allowing a bias. However, personalization requires a modified modeling approach.
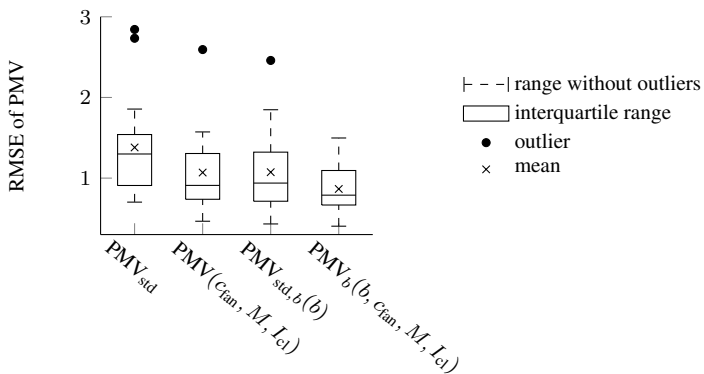
(a) RMSE of PMV prediction.
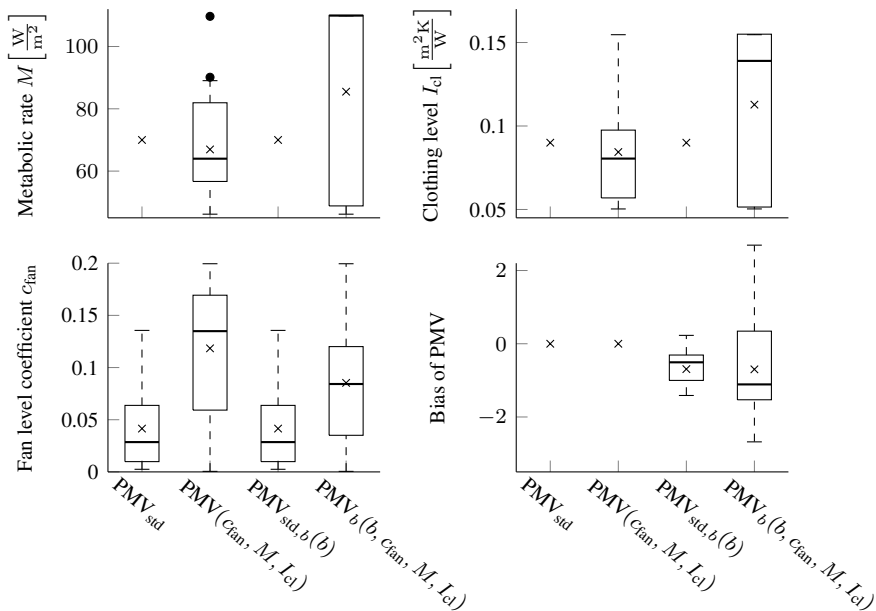
(b) Range of individually identified PMV parameters.

Figure 3.5: Accuracy and parameter ranges for individually optimized PMV parameters.

3.4 Modeling Individual Thermal Comfort

Recently, a great amount of research has been published considering thermal comfort [28], amongst others, due to the difficulties experienced with existing methods. Consequently, new developments focus on data-based approaches to cope with the high complexity. Almost the whole spectrum of ML techniques was applied to the comfort prediction problem where ANN, k-Nearest Neighbors (kNN) [16, 31, 61] and GP regression [9, 32, 42] are only a few examples. However, most models use the same parameter base as the PMV. This entails a sensing problem for most application-oriented approaches. The monitored variables are commonly limited to environmental and building related states, like temperatures, humidity and mass flows. Occupant-related variables, such as individual metabolism, clothing or even psychological conditions are rarely available for comfort-based building control. Currently applied physics-based models handle this issue by using standardized values for all unknowns, similarly to the assumptions of Table 3.2. However, as discussed in Section 3.3, the success for personal comfort modeling is very limited.

Purely data-based approaches, on the other hand, are directly trained based on user feedback to map the individual sensation. Due to the high subjectivity, these approaches either require a very large data base or detailed monitoring of user-specific parameters to result in feasible prediction models. Including useful prior knowledge about well-known comfort relations ameliorates the situation. Therefore, an application-oriented compromise between known physical relations and data-based modeling for successful individualization is derived in the following. As a start, the PMV is analyzed regarding the relations between the environmental conditions and the resulting model output to derive a reasonable personal comfort model structure.

3.4.1 Impact of PMV Comfort Factors

Although Section 3.3 proved a limited validity of the PMV for individual thermal comfort prediction, useful characteristics about how specific comfort factors influence the thermal sensation can be derived. This information is used to define a simplified but meaningful model structure and allows to incorporate prior knowledge for robust predictions. Therefore, the dependencies between the PMV and air temperature T_{air}, velocity v_{air} and mean radiant temperature T_{mr} are evaluated based on the standardized parameters of Table 3.2. The PMV is computed according to Appendix B.3 and shown in Figure 3.6 where either T_{air} and T_{mr} or T_{air} and v_{air} are varied. A clear linear relation of the vote and the air temperature can be observed. The shift introduced by a changing mean radiant temperature is also approximately linear such that PMV $\propto T_{\mathrm{air}} \propto T_{\mathrm{mr}}$ is a valid assumption, as visualized in Figure 3.6a. While T_{air} can be usually directly manipulated by the HVAC system, T_{mr} is a result of surrounding surface temperatures, solar influences and location-related viewing factors.

(a) Effect of T_{mr} assuming $v_{\mathrm{air}} = 0$.

(b) Effect of v_{air} assuming $T_{\mathrm{mr}} = T_{\mathrm{air}}$.
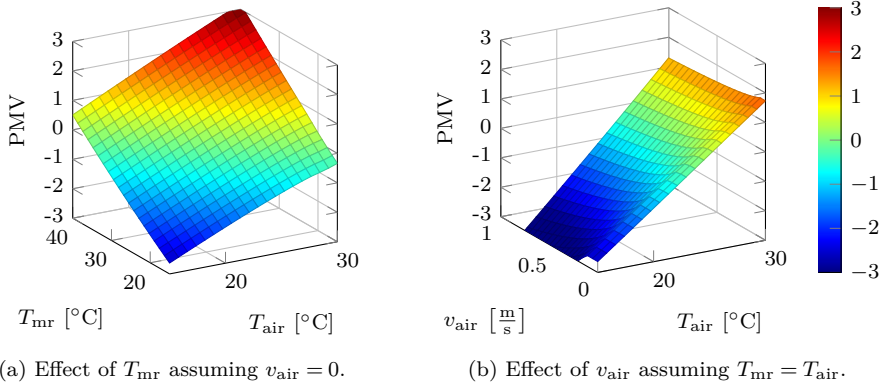
Figure 3.6: Effect of mean radiant temperature T_{mr} and air velocity v_{air} on the PMV under the assumption of office-related parameters for metabolic rate M and clothing level I_{cl} according to Table 3.2.

Consequently, detailed knowledge about the room geometry and boundary conditions is necessary to allow for a model-based estimation of the mean radiant temperature. To simplify the computation of T_{mr} for prediction purposes, an empirical relation can be derived for the considered test-bed. Due to the orientation of the office, direct solar radiation rarely influences the indoor conditions and a dominant linear relation between the air and the mean radiant temperature is observed. Appendix B.4 discusses this relation in more detail and allows to substitute $T_{\mathrm{mr}} = 2.38 + 0.98 T_{\mathrm{air}}$ according to (B.6). The influence of air velocity is shown in Figure 3.6b and reveals a dead band with no velocity impact due to the case discrimination in (B.3). Then, a leveling cooling effect is exposed which is more dominant for lower temperatures.

The last environmental factor that impacts the PMV is relative humidity RH. It influences the heat exchange between the human body and the environment. Higher RH reduces the heat loss by evaporation, thus sweating. The realistic range for the considered air conditioned building is 40 to 60 % such that the PMV is maximally shifted by 0.2. The predominant range for humidity in the test-bed is even lower and varies mainly between 50 and 52 %. For these small variations, no significant impact on the PMV can be noted.

The modeling goal is the derivation of a suitable approach for the prediction of the individual thermal comfort. The dominating linear relations between the PMV and the comfort factors justify a first simple proposal for the Predicted Individual Vote (PIV) model

$$\mathrm{PIV}_j(\boldsymbol{z} = T_{\mathrm{air}}) = \beta_{0,j} + \beta_{j,T_{\mathrm{air}}} T_{\mathrm{air}} = \begin{bmatrix} 1 & T_{\mathrm{air}} \end{bmatrix} \boldsymbol{\beta}_j = \boldsymbol{\phi}(\boldsymbol{z})^{\mathrm{T}} \boldsymbol{\beta}_j. \tag{3.9}$$

The model coefficients $\boldsymbol{\beta}_j = \begin{bmatrix} \beta_{0,j} & \beta_{j,T_{\text{air}}} \end{bmatrix}^{\text{T}}$ are identified for each user j based on

$$\min_{\boldsymbol{\beta}_j} \sum_{i=1}^{n_j} \left(\text{PIV}_{ij} - \nu_{ij} \right)^2 = \min_{\boldsymbol{\beta}_j} \sum_{i=1}^{n_j} \left(\boldsymbol{\phi}(\boldsymbol{z}_i)^{\text{T}} \boldsymbol{\beta}_j - \nu_{ij} \right)^2 . \tag{3.10}$$

The analytical solution for the least square approximation (3.10) is given by

$$\boldsymbol{\beta}_j = \left(\boldsymbol{Z}_j^{\text{T}} \boldsymbol{Z}_j \right)^{-1} \boldsymbol{Z}_j^{\text{T}} \boldsymbol{\nu}_j \tag{3.11}$$

where $\boldsymbol{\nu}_j$ contains all thermal sensation votes ν_{ij} and $\boldsymbol{Z}_j = \begin{bmatrix} \boldsymbol{\phi}(\boldsymbol{z}_{1j}) & \cdots & \boldsymbol{\phi}(\boldsymbol{z}_{n_j j}) \end{bmatrix}^{\text{T}}$ the corresponding observations. Solving (3.11) directly often leads to illogical coefficients due to a low system excitation and limited voting data with high intrinsic variance. To ensure feasibility, prior knowledge is included by introducing physically motivated constraints. In this case, only a positive correlation between the vote and air temperature results in reasonable models so that (3.10) is extended by the constraint $\beta_{T_{\text{air}}} > 0$.

Figure 3.7 compares the individual vote approximation $\text{PIV}_j(T_{\text{air}})$, the PMV for standardized values as well as the individualized PMV. This comparison emphasizes once more the user-specific discrepancies discussed in Section 3.3. The individual comfort models depicted in Figure 3.7b highlight the significant differences regarding the comfort expectations of the test group. The previously identified bias between the standard PMV and the actual voting data is again visible as a downward shift of the average PIV. Although the individual comfort models PIV_j exhibit diverse characteristics, the slope of the average PIV is very similar to the PMV model besides the offset. This supports the validity of the PMV model which aims to map an averaged thermal sensation. However, the significant differences between the individual user models emphasizes the dominant subjectivity that must be dealt with in personalized comfort control concepts.

The achievable mapping accuracy between the voting data and the modeling approaches is shown in Figure 3.7a. The previous results for the standard PMV and the individualized PMV are revisited and compared to the linear PIV model. Already the simple approach (3.9) outperforms the personalized PMV and reduces the average RMSE to 0.8. In conclusion, the linear regression approach, which only uses T_{air} as reference value, surpasses all investigated individualizations of the PMV and leads to the best representation of the individual voting data. However, air temperature is certainly not the only influencing factor that affects the thermal comfort. Therefore, alternative and additional predictors are considered in the following to improve the prediction accuracy.
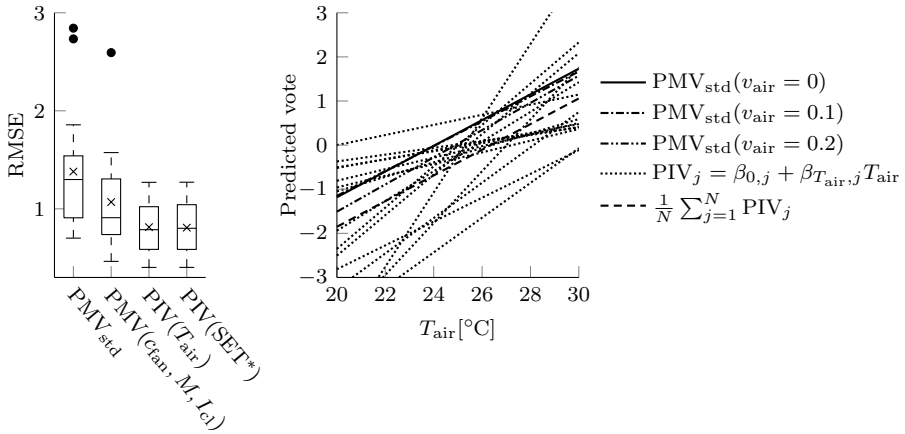
(a) Regression error of PMV and PIV.

(b) Comparison between PMV prediction for different air velocities and individual linear comfort approximation.

Figure 3.7: Comparison of PMV, linear approximation $\text{PIV}(T_{\text{air}})$ (3.9) and $\text{PIV}(\text{SET}^*)$ (3.12).

3.4.2 Standard Effective Temperature = Better Comfort Reference?

The promising results of the linear regression approach support further attempts in this direction. Obviously, thermal comfort is not only a function of temperature but depends on more conditions as discussed in Section 3.2. Therefore, the individual models of Figure 3.7 might vary, e. g. for changing humidity and air velocity values. Environmental indices combine multiple parameters into one value that can be used as comparable reference for defining thermal stress and thermoregulatory strain [3]. These indices are already commonly used as predictor for thermal sensation [37]. Hence, the first regression model (3.9) is replaced by an index-based approach and its suitability is analyzed in this section.

The most common index is the Effective Temperature (ET*). It combines radiation, air temperature and humidity in a single representing measure by computing a temperature equivalent that results in the same heat loss for 50 % humidity. The ET* further depends on the activity and clothing level due to different values for skin wettedness and clothing moisture permeability. Hence, the Standard Effective Temperature (SET*) is introduced that maps the ET* to standardized conditions. The reference conditions for the SET* transformation are defined as

▶ 50 % relative humidity

- ► air velocity $v_{\mathrm{air}} < 0.1 \frac{\mathrm{m}}{\mathrm{s}}$

- ► $T_{\mathrm{air}} = T_{\mathrm{mr}}$

- ► clothing insulation $I_{\mathrm{cl}} = 0.09 \frac{\mathrm{m^2 K}}{\mathrm{W}}$

- ► metabolic rate $M = 58.2 \frac{\mathrm{W}}{\mathrm{m^2}}$

and the SET* defines the temperature equivalent where the heat loss of the human body is equal to the heat loss in the current environment [2]. Previous research supports an improved applicability of this measure in warm climates and identified a proportionality between the thermal comfort vote and the SET* [49]. Therefore, the SET* is used as a substitute for T_{air} in (3.9) and tested according to its usability for predicting the individual comfort of the considered test group. Thus, the modified approach

$$\mathrm{PIV}_j(\mathrm{SET^*}) = \beta_{0,j} + \beta_{\mathrm{SET^*},j} \cdot \mathrm{SET^*} = \begin{bmatrix} 1 & \mathrm{SET^*} \end{bmatrix} \boldsymbol{\beta}_j \tag{3.12}$$

is evaluated for the given voting data. The SET* calculation is also based on the heat balance (3.1) and requires the same six user-related parameters and ambient conditions as the PMV computation. In contrast to the PMV, the evaporation of sweat depending on the air velocity is taken into account so that the influence of a higher air velocity is often better represented by the SET* [37]. The corresponding model equations are described in [36] and the ASHRAE Standard 55 [2] suggests the usage of the *ASHRAE Thermal Comfort Tool*. For an evaluation of the modeling approach (3.12), the observation data of each occupant are used to compute the SET* value for each vote. Subsequently, the coefficients $\beta_{0,j}$ and $\beta_{\mathrm{SET^*},j}$ are identified for each user and the regression error is analyzed to decide on the suitability of this modeling approach. The corresponding distribution of the user's RMSEs is shown in Figure 3.7a.

A more detailed comparison of the SET*-based approach (3.12) with the T_{air}-based model (3.9) is illustrated in Figure 3.8 for the voting data of two exemplary occupants. The plot depicts the user comfort votes in relation to T_{air} and SET* respectively. What catches the eye at first is the very high variance of the scattered user data. Equal sensation votes cover a wide temperature range and the linear fits $\mathrm{PIV}_j(T_{\mathrm{air}})$ and $\mathrm{PIV}_j(\mathrm{SET^*})$ are only able to capture a general trend. Obviously, numerous other factors affect the comfort vote which are not considered in both approaches. However, if the substitution $T_{\mathrm{air}} \rightarrow \mathrm{SET^*}$ achieves a reduction of the variance and thus results in a narrower, clearer shaped point cloud in Figure 3.8, the SET* would provide a better reference than T_{air}. Although the SET* transformation causes a shift of the scattered user data such that the corresponding linear regression model exhibits a modified slope, a significant improvement cannot be observed. This is further supported by the almost unchanged RMSE in Figure 3.7a where the prediction error for $\mathrm{PIV}(T_{\mathrm{air}})$ is approximately identical to the error of the advanced approach
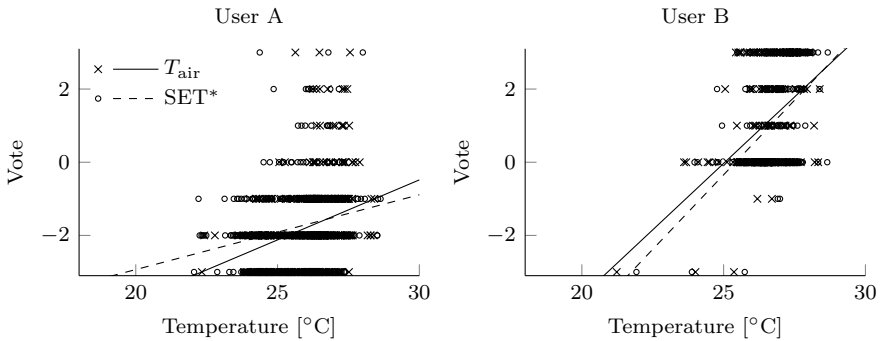
Figure 3.8: Comparison of SET* and T_{air} as comfort predictor based on (3.9) and (3.12).

PIV(SET*). Consequently, the increased complexity of the SET* calculation is not rewarded by an enhanced prediction quality.

These results once more emphasize the complexity of individual comfort modeling and explain the increasing interest in data-driven comfort models [60]. Since the SET* does not provide a better regression parameter than air temperature, the model structure for personal vote prediction is further modified.

3.4.3 Correlation Analysis

The previous analysis showed that standardized comfort models are not practicable for the prediction of personal comfort. Furthermore, the much simpler temperature-based regression approach (3.9) outperforms the standard models but leaves a lot of potential for improvement. The described difficulties are often treated by an adaption of the standard PMV and SET* models, e. g. [58]. However, approaches including the calculation of PMV or SET* incorporate a high complexity which is a major drawback for their usage in the framework of optimization-based control approaches. While these physically motivated relations build a very important basis when no user feedback is available, simpler data-driven approaches can efficiently replace the physical models by combining empirical knowledge and user feedback. Although user-related information about the physical or psychological state has a significant impact on the thermal sensation, the available measurement equipment is restricted to environmental monitoring. Therefore, only the accessible data can be taken into account for personal comfort modeling and accordingly, leads to the question which measurable variables are the most important. Apart from air temperature, for instance outdoor conditions are proven to impact the thermal perception and expectations [50]. To identify the

most essential comfort factors for the considered test group, a correlation analysis and feature selection is performed. The available sensor measurements and thus the set of possible comfort model inputs $\mathcal{Z}$ is given by

- ▶ air temperature T_{air},
- ▶ mean radiant temperature T_{mr},
- ▶ relative humidity RH_{air},
- ▶ fan levels of 8 ceiling fans $l_{\text{fan},i}$, $i = 1, \ldots, 8$ (4 in each office),
- ▶ supply air temperature T_{sup},
- ▶ ambient temperature T_{out},
- ▶ global solar radiation I_{sol},
- ▶ outside relative humidity RH_{out} and
- ▶ time of day DT.

The correlation between the vote ν and one arbitrary environmental variable $z \in \mathcal{Z}$ indicates important dependencies and reveals which parameters have the greatest (linear) impact on the thermal perception. The correlation coefficient of ν and z is calculated by [48]

$$\varrho = \varrho\left(\nu, z\right) = \frac{\sum_{i=1}^{n}(\nu_i - \bar{\nu})(z_i - \bar{z})}{\sqrt{\sum_{i=1}^{n}(\nu_i - \bar{\nu})^2 \sum_{i=1}^{n}(z_i - \bar{z})^2}} \tag{3.13}$$

where $\bar{\nu} = \frac{1}{n}\sum_{i=1}^{n}\nu_i$ and $\bar{z} = \frac{1}{n}\sum_{i=1}^{n}z_i$. Figure 3.9a shows the absolute correlation coefficients $|\varrho|$ for the votes of the test group and the environmental conditions. The absolute value is examined because the direction of impact can vary between different subjects and a generalizing sign presumption contradicts the individualization target. The median and average correlation are depicted to provide further insight regarding the group's characteristic. The median is less influenced by outliers such that a great deviation between the two values indicates an inhomogeneous sensitivity of the different test persons. The three most important parameters are T_{air}, T_{mr} and T_{sup}, followed by RH_{air} and DT. The significant effect of the indoor temperatures corresponds to the natural intuition. However, the temperature values are strongly cross-correlated which leads to a deviating result for the partial correlation coefficient ϱ_{partial}. The partial correlation defines the degree of dependency of two variables if the remaining variables are set to a constant value [48]. Consequently, the effect of cross-correlations is eliminated which changes the results remarkably. The influence of T_{air}, T_{mr}, T_{sup} and DT are reduced significantly while the impact of the fan level l_{fan} gains more relevance. The other variables largely maintain their level of correlation so that the greatest importance based on ϱ_{partial} can be associated with l_{fan} and RH_{air}. Almost no cross-correlation effect can be noted for RH_{air}, T_{out}, I_{sol} and RH_{out}. The great
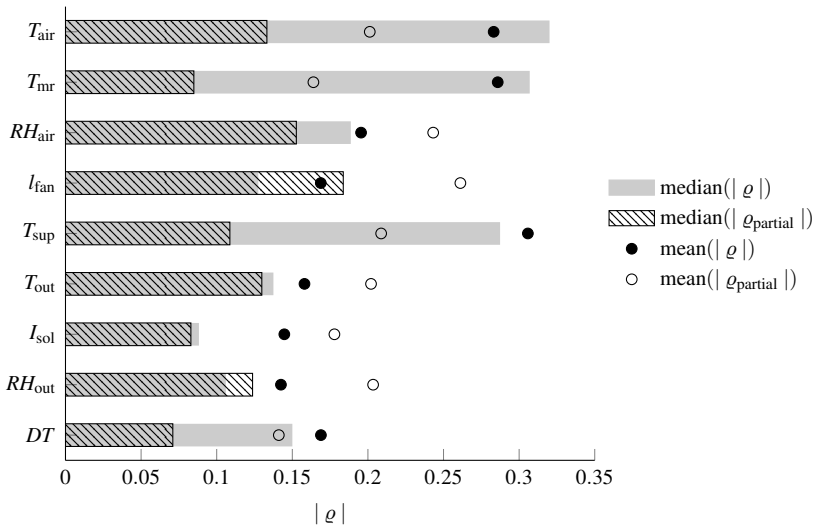
(a) Absolute correlation $| \varrho |$
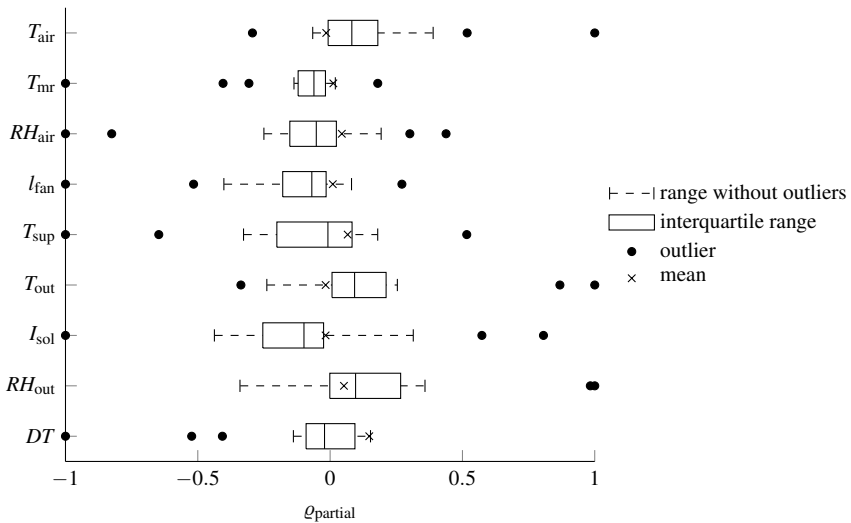
(b) Partial correlation $\varrho_{\mathrm{partial}}$ of all users.

Figure 3.9: Correlation analysis of vote and environmental conditions.

difference between the average and median correlation for nearly all considered factors emphasizes once more the variance among the users and highlights the inconsistency of impacting comfort factors. This observation is further supported by Figure 3.9b which shows the distribution of the signed partial correlation for all users as a box plot. Here, it becomes obvious that the individual coefficients vary widely and a direct reading of the most important parameters is not possible. Some users even exhibit physically inexplicable correlations, e. g. a negative influence of T_{air} or a positive impact of l_{fan}. Therefore, defining a meaningful model structure and a robust identification process requires a well reasoned procedure that copes with high uncertainty of real world voting data.

3.4.4 Model Structure

Previous research applied multiple data-driven (ML) approaches to the comfort prediction problem [28]. Most of this research relies on test data gathered under well-defined lab conditions. However, an application- and control-oriented approach introduces some limitations and requirements on the model structure and data collection process:

1. **Limited data**: The collection of user-specific voting data implies a regular distraction of the occupants during their daily working routine. User acceptance can only be achieved when the amount of interruptions is minimized. This limits the voting frequency significantly and thus the available observation data.

2. **Low system excitation**: The applicability of the final control setup crucially depends on the acceptance of the occupants. This limits the possibilities of system excitation drastically because large variations, which result in very uncomfortable conditions, cannot be explored.

3. **Adaptivity**: Since user preferences can vary over time (e. g. due to varying outside conditions, working tasks, clothing habits, changing metabolism or psychological reasons), the model must be able to adopt the new characteristics.

4. **Simplicity**: Individualized comfort in commercial buildings requires a great amount of computing power due to the high number of occupants. The data collection and processing effort should be kept as low as possible.

5. **Robustness**: The high variance of real-world voting data incorporates a great risk of overfitting and physically illogical predictions. A straightforward interpretability and simple supervision of the model properties must be ensured to avoid delusive model outputs.

To address the described challenges and due to a good interpretability, at first only generalized linear function approaches of the form

$$\text{PIV} = \boldsymbol{\phi}^{\text{T}}(\boldsymbol{z})\boldsymbol{\beta} \tag{3.14}$$

are considered. This structure takes up the dominating linear relations observed in Section 3.3 and 3.4.2 as well as in previous studies [2, 26, 49]. The following definitions of the feature vector $\phi(z)$ are evaluated according to their achievable prediction accuracy:

$$\phi_1(z) = \begin{bmatrix} 1 \\ z \end{bmatrix} \quad \phi_2(z) = \begin{bmatrix} 1 \\ z \\ z^{\circ 2} \end{bmatrix} \quad \phi_3(z) = \begin{bmatrix} 1 \\ z \\ z^{\circ 2} \\ z^{\circ 3} \end{bmatrix} \quad \phi_4(z) = \begin{bmatrix} 1 \\ z \\ z \otimes z \end{bmatrix} \quad (3.15)$$

where $^{\circ k}$ defines the k-th Hadamard (entrywise) product of the vector z, accordingly $z^{\circ 2} = z \circ z$. The tensor product $z \otimes z$ extends the basis vector ϕ_2 by all interactions between the elements. This results in a maximum number of predictors

$$N_{\mathrm{f}} = \begin{cases} 9 & \text{for } \phi_1 \\ 2 \cdot 9 = 18 & \text{for } \phi_2 \\ 3 \cdot 9 = 27 & \text{for } \phi_3 \\ 9 + 36 = 45 & \text{for } \phi_4 \end{cases}$$

under the assumption that the full variable set $\mathcal{Z}$ is used. Note that the coefficient β_0 for the constant bias is always part of the model and excluded from the predictor count. Consequently, simply using ϕ_4 would involve the identification of $46\,(45 + \mathrm{bias})$ model parameters per person and thus require a large amount of observations, where a sufficiently high system excitation must be ensured for every independent model dimension. This contradicts the requirement of a low voting frequency and a data collection during the daily working routine where occupants should not be exposed to very uncomfortable conditions. Furthermore, not all variables are relevant for predicting comfort [64] such that an involvement unnecessarily increases the model's complexity. This and the redundancy introduced by the already discussed cross-correlations entail a high risk of overfitting. Therefore, a detailed feature selection analysis is performed to ensure robust predictions and a well generalizing model structure.

Before the most important features are identified, another application-related restriction is included in the modeling procedure. Due to the Multiple-Input-Single-Output (MISO) model structure of (3.14), personalized thermal comfort can be achieved by numerous combinations of inputs and corresponds to a hyperplane in the N_{f}-dimensional room. Usually, only a subset of model parameters are manipulated variables so that the considered comfort factors $z \in \mathcal{Z}$ can be separated in measurable but immutable disturbances d and controllable variables u:

$$\mathrm{PIV} = \phi^{\mathrm{T}}(u, d)\beta = \begin{bmatrix} 1 & \phi_u{}^{\mathrm{T}} & \phi_d{}^{\mathrm{T}} & \phi_{ud}{}^{\mathrm{T}} \end{bmatrix} \beta. \quad (3.16)$$

The manipulated variables $\boldsymbol{u}$ for the given test bed are T_{air} and l_{fan}.[b] Both are selected as fixed components of the model structure since both are directly related to thermal comfort and required for a subsequent derivation of a comfort-optimal trajectory. This is done by ensuring an occurrence of both in at least one feature. The remaining potential comfort factors are collected in the disturbance vector $\boldsymbol{d}$.[c] For example, the linear model approach $\boldsymbol{\phi}_1$ can be rewritten as

$$\text{PIV} = \boldsymbol{\phi}_1^{\text{T}}(\boldsymbol{u}, \boldsymbol{d})\boldsymbol{\beta} = \begin{bmatrix} 1 & \boldsymbol{u}^{\text{T}} & \boldsymbol{d}^{\text{T}} \end{bmatrix} \boldsymbol{\beta}, \tag{3.17}$$

where the feature selection task searches for the best combination of disturbances which represent the most beneficial extension of $\boldsymbol{u}$ and thus have the highest impact on the individual thermal sensation.

3.4.5 Relevance Analysis of Comfort Factors and Feature Selection

The algorithmic tools for feature subset selection encompass multiple methods [47]. The optimal model can be found by evaluating the full combinational problem where the predictive quality of every possible combination of k features is evaluated. The subset with the best generalizing properties is the most suitable choice. Assuming that k features are selected from the set of N_{f} possible features, the number of required function evaluations is defined by $\binom{N_{\text{f}}}{k}$. This approach quickly leads to a computational infeasible problem, particularly due to the unknown dimension of the optimal feature space and alternative methods must be consulted. Generally, the optimal amount of features can be found by cross-validation. For this, the observation data $\mathcal{D}_j = \{(\boldsymbol{z}_{ij}, \nu_{ij}), i = 1, \ldots, n_j\}$, as presented in Appendix B.2, are separated in multiple pairs of training $\mathcal{T}_j = \{(\boldsymbol{z}_{ij}, \nu_{ij}), i = 1, \ldots, n_{\mathcal{T},j}\}$ and test sets $\mathcal{V}_j = \{(\boldsymbol{z}_{ij}, \nu_{ij}), i = 1, \ldots, n_{\mathcal{V},j}\}$, so that $\mathcal{D}_j = \mathcal{T}_j \cup \mathcal{V}_j$ and $\mathcal{T}_j \cap \mathcal{V}_j = \varnothing$. The training data are used for the identification of the occupant-specific parameters $\boldsymbol{\beta}_j$ and the corresponding test (validation) error defines the quality of the currently selected structure. This procedure ensures that a well generalizing set of features is selected. In the following, the designation MSE always refers to the average validation error.

Computing the unconstrained least square estimate (3.11) based on $\mathcal{T}_j$ directly returns the user-specific coefficients $\boldsymbol{\beta}_j$. However, the former analysis showed that simply solving (3.11) can lead to illogical coefficients $\boldsymbol{\beta}_j$ as also indicated by the partial correlation coefficients in Figure 3.9b, e.g. due to a small set of available observations

---

[b]From the control theory perspective, T_{air} is rather considered as a system state instead of a manipulated variable. However in building control, this is the common manipulated state and therefore taken as representative input which is independent from the actual AC system. Later control concepts make the distinction in system state $\boldsymbol{x}$ and manipulated input $\boldsymbol{u}$.

[c]Similarly to the purposive introduction of $\boldsymbol{u}$, the disturbance vector $\boldsymbol{d}$ contains all measurable conditions although some elements, e.g. RH_{air}, are in fact room states. However, as long as no dynamical room model is assumed, these variables are taken into account as disturbance effects on the thermal comfort state.

or insufficient system excitation during the data collection. Therefore, the good interpretability of the linear model structure can be used to incorporate previous knowledge about comfort relations, particularly regarding the partial gradients. For example, temperature and radiation are known to be positively correlated to the thermal sensation so that

$$\beta_{j,T_{\text{air}}}, \beta_{j,T_{\text{mr}}}, \beta_{j,RH_{\text{air}}}, \beta_{j,T_{\text{sup}}}, \beta_{j,I_{\text{sol}}} \geq 0 \tag{3.18}$$

is a reasonable assumption. The cooling effect of higher air velocities is represented by a negative coefficient:

$$\beta_{j,l_{\text{fan}}} \leq 0. \tag{3.19}$$

The coefficients $\beta_{j,T_{\text{out}}}$, $\beta_{j,RH_{\text{out}}}$ and $\beta_{j,DT}$ remain unconstrained because their impact cannot be preset for certain. Some people are positively affected while other show a reversed behavior [25, 50]. The model's parameter identification is consequently performed by solving the constrained optimization problem

$$
\begin{aligned}
\boldsymbol{\beta}_j^* &= \underset{\boldsymbol{\beta}_j}{\arg\min} \quad \sum_{i=1}^{n_{\mathcal{T},j}} \big(\text{PIV}(\boldsymbol{\phi}(\boldsymbol{z}_{ij})) - \nu_{ij}\big)^2 \\
&= \underset{\boldsymbol{\beta}_j}{\arg\min} \quad \sum_{i=1}^{n_{\mathcal{T},j}} \Big(\boldsymbol{\phi}^{\text{T}}(\boldsymbol{z}_{ij})\boldsymbol{\beta}_j - \nu_{ij}\Big)^2 \\
&= \underset{\boldsymbol{\beta}_j}{\arg\min} \quad \big|\big|\boldsymbol{Z}_j\boldsymbol{\beta}_j - \boldsymbol{\nu}_j\big|\big|_2^2 \\
&\text{s.t.} \qquad \boldsymbol{\beta}_{\min} \leq \boldsymbol{\beta}_j \leq \boldsymbol{\beta}_{\max}
\end{aligned} \tag{3.20}
$$

where $\boldsymbol{\beta}_{\min}$ and $\boldsymbol{\beta}_{\max}$ combine (3.18) and (3.19). The matrix of observations $\boldsymbol{Z}_j$ contains the currently selected set of features based on the training data $\mathcal{T}_j$. In the following, the solution of (3.20) is referred to as Ordinary Least Squares Solution (OLSS).

The measure for the model's quality is the validation error. Thus, the optimal feature set minimizes the cross-validated MSE of the test data $\mathcal{V}_j$ for user j:

$$\boldsymbol{\phi}_j^* = \underset{\boldsymbol{\phi}}{\arg\min} \frac{1}{n_{\mathcal{V},j}} \sum_{i=1}^{n_{\mathcal{V},j}} \Big(\boldsymbol{\phi}^{\text{T}}(\boldsymbol{z}_{ij})\boldsymbol{\beta}_j^* - \nu_{ij}\Big)^2. \tag{3.21}$$

The resulting optimal feature vector $\boldsymbol{\phi}_j^*$ can vary between different users. For instance, an occupant close to the window is more likely affected by solar radiation than someone sitting in the rear part of the room. However, the goal of the subset selection is the

definition of a perfect set that represents all the users without over- or underfitting of the individual comfort functions. Therefore, (3.21) is generalized to

$$\boldsymbol{\phi}^* = \arg\min_{\boldsymbol{\phi}} \sum_{j=1}^{N_{\text{occ}}} \frac{1}{n_{\mathcal{V},j}} \sum_{i=1}^{n_{\mathcal{V},j}} \left(\boldsymbol{\phi}^{\text{T}}(\boldsymbol{z}_{ij}) \boldsymbol{\beta}_j^* - \nu_{ij} \right)^2. \tag{3.22}$$

The vector $\boldsymbol{\phi}^*$ then contains a subset of all possible features depending on the selected shape function basis ϕ_k, $k = 1, \ldots, 4$. For the following feature selection, only occupants with more than 50 observations are taken into account which results in 16 valid user data sets. Otherwise, outliers distort the result.

Combinational Feature Selection

For the simpler approaches $\boldsymbol{\phi}_1$ and $\boldsymbol{\phi}_2$, see (3.15), an evaluation of the combinatorics is computationally feasible so that the global optimum of (3.22) can be evaluated. A 10-fold cross-validation is performed and leads to a minimal accumulated MSE for each $N_{\text{f}} \in \{1, \ldots, 9\}$ or $N_{\text{f}} \in \{1, \ldots, 18\}$ considered features. Note that the first two predictors are predefined by the elements containing T_{air} and l_{fan} respectively. The achievable prediction error for each case is depicted in Figure 3.10. According to the left plot, including more linear features to the model firstly improves the prediction quality and subsequently leads to a slight deterioration for more than $N_{\text{f}} = 6$ predictors. However, the cross-validation result for $\boldsymbol{\phi}_1$ exposes favorable and unfavorable combinations indicated by the vertical range of the scattered marks. Nevertheless, the implemented constraints (3.18) and (3.19) already avoid significant overfitting effects. Solving the unconstrained problem increases the range of the scattered marks drastically as already indicated by the high variance of the user data, e. g. shown in Figure 3.7b and 3.8. The respective optimal feature set for each model dimension $N_{\text{f}} \in \{1, \ldots, 9\}$ is listed in Table 3.3. The combination of linear features minimizing the cross-validated MSE is given by

$$\boldsymbol{\phi}_1^* = \begin{bmatrix} 1 & T_{\text{air}} & l_{\text{fan}} & T_{\text{mr}} & RH_{\text{air}} & RH_{\text{out}} & DT \end{bmatrix}^{\text{T}}. \tag{3.23}$$

The most beneficial disturbance parameters added to the input $\boldsymbol{u}$ is the time of day DT. The importance of DT can be explained by its strong cross-correlation with outside conditions, T_{out}, I_{sol} and RH_{out}, as well as indoor humidity RH_{air} so that this parameter accumulates a high information content in one value. These correlations are further discussed in Section B.5. Furthermore, daily variations of the activity level due to recurring routines (e. g. lunch break, tiredness) can be captured by the daytime. The substitution of DT by T_{mr} and RH_{air} when using 4 instead of 3 predictors can be also explained by the mentioned cross-correlation of these factors. Both are daytime-dependent and capture repetitive disturbance effects based on outside conditions and air conditioning operation. Furthermore, T_{mr} is able to capture the impact of solar
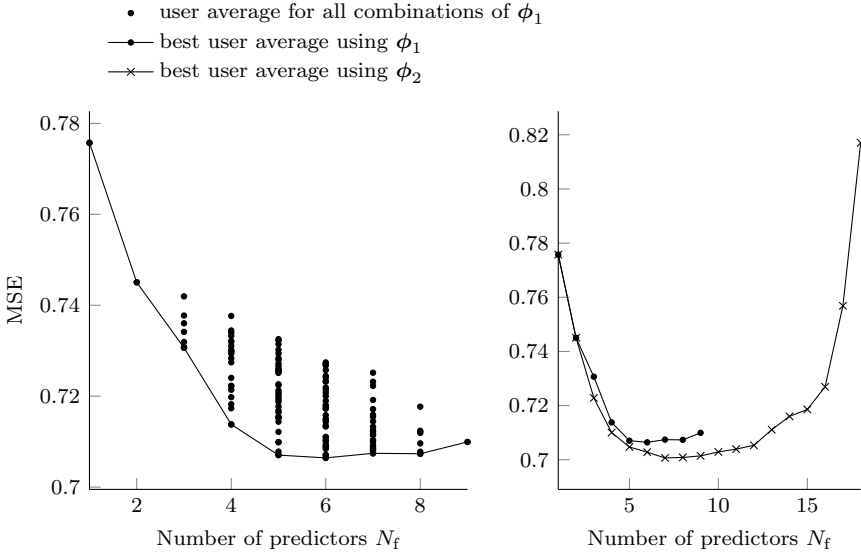
Figure 3.10: Accumulated average and median 10-fold cross-validated prediction error.

loads and provides a better reference for local differences and resulting sensitivities of the occupants. The implication of RH_{out} in the optimal feature combination (3.23) can be explained by its high cross-correlations to the remaining outside conditions so that it is a good representative for their influence. Moreover, one can argue that 5 predictors are sufficient, since the impact on the MSE is negligible. The respective median error even increases for using 6 features. Therefore, the model's dimension can be reduced without remarkable effects on the estimation error.

Adding a second order term to the shape function candidates has the potential to further enhance the achievable model accuracy. This is outlined in Figure 3.10 where the cross-validated MSE for the optimal combinations of features based on ϕ_1 and ϕ_2 are compared. The minimum MSE for ϕ_2 is identified for $N_{\text{f}} = 7$ with the associated vector

$$\phi_2^* = \begin{bmatrix} 1 & T_{\text{air}} & T_{\text{air}}^2 & l_{\text{fan}} & T_{\text{mr}} & RH_{\text{air}} & RH_{\text{out}} & DT \end{bmatrix}^{\text{T}}. \tag{3.24}$$

Comparing the optimal feature vector (3.24) to (3.23) reveals that the elements are almost identical. Only the squared value of T_{air} is added to the optimal linear set ϕ_1^*. The gray elements indicate the model components that are neglected in the optimal 6-dimensional vector (incl. bias). The reduced vector, too, matches the result for ϕ_1 with the only difference of using T_{air}^2. Regarding the associated validation errors, any

Table 3.3: Optimal feature selection for 2 to N_f predictors based on ϕ_1 with fixed basis $\boldsymbol{u} = [T_\text{air} \quad l_\text{fan}]^\text{T}$.

N_f	T_air	T_mr	RH_air	l_fan	T_sup	T_out	I_sol	RH_out	DT	MSE mean (median)
1	✓									0.776 (0.683)
2	✓			✓						0.745 (0.661)
3	✓			✓					✓	0.731 (0.641)
4	✓	✓	✓	✓						0.714 (0.617)
5	✓	✓	✓	✓				✓		0.707 (0.608)
6	✓	✓	✓	✓				✓	✓	0.706 (0.610)
7	✓	✓	✓	✓	✓		✓		✓	0.707 (0.617)
8	✓	✓	✓	✓		✓	✓	✓	✓	0.707 (0.604)
9	✓	✓	✓	✓	✓	✓	✓	✓	✓	0.710 (0.600)

model approach using 5 to 7 well-selected features can be justified. However, the risk of over-fitting increases drastically for ϕ_2 due to the larger selection of insignificant features. This can lead to 8-dimensional combinations with average MSE of up to $1.6 \cdot 10^7$ when the worst feature combination is used as comfort mapping function. Note that this is the reason why the combinational results for ϕ_2 are not shown in Figure 3.10. The required scale exceeds the meaningful range for a graphical presentation. Eventually, the simpler linear feature set is the more robust choice when little knowledge of the comfort factor importance is provided, as demonstrated by the small range of the combinational result in Figure 3.10.

The presumption that $\boldsymbol{u} = \begin{bmatrix} T_\text{air} & l_\text{fan} \end{bmatrix}^\text{T}$ is a fixed part of the model can be justified by previous comfort studies but obviously reduces the degrees of freedom. Therefore, an equivalent analysis for the unconstrained combinatorics is performed in Appendix B.6. However, the unconstrained combinational results lead to the same combinations (3.23) and (3.24) and thus support the feasibility of this assumption. Small deviations between the finding can only be noted for lower dimensional models.

LASSO Regression

For the handling of a greater amount of potential features, like ϕ_3 and ϕ_4, a different approach is introduced. According to the Gauss-Markov theorem, the regarded least squares optimization results in the unbiased estimate with the lowest MSE [47]. However, great validation errors for a bad feature selection occur especially for

high dimensional feature vector candidates. Regarding the MSE of the applied PIV estimator for predicting the true vote ν

$$\text{MSE}(\text{PIV}) = \text{Var}(\text{PIV}) + \text{Bias}^2(\text{PIV}) \tag{3.25}$$

reveals the bias-variance trade-off. Although the OLSS is unbiased, a high variance can lead to a higher MSE than a biased estimator might have. While the combinational subset selection limits the variance by reducing the model parameters and thus the risk of overfitting, regularization of the model coefficients also reduces the variance of (3.25) but introduces an increased bias. A well balanced combination of bias and variance has the potential to improve the cross-validated MSE performance compared to the OLSS. Therefore, the optimization problem (3.20) can be extended by a regularization of the model parameters $\boldsymbol{\beta}_j$ to directly counteract overfitting. Introducing an L_1-norm on $\boldsymbol{\beta}_j = \begin{bmatrix} \beta_{j0} & \cdots & \beta_{jN_{\text{f}}} \end{bmatrix}^{\text{T}}$ results in the Least Absolute Shrinkage and Selection Operator (LASSO) [95] which is defined by

$$
\begin{aligned}
\boldsymbol{\beta}_j^* =\underset{\boldsymbol{\beta}_j}{\arg\min} \quad & \frac{1}{2}\left|\left|\boldsymbol{Z}_j\boldsymbol{\beta}_j - \boldsymbol{\nu}_j\right|\right|_2^2 + \lambda_j \sum_{k=1}^{N_{\text{f}}} |\beta_{jk}| \\
=\underset{\boldsymbol{\beta}_j}{\arg\min} \quad & \frac{1}{2}\left|\left|\boldsymbol{Z}_j\boldsymbol{\beta}_j - \boldsymbol{\nu}_j\right|\right|_2^2 + \lambda_j \left|\left|\boldsymbol{L}\boldsymbol{\beta}_j\right|\right|_1 \\
\text{s.t.} \quad & \boldsymbol{\beta}_{\min} \leq \boldsymbol{\beta}_j \leq \boldsymbol{\beta}_{\max},
\end{aligned}
\tag{3.26}
$$

where $\boldsymbol{L} = \text{diag}([0,1,\ldots,1])$. This shrinkage method incorporates a feature selection functionality by forcing entries of $\boldsymbol{\beta}_j$ to zero depending on the new design parameters $\lambda_j \geq 0$. The value of λ_j limits the error variance of the considered model where $\lambda_j \to 0$ corresponds to the OLSS and $\lambda_j \to \infty$ to the average vote when only the unpenalized bias β_{j0} remains. The optimal choice of λ_j can be found by cross-validation and may vary for different occupants just like the optimal set of features. The advantage of shrinkage methods over a combinational analysis is the lower computational complexity. Thereby, more complex shape vector candidates $\boldsymbol{\phi}$ can be taken into account where evaluating the combinatorics is infeasible. To ensure a balanced regularization of $\beta_{j0}, \ldots, \beta_{jN_{\text{f}}}$, the columns of the observation matrix $\boldsymbol{Z}_j$ are standardized. An equivalent formulation of (3.26) is given by

$$
\begin{aligned}
\boldsymbol{\beta}_j^* =\underset{\boldsymbol{\beta}_j}{\arg\min} \quad & \frac{1}{2}\left|\left|\boldsymbol{Z}_j\boldsymbol{\beta}_j - \boldsymbol{\nu}_j\right|\right|_2^2 = \underset{\boldsymbol{\beta}_j}{\arg\min}\frac{1}{2}\boldsymbol{\beta}_j^{\text{T}}\boldsymbol{Z}_j^{\text{T}}\boldsymbol{Z}_j\boldsymbol{\beta}_j - \boldsymbol{\nu}_j^{\text{T}}\boldsymbol{Z}_j\boldsymbol{\beta}_j \\
\text{s.t.} \quad & \left|\left|\boldsymbol{L}\boldsymbol{\beta}_j\right|\right|_1 \leq \xi_j \\
& \boldsymbol{\beta}_{\min} \leq \boldsymbol{\beta}_j \leq \boldsymbol{\beta}_{\max}
\end{aligned}
\tag{3.27}
$$

where the λ_j-related penalty term is replaced by the bound ξ_j which controls the model parameters $\boldsymbol{\beta}_j$. The value of ξ_j defines the compromise between the model's variance and bias, hence its tendency of over- or underfitting [47].

However, while (3.20) is a standard Quadratic Program (QP) which can be solved efficiently, the L_1-norm adds a nonlinear and non differentiable penalty to the optimization problem. Multiple algorithms for efficiently solving (3.26) and (3.27) were developed to circumvent this problem [89]. One possible solution is the reformulation as linearly constrained quadratic program where the nonlinear constraint $\left|\left|\boldsymbol{L}\boldsymbol{\beta}_j\right|\right|_1 \leq \xi_j$ is linearized by a decomposition in non-negative variables. Each parameter vector is separated in a positive and negative part

$$\beta_{jk} = \beta_{jk}^+ - \beta_{jk}^- \tag{3.28}$$
$$\beta_{jk}^+, \beta_{jk}^- \geq 0, \quad j = 1 \dots N_{\text{occ}}, k = 1 \dots N_{\text{f}}$$

so that

$$\left|\beta_{jk}\right| = \beta_{jk}^+ + \beta_{jk}^-. \tag{3.29}$$

The separated parameters are collected in the vector

$$\boldsymbol{w}_j = \begin{bmatrix} \beta_{j0} & \beta_{j1}^+ & \cdots & \beta_{jN_{\text{f}}}^+ & \beta_{j1}^- & \cdots & \beta_{jN_{\text{f}}}^- \end{bmatrix}^{\text{T}}, \tag{3.30}$$

and the original $\boldsymbol{\beta}_j$ can be recovered by the mapping function

$$\boldsymbol{\beta}_j = \boldsymbol{W}\boldsymbol{w}_j = \begin{bmatrix} 1 & 0 & \cdots & & & & \\ 0 & 1 & -1 & 0 & \cdots & & \\ 0 & 0 & 0 & 1 & -1 & 0 & \cdots \\ & & & & \ddots & & \\ & & & \cdots & 0 & 1 & -1 \end{bmatrix} \boldsymbol{w}_j. \tag{3.31}$$

The linearized L_1-regularization results in

$$\left|\left|\boldsymbol{L}\boldsymbol{\beta}_j\right|\right|_1 = \boldsymbol{r}_{L_1}^{\text{T}} \boldsymbol{w}_j = \begin{bmatrix} 0 & 1 & \cdots & 1 \end{bmatrix} \boldsymbol{w}_j. \tag{3.32}$$

Substituting (3.31) and (3.32) in (3.27) leads to the transformed optimization problem

$$\min_{\boldsymbol{w}_j} \quad \frac{1}{2}\boldsymbol{w}_j^{\text{T}} \underbrace{\boldsymbol{W}^{\text{T}}\boldsymbol{Z}_j^{\text{T}}\boldsymbol{Z}_j\boldsymbol{W}}_{\boldsymbol{H}_j} \boldsymbol{w}_j \underbrace{-\boldsymbol{\nu}_j^{\text{T}}\boldsymbol{Z}_j\boldsymbol{W}}_{\boldsymbol{f}_j^{\text{T}}} \boldsymbol{w}_j$$
$$\text{s.t.} \quad \boldsymbol{r}_{L_1}^{\text{T}} \boldsymbol{w}_j \leq \xi_j \tag{3.33}$$
$$\boldsymbol{\beta}_{\min} \leq \boldsymbol{W}\boldsymbol{w}_j \leq \boldsymbol{\beta}_{\max}$$

which can be solved by a standard QP algorithm.

For the perfect user-specific model, the optimization (3.33) is performed for every user separately based on the individual voting data. Depending on the choice of ξ_j, the corresponding model coefficients $\boldsymbol{\beta}_j$ are regularized stronger or weaker. Figure 3.11 shows the results for two exemplary users when the linear shape function $\boldsymbol{\phi}_1$ is applied.

The trace plot of the coefficients as a function of ξ_j is depicted in Figure 3.11a and represents the effect of the regularization. While the least square estimate considers all provided parameters ($\xi_j \to \infty$), decreasing bound ξ_j forces the entries of $\boldsymbol{\beta}_j$ gradually to zero. The resulting coefficient traces can be very distinct for different users as demonstrated by the deviations between user A and B. While the comfort of user A is firstly affected by T_{sup}, user B is dominated by T_{air}. The seating position of user A is close to an outlet what explains his sensitivity to T_{sup}. Moreover, he is directly located under a fan so that the fan level l_{fan} is another significant comfort factor revealed by his trace plot. Each regularization value ξ_j is associated with an average cross-validation error as depicted in Figure 3.11c. The minimum MSE indicates the optimal bound and results in the perfect combination of features for the two users given by

$$\phi_{1,A}^* = \begin{bmatrix} 1 & T_{\text{air}} & l_{\text{fan}} & T_{\text{mr}} & T_{\text{sup}} & I_{\text{sol}} & RH_{\text{out}} & DT \end{bmatrix}^{\mathrm{T}} \tag{3.34a}$$

$$\phi_{1,B}^* = \begin{bmatrix} 1 & T_{\text{air}} & l_{\text{fan}} & T_{\text{mr}} & RH_{\text{air}} & T_{\text{out}} & RH_{\text{out}} & DT \end{bmatrix}^{\mathrm{T}}. \tag{3.34b}$$

A larger limit ξ_j results in overfitting and increases the prediction error. The opposite case, thus decreasing the bound ξ_j, induces the vanishing of more coefficients which, on the one hand, allows for a reduction of the model's dimension but on the other hand increases the corresponding MSE. Assuming the OLSS (equivalent to $\xi_j \to \infty$) using the full feature vector ϕ_1 represents the desired benchmark, a reduced model can be found that achieves the same validation accuracy. The corresponding minimum model dimension results in the individual feature vectors

$$\phi_{1,A}^{\text{red}} = \begin{bmatrix} 1 & l_{\text{fan}} & T_{\text{mr}} & T_{\text{sup}} & I_{\text{sol}} & DT \end{bmatrix}^{\mathrm{T}} \tag{3.35a}$$

$$\phi_{1,B}^{\text{red}} = \begin{bmatrix} 1 & T_{\text{air}} & T_{\text{mr}} & T_{\text{out}} & RH_{\text{out}} & DT \end{bmatrix}^{\mathrm{T}}. \tag{3.35b}$$

The corresponding regularization factor $\xi_{\{A,B\}}^{\text{red}}$ can be extracted from Figure 3.11c, where the MSE for $\phi_{1,\{A,B\}}^{\text{red}}$ is indicated. Regarding the trace plot of user A, the coefficients for T_{air} and RH_{out} are excluded from the model. The maintained importance of T_{mr} and I_{sol} in the reduced feature vector $\phi_{1,A}^{\text{red}}$ further highlights his seating location close to the window where solar radiation is dominant. Contrarily, user B is rarely affected by the fan level or solar radiation due to his desk shielded from the fan and located in the rear part of the office. This is emphasized by the small or even non-existent coefficients in (3.34b) and (3.35b) respectively. However, his coefficient values cover a larger range compared to user A and expose a generally higher sensitivity to the environmental conditions. Particularly, a high sensitivity to T_{air}, T_{out} and RH_{out} is revealed by his trace plot and the optimal feature vector $\phi_{1,B}^*$. Interestingly, the time of day plays an important role for both users. This can be traced back to the high cross-correlations between DT and multiple other comfort factors such that the daytime is a representative model parameter with a high information content for the comfort models.
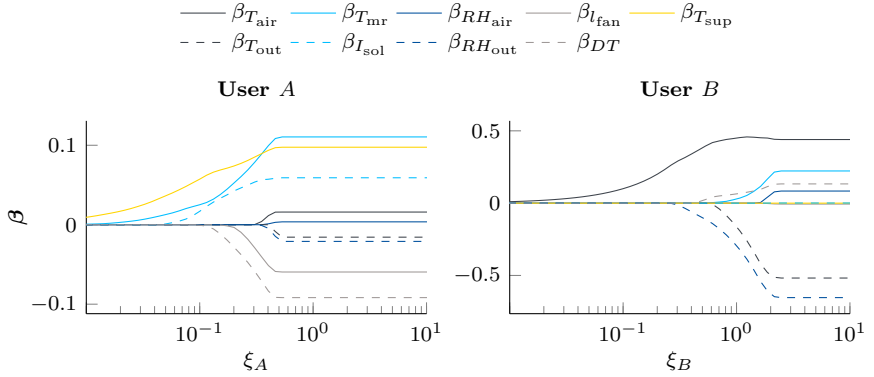
(a) Trace plot of model coefficients $\boldsymbol{\beta}_j$.
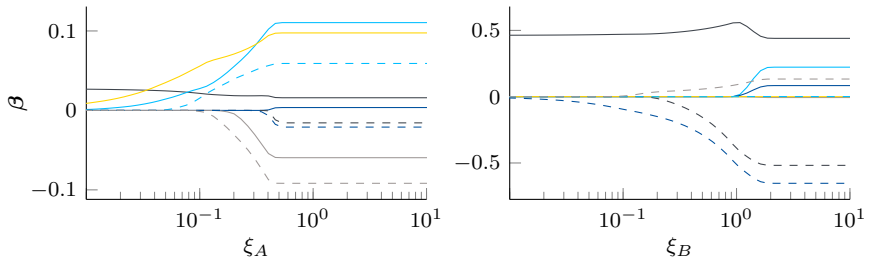
(b) Trace plot of model coefficients $\boldsymbol{\beta}_j$ for unpenalized basis $\boldsymbol{u}$.
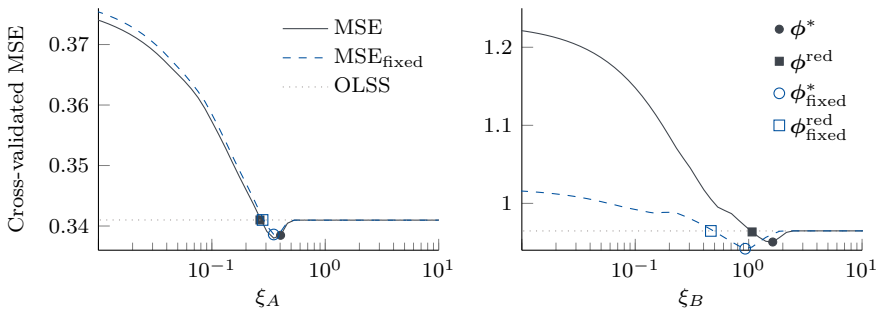
(c) Cross-validated MSE with and without penalization of $\boldsymbol{u}$.

Figure 3.11: Model coefficients and cross-validated MSE for two exemplary users when solving (3.33) for different regularization limits ξ_j.

The combinational analysis showed that the fixed model component $\boldsymbol{u} = \begin{bmatrix} T_{\text{air}} & l_{\text{fan}} \end{bmatrix}^{\text{T}}$ is a meaningful presumption. However, the L_1- regularization can force the corresponding model coefficients to zero as exemplary exposed in (3.35a) and (3.35b) for T_{air} and l_{fan} respectively. This effect can occur for two reasons: Either a user is not sensitive to the parameter itself (although the majority of users is as previously proven) or the parameter is replaced by a highly cross-correlated variable, e. g. T_{air} is substituted by T_{mr}. Since the modeling goal is a common model structure containing the component $\boldsymbol{u}$, the LASSO optimization problem can be adjusted to favor the inclusion of $\boldsymbol{u}$. Therefore, the regularization of the LASSO regression is modified to avoid the disappearance of wanted model components by excluding the subset of certainly significant coefficients from the penalty term $\left\| \boldsymbol{L}\boldsymbol{\beta}_j \right\|_1 \leq \xi_j$. This is achieved by adjusting the selection matrix $\boldsymbol{L}$ or equivalently the entries of $\boldsymbol{r}_{L_1}$. As a result, the feature selection is only applied to the remaining elements whereas the impact of $\boldsymbol{u}$ and its cross-correlations are always inherently taken into account.

Eliminating the penalty for $\beta_{j,T_{\text{air}}}$ and $\beta_{j,l_{\text{fan}}}$ leads to the user-related trace plots of Figure 3.11b. It can be observed that in particular $\beta_{j,T_{\text{air}}}$ dominates the model for a strict regularization of the remaining parameters. The corresponding cross-validated MSE is very similar for user A but remarkably lower for user B where the air temperature was already identified as a highly influential comfort factor. The optimal vectors for a non-penalized $\boldsymbol{u}$ result in

$$\boldsymbol{\phi}_{1,A,\text{fixed}}^* = \begin{bmatrix} 1 & T_{\text{air}} & l_{\text{fan}} & T_{\text{mr}} & T_{\text{sup}} & I_{\text{sol}} & RH_{\text{out}} & DT \end{bmatrix}^{\text{T}} \tag{3.36a}$$

$$\boldsymbol{\phi}_{1,B,\text{fixed}}^* = \begin{bmatrix} 1 & T_{\text{air}} & RH_{\text{air}} & T_{\text{out}} & RH_{\text{out}} & DT \end{bmatrix}^{\text{T}}. \tag{3.36b}$$

Although l_{fan} is not included in the regularization term, the optimal set for user B (3.36b) does not include the fan level. Referring to Figure 3.11b confirms that the coefficient $\beta_{B,l_{\text{fan}}}$ is even zero for the OLSS, thus this user's comfort is unaffected by the fan. The gray elements are neglected in $\boldsymbol{\phi}_{1,\text{fixed}}^{\text{red}}$ according to (3.35) when a reduced prediction accuracy is accepted which is equivalent to using the full vector $\boldsymbol{\phi}_1$. The optimal vector for user A (3.36a) is equal to the previous result (3.34a). This is explained by the small coefficient $\beta_{T_{\text{air}}}$ and the consequently low impact of the penalty. Therefore, the resulting coefficient values and the MSE are comparable. However, a remarkable impact is visible for user B. The dominance of T_{air} leads to a significant error reduction and substitutes the impact of T_{mr} completely. To support the beneficial usage of $\boldsymbol{u}$ as significant comfort factors, the corresponding coefficients are always excluded from the regularization term in the following.

The feature selection property of the LASSO regression can now be applied to more complex shape vectors. While cross-validation of the combinatorics is only feasible for $\boldsymbol{\phi}_{\{1,2\}}$, the shape vectors $\boldsymbol{\phi}_{\{3,4\}}$ can also be evaluated by this approach. The user-specific optimization (3.33) leads to a perfect bound ξ_j^* and a corresponding optimal model approach for each occupant. The cross-validation is performed for
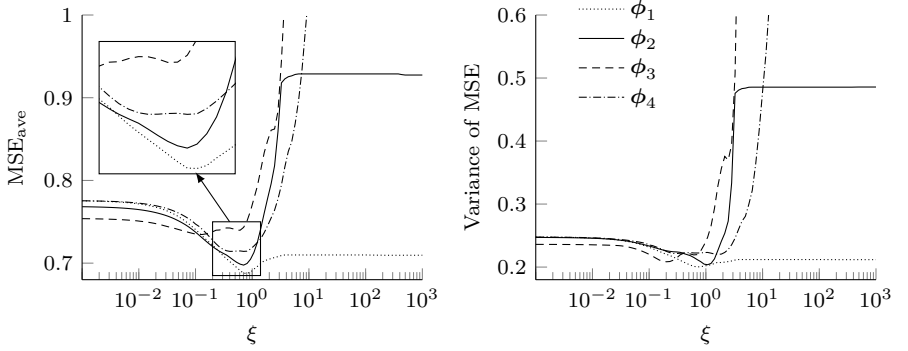
Figure 3.12: Cross-validated $\mathrm{MSE_{ave}} = \frac{1}{N_{\mathrm{occ}}} \sum_{j=1}^{N_{\mathrm{occ}}} ||\boldsymbol{Z}_j \boldsymbol{\beta}_j^* - \boldsymbol{\nu}_j||_2^2$ and corresponding variance of the user-related MSE for the feature vectors $\boldsymbol{\phi}_{\{1,2,3,4\}}$ according to (3.15).

all users and feature vectors separately and the resulting average MSE as well as the variance over all users are compared in Figure 3.12. It can be observed that the achievable $\mathrm{MSE_{ave}}$ is similar for $\boldsymbol{\phi}_{\{1,2,3\}}$ with a comparable optimal bound $\xi^* \approx 0.7$. The shape vector with the highest degree $\boldsymbol{\phi}_3$ requires stronger regularization and reaches its minimum for a smaller bound. Moreover, both higher dimensional vectors $\boldsymbol{\phi}_{\{3,4\}}$ involve a greater risk of overfitting, indicated by the rapid increase of $\mathrm{MSE_{ave}}$ for a relaxation of the bound ξ. Although higher order terms are beneficial for low dimensional models ($\xi \to 0$), the best model accuracy is achieved by the linear approach $\boldsymbol{\phi}_1$. This result highlights the problem when many correlated variables are part of the regression model such that the coefficients are poorly determined and opposing coefficients cancel each other out.

The variance of the user-related MSE reveals how suitable the choice of $\boldsymbol{\phi}_{(\cdot)}$ and ξ is for all considered subjects. The test group's variance for $\boldsymbol{\phi}_{\{1,2,3,4\}}$ is again comparable and corresponds to the shape of the cross-validated MSE. However, the activation of less important features for an increasing bound ξ deteriorates the prediction quality and causes a higher model uncertainty. In particular the high dimensional approaches $\boldsymbol{\phi}_{\{3,4\}}$ result in overfitting. This leads to the conclusion that interactions of the elements of $\mathcal{Z}$ or higher order approaches are not more beneficial for comfort modeling than the linear basis function. Furthermore, these results support the observations for the combinational analysis and suggest the usage of the simplest approach $\boldsymbol{\phi}_1$.

However, the definition of a common reduced optimal feature set is not straightforward for the individual LASSO regression (3.33). The user-specific, regularized coefficients $\boldsymbol{\beta}_j^*$ do not suppress the same elements. Counting the occurrence of features in the user-specific optimal set leads to Table 3.4. Although the amount of occurrences

Table 3.4: Occurrence of features in the optimal user-specific set of $\phi^*_{1,2,3}$ for all 16 considered occupants.

Feature	T_{air} T^2_{air} T^3_{air}	l_{fan} l^2_{fan} l^3_{fan}	T_{mr} T^2_{mr} T^3_{mr}	RH_{air} RH^2_{air} RH^3_{air}	T_{sup} T^2_{sup} T^3_{sup}	T_{out} T^2_{out} T^3_{out}	I_{sol} I^2_{sol} I^3_{sol}	RH_{out} RH^2_{out} RH^3_{out}	DT DT^2 DT^3
Occurrence ϕ_1	16 - -	12 - -	10 - -	11 - -	10 - -	15 - -	6 - -	12 - -	16 - -
Occurrence ϕ_2	16 13 -	11 8 -	6 6 -	10 4 -	7 6 -	12 12 -	4 7 -	11 11 -	16 12 -
Occurrence ϕ_3	15 12 13	9 7 7	5 7 4	7 3 4	3 7 5	9 10 9	5 5 6	9 11 7	13 11 13

gives a hint about the importance of specific features, an interpretation regarding a common comfort approach is rather difficult. The count of occurrences is often similar, in particular for the higher order feature vectors. Moreover, Table 3.4 only answers the question which features are most beneficial for a user. However, the impact of a feature neglect or substitution cannot be measured without additional computational effort. Therefore, an optimization over all occupants must be performed to define the best common set and to incorporate the importance of considered as well as the effect of suppressed comfort factors.

Combining the individual optimization problems (3.33) requires some extensions and modifications. Firstly, the objective function defines now the minimum error over all occupants:

$$
\begin{aligned}
\min_{\boldsymbol{w}} \quad & \sum_{j=1}^{N_{\mathrm{occ}}} \frac{1}{n_{\mathcal{T},j}} \left(\boldsymbol{w}_j^{\mathrm{T}} \boldsymbol{H}_j \boldsymbol{w}_j + \boldsymbol{f}_j^{\mathrm{T}} \boldsymbol{w}_j \right) \\
\text{s.t.} \quad & \boldsymbol{r}_{L_1}^{\mathrm{T}} \boldsymbol{w}_j \leq \xi \\
& \boldsymbol{\beta}_{\min} \leq \boldsymbol{W} \boldsymbol{w}_j \leq \boldsymbol{\beta}_{\max} \qquad \forall j = 1 \ldots N_{\mathrm{occ}}.
\end{aligned}
\tag{3.37}
$$

So far, solving (3.37) is equivalent to the individual optimization due to its decoupled structure. In the next step, the problem must be coupled by an additional condition to ensure that entries of $\boldsymbol{\beta}_j$ are either active or vanish for all users simultaneously.

Thus, the k-th coefficient of an arbitrary user l, β_{lk}, can only be active if β_{jk} appears in all personal comfort models $j = 1, \ldots, N_{\text{occ}}, j \neq l$. Furthermore, all active entries of $\boldsymbol{\beta}_j$ can have individual values to capture the occupant-related sensitivities. This *if*-condition corresponds to the following equality constraint

$$\forall k = 1 \ldots N_{\text{f}}: \quad \text{If } |\beta_{lk}| \geq \epsilon, \text{ then } |\beta_{jk}| \geq \epsilon \quad \forall j = 1 \ldots N_{\text{occ}}, j \neq l \tag{3.38}$$

where $\epsilon > 0$ is an arbitrary constant which defines the significance limit of a comfort feature. An efficient solution of (3.37) under consideration of (3.38) requires a reformulation. Introducing the binary vector $\boldsymbol{\omega} = \begin{bmatrix} \omega_1 & \ldots & \omega_{N_{\text{f}}} \end{bmatrix}^{\text{T}}$, $\omega_k \in \{0, 1\}$ and a suitable upper limit M allows to rewrite (3.38) so that the standard QP form of (3.37) is maintained [100]:

$$\left(|\beta_{jk}| = 0, \forall j = 1 \ldots N_{\text{occ}} \right) \vee \left(|\beta_{jk}| \geq \epsilon, \forall j = 1 \ldots N_{\text{occ}} \right)$$
$$\Rightarrow \quad \epsilon \cdot \omega_k \leq |\beta_{jk}| \leq M \cdot \omega_k, \quad \forall k = 1 \ldots N_{\text{f}}. \tag{3.39}$$

Using (3.29) and (3.30) leads to

$$|\boldsymbol{\beta}_j| = \boldsymbol{W}_a \boldsymbol{w}_j = \begin{bmatrix} 1 & 0 & \cdots & & & & \\ 0 & 1 & 1 & 0 & \cdots & & \\ 0 & 0 & 0 & 1 & 1 & 0 & \cdots \\ & & & & \ddots & & \\ & & & \cdots & 0 & 1 & 1 \end{bmatrix} \boldsymbol{w}_j \tag{3.40}$$

and (3.39) can be reformulated in matrix form

$$\epsilon \cdot \boldsymbol{\omega} \leq \boldsymbol{W}_a \boldsymbol{w}_j \leq M \cdot \boldsymbol{\omega}. \tag{3.41}$$

This ensures that the user-specific coefficients of the k-th feature are either blocked out or activated for all comfort models depending on ω_k

$$\begin{array}{ll} \beta_{jk} = 0 & \text{for } \omega_k = 0 \\ \beta_{jk} \in [\epsilon, M] & \text{for } \omega_k = 1. \end{array}$$

Adding the coupling condition (3.41) to the joint objective (3.37) leads to a Mixed Integer Quadratic Program (MIQP)

$$\begin{aligned} \min_{\boldsymbol{w}} \quad & \boldsymbol{w}^{\text{T}} \boldsymbol{H} \boldsymbol{w} + \boldsymbol{f}^{\text{T}} \boldsymbol{w} \\ \text{s.t.} \quad & \boldsymbol{R}_{L_1} \boldsymbol{w} \leq \boldsymbol{\xi} \\ & \underline{\boldsymbol{w}} \leq \tilde{\boldsymbol{W}} \boldsymbol{w} \leq \overline{\boldsymbol{w}} \\ & \epsilon \cdot \boldsymbol{\Omega} \boldsymbol{w} \leq \tilde{\boldsymbol{W}}_a \boldsymbol{w} \leq M \cdot \boldsymbol{\Omega} \boldsymbol{w} \\ & w_i \in \{0, 1\}, \quad \forall i = N_{\text{occ}}(2N_{\text{f}} + 1) + 1, \ldots, N_{\text{occ}}(2N_{\text{f}} + 1) + N_{\text{f}}. \end{aligned} \tag{3.42}$$

where

$$
\boldsymbol{w} = \begin{bmatrix} \boldsymbol{w}_1 \\ \vdots \\ \boldsymbol{w}_{N_{\mathrm{occ}}} \\ \boldsymbol{\omega} \end{bmatrix}, \quad \boldsymbol{\Omega w} = \begin{bmatrix} \boldsymbol{\omega} \\ \vdots \\ \boldsymbol{\omega} \end{bmatrix}, \qquad \overline{\boldsymbol{w}} = \begin{bmatrix} \overline{\boldsymbol{\beta}} \\ \vdots \\ \overline{\boldsymbol{\beta}} \end{bmatrix}, \quad \underline{\boldsymbol{w}} = \begin{bmatrix} \underline{\boldsymbol{\beta}} \\ \vdots \\ \underline{\boldsymbol{\beta}} \end{bmatrix}, \quad \boldsymbol{\xi} = \begin{bmatrix} \boldsymbol{\xi} \\ \vdots \\ \boldsymbol{\xi} \end{bmatrix},
$$

$$
\boldsymbol{H} = \mathrm{diag}(\boldsymbol{H}_1, \ldots, \boldsymbol{H}_{N_{\mathrm{occ}}}, \boldsymbol{0}^{N_{\mathrm{f}} \times N_{\mathrm{f}}}), \qquad \boldsymbol{f} = \begin{bmatrix} \boldsymbol{f}_1 & \cdots & \boldsymbol{f}_{N_{\mathrm{occ}}} & \boldsymbol{0}^{N_{\mathrm{f}} \times 1} \end{bmatrix},
$$

$$
\boldsymbol{R}_{L_1} = \begin{bmatrix} \mathrm{diag}\left(\{\boldsymbol{r}_{L_1}^T\}^{N_{\mathrm{occ}}}\right) & \boldsymbol{0}^{N_{\mathrm{occ}} \times N_{\mathrm{f}}} \end{bmatrix}, \qquad \tilde{\boldsymbol{W}} = \begin{bmatrix} \mathrm{diag}\left(\{\boldsymbol{W}\}^{N_{\mathrm{occ}}}\right) & \boldsymbol{0}^{N_{\mathrm{occ}}(N_{\mathrm{f}}+1) \times N_{\mathrm{f}}} \end{bmatrix},
$$

$$
\tilde{\boldsymbol{W}}_a = \begin{bmatrix} \mathrm{diag}\left(\{\boldsymbol{W_a}\}^{N_{\mathrm{occ}}}\right) & \boldsymbol{0}^{N_{\mathrm{occ}}(N_{\mathrm{f}}+1) \times N_{\mathrm{f}}} \end{bmatrix}.
$$

The optimal vector $\boldsymbol{w}^*$ contains the personalized model coefficients as well as the information about the (de-)activated features. The significance bound ϵ for the feature activation is an additional design parameter that is chosen under consideration of the occurring coefficient values. A large significance bound decreases the number of activated features but risk the exclusion of users with generally low sensitivities, thus small coefficient values. Decreasing ϵ drives the joint optimization towards the separate optimum because the coupling constraint of (3.42) is eliminated for $\epsilon \to 0$. Since the sensitivity of different users can be very distinct, the maximum absolute values of β_{jk} vary between 0.1 and 1.1 depending on the individual. Therefore, the significance level is set to $\epsilon = 0.01$ which is a reasonable compromise between limiting the feature activation as well as including users with low sensitivity. The joint optimization (3.42) is performed using the solver Gurobi [45].

The resulting cross-validated MSE based on $\phi_{\{1,2,3\}}$ is depicted in Figure 3.13 and compared to the results for the separate optimization (3.33). Two main differences can be observed between the joint and the separate optimization results: Firstly, the error for small regularization bounds is higher for the joint approach which is mainly due to the significance level ϵ. The influence of features is completely suppressed for $\xi < \epsilon$ whereas the user-specific optimization already allows for very small coefficient values. Not until $\xi \geq \epsilon$, additional predictors are activated which leads to a small downward step of the MSE at $\xi = \epsilon$. Note that also for the joint optimization, all features containing the components of $\boldsymbol{u}$ are unpenalized. Thus, the error associated with $\xi \to 0$ corresponds to the model approach only using T_{air} and l_{fan} or their higher order terms and results in an average prediction error of $\mathrm{MSE}_{\mathrm{ave}} \approx 0.78$. The partly non-smooth characteristic of the joint optimization result is explained by the discrete activation and deactivation of features that lead to sudden improvements or deteriorations for the individual user models. Moreover, the separation in different training sets for the cross-validation can cause distinct feature activation for the same regularization parameter ξ and hence impact the corresponding test error unequally.

The second difference is exposed by the achievable prediction error. As already mentioned above, the compromise between all occupants raises the error for small
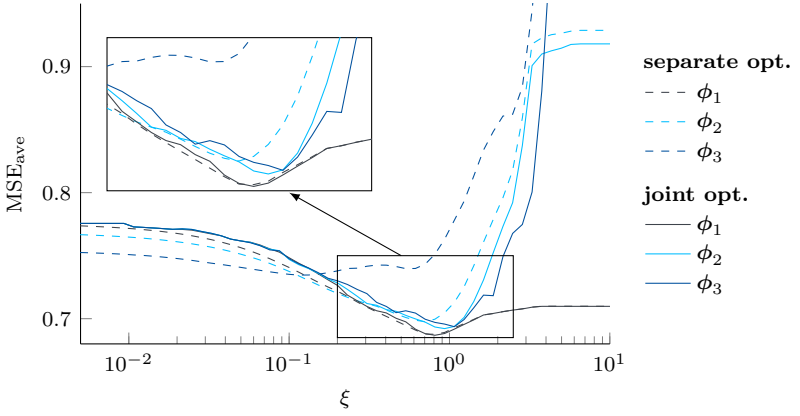
Figure 3.13: Cross-validated MSE for the joint optimization (3.42) compared to the separate optimization (3.33).

values of ξ. However, relaxing the regularization incorporates the risk of overfitting, especially for high dimensional model approaches as observed in Figure 3.12 for the separate optimization. The greater data basis for the joint optimization counteracts the influence of outliers and is consequently less sensitive to the right choice of ξ. Therefore, the common user consideration involves an improved control of the model's variance so that the erroneous inclusion of features is avoided. This leads to better generalizing models and thus reduces the average MSE of $\phi_{\{2,3\}}$ for greater values of ξ compared to the separate user consideration.

The binary variable $\boldsymbol{\omega}(\xi)$ directly defines the active set of features depending on the regularization parameter. The minimum values for the joint optimization correspond to the feature vectors

$$\phi_1^* = \begin{bmatrix} 1 & T_{\text{air}} & l_{\text{fan}} & T_{\text{mr}} & RH_{\text{air}} & T_{\text{sup}} & T_{\text{out}} & I_{\text{sol}} & RH_{\text{out}} & DT \end{bmatrix}^{\text{T}} \quad (3.43\text{a})$$

$$\phi_2^* = \begin{bmatrix} 1 & T_{\text{air}} & T_{\text{air}}^2 & l_{\text{fan}} & l_{\text{fan}}^2 & T_{\text{mr}} & T_{\text{mr}}^2 & RH_{\text{air}} & RH_{\text{air}}^2 & \dots \end{bmatrix}$$
$$\begin{bmatrix} \dots & T_{\text{sup}} & T_{\text{out}} & T_{\text{out}}^2 & I_{\text{sol}} & RH_{\text{out}} & RH_{\text{out}}^2 & DT & DT^2 \end{bmatrix}^{\text{T}} \quad (3.43\text{b})$$

$$\phi_3^* = \begin{bmatrix} 1 & T_{\text{air}} & l_{\text{fan}} & l_{\text{fan}}^3 & T_{\text{mr}} & T_{\text{mr}}^2 & T_{\text{mr}}^3 & RH_{\text{air}} & RH_{\text{air}}^2 & \dots \end{bmatrix}$$
$$\begin{bmatrix} \dots & RH_{\text{air}}^3 & T_{\text{sup}} & T_{\text{sup}}^3 & T_{\text{out}} & T_{\text{out}}^2 & T_{\text{out}}^3 & I_{\text{sol}} & \dots \end{bmatrix}$$
$$\begin{bmatrix} \dots & RH_{\text{out}} & RH_{\text{out}}^2 & RH_{\text{out}}^3 & DT & DT^2 & DT^3 \end{bmatrix}^{\text{T}} . \quad (3.43\text{c})$$

The most obvious difference to the previous combinational result is the optimal model dimension. While the combinational optimum consists of 6-7 predictors, the

L_1-regularization adds more dimensions to the optimum and results in 9-21 features. This effect can be traced back to two properties of the regularization that favor high dimensional models. First, penalizing the model coefficients limits their absolute values and balances the impact of outliers. Therefore, additional comfort factors can be included without resulting in undesirable overfitting. Secondly, the regularization has an equal effect on all model dimensions and as a consequence can cause an unwanted limitation of a truly important model coefficient. This may activate additional features to compensate for the limited absolute coefficient value.

The high dimensional feature vectors are not a surprise when Table 3.4 is revisited. The heterogeneity of the test subjects is already indicated by the diverse distribution of optimal comfort factors. Consequently, the compromise between all users incorporates a wide range of the considered parameters. Nevertheless, a judgment about a perfect predictor set based on the separate feature count is hardly possible. The strong cross-correlations allow for a substitution of some features without a great loss of the model's accuracy. However, this interchangeability cannot be extracted from Table 3.4 and a final assessment can only be drawn from the joint optimization.

Comparing the optimal sets of predictors (3.43) reveals that the linear features are included completely in all approaches. Although the additional higher order terms in $\phi_{2,3}^*$ can be beneficial for some users, the entailed risk of overfitting and increased complexity does not justify a higher dimensional approach. The corresponding MSE shows that the prediction quality for ϕ_1^* outperforms the more complex approaches and leads to an almost identical performance as the separate optimization. It even results in a slightly smaller cross-validated MSE of 0.687 than the combinational optimum (3.23). This outcome emphasizes the benefit of the regularization term when facing the uncertainty of user votes and furthermore implies that a linear shape vector is sufficient and the most robust choice for the comfort predictions.

The effect on the individual user models is illustrated in Figure 3.14 where the results according to Figure 3.11 are compared to the joint optimization. In accordance with the observations in Figure 3.13, the impact on the individual MSE is relatively low using the linear feature vector ϕ_1. The only visible difference for user A are delayed steps of the MSE due to the later activation of features. The separate optimization allows for a smooth activation of an additional feature whereas searching for the best overall compromise imposes a sudden switch of features. The activation of a common subset can even be disadvantageous for the individual user which is particularly visible for the piecewise increased MSE of user B. The trace plot of T_{air} and T_{mr} gives further insight about the effect of the common optimization on the user-specific models. The penalized coefficients are forced to zero until they are beneficial enough for the whole group and exceed the significance bound ϵ. The activation limit for the mean radiant temperature T_{mr} is $\xi \approx 0.08$. User A directly profits from the activation and his MSE steps back towards the separate optimum. Furthermore, the influence of T_{mr} even surpasses the separate result. The higher value originates from compensation effects
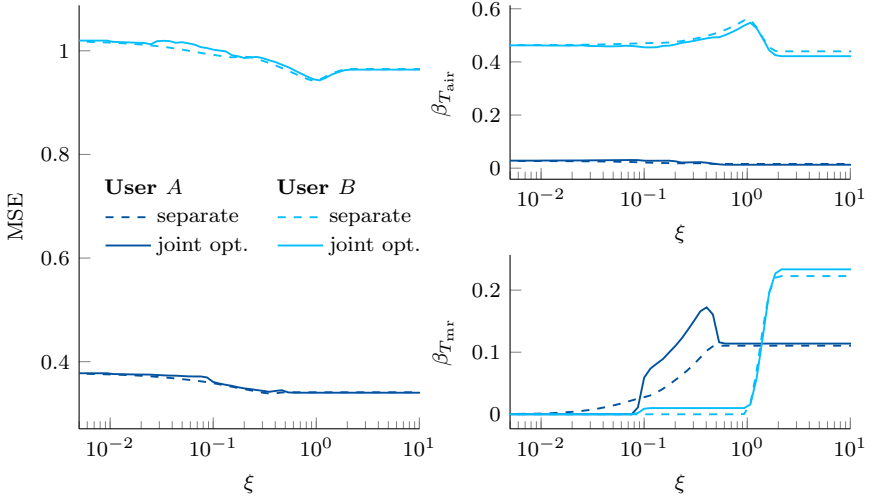
Figure 3.14: Effect of joint optimization on the exemplary user models and coefficients for the linear feature vector ϕ_1.

for still deactivated predictors. The impact of T_{mr} on user B reveals some further implications of the joint optimization. For $0.08 \leq \xi \leq 1$, the mean radiant temperature has a very low impact on this user that the common activation forces the corresponding value to the minimum allowed value $\beta_{B,T_{\mathrm{mr}}} = \epsilon$. This also entails a small reduction of $\beta_{B,T_{\mathrm{air}}}$. The previously identified cross-correlation between T_{air} and T_{mr} results in a compensation for the other value respectively which is further highlighted by the increased coefficient of the joint optimization when the other feature is activated.

Similarly to the separate user consideration, the model dimension can be reduced by decreasing ξ. The OLSS of the linear approach ϕ_1 is again used as reasonable minimal requirement[d]. The thereby allowed dimensional reduction leads to the feature vectors

$$\phi_1^{\mathrm{red}} = \begin{bmatrix} 1 & T_{\mathrm{air}} & l_{\mathrm{fan}} & T_{\mathrm{mr}} & RH_{\mathrm{air}} & T_{\mathrm{out}} & RH_{\mathrm{out}} & DT \end{bmatrix}^{\mathrm{T}} \tag{3.44a}$$

$$\phi_2^{\mathrm{red}} = \begin{bmatrix} 1 & T_{\mathrm{air}} & T_{\mathrm{air}}^2 & l_{\mathrm{fan}} & T_{\mathrm{mr}} & RH_{\mathrm{air}} & T_{\mathrm{out}} & \ldots \\ & \ldots & T_{\mathrm{out}}^2 & RH_{\mathrm{out}} & RH_{\mathrm{out}}^2 & DT & DT^2 \end{bmatrix}^{\mathrm{T}} \tag{3.44b}$$

$$\phi_3^{\mathrm{red}} = \begin{bmatrix} 1 & T_{\mathrm{air}} & T_{\mathrm{air}}^2 & l_{\mathrm{fan}} & l_{\mathrm{fan}}^3 & T_{\mathrm{mr}} & T_{\mathrm{mr}}^2 & T_{\mathrm{mr}}^3 & \ldots \\ & \ldots & RH_{\mathrm{air}} & T_{\mathrm{out}} & RH_{\mathrm{out}} & RH_{\mathrm{out}}^2 & DT & DT^2 \end{bmatrix}^{\mathrm{T}}. \tag{3.44c}$$

---

[d]The OLSS for higher dimensional feature vectors does not provide a reasonable reference due to the significant overfitting effects as visible in Figure 3.13.

The reduced vectors (3.44) support the result of the combinatorics (3.23) and (3.24). The components match the combinational result but also include the outside temperature T_{out} and some higher order terms. The supply temperature and solar radiation are excluded from the optimal set as additionally supported by Table 3.4.

Although the achievable prediction accuracy is comparable for both subset selection methods, the LASSO regression provides additional advantages for handling the high uncertainty of the user data. Particularly when a detailed feature selection analysis cannot be performed, the regularization term allows to use higher dimensional shape functions without incorrect overfitting effects. Another strength of the LASSO regression is the possibility to handle large feature vectors which cannot be investigated by solving the combinatorics. The derived optimization method (3.42) for a common feature selection can be transferred easily to analyze other test groups or shape functions (that are linear in parameters). However, the high uncertainty of voting data without occupant-related measurements suggests an application of simple shape functions with straightforward interpretability. The simplest linear approach ϕ_1 provides the best compromise between accuracy and insensitivity against a badly chosen feature combination. Including the regularization term suggests the usage of the full set of accessible environmental conditions. The combinational optimum (3.23), on the other hand, leads to a reduced feature vector with a similar performance but without the need to define a reasonable value for ξ. Since low complexity is a key requirement for good applicability in large commercial buildings, only the lower dimensional combinational optimum (3.23) is considered for the subsequently derived comfort-optimizing control strategies.

3.4.6 Hybrid Comfort Model

The analysis of comfort factors in Section 3.4.5 recommends the application of the simplest linear feature vector. The limited system excitation and noisy voting data require low dimensional and well-interpretable models for a robust identification process. Furthermore, the results also showed that individual comfort predictions based on environmental data incorporate a great amount of uncertainty. The identification of a suitable polynomial model structure led to an achievable average prediction accuracy of $\text{MSE}_{\text{min}} \approx 0.7$. Although this result is a notable improvement compared to using standard approaches, it additionally exposes that many important influencing factors are still either not available due to missing measurements or the tested shape functions are not able to capture all dominant relations. Consequently, the high complexity of personal comfort can hardly be mapped by these simple structures so that using more complex trial functions would be the logical conclusion. To circumvent the dilemma comfort complexity and robust identification, multiple ML techniques were applied in the field of comfort modeling to capture the subjectivity more accurately [28]. The GP regression method, as already used for the temperature field prediction in Section 2.2,

also proved to be a useful approach for comfort predictions [32, 42]. Therefore, this method is revisited and applied to capture the sophisticated impact of environmental conditions on the personal thermal comfort.

The main problem regarding ML approaches is the limited interpretability of the resulting black box models. In particular, the high uncertainty of voting data demands for approaches which can be supervised easily to avoid physically illogical models. This requirement contradicts the general characteristic of most purely data-driven learning algorithms. Furthermore, the individual prediction models build the basis for a comfort-oriented control strategy and a model inversion is required for defining the optimal set-point based on current conditions and interferences. An incorrectly identified model coefficient directly results in a wrong set-point. Hence, the proposed approach combines the well-interpretable linear regression of Section 3.4.4 with a GP model for being able to capture nonlinear effects. Based on the previous results, it is assumed that the influence of $\boldsymbol{u} = \begin{bmatrix} T_{\text{air}} & l_{\text{fan}} \end{bmatrix}^{\text{T}}$ can be approximated by a linear relation while all other environmental conditions $\boldsymbol{d}$ can incorporate nonlinear dependencies. The extended model structure is defined by

$$\text{PIV}_{\text{GP},j}(\boldsymbol{u}, \boldsymbol{d}) = \begin{bmatrix} 1 & \boldsymbol{u}^{\text{T}} \end{bmatrix} \boldsymbol{\beta}_j + \Delta\nu_j(\boldsymbol{d}) \tag{3.45}$$

where the linear approach represents the general individual comfort trend depending on $\boldsymbol{u}$ and thus allows for a good supervision of the resulting base model. The sign convention for $\beta_{j,T_{\text{air}}}$ (3.18) and $\beta_{j,l_{\text{fan}}}$ (3.19) ensures a physically feasible comfort relation. The base model is again obtained by solving the constrained linear regression problem (3.20) based on the input observations $\boldsymbol{U}_j = \begin{bmatrix} \boldsymbol{u}_{1j} \dots \boldsymbol{u}_{mj} \end{bmatrix}^{\text{T}}$ and the corresponding user votes $\boldsymbol{\nu}_j$. Further deviations due to the influence of disturbances are accounted for by the GP regression model $\Delta\nu_j(\boldsymbol{d}) \sim \mathcal{N}(0, \boldsymbol{K}_j)$. Referring to Section 2.2.1, $\boldsymbol{K}_j$ defines the covariance matrix of the training data $\mathcal{D}_j$ while the GP mean μ_j is set to zero because the linear basis already adjusts the model's intersection[e]. Since every occupant can have a different model characteristic, the hyperparameters of the GP model are identified separately for each subject. Hence, the kernel $\boldsymbol{K}_j$ contains the user-specifically identified hyperparameters. The conditional mean serves as prediction model for the disturbance-dependent vote deviation

$$\Delta\nu_j(\boldsymbol{d}) = \boldsymbol{\kappa}_j^{\text{T}}(\boldsymbol{d}) \underbrace{\boldsymbol{K}_j^{-1}(\boldsymbol{\nu}_j - \begin{bmatrix} \boldsymbol{1} & \boldsymbol{U}_j \end{bmatrix} \boldsymbol{\beta}_j)}_{\boldsymbol{\gamma}_j} = \boldsymbol{\kappa}_j^{\text{T}}(\boldsymbol{d}) \boldsymbol{\gamma}_j. \tag{3.46}$$

The vector $\boldsymbol{\gamma}_j$ only depends on the observation data and is fixed after the model training. Therefore, the prediction step simply consists of a linear combination of kernel evaluations [84], where the current disturbance state is compared to the training data.

---

[e]This is equivalent to using a *pure* GP model with the linear basis function $\begin{bmatrix} 1 & \boldsymbol{u}^{\text{T}} \end{bmatrix} \boldsymbol{\beta}_j$.

Different representatives for $\boldsymbol{K}$ (see Table 2.3) are tested and compared in Figure 3.15a. Similarly to Section 3.4.5, a combinational analysis is performed for each kernel function based on a (sub)set of 1 to 9 predictors from $\mathcal{Z}$ whereas the 1- and 2-dimensional models correspond to the linear and disturbance-independent approaches

$$\mathrm{PIV}_{1,j}(T_{\mathrm{air}}) = \begin{bmatrix} 1 & T_{\mathrm{air}} \end{bmatrix} \boldsymbol{\beta}_j$$
$$\mathrm{PIV}_{2,j}(\boldsymbol{u}) = \begin{bmatrix} 1 & \boldsymbol{u}^{\mathrm{T}} \end{bmatrix} \boldsymbol{\beta}_j.$$

The lowest achievable MSE is used as a measure for the suitability of the applied kernel. Figure 3.15a reveals that the exponential kernel yields the best result. Although the overall minimum for 5 predictors is identical for the exponential, rational quadratic and Matérn 3/2 kernel, the exponential kernel is less sensitive to adding additional (unnecessary) features. Since the previous subset selection analysis emphasized the high uncertainty when defining optimal comfort features, insensitivity to the right feature subset is an important model property. Therefore, the exponential kernel is selected for the further analysis.

For reasons of comparison, the extended model approach

$$\mathrm{PIV}_{\mathrm{GP}_u,j}(\boldsymbol{u},\boldsymbol{d}) = \begin{bmatrix} 1 & \boldsymbol{u}^{\mathrm{T}} \end{bmatrix} \boldsymbol{\beta}_j + \Delta\tilde{\nu}_j(\boldsymbol{u},\boldsymbol{d}), \quad \Delta\tilde{\nu}_j(\boldsymbol{u},\boldsymbol{d}) \sim \mathcal{N}(0,\tilde{\boldsymbol{K}}_j) \qquad (3.47)$$

is also taken into account. The inclusion of $\boldsymbol{u}$ in the GP model allows for a consideration of potentially nonlinear influences related to the air temperature and the fan level. A performance comparison of the different kernels based on (3.47) leads to a similar result as for (3.45). Hence, the exponential kernel is applied accordingly.

The achievable prediction accuracy for both GP approaches is shown in Figure 3.15b depending on the incorporated number of predictors N_{f}. Equivalently to the combinatorics for the purely linear approach (Table 3.3), the third feature added to the hybrid model is the time of day DT for both approaches. Moreover, only including up to three features shows a better performance when nonlinearities can be mapped by the GP model. Therefore, an inclusion of $\boldsymbol{u}$ in the GP deviation model is beneficial. While the usage of more disturbances further improves the prediction accuracy, the simpler hybrid approach (3.45) generalizes better and supports a purely linear consideration of $\boldsymbol{u}$. The global minimum is attained with 5 features and corresponds to the model

$$\mathrm{PIV}_{\mathrm{GP},j}^*(\boldsymbol{u},\boldsymbol{d}) = \begin{bmatrix} 1 & \boldsymbol{u}^{\mathrm{T}} \end{bmatrix} \boldsymbol{\beta}_j + \Delta\nu_j(\boldsymbol{d} = \begin{bmatrix} RH_{\mathrm{air}} & T_{\mathrm{out}} & DT \end{bmatrix}^{\mathrm{T}}). \qquad (3.48)$$

Note that the MSE for 6 and 7 predictors is equal to the prediction error of (3.48). However, the corresponding variance over all user models is smaller for a lower model order and therefore reduces the risk of overfitting. Furthermore, a reduced model complexity simplifies the following comfort optimization problem.

Comparing the hybrid model with the linear regression results of Section 3.4.5 reveals the benefit of the GP extension. The minimum cross-validated MSE is reduced by
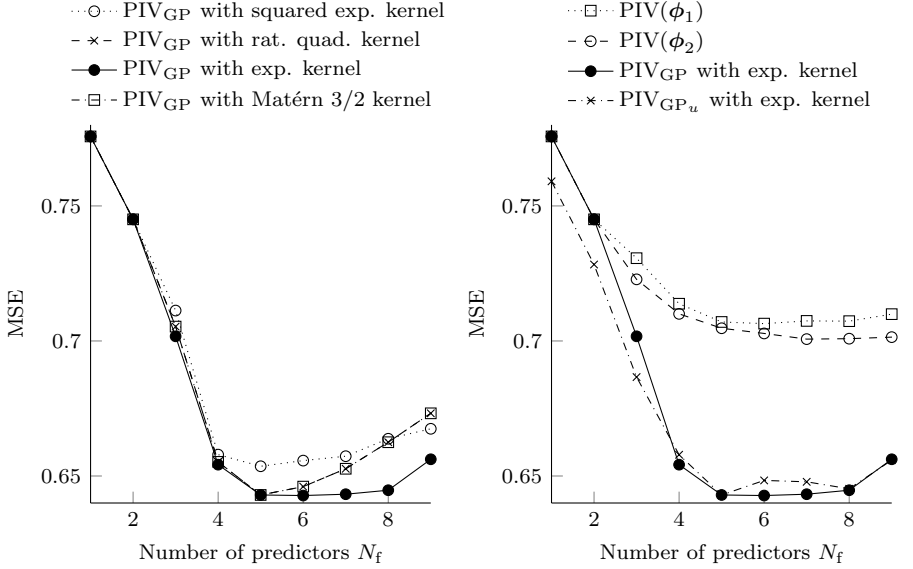
(a) Cross-validated MSE for different kernel functions for $\text{PIV}_{\text{GP},j}(\boldsymbol{u}, \boldsymbol{d})$ (3.45).

(b) Comparison of cross-validated MSE for the linear (3.16) and GP regression models (3.45) and (3.47).

Figure 3.15: Cross-validated MSE for different kernel functions and GP regression approaches.

about $10\,\%$ from 0.71 to 0.64, as depicted in Figure 3.15b. Additionally, already fewer predictors achieve better comfort representations and the optimal model dimension is smaller compared to the linear approaches $\text{PIV}(\boldsymbol{\phi}_{\{1,2\}})$. The optimal feature sets of (3.48) and $\boldsymbol{\phi}^*_{\{1,2\}}$ (3.23) overlap partly. Besides $\boldsymbol{u}$, both sets contain the parameters RH_{air} and DT. Moreover, the environmental conditions are represented by T_{out} in (3.48) instead of RH_{out} and the influence of T_{mr} is neglected. However, increasing the GP model dimension by one, leads to exactly the same model components as identified for $\boldsymbol{\phi}^*_1$ so that the optimal disturbance combination for 6 predictors is given by $\boldsymbol{d} = \begin{bmatrix} T_{\text{mr}} & RH_{\text{air}} & RH_{\text{out}} & DT \end{bmatrix}^{\text{T}}$. While the optimal model components are comparable, the hybrid comfort model structure outperforms all purely linear regression models and is a valuable enhancement. Furthermore, unreasonable model predictions are structurally avoided due to the zero mean of the GP extension. This ensures that predictions far from the training data result in a prediction value of zero so that only the linear base model affects the comfort predictions. Since the

identification of this model part is supervised by meaningful coefficient bounds, a robust and physically feasible output can be guaranteed.

3.5 Conclusion

The previous discussion revealed many challenges that are involved by a personalized user comfort model identification procedure. The subjectivity of thermal sensation in combination with limited access to comfort-related measurements complicate the model identification and incorporate a high uncertainty. This requires a careful selection of the model structure to allow for a good supervision of the resulting model properties. The following conclusions can be drawn and used for the subsequent control strategies:

▶ Simpler (linear) model structures lead to the most reliable predictions.

▶ High dimensional feature vectors incorporate a small potential for model improvement but a high risk of overfitting.

▶ The importance of influencing factors is very user-specific and a common optimal subset definition varies depending on the selected learning method and considered user group. The results for the given test-bed confirm the commonly known importance of air temperature, air velocity and humidity and point towards a major impact of outdoor conditions (represented by T_{out} or RH_{out}) even for the relatively steady weather conditions in Singapore. An inclusion of the time of day can partly compensate for the missing user-related measurements by capturing periodically recurrent activity levels due to daily routines.

▶ The dominating linear relation between T_{air} and the comfort vote is also supported by the presented results.

▶ The effect of elevated air velocities can be mapped by a personalized model by directly using the fan level as model input without the need for a separate air velocity measurement.

▶ A disturbance-dependent GP model is more beneficial than a polynomial model extension. This method also avoids illogical model outputs due to inaccurate extrapolation.

The main motivation for modeling individual thermal comfort in the considered context is the personalization of indoor conditions so that the occupants' satisfaction is improved. Obviously, optimal comfort conditions always stand for a compromise between all subjects. The personal comfort models give the possibility to measure the current comfort state continuously although the user only provides irregular feedback. In the next step, these individual prediction models serve as a basis for an optimal control strategy that maximizes the overall thermal comfort.

4 Adaptive Thermal Comfort Control

The main goal for building operation is maximizing the occupant's comfort while the required energy is minimized. Commonly, standardized comfort assumptions are applied to define the acceptable temperature set-points or ranges [2, 26]. Since the temperature requirements on room level can be achieved by multiple operational strategies for the overall system, these additional degrees of freedom are used to find the strategy with the minimum energy demand on system level [62]. However, as discussed in Chapter 3, the standardized comfort assumptions are not sufficient to ensure individual thermal comfort. Incorporating the derived personal comfort models instead provides an appropriate access to account for the individual expectations in the control approach. The block diagram in Figure 4.1 sketches the general control structure. Common concepts only consider the inner loop consisting of the room dynamics and the controller. To include personal preferences, two different user-in-the-loop control concepts are derived for optimizing the individual thermal comfort. For this, the control loop is extended by the occupant's comfort which is available as infrequent user feedback. As a result, the room is rather considered as actuator that manipulates the thermal comfort of the occupants. The room states $\boldsymbol{x}$ are separated in the component $\boldsymbol{u}$ and the comfort-influencing internal disturbances $\boldsymbol{d}_{\text{int}}$ which contain the room conditions that are not controllable, e.g. relative humidity. The external disturbances $\boldsymbol{d}_{\text{ext}}$ encompass the comfort-affecting weather conditions. Considering the control objective of *manipulating thermal comfort*, the necessity for a valid personal comfort model becomes clear again: Directly using the voting feedback as thermal comfort sensor is not possible due to the time lag between the votes. Furthermore, the number of interruptions by the voting tool should be as low as possible to ensure a productive working environment what further restricts the available voting frequency. Therefore, the results of Chapter 3 are now used to learn the individual thermal comfort and then to define the optimal compromise between all occupants based on the trained models. With this approach personalized office conditions can be achieved whereas the manual voting can even be fully substituted by the comfort prediction models.

At first, the linear regression model is applied and investigated to get a better understanding how the model components influence the optimized room conditions. For this purpose, the analysis starts with the disturbance-independent approaches

$$\mathrm{PIV}_{u,j}(\boldsymbol{u}) = \quad \boldsymbol{\phi_u}^{\mathrm{T}} \boldsymbol{\beta}_{u,j} \quad = \begin{bmatrix} 1 & \boldsymbol{u}_j^{\mathrm{T}} \end{bmatrix}^{\mathrm{T}} \boldsymbol{\beta}_{u,j} \tag{4.1a}$$

$$\mathrm{PIV}_{DT,j}(\boldsymbol{u}, DT) = \quad \boldsymbol{\phi}_{DT}^{\mathrm{T}} \boldsymbol{\beta}_{DT,j} \quad = \begin{bmatrix} 1 & \boldsymbol{u}_j^{\mathrm{T}} & DT \end{bmatrix}^{\mathrm{T}} \boldsymbol{\beta}_{DT,j} \tag{4.1b}$$
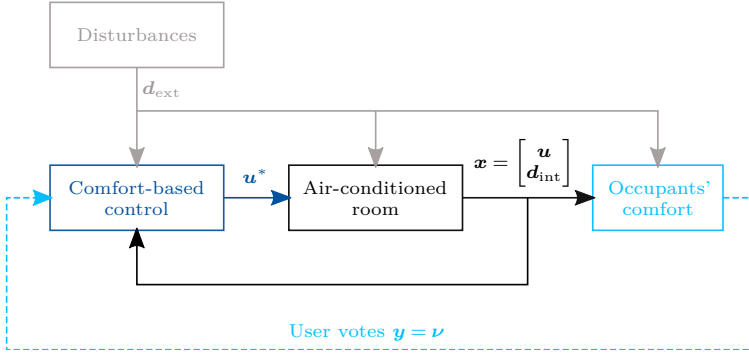
Figure 4.1: Structure for comfort-based control concepts.

to gain knowledge about general temperature preferences as well as time-dependent influences. On that basis, the best linear as well as the optimal hybrid model are evaluated regarding their control performance:

$$
\mathrm{PIV}_{\mathrm{lin},j}(\boldsymbol{u},\boldsymbol{d}) = \boldsymbol{\phi}_{\mathrm{lin}}^{\mathrm{T}}\, \boldsymbol{\beta}_{\mathrm{lin},j} = \begin{bmatrix} 1 & \boldsymbol{u}_j^{\mathrm{T}} & \boldsymbol{d}^{\mathrm{T}} \end{bmatrix}^{\mathrm{T}} \boldsymbol{\beta}_{\mathrm{lin},j}
$$

$$
= \begin{bmatrix} 1 & T_{\mathrm{air}} & l_{\mathrm{fan},j} & T_{\mathrm{mr}} & RH_{\mathrm{air}} & RH_{\mathrm{out}} & DT \end{bmatrix}^{\mathrm{T}} \boldsymbol{\beta}_{\mathrm{lin},j} \tag{4.1c}
$$

$$
\mathrm{PIV}_{\mathrm{GP},j}(\boldsymbol{u},\boldsymbol{d}) = \boldsymbol{\phi_u}^{\mathrm{T}}\, \boldsymbol{\beta}_{\mathrm{GP},j} + \Delta\nu_j(\boldsymbol{d})
$$

$$
= \begin{bmatrix} 1 & T_{\mathrm{air}} & l_{\mathrm{fan},j} \end{bmatrix} \boldsymbol{\beta}_{\mathrm{GP},j} + \Delta\nu_j\left(\begin{bmatrix} RH_{\mathrm{air}} & T_{\mathrm{out}} & DT \end{bmatrix}^{\mathrm{T}} \right) \tag{4.1d}
$$

where $\boldsymbol{d}$ comprises $\boldsymbol{d}_{\mathrm{int}}$ and $\boldsymbol{d}_{\mathrm{ext}}$.

The first proposed control approach is a feedforward controller that is independent from the dynamical properties of the room and only relies on a static optimization to account for the measurable disturbance inputs of the comfort model. As second concept an MPC approach is implemented which allows for the consideration of the dynamical constraints and their effect on the personal comfort estimates. To analyze and evaluate the different approaches, a simulation model for the air-conditioned room is derived which represents the most important dynamical properties of the regarded offices.
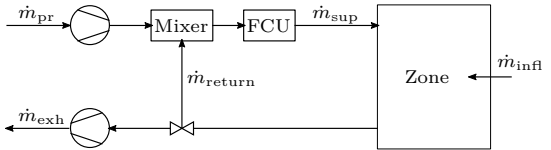
4.1 Simulation Model

The control concept aims for optimized individual thermal comfort in shared office spaces, similarly to the two Singaporean offices depicted in Figure 3.1. Therefore, the simulation model should map their main comfort-influencing characteristics. The thermal conditions of the zone are modeled as an RC network with two nodes as shown in Figure 4.2a and conceptually introduced in Section 1.1. The spatial temperature differences are neglected because of the uniformly distributed ceiling diffusers that are connected to the same Fan Coil Unit (FCU) and thus operated under identical supply conditions. This leads to the valid approximation of well-mixed conditions in the test-bed. The left node of Figure 4.2a describes the indoor air with temperature T_{air} and thermal capacity $C_z = c_p m_z$. The temperature-dependency of the specific heat coefficient c_p is neglected due to small variations for the considered temperature range. The associated heat load $\dot{Q}_z$ encompasses the influence of the AC system as well as internal and external disturbances. The second node represents the walls surrounding the zone with a representative temperature T_w and thermal capacity C_w. Figure 4.2b sketches the interaction between the considered system components. The building's Ventilation and Air Conditioning (VAC) system has a central Air Handling Unit (AHU) for preconditioning the outdoor air whose main task is dehumidification. However, the dynamical properties of the AHU are not relevant for the comfort-oriented room simulation and therefore neglected in the following. The precooled and dehumidified air (primary air), with temperature T_{pr} and mass flow $\dot{m}_{\text{pr}}$, is then distributed to the local FCUs which allow for further cooling $\dot{Q}_{\text{FCU}}$ before the air enters each zone. Condensation at the cooling coils of the FCU is neglected by presuming the mixed air ($\dot{m}_{\text{sup}} = \dot{m}_{\text{pr}} + \dot{m}_{\text{return}}$) is never further cooled down than the corresponding dew point temperature T_{dewpoint}. The room temperature T_{air} is consequently controlled by the FCU operation as well as the supplied amount of primary air. The heat balance for the zone results in

$$\dot{U}_z = c_p \left(m_z \dot{T}_{\text{air}} + \dot{m}_z T_{\text{air}} \right) = \dot{H}_{\text{in}} - \dot{H}_{\text{out}} + \frac{T_w - T_{\text{air}}}{R_{\text{int}}} + \dot{Q}_{\text{dist}} \tag{4.2}$$
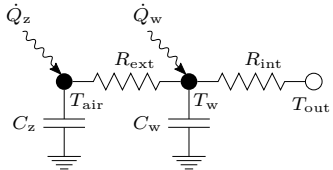
(a) Thermal network for the simulation model (single zone).

(b) Structure of the duct system with considered air flows.

Figure 4.2: Zone model for simulation.

where $\dot{U}_z$ denotes the change rate of the internal energy and $\dot{H}_{\{in,out\}}$ the in or outgoing enthalpy flow [53]. The enthalpy flows depend on the primary air flow $\dot{m}_{pr}$ and the infiltration rate $\dot{m}_{infl}$. Furthermore, the mixing process of primary and return air as well as the FCU are assumed to operate in steady-state. Under the assumption that the zonal mass is maintained

$$\dot{m}_z = \dot{m}_{pr} + \dot{m}_{infl} - \dot{m}_{exh} = 0, \tag{4.3}$$

they result in

$$\begin{aligned}\dot{H}_{in} - \dot{H}_{out} &= c_p \left(\dot{m}_{pr} T_{pr} + \dot{m}_{infl} T_{out} - \dot{m}_{exh} T_{air} \right) \\ &= c_p \dot{m}_{pr} (T_{pr} - T_{air}) + c_p \dot{m}_{infl} (T_{out} - T_{air}). \end{aligned} \tag{4.4}$$

According to DIN V 18599-2 [27], the infiltration rate $\dot{m}_{infl}$ depends on the VAC operation mode and is assumed to be higher during the night when the system is switched off. The corresponding values as well as all introduced parameters are given in Table 4.1. The parameter values are either computed based on physical relations, identified based on measurement data of the test-bed or taken from literature.

The disturbance heat flow $\dot{Q}_{dist}$ contains the effects of all internal disturbances originating from occupancy, lighting, electrical devices etc. For the simulation model, the internal disturbances are separated in the impact of solar radiation I_{sol} and an occupant related heat gain $\dot{Q}_{occ}$:

$$\dot{Q}_{dist} = \eta I_{sol} + N_{occ} \dot{Q}_{occ}. \tag{4.5}$$

The solar gain η determines what proportion of the global solar radiation enters the room through the windows. The identified value according to Table 4.1 is relatively small due to the office's orientation and mostly closed blinds. The average total heat generation of the human body for office work is approximately 130 W [3]. Furthermore, technical devices and lights are assumed to be activated in relation to the occupancy such that the overall occupancy-related heat gain $\dot{Q}_{occ}$ is set to 200 W.

The wall node exchanges heat with the zone and the environment over the thermal resistance R_{int} and R_{ext} respectively. Similarly to (4.2), the heat balance for the wall node results in

$$C_w \dot{T}_w = \frac{T_{air} - T_w}{R_{int}} + \frac{T_{out} - T_w}{R_{ext}}. \tag{4.6}$$

Another comfort-influencing factor is given by the relative humidity of the room. This state is affected by the H_2O generation of the occupants and the primary air flow. The relative humidity RH_{air} is transformed to the specific humidity X_{H_2O} which defines the mass proportion of water vapor m_v in the moist zone air [97] according to

$$X_{H_2O} = \frac{m_v}{m_z} = \frac{m_v}{m_v + m_a} = \frac{R_a}{R_v} \cdot \frac{p_{sat}(T_{air}) RH_{air}}{p_{sat}(T_{air}) RH_{air} \left(\frac{R_a}{R_v} - 1 \right) + p_{amb}}. \tag{4.7}$$

The mass balance for humidity is then given by

$$
\begin{aligned}
m_{\mathrm{z}}\dot{X}_{\mathrm{H_2O}} &= \dot{m}_{\mathrm{v}} \\
&= X_{\mathrm{H_2O,pr}}\dot{m}_{\mathrm{pr}} + X_{\mathrm{H_2O,out}}\dot{m}_{\mathrm{infl}} - X_{\mathrm{H_2O}}\dot{m}_{\mathrm{exh}} + N_{\mathrm{occ}}\dot{m}_{\mathrm{H_2O}} \qquad (4.8) \\
&= \dot{m}_{\mathrm{pr}}(X_{\mathrm{H_2O,pr}} - X_{\mathrm{H_2O}}) + \dot{m}_{\mathrm{infl}}(X_{\mathrm{H_2O,out}} - X_{\mathrm{H_2O}}) + N_{\mathrm{occ}}\dot{m}_{\mathrm{H_2O}}\,.
\end{aligned}
$$

The H_2O generation rate per person for office work [85] can be estimated by the equation

$$
\dot{m}_{\mathrm{H_2O}} = -58 + 5.4 \cdot T \approx -58 + 5.4 \cdot 27 = 87.8, \quad [\dot{m}_{\mathrm{H_2O}}] = \mathrm{g/h \cdot Pers} \qquad (4.9)
$$

using a design temperature T of $27\,^{\circ}\mathrm{C}$ according to the average desired temperature from Table 4.2.

The indoor air quality is also dependent on the CO_2 concentration $X_{\mathrm{CO_2}}$ which should be kept below the level that is hazardous to the occupant's health and well-being. It is a result of the primary air supply and the CO_2 generation of the occupants $N_{\mathrm{occ}}\dot{m}_{\mathrm{CO_2}}$. The average CO_2 generation rate of a person is [85]

$$
\dot{m}_{\mathrm{CO_2}} = 0.02\,\mathrm{m^3/h} \cdot \rho_{\mathrm{CO_2}} = 0.02\,\mathrm{m^3/h} \cdot 2\,\mathrm{kg/m^3} = 0.04\,\mathrm{kg/h}\,. \qquad (4.10)
$$

Equivalently to (4.8), the mass balance for the CO_2 generation results in

$$
m_{\mathrm{z}}\dot{X}_{\mathrm{CO_2}} = \dot{m}_{\mathrm{pr}}(X_{\mathrm{CO_2,pr}} - X_{\mathrm{CO_2}}) + \dot{m}_{\mathrm{infl}}(X_{\mathrm{CO_2,out}} - X_{\mathrm{CO_2}}) + N_{\mathrm{occ}}\dot{m}_{\mathrm{CO_2}}\,. \qquad (4.11)
$$

Combining all heat and mass balances leads to the full simulation model

$$
\begin{aligned}
C_{\mathrm{z}}\dot{T}_{\mathrm{air}} &= c_p\dot{m}_{\mathrm{pr}}(T_{\mathrm{pr}} - T_{\mathrm{air}}) + \dot{Q}_{\mathrm{FCU}} + \frac{T_{\mathrm{w}} - T_{\mathrm{air}}}{R_{\mathrm{int}}} \\
&\quad + c_p\dot{m}_{\mathrm{infl}}(T_{\mathrm{out}} - T_{\mathrm{air}}) + \eta I_{\mathrm{sol}} + N_{\mathrm{occ}}\dot{Q}_{\mathrm{occ}} & (4.12\mathrm{a}) \\
C_{\mathrm{w}}\dot{T}_{\mathrm{w}} &= \frac{T_{\mathrm{air}} - T_{\mathrm{w}}}{R_{\mathrm{int}}} + \frac{T_{\mathrm{out}} - T_{\mathrm{w}}}{R_{\mathrm{ext}}} & (4.12\mathrm{b}) \\
m_{\mathrm{z}}\dot{X}_{\mathrm{H_2O}} &= \dot{m}_{\mathrm{pr}}(X_{\mathrm{H_2O,pr}} - X_{\mathrm{H_2O}}) + \dot{m}_{\mathrm{infl}}(X_{\mathrm{H_2O,out}} - X_{\mathrm{H_2O}}) + N_{\mathrm{occ}}\dot{m}_{\mathrm{H_2O}} & (4.12\mathrm{c}) \\
m_{\mathrm{z}}\dot{X}_{\mathrm{CO_2}} &= \dot{m}_{\mathrm{pr}}(X_{\mathrm{CO_2,pr}} - X_{\mathrm{CO_2}}) + \dot{m}_{\mathrm{infl}}(X_{\mathrm{CO_2,out}} - X_{\mathrm{CO_2}}) + N_{\mathrm{occ}}\dot{m}_{\mathrm{CO_2}}\,. & (4.12\mathrm{d})
\end{aligned}
$$

This model captures all comfort-relevant dynamical properties of the regarded test offices. Furthermore, it is suitable for a model-based control design and the universal structure allows for simple transferability to other building applications. Therefore, the following analysis of the different control strategies is based on (4.12) which also provides the basis for the MPC approach.

Table 4.1: Description of symbols and parameter values of the room model. The values are identified based on measurements (i), computed physical properties (c) or obtained from literature.

Symbol	Description	Value	Unit	Source
η	Solar gain	10^{-5}	m^2	i
c_p	Specific heat coefficient of air	1005	J/kg K	[97]
C_w	Heat capacity of wall node	$3.01 \cdot 10^8$	J/K	i
C_z	Heat capacity of zone node	$3.25 \cdot 10^5$	J/K	c
m_a	Mass of dry air	-	kg	-
$\dot{m}_{CO_2}$	CO_2 generation rate per person	0.04	kg/h	[85]
$\dot{m}_{H_2O}$	H_2O generation rate per person	87.8	g/h Pers	[85]
$\dot{m}_{infl}$	Infiltration rate of zone (day|night)	3.4 | 12.6	g/s	[27]
$\dot{m}_{pr}$	Ventilation rate of zone	70	g/s	[27]
m_v	Mass of water vapor	-	kg	-
m_z	Zonal mass	323	kg	c
N_{occ}	Number of occupants	-	-	-
T_{air}	Zone temperature	-	°C	-
T_w	Wall temperature	-	°C	-
T_{pr}	Primary air temperature	20	°C	i
p_{amb}	Ambient pressure	$1013 \cdot 10^2$	hPa	[97]
p_{sat}	Saturation vapor pressure (Magnus eq.)	$611.2e^{\frac{17.62T}{243.12+T}}$	Pa	[97]
$\dot{Q}_{occ}$	Heat gain of an occupant	200	W	[3]
R_a	Specific gas constant for air	287.1	J/kg K	[97]
R_{ext}	External thermal resistance	$2.44 \cdot 10^{-2}$	K/W	i
R_{int}	Internal thermal resistance	$4.07 \cdot 10^{-3}$	K/W	i
R_v	Specific gas constant of water vapor	461.5	J/kg K	[97]
X_{CO_2}	Carbon dioxide concentration	-	ppm	-
$X_{CO_2,out}$	Carbon dioxide concentration of outside air	400	ppm	i
$X_{CO_2,pr}$	Carbon dioxide concentration of primary air	400	ppm	i
X_{H_2O}	Specific humidity	-	g/kg	-
$X_{H_2O,out}$	Specific humidity of outside air	-	g/kg	-
$X_{H_2O,pr}$	Specific humidity of primary air	8.6	g/kg	c

4.2 Feedforward Comfort Control

Setting the indoor air conditions influences the thermal sensation of the occupants. Therefore, the room can be considered as actor for thermal comfort where the controllable room states should maintain a predefined comfort level. Commonly, this level is transformed to a fixed desired temperature set-point for the whole building that defines the cooling (and heating) demand on room level. Instead of defining a standardized target temperature for all occupied zones, the personal comfort models are used in the following to find the optimal conditions. Due to the high dimensionality of building models, most often a hierarchical control concept is implemented where the room control is separated from the building level [99]. The first approach targets a solution that is independent from the underlying building and HVAC system. It only uses the temperature set-point as interface to the building control. Additionally, the ceiling fans are actuated for varying local air movement. Since the waste heat of their electric drives can be neglected, these actuators only affect the thermal comfort but not the thermal conditions of the zone. Hence, the fan actuation is decoupled from room dynamics. Furthermore, switching the fan levels is performed without noticeable delay so that it is considered as direct feedthrough input for comfort.

Under the assumption that the air conditioning system is fast enough to satisfy the thermal comfort requirements on the room level, a cascaded structure according to Figure 4.3 is proposed to allow for a separation of the comfort optimization and the given air conditioning system. The control structure can be considered as an adaptive feedforward controller for thermal comfort. Since the actual comfort level of the occupants is not provided as a continuous feedback, it can only be used for the adaption of the control algorithm. Hence, a feedforward command is computed based on the individual comfort models which decouples the internal and external disturbances $\boldsymbol{d} = \begin{bmatrix} \boldsymbol{d}_{\text{int}}^{\text{T}} & \boldsymbol{d}_{\text{ext}}^{\text{T}} \end{bmatrix}^{\text{T}}$ by defining the desired set-points for room temperature and fan levels. As soon as new user votes are available, the personal comfort models are updated with the new data. For the given office space, one temperature set-point and four fan levels can be manipulated such that

$$\boldsymbol{u} = \begin{bmatrix} T_{\text{air}} & l_{\text{fan}_1} & l_{\text{fan}_2} & l_{\text{fan}_3} & l_{\text{fan}_4} \end{bmatrix}^{\text{T}}. \tag{4.13}$$

Since the fans are acting locally, a fan mapping must be defined based on the seating position. This results in a mapping function

$$\boldsymbol{u}_j = \boldsymbol{M}_{\boldsymbol{u},j}\boldsymbol{u} = \begin{bmatrix} 1 & 0 & 0 & 0 & 0 \\ 0 & w_{\text{fan}_1,j} & w_{\text{fan}_2,j} & w_{\text{fan}_3,j} & w_{\text{fan}_4,j} \end{bmatrix} \boldsymbol{u} \tag{4.14}$$

which extracts the user-specific fan impact. The fan weights $w_{\text{fan}_r,j}$ of the projection matrix $\boldsymbol{M}_{\boldsymbol{u},j}$ capture the influence of each fan in relation to the employee's position so that $\sum_{r=1}^{4} w_{\text{fan}_r,j} = 1$. The maximum comfort is achieved by forcing all user votes
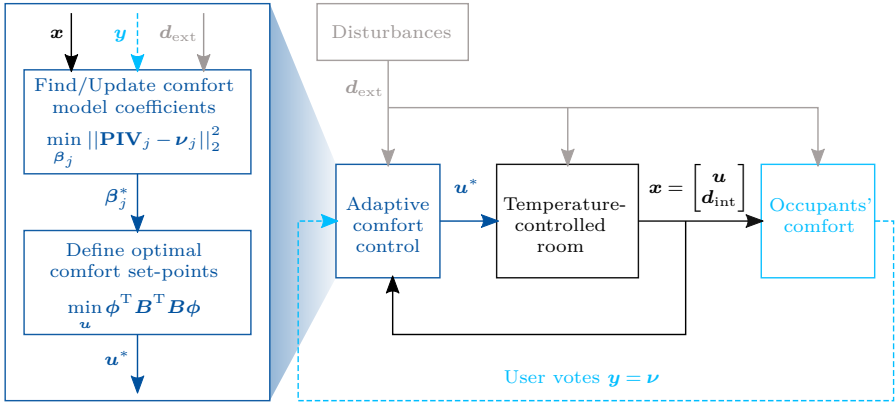
Figure 4.3: Cascaded structure for comfort-based feedforward control.

to zero. Assuming a personal comfort model structure based on linear regression according to (3.14), the corresponding cost function can be formulated as

$$
\begin{aligned}
J(\boldsymbol{u}, \boldsymbol{d}) &= \sum_{j=1}^{N_{\mathrm{occ}}} \mathrm{PIV}_j^2(\boldsymbol{u}, \boldsymbol{d}) &&= \sum_{j=1}^{N_{\mathrm{occ}}} (\boldsymbol{\phi}^{\mathrm{T}} \boldsymbol{M}_j^{\mathrm{T}} \boldsymbol{\beta}_j)^2 \\
&= \sum_{j=1}^{N_{\mathrm{occ}}} \boldsymbol{\phi}^{\mathrm{T}} \boldsymbol{M}_j^{\mathrm{T}} \boldsymbol{\beta}_j \boldsymbol{\beta}_j^{\mathrm{T}} \boldsymbol{M}_j \boldsymbol{\phi} &&= \boldsymbol{\phi}^{\mathrm{T}} \left(\sum_{j=1}^{N_{\mathrm{occ}}} \boldsymbol{M}_j^{\mathrm{T}} \boldsymbol{\beta}_j \boldsymbol{\beta}_j^{\mathrm{T}} \boldsymbol{M}_j \right) \boldsymbol{\phi} &&(4.15) \\
&= \boldsymbol{\phi}^{\mathrm{T}} \boldsymbol{B}^{\mathrm{T}} \boldsymbol{B} \boldsymbol{\phi},
\end{aligned}
$$

where $\boldsymbol{\phi} = \boldsymbol{\phi}(\boldsymbol{u}, \boldsymbol{d})$ consists of the optimal model features defined in Section 3.4.5, $\boldsymbol{\beta}_j$ contains the identified user-specific model coefficients and $\boldsymbol{M}_j$ is a block diagonal matrix composed of the selection matrix $\boldsymbol{M}_{\boldsymbol{u},j}$ and a unit matrix for the considered disturbances. The optimal set-point $\boldsymbol{u}^*$ is the constrained solution of the optimization problem

$$
\begin{aligned}
\boldsymbol{u}^* = \underset{\boldsymbol{u}}{\arg\min} \quad & \boldsymbol{\phi}^{\mathrm{T}} \boldsymbol{B}^{\mathrm{T}} \boldsymbol{B} \boldsymbol{\phi} \\
\text{s.t.} \quad & T_{\min} \leq T_{\mathrm{air}} \leq T_{\max} \\
& l_{\mathrm{fan}_r} \in \{0, 1, 2, 3, 4\}, \quad \forall r = 1, \ldots, 4
\end{aligned}
\tag{4.16}
$$

The box constraint defined by $T_{\min}$ and $T_{\max}$ ensures that the optimal room temperature stays within a feasible range. For a sufficiently large data base, these limits are not necessary. However as demonstrated in Section 3.4, the high variance and

uncertainty of the real-world voting data can lead to extreme set-points, particularly during the early training phase. Therefore, including meaningful bounds is a robust solution to incorporate common knowledge about general comfort ranges and to avoid very uncomfortable settings. Since the fan levels cannot be selected continuously, (4.16) is a MIQP which is solved using Gurobi [45].

For the hybrid model (3.45) consisting of the linear regression combined with the GP model, the objective (4.16) is modified to include the disturbance-dependent shift:

$$
\begin{aligned}
J(\boldsymbol{u}, \boldsymbol{d}) &= \sum_{j=1}^{N_{\text{occ}}} \text{PIV}_j^2(\boldsymbol{u}, \boldsymbol{d}) \\
&= \sum_{j=1}^{N_{\text{occ}}} (\boldsymbol{\phi}^{\text{T}}(\boldsymbol{u}) \boldsymbol{M}_j^{\text{T}} \boldsymbol{\beta}_j + \Delta \nu_j(\boldsymbol{d}))^2 \\
&= \sum_{j=1}^{N_{\text{occ}}} \boldsymbol{\phi}^{\text{T}} \boldsymbol{M}_j^{\text{T}} \boldsymbol{\beta}_j \boldsymbol{\beta}_j^{\text{T}} \boldsymbol{M}_j \boldsymbol{\phi} + 2\boldsymbol{\phi}^{\text{T}} \boldsymbol{M}_j^{\text{T}} \boldsymbol{\beta}_j \Delta \nu_j + \Delta \nu_j^2 \qquad (4.17) \\
&= \boldsymbol{\phi}^{\text{T}} \left(\sum_{j=1}^{N_{\text{occ}}} \boldsymbol{M}_j^{\text{T}} \boldsymbol{\beta}_j \boldsymbol{\beta}_j^{\text{T}} \boldsymbol{M}_j \right) \boldsymbol{\phi} + 2\boldsymbol{\phi}^{\text{T}} \left(\sum_{j=1}^{N_{\text{occ}}} \boldsymbol{M}_j^{\text{T}} \boldsymbol{\beta}_j \Delta \nu_j \right) + \sum_{j=1}^{N_{\text{occ}}} \Delta \nu_j^2 \\
&= \boldsymbol{\phi}^{\text{T}} \boldsymbol{B}^{\text{T}} \boldsymbol{B} \boldsymbol{\phi} + 2\boldsymbol{\phi}^{\text{T}} \boldsymbol{b} + c.
\end{aligned}
$$

The optimal input is then given by

$$
\begin{aligned}
\boldsymbol{u}^* = \underset{\boldsymbol{u}}{\arg\min} \quad & \boldsymbol{\phi}^{\text{T}} \boldsymbol{B}^{\text{T}} \boldsymbol{B} \boldsymbol{\phi} + 2\boldsymbol{\phi}^{\text{T}} \boldsymbol{b} \\
\text{s.t.} \quad & T_{\min} \leq T_{\text{air}} \leq T_{\max} \\
& l_{\text{fan}_r} \in \{0, 1, 2, 3, 4\}, \quad \forall r = 1, \dots, 4
\end{aligned} \qquad (4.18)
$$

For an application in the real world office environment, additional stronger assumptions must be included to ensure meaningful optimization results:

▶ Only users with a minimum number of votes $\underline{m}$ are considered for the set-point optimization to guarantee a well defined model parameter identification.

▶ Occupants with a small training set have a reduced impact on the optimization until a required set size $\overline{m}$ is gained, introduced as a weight depending on the amount of votes

$$
J(\boldsymbol{u}, \boldsymbol{d}) = \sum_{j=1}^{N_{\text{occ}}} w_{\text{obs}}(m_j) \cdot \text{PIV}_j^2(\boldsymbol{u}, \boldsymbol{d}), \quad w_{\text{obs}}(m_j) = \begin{cases} 0 & \text{for } m_j \leq \underline{m} \\ \frac{m_j - \underline{m}}{\overline{m} - \underline{m}} & \text{for } \underline{m} < m_j < \overline{m} \\ 1 & \text{for } m_j \geq \overline{m} \end{cases}
$$

$$(4.19)$$

▶ Prior knowledge about expected sensitivities is included by narrowing the co-efficient bounds for the individual user models to avoid infeasible coefficients due to bad voting data, e.g. $\beta_{T_{\text{air}}}^{\min} \leq \beta_{T_{\text{air}}} \leq \beta_{T_{\text{air}}}^{\max}$ or $\beta_{l_{\text{fan}}}^{\min} \leq \beta_{l_{\text{fan}}} \leq \beta_{l_{\text{fan}}}^{\max}$ where the bounds are selected based on known/common vote-parameter relations (minimum and maximum expected slope for temperature and fan level impact).

The above mentioned parameters $\underline{m}, \overline{m}, \beta_{(\cdot)}^{\min}$ and $\beta_{(\cdot)}^{\max}$ are design parameters and can be used to adjust the conservativity of the comfort-based control.

The resulting optimal trajectory depends on the selected personal modeling approach. As introductorily mentioned, the models (4.1) are analyzed and evaluated for the two offices. The collected voting data are used for the individual model identification and then applied for the definition of optimal room conditions. The comfort optimization that is independent from the room and/or building model can also be interpreted as a disturbance decoupling where the term disturbance refers to the parameters which disturb the thermal comfort (not the room conditions). Inserting all comfort-influencing and measurable but non-controllable room and environmental parameters into (4.16) or (4.18) only leaves $\boldsymbol{u}$ as unknown which is subsequently computed as the best compromise between the individual user models.

For the simulative analysis of the feedforward control approach, the required cooling power of the VAC system is summarized in

$$\dot{Q}_{\text{AC}} = c_p \dot{m}_{\text{pr}}(T_{\text{pr}} - T_{\text{air}}) + \dot{Q}_{\text{FCU}}. \tag{4.20}$$

Consequently, the office temperature is controlled by a PI controller for the combined cooling demand $\dot{Q}_{\text{AC}}$. Equivalently to the real building, the fresh air ventilation rate $\dot{m}_{\text{pr}}$ is set to a constant value for each office (see Table 4.1) under the assumption that it is sufficient to maintain acceptable CO_2 levels even for full occupancy. Moreover, the empirical relation between T_{air} and T_{mr}, as derived in Appendix B.4, is included in the simulation. A random occupancy profile is assumed and applied for the calculation of internal disturbances. Monitored data from the weather station on top of the considered office building in Singapore provide a realistic representation of the external disturbances. The comfort-based set-point optimization is updated every 5 min such that the room conditions are adjusted 12 1/h. This leads to piecewise constant control inputs with a sampling time of $t_{\text{s}} = 5$ min.

4.2.1 Disturbance-Independent Optimization

Before the optimal trajectories based on (4.1c) and (4.1d) are investigated, the individually fitted and disturbance-independent basis function (4.1a)

$$\mathrm{PIV}_{u,j}(\boldsymbol{u}) = \begin{bmatrix} 1 & \boldsymbol{u}_j^{\mathrm{T}} \end{bmatrix}^{\mathrm{T}} \boldsymbol{\beta}_{u,j} = {\boldsymbol{\phi_u}}^{\mathrm{T}} \boldsymbol{\beta}_{u,j}$$

is evaluated for the considered occupants to gain a better understanding of the following optimal set-points. Figure 4.4 sketches the resulting comfort planes $\mathrm{PIV}_{u,j}$ corresponding to each personalized user model. The intersection of each plane with $\mathrm{PIV}_{u,j} = 0$ corresponds to the optimal combination of room temperature T_{air} and fan level l_{fan} for the occupant j and is indicated by the thick lines. As visible by the intersecting lines in the lower plots, the comfortable set-point combinations vary significantly between different users and some lines of intersection even exceed the plotted temperature range of 20 to 30 °C. Furthermore, the sensitivity to changes of T_{air} and l_{fan} differs notably. The variation regarding the fan speed is mostly dependent on the seating position and thus the effective air movement as a result of the fan level and distance. The high variance of the comfortable temperature mainly originates from the subjective differences in combination with clothing habits and unconsidered solar influences due to the occupants location. Moreover, the limited system excitation results in some extreme profiles (planes that are shifted far upwards or downwards): Assuming the temperature range of the observation data is in the range 23 to 26 °C but the user prefers temperatures higher (lower) than this range, most votes are concentrated below (above) the zero plane. This reduces the range of the output data so that the fitted temperature slope is blurred by missing positive (negative) voting data. Figure 4.4 vividly reveals the complexity of personal comfort mapping and emphasizes the required care for a user-in-the-loop application. It can be observed that no combination of $\boldsymbol{u}$ satisfies all occupants simultaneously.

The optimal set-point $\boldsymbol{u}^*$ for each office can be directly derived solving the MIQP (4.16) and inserting the feature vector $\boldsymbol{\phi_u}$ of (4.1a). The solution for the two offices based on the identified user profiles of Figure 4.4 is shown in Table 4.2. The first row refers to the result for integer fan levels and the second row is the result when the integer constraint is relaxed to allow for continuous fan speeds $l_{\mathrm{fan}_r} \in [0,4]$. Note that rounding the continuous optimal fan speeds matches the MIQP solution for this case. Consequently, solving the corresponding QP, rounding the fan speeds and then solving the reduced QP for T_{air} leads to the identical result as directly solving the MIQP. Therefore, the MIQP could be validly approximated by solving two QPs. Moreover, the box constraint for the fan levels always ensures feasible solutions for the two-step solution. Nevertheless, the MIQP is solved sufficiently fast ($\ll t_{\mathrm{s}} = 5\,\mathrm{min}$) and a constraint relaxation not necessary.

Comparing the optimal fan levels for both offices exposes that $l_{\mathrm{fan}_{3,4}}$ is higher than $l_{\mathrm{fan}_{1,2}}$. Referring to Figure 3.1 reveals that fan 3 and 4 affect the users close to the
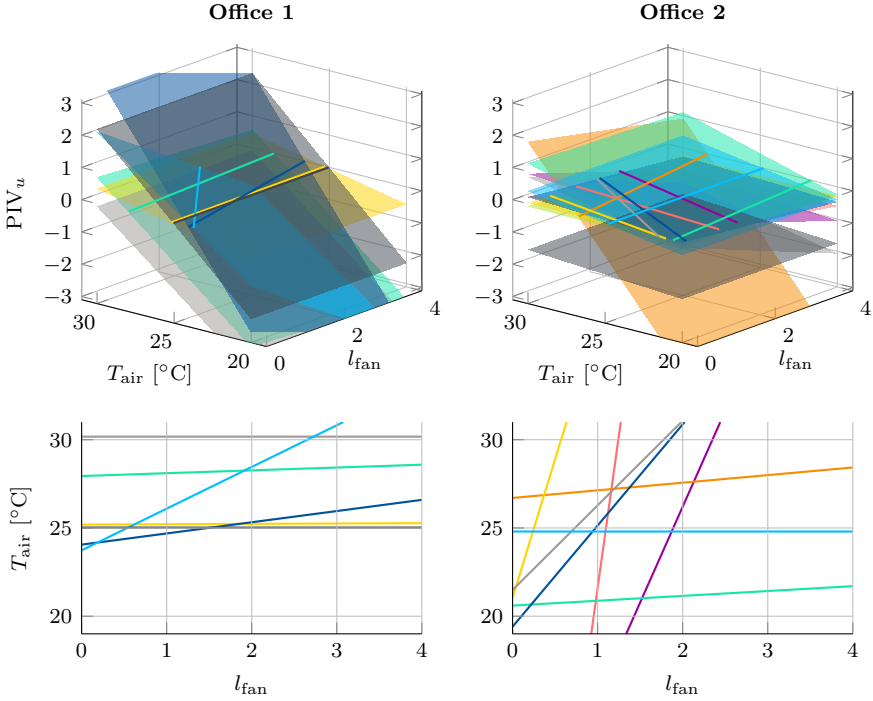
Figure 4.4: Personal relation between the predicted thermal sensation vote $PIV_{u,j}$ (4.1a) and the inputs $\boldsymbol{u}$ (each color represents one user). Upper show the plane $PIV_{u,j}(\boldsymbol{u})$ and the lower plots indicates the intersection line $PIV_{u,j} = 0$ representing thermal comfort.

window while fan 1 and 2 take care of the rear part of the offices. Since the window side is more influenced by solar radiation, the corresponding fans must compensate for these additional loads. Another interesting result is the relatively high desired temperature of about $27\,°C$. This result exceeds the standardized assumptions [2] by 2-3 K but corresponds to previous research in tropical regions [68].

The most beneficial disturbance feature for the 3-dimensional linear model is the usage of the time of day (see Table 3.3). Extending (4.1a) by DT according to (4.1b)

$$\mathrm{PIV}_{DT,j}(\boldsymbol{u}, DT) = \begin{bmatrix} 1 & \boldsymbol{u}_j^{\mathrm{T}} & DT \end{bmatrix}^{\mathrm{T}} \boldsymbol{\beta}_{DT,j}$$

leads to the daytime-dependent comfort profiles of Figure 4.5, where the depicted time range is limited to the general office hours from 7 am to 7:30 pm. The upper

Table 4.2: Optimal set-points for the disturbance-independent comfort model.

Type of fan level	Office 1					Office 2				
	T_{air}	l_{fan_1}	l_{fan_2}	l_{fan_3}	l_{fan_4}	T_{air}	l_{fan_1}	l_{fan_2}	l_{fan_3}	l_{fan_4}
Discrete	26.9	0	1	4	4	27.7	1	0	2	1
Continuous	27.0	0	1.3	4	4	27.7	1.3	0.2	1.8	0.9

charts show the optimal temperature profiles and fan levels. The associated predicted user votes are depicted below. The consideration of DT leads to larger deviations between the optimal office conditions compared to (4.1a). Averaging the desired temperature leads to a daily average of $27.0\,^{\circ}\mathrm{C}$ for office 1 and $27.7\,^{\circ}\mathrm{C}$ for office 2 such that particularly the optimized conditions of office 2 change when DT is considered.

The optimal temperature profile of office 1 decreases monotonically over the day and exhibits a remarkable step around the lunch break which usually started at 11:30 am. Hence, the occupants of office 1 prefer higher temperatures in the morning and lower temperatures after the lunch break. An explanation is given by higher solar loads in the afternoon which increase the operative temperature, particularly close to the window. As a consequence, the fan levels are increased during the afternoon to compensate for radiation effects. Note that the algorithm incorporates the feature that a fan is switched off when no occupants are present. Therefore, the fans are switched off for a short period around noon due to the lunch break. The predicted votes give further insight about the desired fan levels. Fan 4 of office 1, for example, runs permanently on full speed because the only person mapped to this fan feels always too warm for the optimal temperature compromise. Equivalently, fan 1 is primarily switched off due to an assigned person that feels too cold. Fan level 3 is stepwise increased over the day to balance the daytime-dependent user preferences. The second fan is shared by three users and consequently operated by a compromise solution.

The desired temperature trend of the occupants in office 2 is reversed to office 1, thus increases over the day. However, similarities can be identified such as the downward step around lunch time. Furthermore, most occupants of office 2 are more sensitive to varying fan levels, also indicated by the steeper slopes in Figure 4.4. This results in more frequent and larger steps of the desired temperature trajectory when a fan level is changed.

The previous analysis creates a first idea of the characteristics of the comfort-optimized trajectories. However, the identified optimal model structures (4.1c) and (4.1d) require the consideration of environmental disturbances $\boldsymbol{d}$. Therefore, these influences are included in the optimization in the next step.
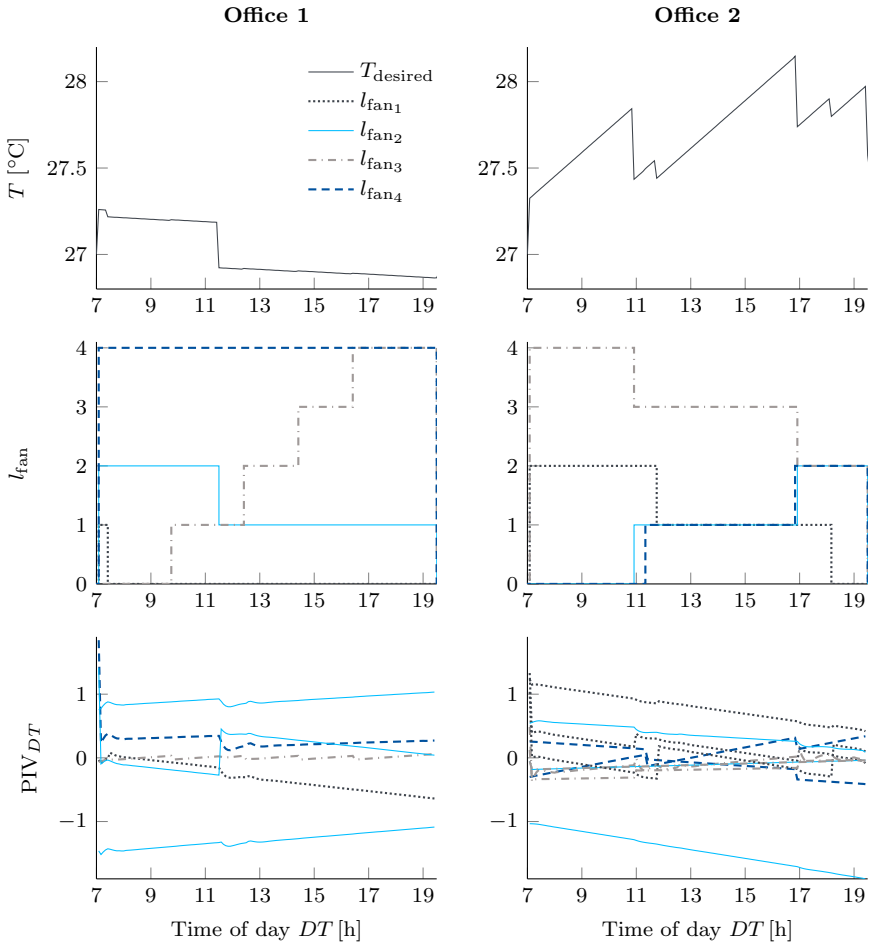
Figure 4.5: Optimal daytime-dependent temperature and fan level profiles for the personalized models (4.1b) (upper plots). The lower depictions show the corresponding PIVs of all occupants where the colors match the mapped fan for each user.

4.2.2 Disturbance-Dependent Optimization

The consideration of the comfort disturbing parameters $\boldsymbol{d}$ is realized by simulating the office conditions based on the derived temperature-controlled zone model (4.12). Instead of the reduced disturbance-independent comfort model approaches, the full linear PIV_{lin} (4.1c) and the GP approach PIV_{GP} (4.1d) are evaluated using the corresponding disturbance inputs. The optimal input trajectory is obtained by iteratively solving for $\boldsymbol{u}^*$ based on (4.16) and (4.18). It is assumed that the air conditioning system is operated daily from 7 am to 7:30 pm. Outside these limits, the desired temperature is set to the current room conditions so that no control action is required to satisfy the target of the comfort optimization. The weather data of two typical Singaporean days are used for the simulation of the comfort-based feedforward control. Figure 4.6 compares the resulting desired room conditions for the linear and the hybrid modeling approach.

The main difference between the linear and the GP-based approach is the varying influence of humidity. The coefficients of the linear comfort models result in a strong reduction of the desired temperature T_{desired} for higher humidity levels which corresponds to the decreased heat loss via evaporation. Due to the increasing humidity during the night, when the VAC system is switched off, the desired morning set-point is about $3\,^{\circ}\text{C}$ lower than in the afternoon. This effect mainly superimposes the daytime-related trend observed in Figure 4.5. Only in the afternoon, the time-related downward trend for office 1 and the upward trend for office 2 is still visible. Comparing these observations to the GP model reveals that the impact of humidity is not as prominent for PIV_{GP}. A small upward trend during the morning can still be noted and explained with the declining humidity. However, the nonlinear disturbance consideration of this approach leads to generally smaller temperature variations during the day which are not as easily interpretable as the linear model. Therefore, the desired temperatures based on PIV_{GP} are computed again while only one disturbance parameter is varied and the fans are switched off. The corresponding results are shown in Figure 4.7. The influence of daytime is very distinct for different users and consequently deviates between the two offices. The linearized impact of DT was already discussed based on Figure 4.5 which revealed a downward trend for office 1 and an upward trend for office 2. This trend is also visible in Figure 4.7 but the GP approach is able to capture the nonlinear relations and exposes several variation over the day. The occupants of office 1 prefer increasing temperatures during the morning, a significant reduction after lunch and a small raise in the afternoon. The second office's daytime dependence is rather low during the morning but exhibits a significant drop in the afternoon with a subsequent strong rise. The impact of humidity RH_{air} and outside temperature T_{out} shows a negative correlation regarding the desired temperature such that a higher humidity and a higher outside temperature lead to lower temperature set-points and vice versa. The reverse influence of RH_{air} corresponds to the linear model and the
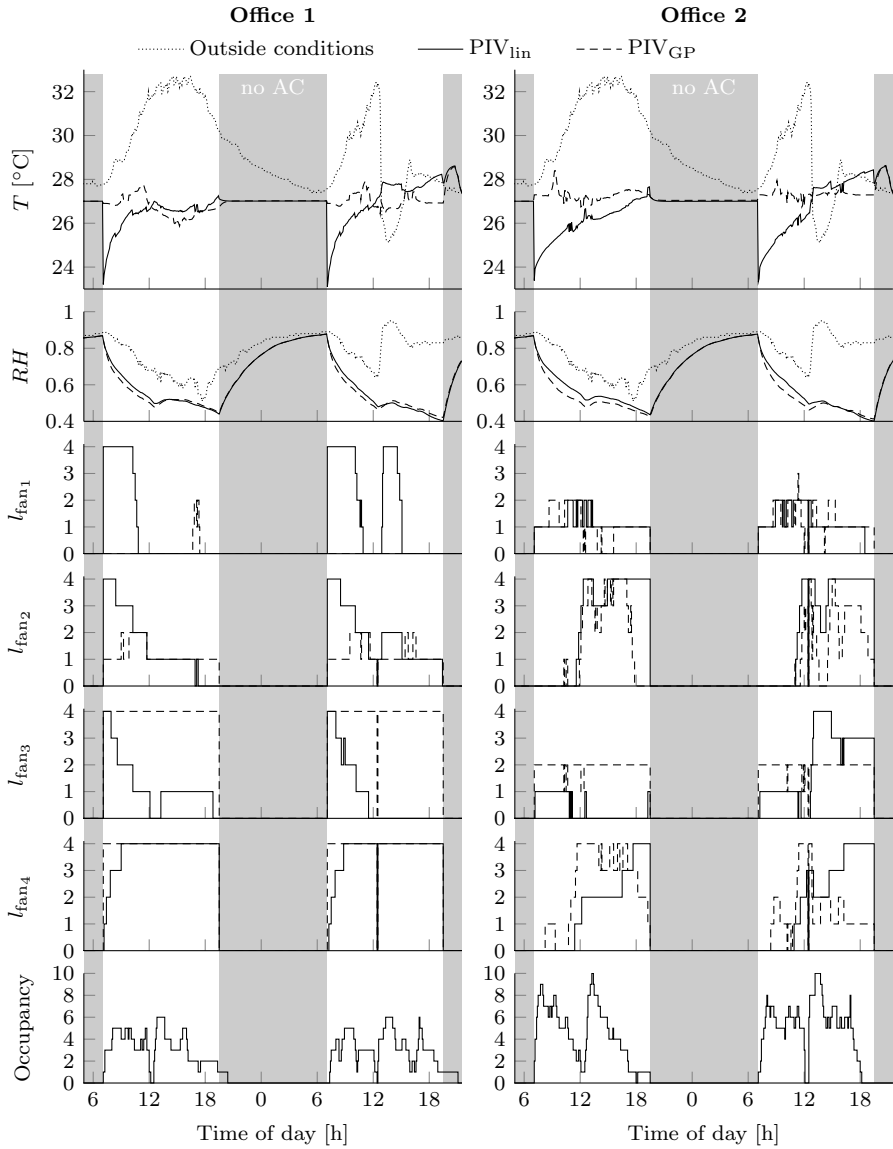
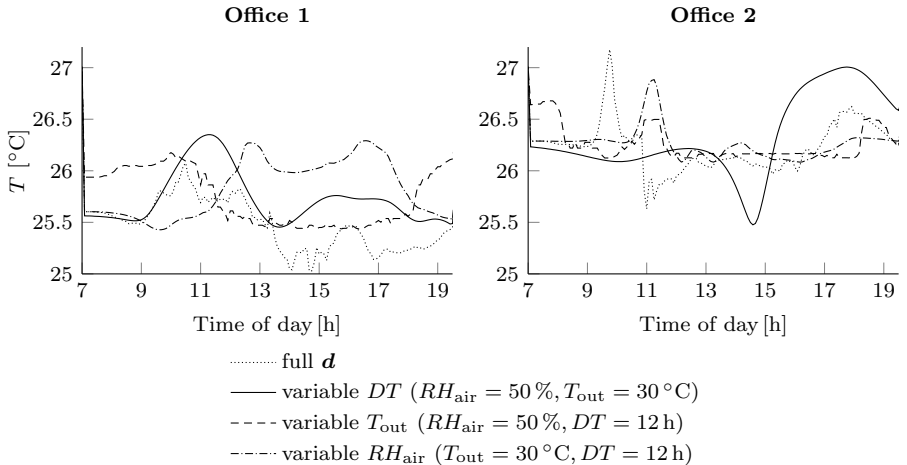Figure 4.6: Optimal desired trajectories for the disturbance-dependent comfort models (4.1c) and (4.1d).

Figure 4.7: Investigation of the nonlinear impact of $\boldsymbol{d}$ on the optimal trajectories for the GP comfort model (4.1d) (results correspond to first day of Figure 4.6 and $\boldsymbol{l}_{\mathrm{fan}} = \boldsymbol{0}$).

reduced evaporation rate. The negative impact of T_{out} can be correlated to higher thermal loads and thus a warmer sensation of the thermal conditions.

Furthermore, the investigation of the separated disturbance effects emphasizes the weaknesses of a polynomial basis function compared to the GP approach. The nonlinear relation between e. g. DT and vote, hence the desired temperature, would require high dimensional shape functions entailing the identification of numerous model parameters and a high risk of overfitting. The notable difference between the solutions for $\mathrm{PIV}_{\mathrm{lin}}$ and $\mathrm{PIV}_{\mathrm{GP}}$ further highlights the sensitivity of the resulting comfort optimum to the modeling assumptions. These differences are also visible for the optimal fan levels. Although general similarities can be observed, particularly the strong impact of the humidity for the linear approach results in higher fan speeds in the morning. Moreover, another problem related to the discrete fan levels can be noted for both models. The different user preferences and changing disturbance effects lead to multiple switching commands for the fans within a short time period. As a consequence, the corresponding temperature profile also exhibits discontinuous steps that can never be realized by the AC system. To achieve realizable temperature trajectories, a rate constraint

$$\Delta T_{\mathrm{desired}} = |T_{\mathrm{desired}}(t + t_{\mathrm{s}}) - T_{\mathrm{air}}(t)| \leq \Delta T_{\mathrm{max}} \tag{4.21}$$

can be added to (4.16) and (4.18). This smoothens the generated trajectory and

remedies sudden steps so that dynamical limitations for the office temperature are accounted for. An exemplary result for PIV_{GP} with temperature rate constraint is given in Appendix C.1. Note that the switching rate of the fan levels could be limited equivalently. However, the reaction time of the fans is negligible small and immediate changes are generally realizable.

The comparison of PIV_{lin} and PIV_{GP} revealed significant differences for the optimal comfort trajectories. The highly nonlinear influences of the comfort parameters, as demonstrated in Figure 4.7, and the improved prediction accuracy, as shown in Figure 3.15b, suggest to focus on the hybrid comfort model approach (4.1d) for further investigation. Therefore, all following results are based on PIV_{GP}.

Comfort Benefit and Energy Saving Potential by Fan Operation

Comparing the optimal temperature levels of Figure 4.6 and Figure 4.7 already reveals the cooling effect of the fans and hence the incorporated energy saving potential. The constraint $l_{\text{fan}} = 0$ is equivalent to only optimizing the temperature set-point as a compromise between all occupants of the office. Individualization is consequently only possible in terms of office-related temperature levels. Local adjustments within one office space cannot be realized due to missing local actuators.

The impact of missing or limited fan operation is compared in terms of the average temperature levels and the thereby required average cooling demand. The values are computed based on the disturbance situation for the two exemplary days of Figure 4.6. The corresponding time interval I_{op} defines the operating hours from 7 am to 7:30 pm over the examined days and t_{op} the associated accumulated time period. Consequently, the average desired temperature results in

$$\bar{T}_{\text{desired}} = \frac{1}{t_{\text{op}}} \int_{I_{\text{op}}} T_{\text{desired}}(t) \, dt \tag{4.22}$$

and the required cooling demand is given by

$$\bar{Q}_{\text{demand}} = \frac{1}{2} \int_{I_{\text{op}}} |\dot{Q}_{\text{AC}}(t)| \, dt. \tag{4.23}$$

Table 4.3 summarizes the results for different fan operation modes. The temperature set-point must be decreased by more than $1\,\text{K}$ when no fans are available. This results in an approximately $20\,\%$ higher cooling demand for each office. Furthermore, individual preferences cannot be taken into account and worsen the comfort cost

Table 4.3: Impact of fan operation on average temperature level and consequent energy consumption. All values are averaged over the two exemplary days of Figure 4.6.

Office			$l_{\text{fan}} \in \{0,\dots,4\}$	$l_{\text{fan}} = 0$	$l_{\text{fan}} = 4$	$\max_r(l_{\text{fan},r}) = 4$
1	$\bar{T}_{\text{desired}}$	°C	26.9	25.6	27.7	26.9
	$\bar{Q}_{\text{demand}}$	$\frac{\text{kWh}}{\text{day}}$	17.1	20.9	14.4	17.1
	$\overline{\text{PIV}}_{\text{ave}}$	-	0.92	1.08	1.14	0.92
2	$\bar{T}_{\text{desired}}$	°C	27.3	26.3	28.6	27.9
	$\bar{Q}_{\text{demand}}$	$\frac{\text{kWh}}{\text{day}}$	15.7	18.8	12.1	13.7
	$\overline{\text{PIV}}_{\text{ave}}$	-	0.62	0.66	0.71	0.64

significantly for both offices. The average predicted individual comfort level

$$\overline{\text{PIV}}(t) = \sqrt{\frac{1}{N_{\text{occ}}} \sum_{j=1}^{N_{\text{occ}}} \text{PIV}_j^2(t)}, \tag{4.24a}$$

$$\overline{\text{PIV}}_{\text{ave}} = \frac{1}{t_{\text{op}}} \int_{I_{\text{op}}} \overline{\text{PIV}}(t)\, dt \tag{4.24b}$$

of the N_{occ} occupants is a representative for the actual comfort state. The results of Table 4.3 highlight how individualized air movement can improve the personal comfort, particularly for a very diverse group of occupants. The predicted comfort level without fan operation ($l_{\text{fan}} = 0$) is worsened remarkably compared to individualized fan operation.

The energy saving potential can even be further improved when the general air velocity is set to the maximum level, here $l_{\text{fan}} = 4$. This reduces the demand by 16-23 % compared to the most comfortable solution due to the increased temperature. However, the high air movement results in discomfort such that the overall comfort sensation suffers. Instead of fixed fan levels, a compromise between the extreme cases is given by introducing the constraint that the maximum optimal fan level must always reach the upper boundary: $\max_r(l_{\text{fan},r}) = 4$. This still leaves degrees of freedom for individualization but also includes the exploitation of the energy saving potential by the ceiling fans. The compromise solution leads to comparable comfort levels as the full personalization and reduces the energy consumption. However, the corresponding results only differ from (4.18) when the comfort optimum does not already include the maximum fan level. Hence, according to the optimal fan speeds in Figure 4.6,
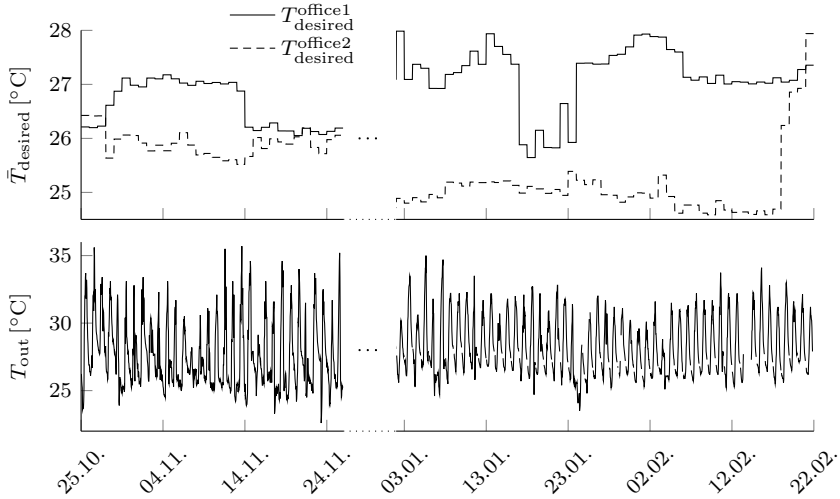
Figure 4.8: Development of average comfort temperature for the two offices over the test period.

the result for office 1 is equal to (4.18) whereas a small potential can be exploited in office 2 while the comfort level is almost maintained.

4.2.3 Development of Individual Comfort over the Test Period

So far, the analysis was performed on the accumulated data of all test subjects. However, changes in personnel led to varying occupancy structures during the test phase. Therefore, the corresponding desired comfort conditions evolve over time and the adaptive algorithm adjusts to the current test group. The evolution of the desired temperature level is depicted in Figure 4.8. For greater clarity, the optimal temperatures are represented by their daily average. Note that the presented temperatures are the result of a simultaneous fan level optimization according to (4.18). Furthermore, no measurements are available during December due to a sensor failure.

For the definition of the optimal conditions, a new employee is always added to the computation as soon as his observation data reach the minimum required size $\underline{m}$. Resignations are automatically included by discarding a user from the comfort calculation when he was inactive for more than 21 days.

Although the outside conditions are fairly constant in Singapore, the optimal indoor

conditions vary significantly over time. This demonstrates the high subjectivity and diversity of the dynamically changing test groups. Variations between $24.5\,^\circ\mathrm{C}$ and $27.5\,^\circ\mathrm{C}$ can be observed during the monitored period. In this context, a constant set-point of the air conditioning system appears as a rather bad approach regarding the thermal well-being of the occupants. It also emphasizes the ability of the algorithm to adapt to a changing occupancy structure. Additionally, the identified diversity further supports the great benefit of individualized air movement, as discussed in Section 4.2.2 because the corresponding additional degrees of freedom allow for better compromise between the very distinct thermal sensation.

4.2.4 Influence of Occupancy

The computation of the optimal room conditions for the previous analysis always considered all available comfort models independent whether or not a user was present. In the case that the presence of specific occupants can be detected, comfort can certainly be improved when only attendant users are considered in the optimization algorithm. This can be realized by multiplying the predicted individual vote with the binary presence value φ_j

$$J(\boldsymbol{u},\boldsymbol{d}) = \sum_{j=1}^{N_{\mathrm{occ}}} \varphi_j \cdot w_{\mathrm{obs}}(m_j) \cdot \mathrm{PIV}_j^2(\boldsymbol{u},\boldsymbol{d},t), \quad \varphi_j = \begin{cases} 0 & \text{when user is absent} \\ 1 & \text{when user is present.} \end{cases} \quad (4.25)$$

However, (de-)activation of particular comfort functions has a similar or even more pronounced effect as switching a fan level. The suddenly changing comfort requirements cannot be fulfilled instantaneously due to the inertia of the thermal room dynamics. Furthermore, the immediate reaction to a short absence (e. g. visit of the bathroom) can be energetically unfavorable because multiple changes of the operating point is most often accompanied by an additional energy demand. The already presented rate constraint (4.21) is one possible approach to handle the fast switching of the comfort requirements also for occupancy related variations of the comfort conditions. Alternatively, the comfort models can be slowly faded in and out when a subject enters or leaves the room. This smoothens the effects on the optimal temperature trajectory and avoids unnecessary reaction to a short absence. Figure 4.9 demonstrates the latter concept and shows an example using a first order low-pass filter with time constant $20\,\mathrm{min}$. The binary occupancy value for each user is transformed to a continuous weighting function with PT1-behavior so that the cost function (4.25) is continuous. Certainly, the first order filter can be replaced by higher order filters to ensure sufficient continuous differentiability of the cost function.

Another aspect must be taken into account when occupancy is detected. Solving

$$\boldsymbol{u}^* = \operatorname*{arg\,min}_{\boldsymbol{u}} J(\boldsymbol{u},\boldsymbol{d})$$
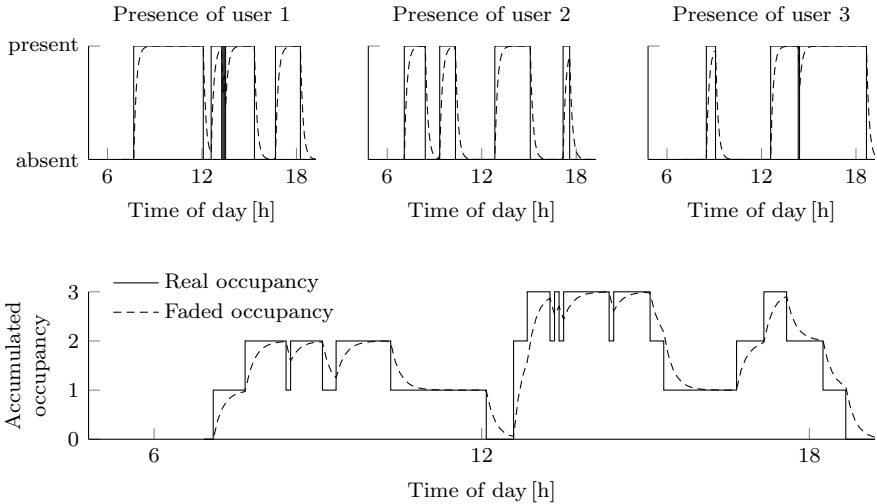
Figure 4.9: Concept of fading the occupancy signal for smoothing the cost function.

does not necessarily lead to a unique solution if a fan is unoccupied because it could operate on any level without affecting the comfort level. Therefore, an upstream check is included that determines unoccupied fans, switches them off and excludes them from the optimization.

Figure 4.10 visualizes and compares the effect of the two different smoothing methods. The desired temperature T_{desired} represents the optimal set-point as a result of (4.18). However, the implemented room controller cannot always fulfill the desired command such that the real (simulated) office temperature T_{office} deviates from T_{desired}. This consequently results in a theoretically optimal value for $\overline{\mathrm{PIV}}_{\mathrm{desired}}$ based on the desired conditions and a realistic prediction $\overline{\mathrm{PIV}}$ based on the actual room conditions. Both predictions of the comfort level are depicted in Figure 4.10 and summarized in Table 4.4 as averaged values for the two discussed days.

The solution without occupancy detection is used as benchmarking reference. The theoretically optimal set-point is given by the direct consideration of the occupancy according to (4.25). The deviation between the corresponding optimal temperature set-points indicates the potential of taking occupancy into account. This theoretical potential is quantified by a 20 % reduction of the average comfort vote $\overline{\mathrm{PIV}}_{\mathrm{desired}}$ in Table 4.4 and illustrated in Figure 4.10. However, a direct consideration of the occupancy results in large temperature steps over the day which also increases the associated energy consumption. Particularly when the personal sensation is very distinct between the occupants, the requirements change drastically and lead to an

Table 4.4: Comparison of the averaged comfort levels and cooling demands depending on the applied occupancy handling.[a]

Consideration of occupancy	no	direct	faded	direct with rate constraint
$\overline{\mathrm{PIV}}_{\mathrm{ave,desired}}$	0.552	0.446	0.516	0.492
$\overline{\mathrm{PIV}}_{\mathrm{ave}}$	0.555	0.538	0.526	0.522
$\bar{Q}_{\mathrm{demand}} \left[\frac{\mathrm{kWh}}{\mathrm{day}} \right]$	16.3	17.8	17.7	17.5

[a] Note that the general comfort level of Table 4.4 is better than in Table 4.3 because only the PIV for present users is taken into account. This leads incidentally to a reduced average cost.

infeasible cooling demand. These steps primarily occur during lunch time and in the evening when many employees are coming or leaving. This results in remarkable deviations between the desired and real temperature which diminishes the potential from 20 % to negligible 3 %. Moreover, it must be noted that the simulation uses a well-tuned PI controller with an ideal AC system so that extreme overshoots are already prevented. However, the real-world performance is likely to be even worse due to often badly tuned room controllers.

Therefore, the filtered (faded) occupancy value can be used to achieve a more realizable temperature command. Figure 4.10 shows the corresponding simulation results for a filter time constant of 35 min. Comparing T_{desired} with the real temperature T_{office} shows that large overshoots are reduced which decreases the difference between the command and the office temperature and equivalently the difference between $\overline{\mathrm{PIV}}_{\mathrm{desired}}$ and $\overline{\mathrm{PIV}}$. The ongoing/missing inclusion of already absent/present occupants in the cost function downgrades the expected comfort levels $\overline{\mathrm{PIV}}_{\mathrm{desired}}$ but results in a trackable command so that the actual comfort level $\overline{\mathrm{PIV}}$ is improved compared to the direct (de-)activation based on occupancy. An adjustment of the applied filter and time constant provides additional potential for improvement but also increases the complexity of the algorithm design.

An even more intuitive adjustment is given by considering the actual occupancy but including a rate constraint on temperature which represents the achievable change rate of the real system. Consequently, the rate constraint has a clear technical interpretation which simplifies the parameter selection. Accordingly, the calculated optimal temperature can be tracked by the system and the theoretical optimum corresponds to the real conditions. Taking into account the dynamical properties, furthermore, allows for using the fans to compensate for the slower temperature behavior. Choosing the change rate as 5 K/h not only reduces the deviation between the theoretical and real optimum but additionally leads to the best actual comfort level $\overline{\mathrm{PIV}}$. Moreover, the smoothened trajectory slightly reduces the required cooling power.

However, the main driver for the energy consumption are the thermal preferences of the present occupants. As a result, longer attendance times of users who prefer warmer conditions will always lead to a reduction of the energy demand and vice versa. Thus, $\bar{Q}_{\mathrm{demand}}$ is mainly a result of the user's comfort demands and the controller design only has a subordinate impact. Note that the rate constraint is only applied to the temperature command since fan levels can be directly accessed and changed instantaneously with negligible delay. Moreover, unoccupied fans are switched off immediately without affecting the remaining occupants to minimize the energy demand of the ceiling fans.

Another interesting effect can be observed in Figure 4.10. Although the average $\overline{\mathrm{PIV}}_{\mathrm{desired}}$ is reduced when occupancy is taken into account, there are some short periods during the day where the consideration of occupancy leads to a slightly worse comfort level. This is explained by the neglect of the system dynamics and couplings of comfort factors. A change of the room temperature has also an effect on the relative humidity. This effect cannot be regarded as long as the control approach is independent from the building and room dynamics. As a result, it can happen that the supposedly beneficial change of the temperature involves a negative humidity-related impact.

The discussed results investigated the potential as well as different aspects of applying a comfort-based control algorithm. However, the neglect of the system dynamics leads to partially suboptimal results. Although the rate constraint is a first step towards an optimization which considers dynamical properties, an optimized control approach must combine the comfort requirements, the room model and the impact of disturbances. This is only achieved by regarding the Optimal Control Problem (OCP) under consideration of dynamical constraints.
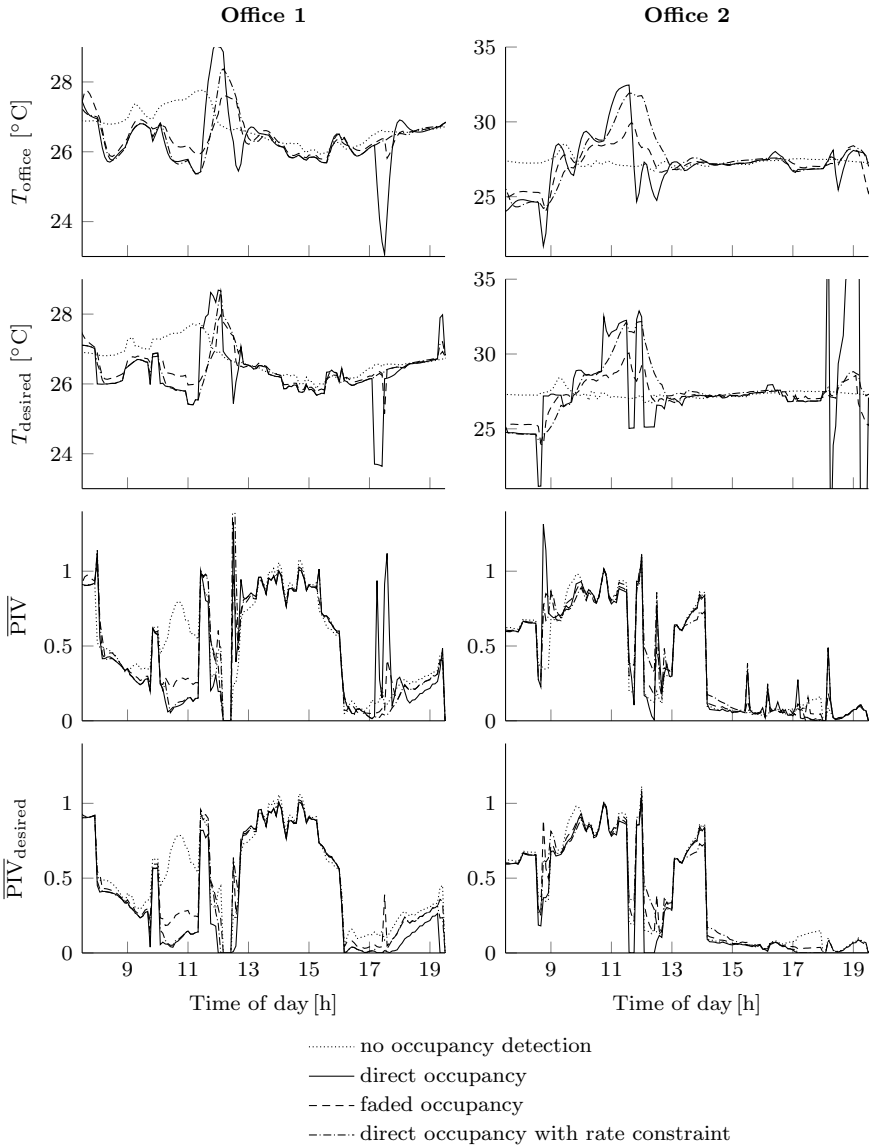
Figure 4.10: Impact of the occupancy detection and different approaches for the comfort optimization.

4.3 Model Predictive Control for Optimizing Personal Comfort

The adaptive feedforward control of Chapter 4.2 is based on a hierarchical design, where the temperature control is separated from the comfort-oriented set-point definition. The room or building dynamics are considered as a black-box, where at most the achievable temperature change rate could be defined. A model-based control approach allows for the consideration of physical relations between the comfort-influencing conditions, e. g. temperature and humidity. If desired, the pure thermal comfort optimization can be extended to a combined optimization of individual comfort and energy demand. Therefore, the feedforward control is replaced by an MPC approach which takes into account the system dynamics, supply conditions and disturbances. Figuratively, the room conditions as actuator for thermal comfort are now included in the control concept.

The dynamical model assumption for the MPC formulation corresponds to the simulation model (4.12). For control design, the nonlinear system dynamics are reformulated in state-space form $\dot{\boldsymbol{x}} = \boldsymbol{f}(\boldsymbol{x}, \boldsymbol{u}, \boldsymbol{d})$, where $\boldsymbol{x}$ contains the room states, $\boldsymbol{u}$ the manipulated variables of the AC system actuators and $\boldsymbol{d}$ the remaining external and internal disturbances.

The system states of the room model are collected in

$$\boldsymbol{x} = \begin{bmatrix} T_{\text{air}} & T_{\text{w}} & X_{\text{H}_2\text{O}} & X_{\text{CO}_2} \end{bmatrix}^{\text{T}}. \tag{4.26}$$

Consequently, the room conditions, that were considered as internal comfort disturbances $\boldsymbol{d}_{\text{int}}$ for the feedforward controller, are now part of the system model. Hence, their dynamical relations are included during the comfort optimization.

Since the feedforward control is independent from the AC system, only the overall cooling demand $\dot{Q}_{\text{AC}}$ is taken into account which already incorporates the enthalpy flow of the primary air supply. For the MPC approach, it is assumed that not only the overall cooling demand $\dot{Q}_{\text{AC}}$ is controlled but the cooling power at the FCU $\dot{Q}_{\text{FCU}}$ as well as the primary mass flow $\dot{m}_{\text{pr}}$ are manipulated variables. This provides an additional degree of freedom to control the humidity and CO_2 level apart from the temperature. Furthermore, a demand driven fresh air supply does not only enable the compliance with upper CO_2 bounds but also entails energy saving potential. Commonly, $\dot{m}_{\text{pr}}$ is one of the most expensive components of the air conditioning task in tropical regions due to the high latent heat losses by dehumidification. Therefore, it is meaningful to reduce the primary air flow while harmless CO_2 levels are maintained. Thus, the extended vector of manipulated inputs results in

$$\boldsymbol{u} = \begin{bmatrix} \dot{Q}_{\text{FCU}} & \dot{m}_{\text{pr}} & \boldsymbol{l}_{\text{fan}}^{\text{T}} \end{bmatrix}^{\text{T}}. \tag{4.27}$$

All remaining parameters that influence the thermal comfort or the zone conditions are collected in the redefined disturbance vector $\boldsymbol{d}$. Hence, it consists of the occupancy,

the supply conditions of the primary air and the outside conditions:

$$\boldsymbol{d} = \begin{bmatrix} N_{\text{occ}} & T_{\text{pr}} & X_{\text{H}_2\text{O,pr}} & X_{\text{CO}_2,\text{pr}} & T_{\text{out}} & I_{\text{sol}} & X_{\text{H}_2\text{O,out}} & X_{\text{CO}_2,\text{out}} \end{bmatrix}^{\text{T}}.$$

(4.28)

Equivalently to Section 4.2.2, the control of the zone is separated from the building control. Therefore, the dynamic of the central AHU is neglected and the state of the primary air (T_{pr}, $X_{\text{H}_2\text{O,pr}}$ and $X_{\text{CO}_2,\text{pr}}$), which also depends on the losses in the duct system, is only considered as disturbance input for the local zone model. Since preconditioning of the outside air in the AHU does not effect the CO_2 level, the primary air's CO_2 concentration $X_{\text{CO}_2,\text{pr}}$ is equal to the outside concentration. For the simulative analysis, both values are assumed to have a constant level of 400 ppm. Moreover, temperature and humidity of the primary air are set to $T_{\text{pr}} = 20\,^{\circ}\text{C}$ and $X_{\text{H}_2\text{O,pr}} = 8.6\,\text{g/kg}$. For reasons of comparison, the same weather conditions and occupancy profiles as used in Section 4.2.2 are adopted for the following analysis.

Substituting the entries of (4.26), (4.27) and (4.28) in the simulation model (4.12) finally results in the system dynamics in state space form

$$\dot{\boldsymbol{x}} = \boldsymbol{f}(\boldsymbol{x}, \boldsymbol{u}, \boldsymbol{d})$$
$$= \begin{bmatrix} \frac{x_2 - x_1}{C_z R_{\text{int}}} + \frac{c_p}{C_z}\left(u_2(d_2 - x_1) + \dot{m}_{\text{infl}}(d_5 - x_1)\right) + \frac{u_1}{C_z} + \frac{\eta}{C_z}d_6 + \frac{\dot{Q}_{\text{occ}}}{C_z}d_1 \\ \frac{x_1 - x_2}{C_w R_{\text{int}}} + \frac{d_5 - x_2}{C_w R_{\text{ext}}} \\ m_z^{-1}\left(u_2(d_3 - x_3) + \dot{m}_{\text{infl}}(d_7 - x_3) + \dot{m}_{\text{H}_2\text{O}}d_1\right) \\ m_z^{-1}\left(u_2(d_4 - x_4) + \dot{m}_{\text{infl}}(d_8 - x_4) + \dot{m}_{\text{CO}_2}d_1\right) \end{bmatrix}.$$

(4.29)

For the comfort-oriented control design, the system output of interest is not given by the physical states $\boldsymbol{x}$ of the zone but by the current comfort level and hence the predicted votes of the occupants:

$$\boldsymbol{y} = \mathbf{PIV}(\boldsymbol{x}, \boldsymbol{u}, \boldsymbol{d}, t)$$

(4.30)

where $\mathbf{PIV}(\boldsymbol{x}, \boldsymbol{u}, \boldsymbol{d}, t) \in \mathbb{R}^{N_{\text{occ}}}$ is a vector containing all predicted thermal sensation votes of the considered occupants. The described system is bilinear with a nonlinear, time-variant output due to the comfort relation using a GP model

$$\text{PIV}_j(\boldsymbol{x}, \boldsymbol{u}, \boldsymbol{d}, t) = \begin{bmatrix} 1 & x_1 & u_j \end{bmatrix} \boldsymbol{\beta}_{\text{GP},j} + \Delta\nu_j(x_1, x_3, d_5, t)$$
$$= \text{PIV}_0 + \boldsymbol{\beta}_{\boldsymbol{x}j}^{\text{T}}\boldsymbol{x} + \boldsymbol{\beta}_{\boldsymbol{u}j}^{\text{T}}\boldsymbol{u} + \boldsymbol{\kappa}_j^{\text{T}}(\boldsymbol{x}, \boldsymbol{d}, t)\boldsymbol{\gamma}_j$$

(4.31)

where the input element u_j corresponds to the user-assigned fan. The relation (4.31) is separated in a linear component and the nonlinear kernel evaluation. The dependency of $\Delta\nu_j$ on the air temperature x_1 and the mass fraction of water x_3 originates from the required relative humidity RH_{air} of the GP term which is acquired by (4.7).

4.3.1 Control Objective

The control aims for an operational strategy that finds the best compromise between all considered users. Similarly to Chapter 4.2, this involves the maximization of thermal comfort which can be expressed as minimization of the quadratic votes over the control horizon $t \in [t_0, t_f]$. Hence, the objective function results in

$$J(\boldsymbol{x}, \boldsymbol{u}, \boldsymbol{d}, t) = \frac{1}{2} \int_{t_0}^{t_f} \boldsymbol{y}^{\mathrm{T}}(\boldsymbol{x}, \boldsymbol{u}, \boldsymbol{d}, t) \boldsymbol{Q} \boldsymbol{y}(\boldsymbol{x}, \boldsymbol{u}, \boldsymbol{d}, t) + \boldsymbol{u}^{\mathrm{T}}(t) \boldsymbol{R} \boldsymbol{u}(t) \, dt \tag{4.32}$$

where the diagonal matrix $\boldsymbol{Q} \succeq 0$ can be used to introduce diverse weighting on the different user models. Furthermore, the objective function is extended by an input-related penalty that is realized as quadratic cost due to its favorable properties for the optimization. The matrix $\boldsymbol{R}$ allows to incorporate economic aspects as well as it is used to ensure the existence of a unique optimal solution when particular entries of $\boldsymbol{u}$ do not affect the output $\boldsymbol{y}$. In contrast to the feedforward control, the OCP incorporates the dynamic, state and input constraints so that defining an optimal control strategy requires to solve

$$\begin{aligned} \min_{\boldsymbol{u}} \quad & J(\boldsymbol{x}, \boldsymbol{u}, \boldsymbol{d}, t) \\ \text{s.t.} \quad & \dot{\boldsymbol{x}}(t) = \boldsymbol{f}(\boldsymbol{x}, \boldsymbol{u}, \boldsymbol{d}), \quad \boldsymbol{x}(t_0) = \boldsymbol{x}_{\mathrm{init}}, \quad t \in [t_0, t_f] \\ & \boldsymbol{x} \in \mathcal{X} \\ & \boldsymbol{u} \in \mathcal{U}. \end{aligned} \tag{4.33}$$

The admissible solution space defined by $\mathcal{X}$ and $\mathcal{U}$ satisfies the minimal requirements for comfort and building physical aspects which are described in the following.

4.3.2 State and Input Constraints

One central reason for choosing an optimization-based control method is the straight-forward inclusion of input and state constraints that are not negligible in the context of building control. As already mentioned in Chapter 4.2, a bounded temperature range can be introduced to ensure plausible temperature set-points e. g. originating from a poor comfort model quality in the early training phase. However, for a sufficient amount of voting data the temperature limits are not necessary which is why the corresponding state constraint is neglected for the simulation.

The input constraints $\boldsymbol{u} \in \mathcal{U}$ depend on the system prerequisites. The FCU of the considered test-bed only allows cooling such that the range for $u_1 = \dot{Q}_{\mathrm{FCU}}$ is defined by the maximum cooling power $\dot{Q}_{\mathrm{FCU,max}} = 21.6 \, \mathrm{kW}$ [13] and bounded by 0

$$-\dot{Q}_{\mathrm{FCU,max}} \leq u_1 \leq 0. \tag{4.34}$$

For reasons of comparison, the subsequent simulative analysis extends the VAC system to an HVAC system which also allows for heating so that (4.34) is modified to

$$-\dot{Q}_{\text{FCU,max}} \leq u_1 \leq \dot{Q}_{\text{FCU,max}}. \tag{4.35}$$

To differentiate between the two system characteristics, the terms VAC and HVAC are used respectively to refer to the applied bounds on $\dot{Q}_{\text{FCU}}$. The available primary air flow rate $u_2 = \dot{m}_{\text{pr}}$ allows for at most $3\,\text{ACH}$ and cannot be negative, thus

$$0 \leq u_2 \leq \dot{m}_{\text{pr,max}} \approx 0.27\,\text{kg/s}. \tag{4.36}$$

The main purpose of the primary air supply is the maintenance of non-hazardous CO_2 levels. Although, the human's sensibility to variations of the CO_2 concentration is rather low and recommended ranges do not necessarily demand for strict compliance with a fixed limit, long exposure to high CO_2 concentrations can cause side effects like headache or drowsiness [3]. Consequently, an upper bound

$$x_4 = X_{CO_2} \leq X_{CO_2,\text{max}} = 800\,\text{ppm} \tag{4.37}$$

is taken into account for the comfort optimization [85]. Directly including the constraints (4.36) and (4.37) can lead to an infeasible set for the OCP in the event that the maximum primary air flow $\dot{m}_{\text{pr,max}}$ cannot compensate for the CO_2 generation of the occupants. Therefore, (4.37) is reformulated in terms of the required air flow $\dot{m}_{\text{pr}}$ based on the steady-state equation for the CO_2 level:

$$0 = \dot{m}_{\text{pr}} X_{CO_2,\text{pr}} + \dot{m}_{\text{infl}} X_{CO_2,\text{out}} - X_{CO_2}(\dot{m}_{\text{pr}} + \dot{m}_{\text{infl}}) + N_{\text{occ}} \dot{m}_{CO_2}$$

$$\Rightarrow \quad X_{CO_2,\text{max}} \geq \frac{\dot{m}_{\text{pr}} X_{CO_2,\text{pr}} + \dot{m}_{\text{infl}} X_{CO_2,\text{out}} + N_{\text{occ}} \dot{m}_{CO_2}}{\dot{m}_{\text{pr}} + \dot{m}_{\text{infl}}}$$

$$\dot{m}_{\text{pr}} \geq \frac{\dot{m}_{\text{infl}}(X_{CO_2,\text{out}} - X_{CO_2,\text{max}}) + N_{\text{occ}} \dot{m}_{CO_2}}{X_{CO_2,\text{max}} - X_{CO_2,\text{pr}}}$$

$$\Rightarrow \quad \dot{m}_{\text{pr,min}} = \frac{\dot{m}_{\text{infl}}(d_8 - X_{CO_2,\text{max}}) + d_1 \dot{m}_{CO_2}}{X_{CO_2,\text{max}} - d_4}. \tag{4.38}$$

In the case that this minimum required air flow is greater than the upper bound $\dot{m}_{\text{pr,max}}$, a violation of the CO_2 bound (4.37) must be accepted. Therefore, (4.36) and (4.38) are combined to ensure a feasible solution set and to redefine the lower and upper bounds for the primary air flow

$$\min(\dot{m}_{\text{pr,min}}, \dot{m}_{\text{pr,max}}) \leq u_2 \leq \dot{m}_{\text{pr,max}}. \tag{4.39}$$

In addition, the reformulation of the CO_2 constraint entails the advantage that the dynamic of X_{CO_2} can be excluded from the OCP. This simplifies the dynamical constraint and reduces the computational effort.

Eventually, as already known from the previous chapter, the fan levels can only take integer values from 0 to 4

$$u_{r+2} = l_{\text{fan}_r} \in \{0, 1, 2, 3, 4\}, \quad r = 1, \ldots, 4. \tag{4.40}$$

Furthermore, latent heat loss by condensation is neglected and unwanted at the local FCU. Hence, the mixing ratio of primary and return air in combination with the applied cooling power $\dot{Q}_{\text{FCU}}$ must result in a relative humidity of the supply air RH_{sup} lower than 100 %. The steady-state mass balance for the mixer results in

$$\dot{m}_{\text{sup}} = \dot{m}_{\text{pr}} + \dot{m}_{\text{return}} \tag{4.41}$$

$$X_{\text{H}_2\text{O,sup}} = X_{\text{H}_2\text{O,pr}} \frac{\dot{m}_{\text{pr}}}{\dot{m}_{\text{sup}}} + X_{\text{H}_2\text{O,return}} \frac{\dot{m}_{\text{return}}}{\dot{m}_{\text{sup}}}$$

$$= \frac{d_3 u_2 + x_3 \dot{m}_{\text{return}}}{u_2 + \dot{m}_{\text{return}}}. \tag{4.42}$$

Similarly, the steady-state heat balance leads to the temperature of the mixed air

$$T_{\text{mixed}} = T_{\text{pr}} \frac{\dot{m}_{\text{pr}}}{\dot{m}_{\text{sup}}} + T_{\text{return}} \frac{\dot{m}_{\text{return}}}{\dot{m}_{\text{sup}}}$$

$$= \frac{d_2 u_2 + x_1 \dot{m}_{\text{return}}}{u_2 + \dot{m}_{\text{return}}} \tag{4.43}$$

such that the supply air temperature T_{sup} for steady-state operation of the FCU is given by

$$T_{\text{sup}} = T_{\text{mixed}} + \frac{\dot{Q}_{\text{FCU}}}{c_p \dot{m}_{\text{sup}}} = \frac{d_2 u_2 + x_1 \dot{m}_{\text{return}} + u_1/c_p}{u_2 + \dot{m}_{\text{return}}}. \tag{4.44}$$

Since the applied cooling power is directly scaled by the mass flow $\dot{m}_{\text{sup}}$, the maximum value for $\dot{Q}_{\text{FCU}}$ without the risk of condensation can be achieved by maximizing the amount of recirculated air. The maximum achievable mass flow trough the FCU is $\dot{m}_{\text{sup,max}} = 1.26 \frac{\text{kg}}{\text{s}}$ [13] and consequently the maximum return flow results in $\dot{m}_{\text{return}} = \dot{m}_{\text{sup,max}} - u_2$ (neglecting the impact of infiltration). To keep the relative humidity of the supplied air RH_{sup} below 100 %, the coupled state and input constraint based on (4.7)

$$RH_{\text{sup}} = \frac{R_{\text{v}}}{R_{\text{a}}} \cdot \frac{p_{\text{amb}} X_{\text{H}_2\text{O,sup}}}{p_{\text{sat}}(T_{\text{sup}}) \left(1 + \left(\frac{R_{\text{v}}}{R_{\text{a}}} - 1\right) X_{\text{H}_2\text{O,sup}}\right)}$$

$$= \frac{R_{\text{v}}}{R_{\text{a}}} \cdot \frac{p_{\text{amb}} (u_2(d_3 - x_3) + x_3 \dot{m}_{\text{sup,max}})}{p_{\text{sat}}(T_{\text{sup}}) \left(\dot{m}_{\text{sup,max}} + \left(\frac{R_{\text{v}}}{R_{\text{a}}} - 1\right)(u_2(d_3 - x_3) + x_3 \dot{m}_{\text{sup,max}})\right)}$$

$$\leq 1 \tag{4.45}$$
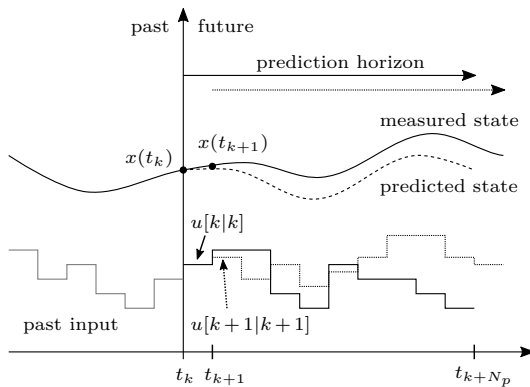
must be satisfied during the operation.

Figure 4.11: Moving horizon prediction scheme.

4.3.3 Comfort-Based Optimal Control and Nonlinear MPC (NMPC) Scheme

The computation of an optimal control input for the system (4.29) with output (4.30) requires to solve the nonlinear OCP (4.33) over the prediction horizon $t_{\mathrm{p}} = t_f - t_0$. This is done using direct multiple shooting implemented with the optimization tool CasADi [4]. For this, the control input is parameterized in time intervals $t_{\mathrm{s}} = t_{k+1} - t_k$ of piecewise constant values

$$\boldsymbol{u}(t) = \boldsymbol{u}[k], \quad t \in [t_k, t_{k+1})$$

and solved by stepwise numerical integration of the differential equation (4.29) as well as the objective (4.32) using a Runge-Kutta scheme of order four. Continuity of the states are ensured by additional equality constraints at the transition points t_k, $k = 0, \ldots, N_{\mathrm{p}} - 1$, where N_{p} denotes the number of prediction steps. To avoid the computational burden of solving the underlying Mixed Integer Nonlinear Program (MINLP), the solution is gained in two steps based on the corresponding relaxed Nonlinear Program (NLP). In the first iteration, the NLP is solved allowing continuous fan speeds $l_{\mathrm{fan},r} \in [0,4]$. The resulting fan levels are then rounded to the closest integer value and the reduced OCP is solved again with the predefined fan levels. This procedure always leads to a feasible solution because of the box constraint $0 \leq l_{\mathrm{fan},r} \leq 4$ and no notable loss of potential could be identified compared to more elaborate branch and bound algorithms.

Optimality of the solution $\boldsymbol{u}^*$ is only ensured if the modeling approach is a valid representation of the reality and disturbances can be predicted for the considered control horizon. Obviously, both assumptions are prone to error such that the control

trajectory results in a sub-optimal system behavior. To cope with model and estimation errors, the MPC scheme relies on the iterative solution of (4.33) using the plant model (4.29) and disturbance predictions. Figure 4.11 sketches the moving horizon approach of the optimization scheme. In each MPC iteration, the OCP is solved for the finite prediction horizon $t_\mathrm{p} = N_\mathrm{p} \cdot t_\mathrm{s}$. However, instead of applying the whole input trajectory $\boldsymbol{u}^*(t)$ only the first control segment is used. Subsequently, the optimization is repeated based on the true system response using the updated state and disturbance measurements or estimations. A commonly used notation indicates the considered time step of the prediction $k+i$ as well as the time instance for the initialization k:

$$\mathbf{u}[k] = \begin{bmatrix} \boldsymbol{u}[k|k] & \boldsymbol{u}[k+1|k] & \dots & \boldsymbol{u}[k+N_\mathrm{p}|k] \end{bmatrix}^\mathrm{T}. \tag{4.46}$$

For reasons of brevity, the reference to the start time $[\cdot|k]$ of the prediction is omitted in the following.

4.3.4 Comfort-Based Linear MPC (LMPC) Scheme

Although solving the nonlinear objective (4.33) with CasADi is already real-time capable on an ordinary notebook for the regarded offices, scaling effects for large commercial buildings result in a high and potentially infeasible computational effort. Under the assumption that a linearization around the desired trajectory results in valid predictions, this effort can be reduced significantly by applying linear control concepts. Therefore, the bilinear system (4.29) with the nonlinear and time-varying output (4.30) is linearized at an arbitrary operating point $\boldsymbol{x}_0$ and $\boldsymbol{u}_0$. Introducing

$$\boldsymbol{A} = \left.\frac{\partial \boldsymbol{f}}{\partial \boldsymbol{x}}\right|_{\boldsymbol{x}_0, \boldsymbol{u}_0}, \qquad\qquad \boldsymbol{B}(\boldsymbol{d}(t)) = \left.\frac{\partial \boldsymbol{f}}{\partial \boldsymbol{u}}\right|_{\boldsymbol{x}_0, \boldsymbol{u}_0},$$

$$\boldsymbol{C}(\boldsymbol{d}(t),t) = \left.\frac{\partial \mathbf{PIV}}{\partial \boldsymbol{x}}\right|_{\boldsymbol{x}_0, \boldsymbol{u}_0}, \qquad\qquad \boldsymbol{D} = \left.\frac{\partial \mathbf{PIV}}{\partial \boldsymbol{u}}\right|_{\boldsymbol{x}_0, \boldsymbol{u}_0}$$

result in the linear approximation for the system dynamics

$$
\begin{aligned}
\dot{\boldsymbol{x}}(t) = {} & \boldsymbol{A}\boldsymbol{x}(t) + \boldsymbol{B}(\boldsymbol{d}(t))\boldsymbol{u}(t) + \overbrace{\boldsymbol{f}(\boldsymbol{x}_0, \boldsymbol{u}_0, \boldsymbol{d}(t)) - \boldsymbol{A}\boldsymbol{x}_0 - \boldsymbol{B}(\boldsymbol{d}(t))\boldsymbol{u}_0}^{\boldsymbol{f}_0(\boldsymbol{d}(t))} \\[2mm]
= {} & \begin{bmatrix} -\frac{1/R_\mathrm{int}+c_p(u_{0,2}+\dot{m}_\mathrm{infl})}{C_\mathrm{z}} & \frac{1}{C_\mathrm{z} R_\mathrm{int}} & 0 & 0 \\[2mm] \frac{1}{C_\mathrm{w} R_\mathrm{int}} & -\frac{1}{C_\mathrm{w}}\left(\frac{1}{R_\mathrm{int}}+\frac{1}{R_\mathrm{ext}}\right) & 0 & 0 \\[2mm] 0 & 0 & -\frac{u_{0,2}+\dot{m}_\mathrm{infl}}{m_\mathrm{z}} & 0 \\[2mm] 0 & 0 & 0 & -\frac{u_{0,2}+\dot{m}_\mathrm{infl}}{m_\mathrm{z}} \end{bmatrix} \boldsymbol{x}(t) \\[2mm]
& + \begin{bmatrix} C_\mathrm{z}^{-1} & C_\mathrm{z}^{-1}c_p(d_2(t)-x_{0,1}) & 0 & 0 & 0 & 0 \\ 0 & 0 & 0 & 0 & 0 & 0 \\ 0 & m_\mathrm{z}^{-1}(d_3(t)-x_{0,3}) & 0 & 0 & 0 & 0 \\ 0 & m_\mathrm{z}^{-1}(d_4(t)-x_{0,4}) & 0 & 0 & 0 & 0 \end{bmatrix} \boldsymbol{u}(t) + \boldsymbol{f}_0(\boldsymbol{d}(t)) \tag{4.47a}
\end{aligned}
$$

$$
\begin{aligned}
\boldsymbol{y}(t) \;=\;\; & \boldsymbol{C}(\boldsymbol{d}(t),t)\boldsymbol{x}(t)+\boldsymbol{D}\boldsymbol{u}(t)+\overbrace{\mathbf{PIV}(\boldsymbol{x}_0,\boldsymbol{u}_0,\boldsymbol{d}(t),t)-\boldsymbol{C}(\boldsymbol{d}(t),t)\boldsymbol{x}_0-\boldsymbol{D}\boldsymbol{u}_0}^{\boldsymbol{g}_0(\boldsymbol{d}(t),t)} \\[2mm]
=\;\; & \begin{bmatrix} \left(\boldsymbol{\beta}_{\boldsymbol{x},1}+\frac{\partial\Delta\nu_1}{\partial\boldsymbol{x}}\Big|_{\boldsymbol{x}_0,\boldsymbol{u}_0}\right)^{\mathrm{T}} \\ \vdots \\ \left(\boldsymbol{\beta}_{\boldsymbol{x},N_{\mathrm{occ}}}+\frac{\partial\Delta\nu_{N_{\mathrm{occ}}}}{\partial\boldsymbol{x}}\Big|_{\boldsymbol{x}_0,\boldsymbol{u}_0}\right)^{\mathrm{T}} \end{bmatrix}\boldsymbol{x}(t)+\begin{bmatrix} \boldsymbol{\beta}_{\boldsymbol{u},1}^{\mathrm{T}} \\ \vdots \\ \boldsymbol{\beta}_{\boldsymbol{u},N_{\mathrm{occ}}}^{\mathrm{T}} \end{bmatrix}\boldsymbol{u}(t)+\boldsymbol{g}_0(\boldsymbol{d}(t),t)
\end{aligned}
$$

$$(4.47\text{b})$$

with the initial conditions $\boldsymbol{x}(t_0)=\boldsymbol{x}_{\mathrm{init}}$ and presumed validity of the linearization on the time interval $t\in[t_0,t_f]$. Note that all system matrices and drift terms except for $\boldsymbol{A}$ and $\boldsymbol{D}$ depend on time via the disturbance vector $\boldsymbol{d}(t)$ or in case of the comfort output $\boldsymbol{y}$ incorporate an explicit dependency on t. For better readability in the following, the arguments are only shown when it directly influences the derivations.

The computation of $\boldsymbol{C}$ requires the gradient of (4.31) which is a combination of the linear term depending on x_1 and $u_{\{3,4,5,6\}}$ and the GP model for the time-variant vote deviation that is a function of x_1, x_3 and d_4. Collecting the model inputs in $\boldsymbol{z}=\begin{bmatrix} RH(x_1,x_3) & d_4 & t \end{bmatrix}$ leads to the partial derivative of the GP prediction with respect to the states x_n

$$
\begin{aligned}
\frac{\partial\Delta\nu_j(\boldsymbol{z})}{\partial x_n} &= \frac{\partial}{\partial x_n}\boldsymbol{\kappa}_j^{\mathrm{T}}(\boldsymbol{z})\boldsymbol{\gamma}_j = \frac{\partial}{\partial x_n}\left(\sigma_{f,j}e^{-\frac{R(\boldsymbol{z})}{\sigma_{l,j}}}\right)^{\mathrm{T}}\boldsymbol{\gamma}_j \\[2mm]
&= -\frac{1}{\sigma_{l,j}}\left(\boldsymbol{\kappa}_j(\boldsymbol{z})\circ\frac{\partial\boldsymbol{R}(\boldsymbol{z})}{\partial x_n}\right)^{\mathrm{T}}\boldsymbol{\gamma}_j, \quad n=1,3
\end{aligned}
$$

$$(4.48)$$

where $\boldsymbol{R}(\boldsymbol{z})=\sqrt{\left(\boldsymbol{Z}_j-\boldsymbol{z}\right)^{\mathrm{T}}\left(\boldsymbol{Z}_j-\boldsymbol{z}\right)}$ contains the Euclidean distances between the observation data $\boldsymbol{Z}_j=\begin{bmatrix} RH(x_{1,ij},x_{3,ij}) & d_{4,ij} & t_{ij} \end{bmatrix}_{i=1,\ldots,m_j}$ of user j and the current condition $\boldsymbol{z}$. The comfort model only uses the states x_1 and x_3 such that the matrix $\boldsymbol{C}$ has a rank of 2. The model's dependency on $\boldsymbol{u}$ is inherently linear so that the feedthrough $\boldsymbol{D}$ is a constant matrix containing the user-specific coefficients for the fan level.

The linearized system (4.47) is discretized to apply discrete-time linear MPC concepts. The control input as well as the disturbances are assumed to be piecewise constant so that the discrete representation of the differential equations results in

$$
\boldsymbol{x}[k+1]=\underbrace{e^{\boldsymbol{A}t_{\mathrm{s}}}}_{\bar{\boldsymbol{A}}}\boldsymbol{x}[k]+\underbrace{\boldsymbol{A}^{-1}\left(e^{\boldsymbol{A}t_{\mathrm{s}}}-\boldsymbol{I}\right)\boldsymbol{B}[k]}_{\bar{\boldsymbol{B}}[k]}\boldsymbol{u}[k]+\underbrace{\boldsymbol{A}^{-1}\left(e^{\boldsymbol{A}t_{\mathrm{s}}}-\boldsymbol{I}\right)\boldsymbol{f}_0[k]}_{\bar{\boldsymbol{f}}_0[k]} \qquad (4.49\text{a})
$$

$$
\boldsymbol{y}[k+1]=\boldsymbol{C}[k+1]\boldsymbol{x}[k+1]+\boldsymbol{D}\boldsymbol{u}[k+1]+\boldsymbol{g}_0[k+1] \qquad (4.49\text{b})
$$

where $k = t_0 + k t_\mathrm{s}$ and t_s denotes the sampling time. The discrete system equivalent (4.49) is only well defined if the inverse of $\boldsymbol{A}$ exists, hence $\det(\boldsymbol{A}) \neq 0$. For the cases $u_{0,2} \in \left\{ -\dot{m}_\mathrm{infl}, -\frac{1+c_p \dot{m}_\mathrm{infl}(R_\mathrm{int}+R_\mathrm{ext})}{c_p(R_\mathrm{int}+R_\mathrm{ext})} \right\}$, two of the four eigenvalues of $\boldsymbol{A}$ become zero. Both cases can be neglected since only positive values for the primary mass flow are allowed so that the discretization is always well defined.

Using (4.49), the system behavior can be predicted for a given number of N_p time steps:

$$\boldsymbol{x}[k+1] = \bar{\boldsymbol{A}}\boldsymbol{x}[k] + \bar{\boldsymbol{B}}[k]\boldsymbol{u}[k] + \bar{\boldsymbol{f}}_0[k]$$
$$\boldsymbol{x}[k+2] = \bar{\boldsymbol{A}}\left(\bar{\boldsymbol{A}}\boldsymbol{x}[k] + \bar{\boldsymbol{B}}[k]\boldsymbol{u}[k] + \bar{\boldsymbol{f}}_0[k]\right) + \bar{\boldsymbol{B}}[k+1]\boldsymbol{u}[k+1] + \bar{\boldsymbol{f}}_0[k+1]$$
$$\vdots$$
$$\boldsymbol{x}[k+N_\mathrm{p}] = \bar{\boldsymbol{A}}^{N_\mathrm{p}}\boldsymbol{x}[k] + \left[\bar{\boldsymbol{A}}^{N_\mathrm{p}-1}\bar{\boldsymbol{B}}[k] \quad \cdots \quad \bar{\boldsymbol{B}}[k+N_\mathrm{p}-1] \quad \boldsymbol{0}\right]\mathbf{u} \qquad (4.50)$$
$$+ \left[\bar{\boldsymbol{A}}^{N_\mathrm{p}-1} \quad \cdots \quad \boldsymbol{I} \quad \boldsymbol{0}\right]\mathbf{f}_0$$

where

$$\mathbf{f}_0 = \left[\bar{\boldsymbol{f}}_0[k] \quad \cdots \quad \bar{\boldsymbol{f}}_0[k+N_\mathrm{p}]\right]^\mathrm{T}, \qquad \mathbf{g}_0 = \left[\boldsymbol{g}_0[k] \quad \cdots \quad \boldsymbol{g}_0[k+N_\mathrm{p}]\right]^\mathrm{T}.$$

Consequently, the predicted system output (linearized comfort) is given by

$$\boldsymbol{y}[k] = \boldsymbol{C}[k]\boldsymbol{x}[k] + \boldsymbol{D}\boldsymbol{u}[k]$$
$$\boldsymbol{y}[k+1] = \boldsymbol{C}[k+1]\left(\bar{\boldsymbol{A}}\boldsymbol{x}[k] + \bar{\boldsymbol{B}}[k]\boldsymbol{u}[k] + \bar{\boldsymbol{f}}_0[k]\right) + \boldsymbol{D}\boldsymbol{u}[k+1] + \boldsymbol{g}_0[k+1]$$
$$\vdots \qquad\qquad\qquad\qquad\qquad (4.51)$$
$$\boldsymbol{y}[k+N_\mathrm{p}] = \boldsymbol{C}[k+N_\mathrm{p}]\bar{\boldsymbol{A}}^{N_\mathrm{p}}\boldsymbol{x}[k]$$
$$+ \underbrace{\left[\boldsymbol{C}[k+N_\mathrm{p}]\bar{\boldsymbol{A}}^{N_\mathrm{p}-1}\bar{\boldsymbol{B}}[k] \quad \cdots \quad \boldsymbol{C}[k+N_\mathrm{p}]\bar{\boldsymbol{B}}[k+N_\mathrm{p}-1] \quad \boldsymbol{D}\right]}_{\boldsymbol{S}_y}\mathbf{u}$$
$$+ \left[\boldsymbol{C}[k+N_\mathrm{p}]\bar{\boldsymbol{A}}^{N_\mathrm{p}-1} \quad \cdots \quad \boldsymbol{C}[k+N_\mathrm{p}] \quad \boldsymbol{0}\right]\mathbf{f}_0 + \boldsymbol{g}_0[k+N_\mathrm{p}]$$

Output controllability of (4.51) is ensured when

$$\operatorname{rank}\boldsymbol{S}_y = \dim\boldsymbol{y}.$$

A minimum rank is always defined by the feedthrough matrix which contains the direct impact of the fan levels:

$$\operatorname{rank}\boldsymbol{D} = \dim\boldsymbol{l}_\mathrm{fan} = \dim\boldsymbol{y} - 4. \qquad (4.52)$$

Hence, the remaining components of $\boldsymbol{S}_y$ must provide $N_{\text{occ}} - 4$ additional independent rows or columns. This criterion can be transferred to the nonlinear system to show local output controllability.

The vector containing all vote predictions for the current MPC iteration results in

$$\mathbf{y} = \begin{bmatrix} \boldsymbol{y}[k] & \cdots & \boldsymbol{y}[k+N_{\text{p}}] \end{bmatrix}^{\text{T}} = \boldsymbol{F}\boldsymbol{x}[k] + \boldsymbol{H}\mathbf{u} + \boldsymbol{G}\mathbf{f}_0 + \mathbf{g}_0 \tag{4.53}$$

where

$$\boldsymbol{F} = \begin{bmatrix} \boldsymbol{C}[k] \\ \boldsymbol{C}[k+1]\bar{\boldsymbol{A}} \\ \boldsymbol{C}[k+2]\bar{\boldsymbol{A}}^2 \\ \vdots \\ \boldsymbol{C}[k+N_{\text{p}}]\bar{\boldsymbol{A}}^{N_{\text{p}}} \end{bmatrix}, \quad \boldsymbol{G} = \begin{bmatrix} \boldsymbol{0} & & \cdots & & \\ \boldsymbol{C}[k+1] & \boldsymbol{0} & \cdots & & \\ \boldsymbol{C}[k+2]\bar{\boldsymbol{A}} & \boldsymbol{C}[k+2] & \boldsymbol{0} & \cdots & \\ \vdots & \vdots & & \ddots & \\ \boldsymbol{C}[k+N_{\text{p}}]\bar{\boldsymbol{A}}^{N_{\text{p}}-1} & \boldsymbol{C}[k+N_{\text{p}}]\bar{\boldsymbol{A}}^{N_{\text{p}}-2} & \cdots & \boldsymbol{C}[k+N_{\text{p}}] & \boldsymbol{0} \end{bmatrix},$$

$$\boldsymbol{H} = \begin{bmatrix} \boldsymbol{D} & \boldsymbol{0} & \cdots & & \\ \boldsymbol{C}[k+1]\bar{\boldsymbol{B}}[k] & \boldsymbol{D} & \boldsymbol{0} & \cdots & \\ \boldsymbol{C}[k+2]\bar{\boldsymbol{A}}\bar{\boldsymbol{B}}[k] & \boldsymbol{C}[k+2]\bar{\boldsymbol{B}}[k+1] & \boldsymbol{D} & \boldsymbol{0} & \cdots \\ \vdots & \vdots & & \ddots & \\ \boldsymbol{C}[k+N_{\text{p}}]\bar{\boldsymbol{A}}^{N_{\text{p}}-1}\bar{\boldsymbol{B}}[k] & \boldsymbol{C}[k+N_{\text{p}}]\bar{\boldsymbol{A}}^{N_{\text{p}}-2}\bar{\boldsymbol{B}}[k+1] & \cdots & \boldsymbol{C}[k+N_{\text{p}}]\bar{\boldsymbol{B}}[k+N_{\text{p}}-1] & \boldsymbol{D} \end{bmatrix}$$

The LMPC cost for optimizing thermal comfort equals (4.32) whereas the integral is replaced by a summation due to the discretization. The prediction vector $\mathbf{y}$ containing the estimated comfort states should be forced to zero for achieving comfortable conditions. The discrete cost is consequently given by

$$J_{\text{discrete}} = \sum_{k=1}^{N_{\text{p}}} \frac{1}{2}\mathbf{PIV}^{\text{T}}[k]\boldsymbol{Q}\mathbf{PIV}[k] + \frac{1}{2}\boldsymbol{u}^{\text{T}}[k]\boldsymbol{R}\boldsymbol{u}[k]$$

$$= \frac{1}{2}\mathbf{y}^{\text{T}} \underbrace{\begin{bmatrix} \boldsymbol{Q} & & \\ & \ddots & \\ & & \boldsymbol{Q} \end{bmatrix}}_{\tilde{\boldsymbol{Q}}} \mathbf{y} + \frac{1}{2}\mathbf{u}^{\text{T}} \underbrace{\begin{bmatrix} \boldsymbol{R} & & \\ & \ddots & \\ & & \boldsymbol{R} \end{bmatrix}}_{\tilde{\boldsymbol{R}}} \mathbf{u} \tag{4.54}$$

where $\boldsymbol{R}$ corresponds to (4.32) and allows to introduce a penalty on the manipulated inputs for defining a compromise between thermal comfort and energy consumption. The comfort weighting matrix $\boldsymbol{Q}$ is the identity matrix if all comfort models are included with equal importance for the optimization. When occupancy is considered, different weights on the diagonal of $\boldsymbol{Q} \succeq 0$ can be used to exclude absent users. Using (4.53) and omitting the terms that are independent of the control input leads to

$$J_{\text{discrete}} = \frac{1}{2}\mathbf{u}^{\text{T}}\left(\boldsymbol{H}^{\text{T}}\tilde{\boldsymbol{Q}}\boldsymbol{H} + \tilde{\boldsymbol{R}}\right)\mathbf{u} + (\boldsymbol{F}\boldsymbol{x}[k] + \boldsymbol{G}\mathbf{f}_0 + \mathbf{g}_0)^{\text{T}}\tilde{\boldsymbol{Q}}\boldsymbol{H}\mathbf{u}. \tag{4.55}$$

If $\boldsymbol{H}^{\mathrm{T}}\tilde{\boldsymbol{Q}}\boldsymbol{H} + \tilde{\boldsymbol{R}} \succ 0$, this objective can be solved under consideration of the input and state constraints using standard MIQP solvers. By definition, the positive semi-definiteness of $\boldsymbol{H}^{\mathrm{T}}\tilde{\boldsymbol{Q}}\boldsymbol{H}$ is already ensured. However, a unique solution can only be found if $\boldsymbol{H}$ has full rank and $\boldsymbol{Q}$ does not decouple inputs completely due to the exclusion of users (e. g. all users mapped to one specific fan). In the event of any of the described scenarios, the input penalty matrix $\boldsymbol{R}$ is used to guarantee a positive definite optimization matrix, thus uniqueness of the solution.

Linearization of Constraints

The linear constraints for the cooling power (4.34) and the primary air flow (4.39) can be directly included in the LMPC problem description. This also allows for a neglect of the CO_2 concentration X_{CO_2} and thus reduces the problem dimension by a quarter. The nonlinear constraint to prevent condensation at the FCU (4.45), on the other hand, must be linearized. For this purpose, a conservative estimate for the maximum cooling power is derived. To ensure a relative humidity lower than $100\,\%$ at the FCU, the supply air temperature T_{sup} must be higher than the dew point temperature T_{dewpoint}. Therefore, the nonlinear relation between RH_{air}, T_{air} and X_{H_2O} is replaced by a linear estimate for T_{dewpoint} as a function of X_{H_2O}. Using the Magnus equation for the saturation vapor pressure according to Table 4.1 [97] and (4.7) leads to the relation shown in Figure 4.12. A linear and a nonlinear approximation are derived to provide a simplified representation. The actually occurring supply temperatures are assumed to stay in a range between $5\,^{\circ}\mathrm{C} \leq T_{\mathrm{sup}} \leq 28\,^{\circ}\mathrm{C}$. Since only cooling operation is possible, the supply temperature cannot be higher than the return air temperature of the room and thus a feasible upper bound is chosen according to expected room conditions. The lower limit is rather motivated by the minimum achievable temperature of the fan coil unit. The nonlinear fit

$$T_{\mathrm{dewpoint}}^{\mathrm{nl}} = 48.13\sqrt[3]{X_{H_2O}} - 12.10\sqrt{X_{H_2O}} - 51.20 \tag{4.56}$$

provides a very accurate approximation for the considered temperature range. For the application of linear control concepts, a conservative estimation is derived where the expected supply temperature is assumed to stay in the region of $15\,^{\circ}\mathrm{C}$. Using the resulting linear relation

$$T_{\mathrm{dewpoint}}^{\mathrm{lin}} = 1.28 \cdot 10^3\, X_{H_2O} + 1.76 \tag{4.57}$$

as lower bound for the supply temperature always ensures that condensation is avoided.
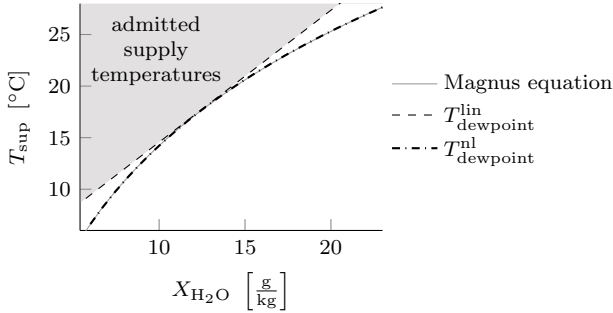
Figure 4.12: Approximation of the dew point temperature T_{dewpoint} in relation to the specific humidity $X_{\text{H}_2\text{O}}$.

Combining (4.42), (4.44) and (4.57) limits the cooling power as follows

$$
T_{\text{dewpoint}}^{\text{lin}} = 1.28 \cdot 10^3 \, X_{\text{H}_2\text{O}} + 1.76 \leq \frac{\dot{m}_{\text{pr}}^{wc}(d_2 - x_1) + x_1 \dot{m}_{\text{sup,max}} + u_1/c_p}{\dot{m}_{\text{sup,max}}}
$$

$$
\Rightarrow \quad \frac{u_1}{c_p} \geq \dot{m}_{\text{sup,max}} \left(1.28 \cdot 10^3 \left(\frac{\dot{m}_{\text{pr}}^{wc}(d_3 - x_3)}{\dot{m}_{\text{sup,max}}} + x_3 \right) + 1.76 - x_1 \right) - \dot{m}_{\text{pr}}^{wc}(d_2 - x_1)
$$

$$
u_1 \geq c_p \left(\dot{m}_{\text{pr}}^{wc} \underbrace{(x_1 - d_2 - 1.28 \cdot 10^3 \, (x_3 - d_3))}_{\omega} \right.
$$

$$
\left. + \dot{m}_{\text{sup,max}}(1.28 \cdot 10^3 \, x_3 + 1.76 - x_1) \right) = u_{1,\text{min}}^{\text{noCond}} \left(\boldsymbol{x}, \boldsymbol{d}, \dot{m}_{\text{pr}}^{wc} \right).
$$
(4.58)

where $\dot{m}_{\text{pr}}^{wc}$ describes the worst case scenario for the unknown primary mass flow u_2. Since the dew point is always defined by temperature and humidity, the worst case depends on the multiplication factor ω:

$$
\dot{m}_{\text{pr}}^{wc} = \begin{cases} 0, & \omega < 0 \\ \text{arbitrary}, & \omega = 0 \, . \\ \dot{m}_{\text{pr,max}}, & \omega > 0 \end{cases}
$$

The constraint (4.58) still depends on the state vector $\boldsymbol{x}$ and the disturbance vector $\boldsymbol{d}$. The unknown future states within the prediction horizon are approximated by the operating point $\boldsymbol{x}_0$ so that the linear estimate for the time-dependent lower limit of the cooling power results in

$$
u_{1,\text{min}} = \max \left(-\dot{Q}_{\text{FCU,max}}, u_{1,\text{min}}^{\text{noCond}} \left(\boldsymbol{x}_0, \boldsymbol{d}(t), \dot{m}_{\text{pr}}^{wc} \right) \right).
$$
(4.59)

In the following the nonlinear and the linear MPC approach are evaluated to analyze and compare the corresponding control performances. Furthermore, the weighting matrix $\boldsymbol{Q}$ of (4.32) and (4.55) is the identity matrix to include all users equally. As mentioned above, the input weighting matrix $\boldsymbol{R}$ is selected to ensure a unique solution. The uniqueness of the fan levels $u_{\{3,4,5,6\}}$ is always assured by a full rank of the fan-related part of $\boldsymbol{D}$. This is guaranteed if all fans are mapped to an active comfort model (assuming the corresponding fan coefficient $\beta_{j,l_{\text{fan}}} \neq 0$ which is ensured during the identification process). Similarly to Section 4.2.4, unoccupied fans are set to 0 and excluded from the OCP. A unique solution for $u_{\{1,2\}}$, on the other hand, is not generally guaranteed. The comfort output is coupled to the system inputs $u_{\{1,2\}}$ solely through the room conditions, namely temperature and humidity. The cooling power u_1 has a direct impact on the room temperature. The primary air flow u_2 affects the room conditions in multiple ways. The temperature is changed by the corresponding enthalpy flow depending on $d_2 = T_{\text{pr}}$ and $d_3 = X_{\text{H}_2\text{O,pr}}$. The humidity $X_{\text{H}_2\text{O}}$ can only be controlled within a certain range related to $X_{\text{H}_2\text{O,pr}}$ and the occupants' humidity generation. In the case that the water content $X_{\text{H}_2\text{O}}$ approaches the primary air water content $X_{\text{H}_2\text{O,pr}}$, controllability for humidity is lost. The thermally decoupled humidity state cannot be changed via $u_2 = \dot{m}_{\text{pr}}$ which is also demonstrated by the resulting zero rows in $\boldsymbol{B}$ of (4.47a). Consequently, as long as no input constraints are active, the desired room temperature can be achieved by multiple combinations of the cooling power u_1 and the enthalpy flow related to u_2. To ensure uniqueness of the optimal solution, a meaningful penalty for u_1 and/or u_2 must be introduced. Generally, arbitrary weights can be used to either penalize the required cooling power u_1 or the primary air flow u_2. Hereafter, only u_2 is penalized motivated by the goal of reducing the required amount of fresh air because dehumidification of the outside air is one of the most energy consuming factors of the air conditioning task.

4.3.5 Impact of Sampling Time on Comfort-Optimizing Control

In a first analysis the nonlinear offline OCP is considered to serve as benchmark for the control performance, and to define a suitable sampling time t_{s} for the control parametrization. A large sampling time limits the reaction time towards disturbances such that variations (e. g. immediate changes in occupancy) cannot be compensated within one sampling step. Since the AC system is switched of during the night, the benchmark solution is computed as optimum of (4.33) for the operating hours over an entire day. It is assumed that all disturbances are perfectly known at the beginning of each control interval $\boldsymbol{u}[k]$ for the whole prediction horizon from 7 am to 7:30 pm. The associated OCP is solved for three different sampling intervals $t_{\text{s}} = \{5\,\text{min}, 15\,\text{min}, 30\,\text{min}\}$ and the simulation results are depicted in Figure 4.13. As already identified in Chapter 4.2, the optimal temperature set-point varies approximately between $26\,°\text{C}$ and $28\,°\text{C}$ whereas office 2 prefers higher temperatures than office 1. The smaller the sampling time t_{s} the higher is the variability of the input

Table 4.5: Summary of control performance depending on t_s. The two values refer to the result for office 1 and 2 respectively averaged over the operating hours of the two considered days according to Section 4.2.2.

t_s [min]	$\overline{\mathrm{PIV}}_{\mathrm{ave}}$	$\dfrac{\int_{I_{\mathrm{op}}} \sum_{j=1}^{N_{\mathrm{occ}}} \mathrm{PIV}_j \, dt}{t_{\mathrm{op}}}$	$\dfrac{\int_{I_{\mathrm{op}}} |\dot{Q}_{\mathrm{FCU}}| \, dt}{2}$	$\dfrac{\int_{I_{\mathrm{op}}} X_{\mathrm{CO_2}} (>800\,\mathrm{ppm}) \, dt}{t_{\mathrm{op}}}$
5	0.636 | 0.562	-0.31 | -0.65	1.76 | 0.47 $\frac{\mathrm{kWh}}{\mathrm{day}}$	0.1 | 1.2 ppm
15	0.644 | 0.565	-0.27 | -0.65	1.73 | 0.50 $\frac{\mathrm{kWh}}{\mathrm{day}}$	14.1 | 13.6 ppm
30	0.667 | 0.572	-0.20 | -0.65	1.58 | 0.44 $\frac{\mathrm{kWh}}{\mathrm{day}}$	30.2 | 28.5 ppm

$\boldsymbol{u}$ and a faster reaction to disturbances is possible. Since the disturbance is only provided at the beginning of a control interval and then assumed to be constant, the unconsidered disturbance variations (in particular in N_{occ}) lead to unwanted temperature changes within the time interval. This is accompanied by a greater discomfort for increasing sampling periods.

Furthermore, it can be observed that the primary mass flow $\dot{m}_{\mathrm{pr}}$ always tries to track the occupancy profile to maintain an acceptable CO_2 level while minimizing the demand for fresh air. However, due to occupancy changes during the control interval, the precalculated boundaries according to (4.39) cannot ensure full compliance with the upper limit of 800 ppm. Table 4.5 lists the average comfort state, cooling demands and violations of the upper CO_2 bound in relation to the sampling period t_s. The considered time period $t \in I_{\mathrm{op}}$ denotes the two exemplary days as specified in Section 4.2.2 where only the operation hours from 7 am to 7:30 pm are taken into account. The discomfort due to unconsidered disturbance changes results in a worsened average comfort level $\overline{\mathrm{PIV}}_{\mathrm{ave}}$ for greater sampling periods. The same tendency is visible for the CO_2 level violation where frequent updates of the current occupancy situation allow to balance the CO_2 concentration more adequately. The required cooling power is very similar for all sampling intervals but more numerous changes can be observed for smaller t_s in Figure 4.13 to account for varying disturbance effects. In contrast, longer control intervals result in a smoothed command for the cooling power $\dot{Q}_{\mathrm{FCU}}$.

The negativity of the sum of signed votes

$$\frac{1}{t_{\mathrm{op}}} \int_{I_{\mathrm{op}}} \sum_{j=1}^{N_{\mathrm{occ}}} \mathrm{PIV}_j(t) \, dt$$

indicates that the system restriction $\dot{Q}_{\mathrm{FCU}} \leq 0$ is partly active. Optimal compliance with the comfort requirements would require additional heating because the minimal
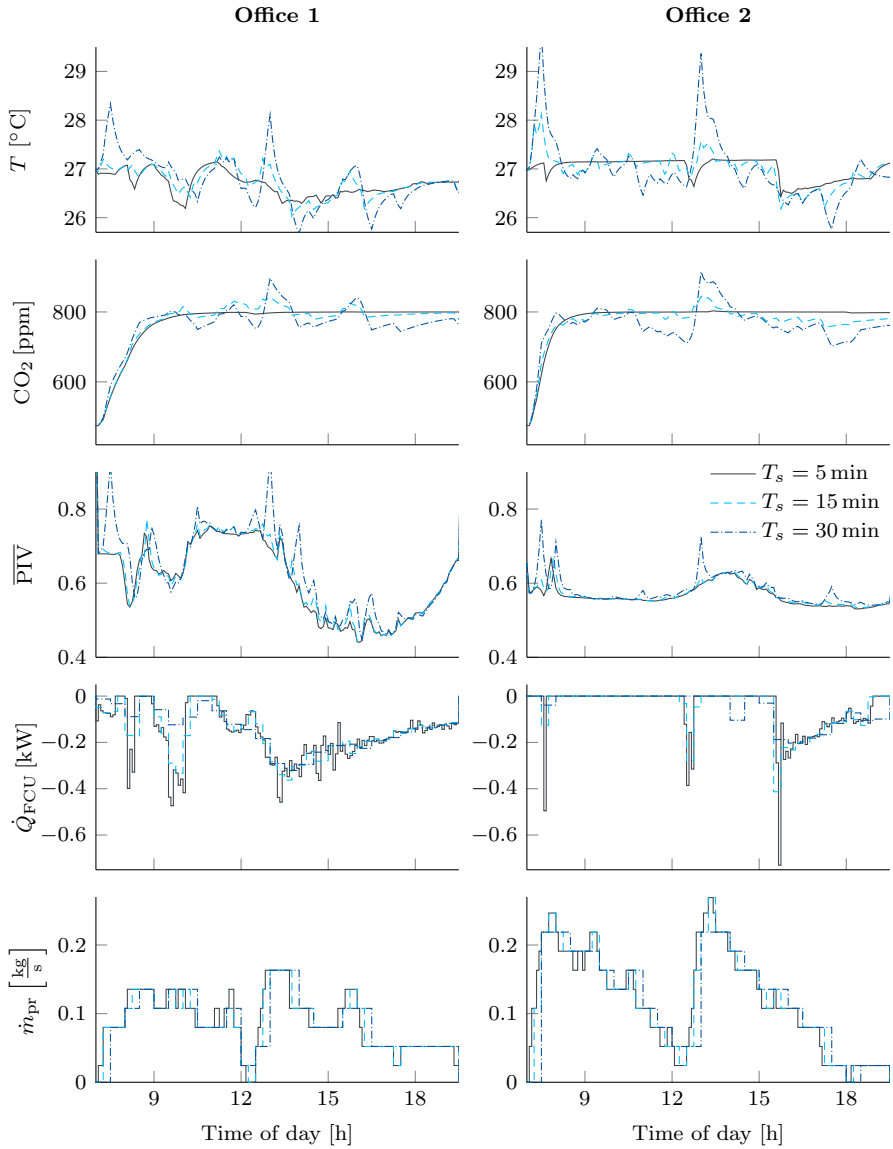
Figure 4.13: Impact of sampling time t_s on the achievable control performance based on the first day as used in Section 4.2.2.

primary air flow for maintaining acceptable CO_2 levels already provides higher cooling than needed. This allows for raising the primary air temperature which opens up additional energy saving potential on the building level. Since the comfort preferences of office 2 relate to even higher desired temperatures, the FCU is only activated in the morning when occupancy is increasing rapidly. Otherwise, the fresh air supply leads to more than sufficient cooling and the corresponding temperature trajectory is a trade-off between the thermal preferences and requirements on the CO_2 concentration.

Although only the solution for the nonlinear OCP (4.33) is considered in Figure 4.13 and Table 4.5, the sampling time t_s also affects the quality of the linearization (4.47) as well as the discretization (4.49) what influences the later considered LMPC implementation. Since the system is always linearized around the current condition (beginning of the next control interval), the validity of the linearization must be maintained over the whole sampling period so that a smaller sampling time leads to a better match between the linearization and the original model. Additionally, the discretization is only valid for piecewise constant control and disturbance inputs which is only ensured for the inputs $\boldsymbol{u}$. Hence, the neglected disturbance variations lead to discretization errors. Nevertheless, the linearization and discretization of the bilinear system dynamics is valid in a large region around the operating point such that the t_s-related disturbance effects exceed the linearization and discretization errors. Only the nonlinear comfort output is more sensitive to t_s. The linearized GP model deviates significantly with increasing distance to the operating point. This linearization error can even cause an oscillating effect of the optimal conditions when the gradient of a comfort model is very steep for the current conditions. As a consequence, the linearized model over- or underestimates the future development of the user comfort and results in an exaggerated control command for u_1. In the next step, this command must be balanced by a contrary control input. For unfortunate boundary conditions, infeasible steps of the control trajectory are the result. To curb this effect, a rate penalty for the cooling power u_1 is added to (4.55)

$$J_{\text{discrete}}^{\text{LMPC}} = J_{\text{discrete}} + \Delta\mathbf{u}^{\text{T}} \boldsymbol{R}_\Delta \Delta\mathbf{u} \tag{4.60}$$

where

$$\Delta\mathbf{u} = \begin{bmatrix} \Delta\boldsymbol{u}[k] & \cdots & \Delta\boldsymbol{u}[k+N_p-1] \end{bmatrix}^{\text{T}}$$
$$= \begin{bmatrix} \boldsymbol{u}[k+1] - \boldsymbol{u}[k] & \cdots & \boldsymbol{u}[k+N_p] - \boldsymbol{u}[k+N_p-1] \end{bmatrix}^{\text{T}}$$

and $\boldsymbol{R}_\Delta$ is a zero matrix with weighting coefficients for Δu_1 on the diagonal. A weighting factor of $2 \cdot 10^{-4}$ is able to suppress the oscillations in the optimal control trajectory while ensuring satisfying comfort levels.

In summary, the final choice of t_s is a trade-off between the disturbance rejection ability and the desired computational effort. For the following analysis t_s is set to 5 min because computation time is not a limiting factor.

4.3.6 Influence of the Prediction Horizon on MPC Performance

Apart from the sampling time, the prediction horizon t_p has a direct impact on the closed-loop performance of the MPC approaches. So far, the optimal control trajectory was the solution of the open-loop control problem computed based on known disturbance inputs and optimized over the entire day. Usually, exact disturbance predictions are not available and the moving horizon of the MPC implementation (see Figure 4.11) changes the open-loop OCP to a closed-loop control scheme that adjusts the control input based on measurements of the actual current state. Without advanced prediction algorithms, a steady-state disturbance model $\dot{\boldsymbol{d}} = \boldsymbol{0}$ is the best guess for the next prediction horizon. The sampling time is already selected to ensure a reasonable impact of the disturbance prediction errors. A meaningful length of the prediction horizon $t_\mathrm{p} = N_\mathrm{p} \cdot t_\mathrm{s}$, on the other hand, is related to the system dynamics. Additionally, it must be long enough to allow for the consideration of the effect of state and input constraints. For example, an early counteraction by the control may be beneficial when the unconstrained optimum cannot be realized by the real system.

At first the NMPC approach is analyzed for three different prediction horizons: $N_\mathrm{p} = \{1, 5, 10\}$. In Figure 4.14, the corresponding simulation results are compared to the benchmark solution of Section 4.3.5. The resulting temperature trajectories in Figure 4.14a are relatively similar for all prediction horizons but expose multiple deviations mainly during the morning and the afternoon. These deviations affect the average comfort level $\overline{\mathrm{PIV}}$ negatively as emphasized in Figure 4.14b. Optimizing the thermal comfort over a short prediction horizon leads to a temperature reduction around 9 am. The corresponding actual comfort cost is therefore even lower for $N_\mathrm{p} \in \{1, 5\}$. However, the need for warmer conditions shortly after 9 am cannot be met by the system such that the successive comfort cost increases. A greater horizon avoids premature cooling and leads to an overall improvement of the occupant's comfort. A similar effect is also visible around 8 am where $N_\mathrm{p} = 1$ overestimates the cooling demand but $N_\mathrm{p} \geq 5$ reduces the cooling earlier to meet the future requirements. Only a prediction horizon of $t_\mathrm{p} = 10 \cdot t_\mathrm{p} = 50\,\mathrm{min}$ is able to account for this effect in the afternoon and thus leads to a similar performance as the benchmark solution.

A more detailed analysis of the influence of the prediction horizon is given in Figure 4.15. It compares the overall impact on the comfort level and the resulting energy consumption of the FCU for the two exemplary days. For better interpretability, the results are evaluated for the VAC as well as the HVAC system according to (4.34) and (4.35) respectively. Since the results of Table 4.5 already indicated that the upper boundary for u_1 is repeatedly active, a comparison with the unconstrained case gives further insight for the selection of the prediction horizon. Regarding the comfort levels $\overline{\mathrm{PIV}}_\mathrm{ave}$ for both systems shows that the HVAC system improves the control performance because the overcooling effect of the primary air flow can be compensated. This is also highlighted by the sum of votes, shown in the second column of Figure 4.15. The higher values for the HVAC system demonstrate that the
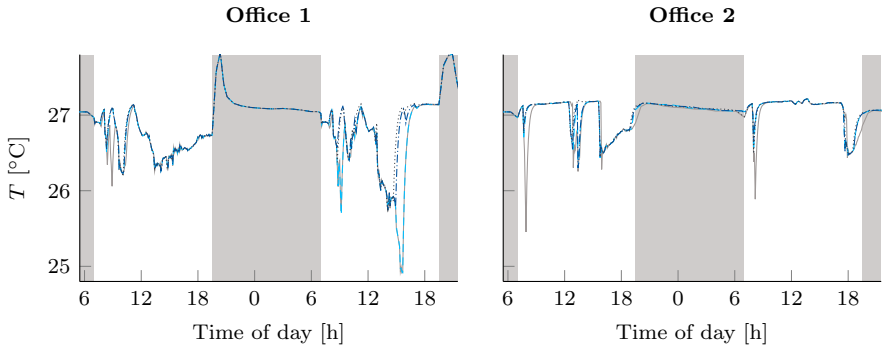
(a) Comparison of the resulting temperature trajectories for the two exemplary days of Section 4.2.2.
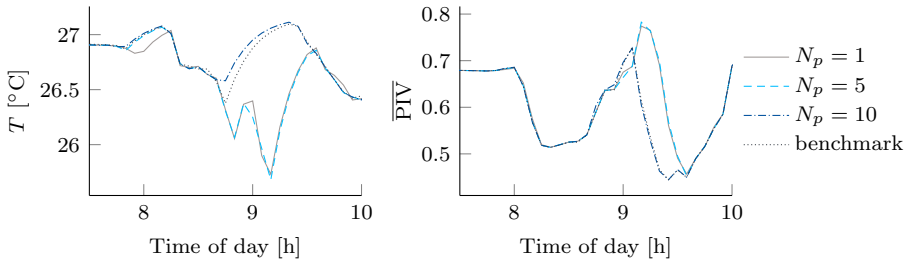
(b) Visualization of the differences during the morning of the second day, exemplary shown for office 1.

Figure 4.14: Control performance for different prediction horizons $t_\mathrm{p} = N_\mathrm{p} \cdot 5\,\mathrm{min}$.

desired conditions cannot be fully achieved by the VAC system. Another indicator is the higher energy demand of the HVAC system which incorporates the heating power to balance the cooling effect from the fresh air supply.

The same analysis is conducted for the LMPC approach. The corresponding control performance is also depicted in Figure 4.15. Compared to the nonlinear system, the linear approach does not expose a great improvement for an increasing prediction horizon. The propagated linearization error counterbalances the benefit of the gained knowledge about future system states. For office 1, $t_\mathrm{p} \geq 15\,\mathrm{min}$ is already a suitable choice. The linear approach for office 2 is even completely insensitive to the horizon such that any choice of N_p is appropriate.

The final decision regarding an appropriate prediction horizon requires a compromise between different properties. As observed in Figure 4.14, only predicting one step
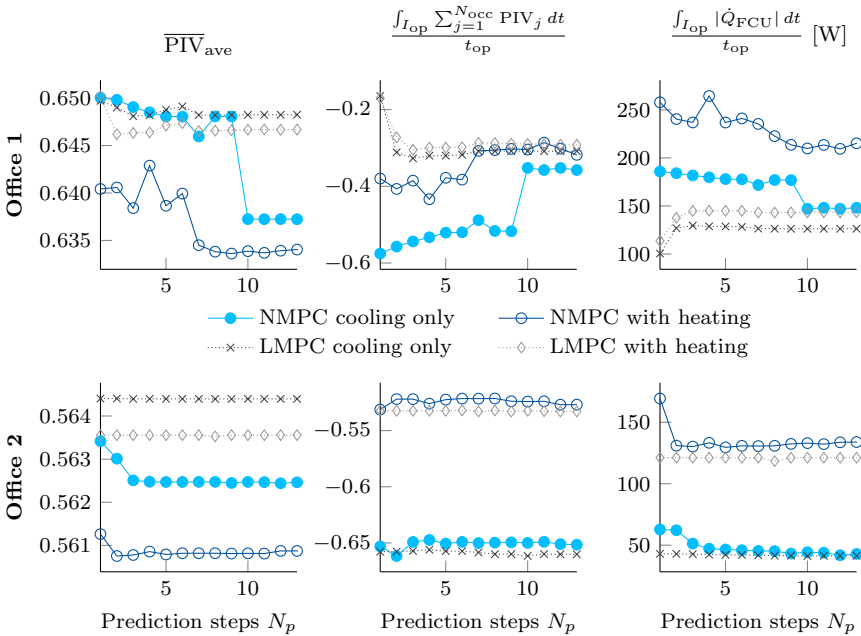
Figure 4.15: Impact of the prediction horizon N_{p} on the overall control performance for $t_{\mathrm{s}} = 5\,\mathrm{min}$.

ahead has the worst performance for (almost) all cases due to the missing knowledge of the future requirements and the relatively inert system behavior. The time constant of the office is defined by

$$\tau \approx \frac{C_{\mathrm{z}}}{c_p \left(u_2 + \dot{m}_{\mathrm{infl}}\right) + R_{\mathrm{int}}^{-1}}, \tag{4.61}$$

thus depends on the primary air flow. Considering the boundaries for u_2, the time constant lies between $10\,\mathrm{min}$ and $22\,\mathrm{min}$. Therefore, a prediction horizon of $5\,\mathrm{min}$ cannot account for future effects of the currently optimal control input and leads to a suboptimal comfort level. Increasing the prediction horizon enables the consideration of repercussions and improves the overall comfort so that the NMPC almost matches the benchmark solution. However, further extension of the prediction horizon does not lead to additional benefits due to the incorrect disturbance estimate. The actual optima depend on the underlying comfort models and the boundaries for the control input. The limitation to cooling rewards longer prediction horizons because of the possibility to reduce cooling earlier when higher target temperatures are desired in

the near future. Considering the nonlinear optimization, this suggests a prediction horizon greater than 50 min so that the effects of input constraints can be taken into account in advance. When the system is extended by a heating mode, the horizon can be reduced to 35 min.

Henceforth, N_p is set to 10 as it is the minimum prediction horizon for a good NMPC performance in office 1. All other cases would allow for fewer prediction steps but do not suffer from a greater horizon. Therefore, any prediction horizon ≥ 50 min can be justified which corresponds approximately to 2-5 times the response time of the system. The average energy demand, as shown in the last column of Figure 4.15, further supports this choice. The associated energy consumption mostly decreases with a larger horizon and approaches the global optimum according to Table 4.5. A shorter horizon augments the energy demand to balance former suboptimal control inputs.

4.3.7 Simulative Comparison of MPC and Feedforward Control Performance

Solving the MPC problems incorporates a higher computational effort than the static feedforward control approach discussed in Chapter 4.2. Furthermore, an integration in large buildings entails up-scaling effects which affect the applicability of the control method. Therefore, the following section investigates and compares the performance of the nonlinear and linear MPC method as well as the feedforward control approach to reveal the corresponding (dis-)advantages. Based on the results of Section 4.3.5 and 4.3.6, the sampling time is set to $t_s = 5$ min with a prediction horizon of $t_p = 50$ min $(N_p = 10)$.

To obtain comparability, the simulation of the adaptive feedforward control algorithm from Section 4.2.2 must be slightly modified. The simplification that the combined cooling demand $\dot{Q}_{AC}$ can be controlled directly does not account for occupancy-related adaptions of the primary air flow. In contrast to Section 4.1, the primary air flow is not assumed to be constant but uses the occupancy level to define the minimum air flow $\dot{m}_{pr,min}$ according to (4.38). This property is included to cause the same cooling effect and to comply with the CO_2 concentration limit. Accordingly, the PI controller specifies the cooling demand $\dot{Q}_{FCU}$. Therefore, the following results deviate from Section 4.2.2.

The optimized office conditions for all three approaches are shown in Figure 4.16. For better readability the benchmark is not shown since it almost matches the NMPC solution, as observed in Figure 4.14. Equivalently to the results from Section 4.3.6, the main differences between the NMPC and the LMPC approach are due to the large variations between 7 and 10 am. The main driver for these variations is the impact of the relative humidity as well as the different arrival times of the occupants which

lead to very distinct thermal expectations within this period. Both, the humidity and the daytime, affect the predicted vote via the GP model. Therefore, the comfort models exhibit dominant nonlinearities. This behavior explains the poor performance of the LMPC approach during this period where the linearization of the comfort output is only valid within a small region around the operating point. Therefore, the quickly changing room conditions and time-varying comfort requirements imply linearization errors that are propagated to the OCP. This results in an overestimated cooling demand in the early morning, similarly to the optimal trajectory based on the purely linear comfort model (4.1c) (see Figure 4.6). As a consequence, the overall comfort level is slightly worse compared to the NMPC.

The cascade of the comfort-optimizing feedforward controller and the PI room controller deviates significantly from the NMPC results. In particular, the coupling between the humidity and the temperature is not taken into account by the feedforward control algorithm. The algorithm only reacts to the measured humidity state so that the interaction between the new desired temperature and the relative humidity is not considered by the static optimization. Furthermore, the desired temperature cannot be reached immediately but depends on the PI control performance. Neglecting the coupling of comfort, temperature and humidity leads to visible deviations and a worsened comfort level.

Table 4.6 summarizes the control performance for all approaches. The already observed differences are reflected by the average comfort state $\overline{\mathrm{PIV}}_{\mathrm{ave}}$ which deteriorates with decreasing complexity of the applied algorithm. The small differences for office 2 can be traced back to two reasons. Firstly, office 1 is optimized based on six valid comfort models whereas office 2 defines a compromise for ten occupants. The higher number of user models smoothens out the individual differences and leads to a more even desired trajectory. Consequently, the corresponding control task can also be fulfilled by simpler control concepts. The second factor is the missing heating mode. The upper limit for the cooling power is mostly active, as emphasized by the very small energy demand for office 2, and thus limits the control options. That the feedforward control has a generally lower average cooling demand than the predictive approaches for the exemplary days is only due to the higher desired temperatures which are the result of the neglected coupling between T_{air} and RH_{air}. This energy saving is accompanied by a deteriorated comfort level.

Generally, the differences between the approaches are relatively small and the resulting comfort state $\overline{\mathrm{PIV}}_{\mathrm{ave}}$ is maximally worsened by 4.6 % compared to the benchmark for office 1. This corresponds to temperature deviations of approximately 0.5 K. Full compliance with these desired trajectories are challenging for real applications such that a test-bed application might even swallow the observed simulative advantages and disadvantages of the different control approaches. Therefore, a more detailed analysis of a real-world application must be performed to evaluate the different potentials where the impact of so far neglected disturbances can lead to more distinct results. On the
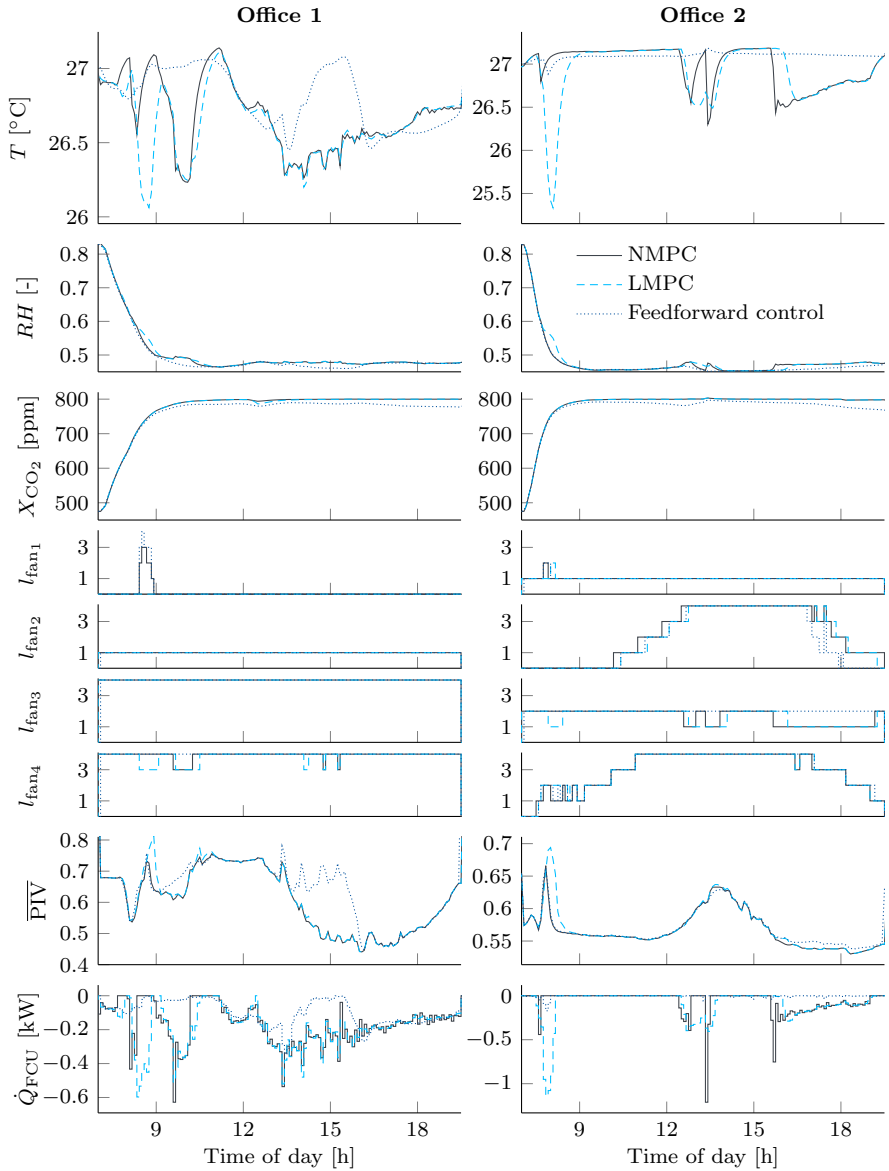
Figure 4.16: Comparison of the MPC and feedforward control results.

Table 4.6: Comparison of the linear MPC, nonlinear MPC and the adaptive feedforward control (office 1 | office 2).

Method	$\overline{\mathrm{PIV}}_{\mathrm{ave}}$	$\max\limits_{t}(\overline{\mathrm{PIV}}(t))$	$\frac{1}{2}\int_{I_{\mathrm{op}}}|\dot{Q}_{\mathrm{FCU}}|\,dt$
Benchmark	0.636 | 0.562	0.796 | 0.666	1.76 | 0.47 $\frac{\mathrm{kWh}}{\mathrm{day}}$
NMPC	0.638 | 0.563	0.825 | 0.666	1.84 | 0.56 $\frac{\mathrm{kWh}}{\mathrm{day}}$
LMPC	0.649 | 0.565	0.812 | 0.694	1.59 | 0.68 $\frac{\mathrm{kWh}}{\mathrm{day}}$
Feedforward control	0.667 | 0.565	0.803 | 0.663	0.98 | 0.11 $\frac{\mathrm{kWh}}{\mathrm{day}}$

other hand, building control concepts that incorporate more advanced system models open up a great potential for the investigated MPC concepts. While most of the available research focuses on energy savings, the presented methodologies can be easily included to other linear as well as non-linear model-based control approaches and hence enable a combined optimization of individual comfort as well as the overall energy demand. In summary, the previous analysis proved the applicability and feasibility of all comfort-driven control concepts at which the proposed personal comfort model leads to reasonable trajectories although the collected user data incorporate a very high uncertainty.

4.3.8 Potential Assessment for Thermal Sensation Based Seating

The achievable comfort level $\overline{\mathrm{PIV}}$ (4.24) fluctuates approximately between 0.5 and 0.8 for both offices. The great diversity of the occupants' thermal sensation and the limited number of manipulated variables prevents further improvement. The only way to bypass this issue is a comfort based office assignment. To evaluate the potential of an intelligent seating approach, the test group is split according to their thermal sensation. The boundary conditions and occupancy profiles are again copied from Section 4.2.2. Therefore, six people are assigned to office 1 and ten to office 2 but based on their thermal preferences. The variance of these preferences is minimized when the smaller group in office 1 aims for colder conditions and office 2 contains the group with warmer preferences.

Table 4.7 summarizes the performance indices for the intelligently divided occupants. The main benefit is visible for the colder office. The average comfort level is improved by about 60 % compared to the results for the original office affiliation. The resulting average optimized temperature is reduced to 25 °C from earlier 27 °C. Sorting the occupants minimizes the range between the "coldest" and "warmest" user. This is emphasized by the minimum and maximum values of the average individual comfort

Table 4.7: Performance evaluation for thermal sensation based seating.

Office	$\overline{\mathrm{PIV}}_{\mathrm{ave}}$	$\max\limits_{t}(\overline{\mathrm{PIV}}(t))$	$\min\limits_{j}|\max\limits_{j}\mathrm{PIV}_{\mathrm{int},j}$	$\dfrac{\int_{I_{\mathrm{op}}}|\dot{Q}_{\mathrm{FCU}}|\,dt}{2}$	$\dfrac{\int_{I_{\mathrm{op}}}T_{\mathrm{air}}(t)\,dt}{t_{\mathrm{op}}}$
1	0.26	0.50	-0.08 | 0.48	$8.16\,\frac{\mathrm{kWh}}{\mathrm{day}}$	$25.2\,^\circ\mathrm{C}$
2	0.63	0.76	-1.54 | 0.19	$0.41\,\frac{\mathrm{kWh}}{\mathrm{day}}$	$27.1\,^\circ\mathrm{C}$

level of an occupant j

$$\mathrm{PIV}_{\mathrm{int},j} = \frac{1}{t_{\mathrm{op}}} \int_{I_{\mathrm{op}}} \mathrm{PIV}_j(t)\,dt. \tag{4.62}$$

While the original office assignment led to a thermal comfort sensation range between $\min_j \mathrm{PIV}_{\mathrm{ave},j} = -1.15$ and $\max_j \mathrm{PIV}_{\mathrm{ave},j} = 0.76$ for office 1, the optimized seating positions reduce this range by over $70\,\%$. The missing improvement for office 2 is again due to the larger number of occupants which must be satisfied simultaneously as well as the CO_2 driven primary air supply. The centrally precooled air provides too much cooling such that the maximum office temperature cannot become significantly higher than $27\,^\circ\mathrm{C}$. A differently designed (downsized) air conditioning system would also improve the result for the group with warmer preferences.

4.4 Conclusion

Generally, the previous analysis showed that a well tuned PI controller as well as an MPC approach are able to achieve comfort-optimized conditions. The performance differences between the discussed control approaches are small compared to the uncertainty that is incorporated by the user comfort models. Therefore, the performance under real conditions depends mainly on the dynamical properties of the HVAC system which define the response time to variations of the comfort requirements. This property is particularly important when occupancy detection is included so that the control algorithm adjusts the conditions based on the presence of the occupants. In this case, fast responding systems are beneficial to track the optimal trajectory. Since the cooling system of the investigated simulation model is assumed to be ideal, such that latencies or other dynamical properties of a real HVAC system are neglected, all controllers accomplish fast responses and thus similar comfort levels. Therefore, a subsequent evaluation in the real test-bed must be performed to challenge the simulative results and to reveal additional bottlenecks.

Nevertheless, the exposed differences between the different control methods can be traced back to multiple system properties. The knowledge base of the adaptive

feedforward control algorithm is identical to the MPC approach except for the room model. Both use current measurements of the system states and disturbances to improve the indoor conditions. Only the interface between the algorithm and the system is different. The feedforward control algorithm optimizes the temperature set-point without any knowledge about the room dynamics whereas the MPC includes the dynamical characteristics. Hence, both approaches result in the same conditions except for two scenarios:

▶ The desired comfort trajectory brings the HVAC system to its (dynamical) limits and a predictive control strategy allows for more comfortable air conditioning.

▶ The coupling between air temperature, humidity and supply conditions incorporates a great potential for improving the occupant's comfort.

The first scenario is mainly important for selecting the prediction horizon of the MPC algorithm. Although the feedforward controller misses the predictive property, the system limits do not affect the results significantly. The appropriately tuned PI-controller already damps the output of the comfort-based feedforward control and avoids infeasible steps in the control command. However, the tuning of the PI controller is a crucial factor for the performance. In reality, badly tuned controllers are most often the main issue when room conditions are not satisfying. The model-based MPC approach with identified zone models provides a more intuitive interface for the user and allows for simple consideration of input and state constraints as well as the possibility to intuitively incorporate an energy saving goal. Consequently, a lot of research is performed in this field [1, 75] and a combination of the personal comfort model with more advanced MPC algorithms encompasses a promising potential for real applications on building level. Since linear(ized) models are quite common for building control, the linearized comfort implementation allows for a simple integration to other approaches. Although the linearization error leads to small deviations from the nonlinear evaluation, the resulting deterioration of the comfort level is negligible compared to the uncertainty of the personal comfort models.

The second scenario is piecewise visible in Figure 4.16 where the coupling between humidity and temperature leads to different optimal trajectories. Particularly during the startup phase, when humidity and temperature change significantly, benefits occur for the MPC approaches and lead to temperature deviations of up to $0.8\,\mathrm{K}$. Hence, a test group that is even more sensitive to humidity or a HVAC system that leads to greater humidity variations are likely to emphasize the MPC performance. Furthermore, tracking the desired conditions with the required accuracy is a challenging task for real applications where measurement uncertainties impede the possible attainment so that more advanced control approaches can achieve additional profits.

Independent from the controller design, the comfort-driven trajectory definition revealed a great potential with respect to energy saving and user satisfaction. The surprisingly high target temperatures indicate that the standard set-point of commonly

24 °C is not desirable or necessary. In particular in combination with elevated air movement, significantly higher set-points can be implemented which provides potential for downsizing of the system components and remarkable energy savings during the operation. Moreover, the carefully considered comfort model structure allows for an intuitive supervision of the learning process. Including new users gradually according to their available voting data ensures reasonable optimal trajectories although a high uncertainty is incorporated by the real-world user feedback.

With the trend towards open and inspiring working conditions where employees can choose their working place freely, an introduction of thermally different zones incorporates a great potential for improving the individual thermal comfort. Apart from the influence of the office facilities and equipment, individualized thermal conditions promote the occupants' productivity and working performance. Therefore, thermal comfort profiling based on personalized trained models opens up multiple chances for greater user satisfaction.

5 Conclusion

The main objective of climate control is to satisfy the occupants of a building. Usually, standardized assumptions are applied to translate the thermal comfort requirements to air-conditioning target values. These target values are then used as fixed set-points for the HVAC system operation. The building control is commonly based on a multi-zone approach where it is separated into multiple zones that are assumed to be well-mixed. Therefore, only a single (or averaged) sensor measurement is used as a feedback signal for the AC system. Hence, local differences within the commonly large zones are neglected. As a consequence, this approach entails two difficulties: limited knowledge about the actual local room conditions and subjective differences regarding the true relation between thermal comfort and indoor air conditions. Both problems were addressed in this thesis by developing multiple methods to pave the way towards personalized comfort control for shared office spaces.

The first objective stated in Section 1.2

> ✓ *A data-based modeling approach for a more detailed representation of the spatial room conditions to enable the possibility of localized temperature control without the need for exact knowledge about the boundary conditions and expensive CFD simulations.*

was addressed in the first part of this thesis by deriving a data-based modeling approach to close the gap between complex CFD simulations and the assumption of well-mixed conditions. A GP regression model was trained based on distributed sensor measurements using location information and the operational mode of the HVAC system as model input. This model was then able to predict the spatial temperature field to obtain a more detailed representation of the actual room conditions and local differences. It was shown that a well selected mean for the GP improved the prediction quality significantly. Moreover, distance-based input data led to a better match between the model output and the real conditions instead of using Cartesian coordinates. The model quality could be even further improved by optimizing the sensor placement. Since the training data was provided entirely by the discrete sensor measurements, it was concluded that an intelligent sensor configuration increases the information content of the training data. In order to evaluate this assumption, two measures were applied and assessed based on CFD simulation results.

The first measure targeted to improve the prediction accuracy, hence reducing the MSE between the estimated temperature field and the ground truth represented by the

CFD data. For the evaluation of the MSE, holistic knowledge about the temperature field is required. However, since the measurement equipment in real buildings is usually limited, the analysis aimed to derive a general placement strategy that could later be transferred to arbitrary applications: The corresponding MSE-based sensor placement strategy depends on the amount of distributed sensors, i.e. a small sensor network initially has to capture the average temperature level but with an increasing number of sensors, local effects must be taken into account by building sensor clusters in areas of high temperature gradients.

The second approach applied to optimize the sensor configuration maximized the MI between the sensor data and the remaining room data. This optimal placement method uses the structural properties of the GP modeling approach and can be applied without extensive reference measurements. The MI method relies on the incorporated covariance information of the GP and makes use of the interpretation that entropy is a measure for uncertainty of the model output. The concept tries to maximize the reduction of uncertainty about the room conditions by knowing local sensor measurements. Since this approach focuses on the reduction of uncertainty that is accompanied by a reduced variance, uniformly distributed sensor configurations are the result and monitoring local effects is avoided. While both general placement guidelines can be easily transferred to real-world applications, an optimization is only feasible using the MI-based approach. Solely the hyperparameters of the GP model must be identified for its evaluation which is realizable e. g. based on the available sensor measurements. In conclusion, the GP model for temperature field estimation provides an easily implementable advancement to the commonly applied room models and does not require detailed knowledge about the exact boundary conditions and geometry. It can be trained based on commonly available sensor data and allows an online adaption due to its purely data-based structure. Therefore, the implementation effort is minimized and the foundation for focused local actuation is created. Future developments could target the extension to dynamic modeling. Furthermore, actuator placement and optimal operational strategies can be developed if a greater data basis from real applications is available.

The assumption that local actuation and individualization of indoor conditions is only meaningful when personalized target states can be defined motivated the second objective of this thesis:

> ✓ *A methodology for the derivation of well predicting personal thermal comfort models is developed based on real world voting data. A scalable modeling approach is derived that can be used in the context of optimal control.*

The commonly applied models for thermal comfort in buildings aspire to define the best compromise for a large group. Although these assumptions are suitable for common building control algorithms, they contradict the idea of personalized conditions. The main challenge for individual control is the highly subjective sensation and the limited measurements of comfort-related variables. In the building context,

environmental data only can usually be accessed whereas personal influencing factors are invisible to the control algorithm. These limitations complicate the modeling of individual thermal comfort. In the second part of this thesis, a detailed analysis of suitable model structures and important comfort factors was performed to define a modeling approach appropriate for comfort-based building control. Standard models were evaluated regarding their transferability to personalized comfort prediction but exhibited unsatisfactory accuracy by incorporating a high level of complexity. Motivated by dominant linear relations between the thermal sensation vote and environmental conditions, generalized linear regression approaches were investigated regarding their suitability for personal comfort modeling. It was found that even the simplest linear regression approaches result in a better individual predictability than standard models. Moreover, this simple structure allows for good supervision during the model training which is a crucial factor to ensure physically feasible prediction models based on the extremely noisy voting data. A hybrid modeling approach consisting of a linear basis model and a GP model further improved the prediction quality. This extension combines the benefits of the linear approach with the possibility to map the nonlinear relations between personal thermal comfort and environmental conditions. A detailed feature selection process was performed to find the best compromise between model complexity and prediction quality but also to minimize the risk of overfitting. Different methods were derived for an optimal definition of the common feature set. The analysis resulted in a control-oriented model structure which allows for reliable online training and adaption while enabling a robust application to optimization-based control approaches.

The last part of this thesis focused on the development of comfort-based control strategies to address the third and last objective:

> ✓ *Optimization-based control approaches are devised for improving the individual thermal comfort in a shared office space by the use of multiple ceiling fans.*

Based on the previously derived comfort models, optimal conditions were deduced by defining the best compromise between all users' preferences and the available manipulated variables. The controllable states for the regarded case were defined by a common temperature set-point and the speed of additional ceiling fans providing local actuation of the air velocity. On that basis, an adaptive feedforward control algorithm was implemented which computes the optimal temperature and fan level set-points based on the current office and outside conditions. This method considered the room dynamics as a black box. As such it can be applied as retrofit option which is independent from the present AC system. The impact of different comfort model structures and the online learning process was investigated. An application in the test-bed showed feasible performance for all model structures but further evaluation regarding the required training data set size and online adaption will be necessary. An additional challenge is the handling of changing occupancy. Sudden (de-)activation of comfort models, when users leave or enter the room, results in steps of the comfort

requirements. Thus, two different methods were proposed for a feasible handling of occupancy changes. The resulting occupancy-based control trajectory was smoothed so that the HVAC system was able to follow the comfort-optimal command. Apart from optimizing the comfort level, this approach also revealed significant energy saving potential as by-product. The desired temperature level turned out to be about 2-3 K higher than the commonly applied standard set-point. Furthermore, the cooling effect of the locally increased air movement incorporated two additional benefits: improvement of the overall comfort level and further energy saving possibilities by forcing the feedforward control algorithm to favor higher fan levels.

The adaptive feedforward control approach did not consider the building dynamics. Control-performance, thus the comfort level, could be further improved by extending the algorithm with a dynamical office model. Since input and state constraints as well as disturbance effects are dominating aspects for building control, an MPC structure was selected to fulfill the comfort-based control task. Hence, the comfort optimization directly included the dynamical limitations and took into account the coupling between system states and personal thermal comfort. Consequently, the considered coupling between relative humidity and temperature improved the performance of the MPC approach compared to the feedforward control. The benefit of including input constraints proved to be even more significant: The present system had no local heating device. Therefore, the predictive strategy reduced cooling earlier when an input constraint limited the future control options. This enhanced the overall comfort. Also a linear MPC was implemented to investigate the feasibility and achievable performance when computational effort is a limiting criteria for an application. The results proved the general validity of this approach although small performance losses had to be accepted. The thoughtful comfort modeling approach enabled well-performing control approaches with all applied concepts so that the final way of implementation depends on the system requirements. The retrofit option can be applied to any system with low modeling effort whereas the MPC formulation allows for an integration to more advanced model-based control strategies.

The presented work derived a large set of methods that allow for an integration of individualized comfort-based control strategies. However, the voting data and application was limited to a small group of employees in Singapore. Although modeling approaches can be applied to different user groups, the optimal set of common features and achievable comfort levels may vary for other test groups and locations. Particularly the high desired temperatures likely differ for other subjects and an application in distinct climatic circumstances. Furthermore, the air temperature in the considered offices were bounded above due to the constant fresh air supply and the associated fixed cooling enthalpy flow. Consequently, the training data do not include the actual sensation for very high temperature set-points. It can be expected that these extremely up- or downwards shifted personal comfort models are self-regulated if the room controller is able to explore the full temperature range. These effects during the model training and adaption must be investigated in future studies to define meaningful

boundaries and relaxations for the model's coefficient bounds. So far, the models were included to the comfort optimization algorithm depending on the number of available votes. However, further weighting strategies can be included for the comfort optimization. For example, it can be meaningful to use the variance information of the GP modeling approach and weight the comfort models according to their variance so that certain predictions have a greater influence on the desired conditions than uncertain estimations. Another open question remains in the reaction of the occupants when the office temperature really varies notably during the day. Commonly, the target conditions for buildings are based on maintaining constant conditions. Although the optimization results suggest variations over the day, the voting data were collected under predominantly steady conditions (due to the limited access to the AC control) and only set-point changes over longer periods could be investigated. Consequently, the actual impact of dynamic temperature trajectories on the users' comfort must be evaluated. Possibly, an automatic leveling of the daytime-dependent variations could be observed when the optimal trajectories are applied over a longer test period. An application to larger open office spaces with distributed actuation incorporates a great potential for combining the derived temperature field prediction model and the personal comfort optimization. Not only elevated air movement can be used for personalization but also individually controllable supply conditions. Since local changes of the supply conditions have a large radius of influence due to convective mixing, these effects must be investigated and included for the comfort optimization in future applications.

A Appendix - Temperature Field Prediction

A.1 Derivation of Posterior Distribution for GP Model

The calculation of the predictive posterior distribution using a GP model is derived in the following based on [38]. Given the training set of pairwise observations $\mathcal{D} = \{(z_i, T_i) \,|\, i = 1, \ldots, m\}$, the $m \times m$ covariance matrix $\boldsymbol{K}$ and the mean $\boldsymbol{\mu}$, the conditional probability density

$$P(T_* | \boldsymbol{T}, \boldsymbol{Z}, \boldsymbol{z}_*, \boldsymbol{K}) = \frac{P\left(\begin{bmatrix} \boldsymbol{T} \\ T_* \end{bmatrix} \middle| \boldsymbol{Z}, \boldsymbol{z}_*, \boldsymbol{K} \right)}{P(\boldsymbol{T} | \boldsymbol{Z}, \boldsymbol{K})} \tag{A.1}$$

can be evaluated to predict an unknown value T_* for a given input $\boldsymbol{z}_*$. The joint probability distribution function is given by

$$P\left(\begin{bmatrix} \boldsymbol{T} \\ T_* \end{bmatrix} \middle| \boldsymbol{Z}, \boldsymbol{z}_*, \boldsymbol{K} \right) = (2\pi)^{-\frac{m+1}{2}} |\boldsymbol{K}_{m+1}|^{-\frac{1}{2}} \exp\left(-\frac{1}{2} \boldsymbol{y}^{\mathrm{T}} \boldsymbol{K}_{m+1}^{-1} \boldsymbol{y} \right) \tag{A.2}$$

with

$$\boldsymbol{K}_{m+1} = \begin{bmatrix} \boldsymbol{K} & \boldsymbol{\kappa}(\boldsymbol{Z}, \boldsymbol{z}_*) \\ \boldsymbol{\kappa}^{\mathrm{T}}(\boldsymbol{Z}, \boldsymbol{z}_*) & \kappa(\boldsymbol{z}_*, \boldsymbol{z}_*) \end{bmatrix} = \begin{bmatrix} \boldsymbol{K} & \boldsymbol{\kappa} \\ \boldsymbol{\kappa}^{\mathrm{T}} & \kappa \end{bmatrix},$$

$$\boldsymbol{y} = \begin{bmatrix} \boldsymbol{T} - \boldsymbol{\mu} \\ T_* - \mu \end{bmatrix} = \begin{bmatrix} \boldsymbol{\tau} \\ \tau_* \end{bmatrix},$$

$$|\boldsymbol{K}| = \det \boldsymbol{K}.$$

Substituting $P(\boldsymbol{T} | \boldsymbol{Z}, \boldsymbol{K})$ and using (A.2) in (A.1) results in

$$P(T_* | \boldsymbol{T}, \boldsymbol{Z}, \boldsymbol{z}_*, \boldsymbol{K}) = \frac{|\boldsymbol{K}|^{\frac{m}{2}}}{(2\pi)^{\frac{1}{2}} |\boldsymbol{K}_{m+1}|^{\frac{m+1}{2}}} \exp\left(-\frac{1}{2} \left(\boldsymbol{y}^{\mathrm{T}} \boldsymbol{K}_{m+1}^{-1} \boldsymbol{y} - \boldsymbol{\tau}^{\mathrm{T}} \boldsymbol{K}^{-1} \boldsymbol{\tau} \right) \right) \tag{A.3}$$

Defining

$$\boldsymbol{K}_{m+1}^{-1} = \begin{bmatrix} \boldsymbol{\Lambda} & \boldsymbol{\lambda} \\ \boldsymbol{\lambda}^{\mathrm{T}} & \lambda \end{bmatrix} \tag{A.4}$$

and using $\boldsymbol{K}_{m+1}\boldsymbol{K}_{m+1}^{-1} = \boldsymbol{I}_{m+1}$ leads to the following expressions

$$\boldsymbol{K}\boldsymbol{\lambda} + \lambda\boldsymbol{\kappa} = \boldsymbol{0} \qquad \xrightarrow{\hspace{2cm}} \qquad \boldsymbol{\lambda} = -\lambda\boldsymbol{K}^{-1}\boldsymbol{\kappa} \tag{A.5}$$

$$\boldsymbol{K}\boldsymbol{\Lambda} + \boldsymbol{\kappa}\boldsymbol{\lambda}^{\mathrm{T}} = \boldsymbol{I}_m \qquad \xrightarrow{\text{(A.5)}} \qquad \boldsymbol{\Lambda} = \boldsymbol{K}^{-1} + \frac{1}{\lambda}\boldsymbol{\lambda}\boldsymbol{\lambda}^{\mathrm{T}} \tag{A.6}$$

$$\boldsymbol{\kappa}^{\mathrm{T}}\boldsymbol{\lambda} + \kappa\lambda = 1 \qquad \xrightarrow{\text{(A.6)}} \qquad \lambda = \left(\kappa - \boldsymbol{\kappa}^{\mathrm{T}}\boldsymbol{K}^{-1}\boldsymbol{\kappa}\right)^{-1} \tag{A.7}$$

$$\xrightarrow{\text{(A.5, A.7)}} \qquad \boldsymbol{\lambda} = \frac{-\boldsymbol{K}^{-1}\boldsymbol{\kappa}}{\kappa - \boldsymbol{\kappa}^{\mathrm{T}}\boldsymbol{K}^{-1}\boldsymbol{\kappa}}. \tag{A.8}$$

The exponent of (A.3) can be expressed in terms of the inverse covariance matrix (A.4) and in dependence of τ_* as

$$\boldsymbol{y}^{\mathrm{T}}\boldsymbol{K}_{m+1}^{-1}\boldsymbol{y} - \boldsymbol{\tau}^{\mathrm{T}}\boldsymbol{K}^{-1}\boldsymbol{\tau} = \lambda\tau_*^{\,2} + 2\lambda\boldsymbol{\lambda}^{\mathrm{T}}\boldsymbol{\tau}\tau_* + \text{const.} \tag{A.9}$$

Using the results of (A.5) to (A.8) leads to the expression for the mean and covariance of the normal predictive distribution $P(T_*|\boldsymbol{T}, \boldsymbol{Z}, \boldsymbol{K}, \boldsymbol{z}_*)$

$$\mu_* = \mu + \boldsymbol{\kappa}^{\mathrm{T}}\boldsymbol{K}^{-1}\boldsymbol{\tau} \tag{A.10}$$

$$\sigma_*^{\,2} = \kappa - \boldsymbol{\kappa}^{\mathrm{T}}\boldsymbol{K}^{-1}\boldsymbol{\kappa}. \tag{A.11}$$

A.2 CFD Simulation Setups

The reference data for the temperature field prediction model in Chapter 2 are provided by multiple CFD simulations. According to Figure 2.1a, the office is separated in 3 zones and the zone-related supply and exhaust conditions are varied as listed in Table A.1. Figure A.1 visualizes the resulting temperature distribution in the occupied zone ($x_2 = 1.2\,\text{m}$) for each simulation setup.

Table A.1: Description of CFD simulation setups.

Zone	1		2		3	
AC mode	inlet	outlet	inlet	outlet	inlet	outlet
Setup 1	3 ACH	✗	3 ACH	✓	3 ACH	✓
Setup 2	3 ACH	✓	3 ACH	✗	3 ACH	✓
Setup 3	3 ACH	✓	3 ACH	✓	3 ACH	✓
Setup 4	5 ACH	✗	3 ACH	✓	5 ACH	✓
Setup 5	4 ACH	✓	3 ACH	✗	4 ACH	✓
Setup 6	5 ACH	✓	3 ACH	✗	5 ACH	✓
Setup 7	4 ACH	✓	3 ACH	✓	4 ACH	✓
Setup 8	5 ACH	✓	3 ACH	✓	5 ACH	✓
Setup 9	1 ACH	✗	3 ACH	✓	1 ACH	✓
Setup 10	1 ACH	✓	3 ACH	✗	1 ACH	✓
Setup 11	1 ACH	✓	3 ACH	✓	1 ACH	✓
Setup 12	5 ACH	✗	1 ACH	✓	5 ACH	✓
Setup 13	5 ACH	✓	1 ACH	✗	5 ACH	✓
Setup 14	5 ACH	✓	1 ACH	✓	5 ACH	✓
Setup 15	5 ACH	✗	0 ACH	✓	5 ACH	✗
Setup 16	0 ACH	✓	0 ACH	✗	3 ACH	✗
Setup 17	0 ACH	✓	0 ACH	✗	8 ACH	✗
Setup 18	9 ACH	✗	2 ACH	✗	0 ACH	✓
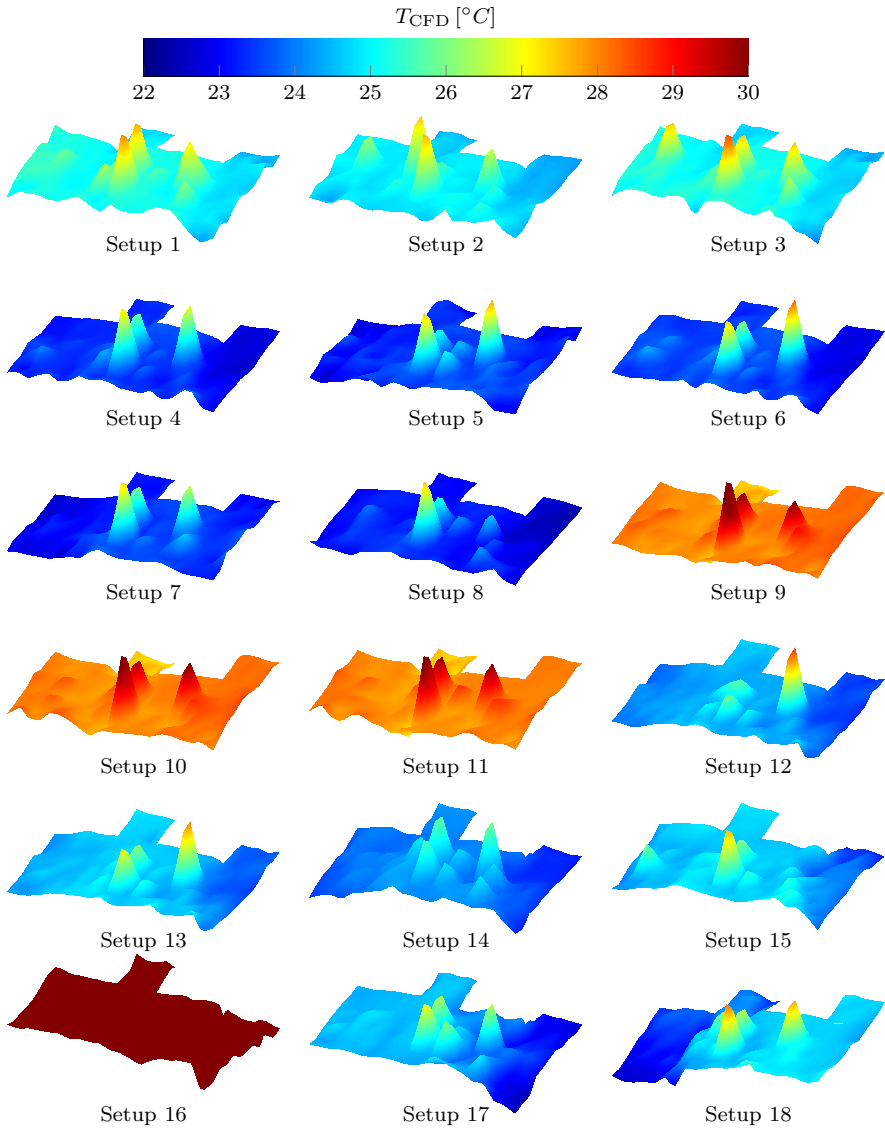
Figure A.1: CFD simulation results for the temperature distribution under different operation modes.

A.3 Greedy Optimization Algorithms for Sensor Placement

To avoid the infeasible evaluation of the combinational analysis for the optimal sensor placement, two greedy algorithms are introduced for the optimization. The pseudo code of Algorithm A.1 and A.2 describes the working principle for stepwise forward and backward selection respectively. The cost function $J(\mathcal{S})$ denotes the objective applied to rate the sensor setup $\mathcal{S}$.

Algorithm A.1 : Sequential forward selection of sensor locations

---

1 ForwardSensorSelection $(\mathcal{D}, \mathcal{M})$;

   Input : Observation data $\mathcal{D} = \{(\boldsymbol{z}_i, T_i) | i = 1, \dots, m\}$ from the distributed sensors $\mathcal{S} \subseteq \mathcal{M}$.

   Output : Define best set of sensor locations $\mathcal{S}_k$ of k distributed sensors.

2 Initialize $\mathcal{S}_k = \{\emptyset\}, k = 0$;

3 **while** $k < M$ **do**

4   Find best next sensor locations $s_k^* = \underset{s_k \in \mathcal{M} \setminus \mathcal{S}_k}{\arg\min} \left(\sum_{j=1}^m J(\mathcal{S}_k \cup s_k) \right)$;

5 $\mathcal{S}_{k+1} = \mathcal{S}_k \cup s_k^*$;

6 $k = k + 1$;

7 **end**

Algorithm A.2 : Sequential backward selection of sensor locations

---

1 BackwardSensorSelection $(\mathcal{D}, \mathcal{M})$;

   Input : Observation data $\mathcal{D} = \{(\boldsymbol{z}_i, T_i) | i = 1, \dots, m\}$ from the distributed sensors $\mathcal{S} \subseteq \mathcal{M}$.

   Output : Define best set of sensor locations $\mathcal{S}_k$ of k distributed sensors.

2 Initialize $\mathcal{S}_k = \mathcal{M}, k = M$;

3 **while** $k > 0$ **do**

4   Find least useful sensor $s_k^- = \underset{s_k \in \mathcal{S}_k}{\arg\max} \left(\sum_{j=1}^m J(\mathcal{S}_k \setminus s_k) \right)$;

5 $\mathcal{S}_{k-1} = \mathcal{S}_k \setminus s_k^-$;

6 $k = k - 1$;

7 **end**

B Appendix - Personal Thermal Comfort Modeling

B.1 Sensor Specifications

The thermal comfort test-bed is equipped with Libelium Waspmote sensor boards [72] for indoor air quality measurement. It contains Sensirion air and mean radiant temperature sensors [90] and the black globe thermometer THERMASGARD® RPTF 2 [87]. The outdoor conditions are monitored by a Wireless Vantage Pro2™ weather station [22]. Table B.1 lists the main sensor specifications.

Table B.1: Sensor specifications

Sensor type	Measurement range			Accuracy
Air temperature sensor	0	to	70 °C	±0.4 °C
Humidity sensor	0	to	100 %	±1.8 %
Black globe thermometer	−30	to	80 °C	DIN EN 60751, class B
Outdoor temperature	−40	to	65 °C	±0.3 °C
Solar radiation	0	to	1800 $\frac{W}{m^2}$	±5 %

B.2 Voting Data

The voting data that are used for the personal thermal comfort modeling are collected during the daily working routine. The voting feedback of 16 occupants is considered for the analysis. The associated sample sizes n and office assignments are given in Table B.2. Figure B.1 shows the data ranges that were covered over the test period from September until February for the 16 considered users. The occupants were exposed to various temperature settings and fan levels. To maintain employable room conditions the temperature ranges are mostly limited to acceptable conditions. Therefore, over 50 % of the temperature values that correspond to a recorded vote are within the interval of 25.0 °C and 26.5 °C. The range without outliers reaches from

23.0 °C to 28.5 °C. The Interquartile Ranges (IQRs) and ranges between the minimum and maximum values without outliers, denoted as whiskers, for the accumulated voting data are given in Table B.3. A data point is considered as outlier when it has a distance of $1.5 \cdot$ IQR from the IQR upper or lower limits. Note that the ranges are not listed for the discrete fan level l_{fan} because over 50 % of the data points are collected for $l_{\text{fan}} = 1$ such that the accumulated data range does not provide meaningful insights.

Table B.2: Sample size and office for each user.

User	1	2	3	4	5	6	7	8	9	10	11	12	13	14	15	16
n	66	362	375	135	50	551	289	234	149	530	82	382	305	64	163	62
Office	2	1	2	2	1	2	1	1	2	2	2	2	2	1	1	2

Table B.3: Accumulated ranges of recorded voting data.

Parameter	Unit	Interquartile range	Whiskers
T_{air}	°C	[25.1, 26.5]	[23.1, 28.5]
T_{mr}	°C	[27.0, 28.6]	[24.8, 30.7]
RH_{air}	%	[51.1, 55.9]	[44.0, 63.1]
T_{sup}	°C	[22.2, 25.4]	[17.5, 28.6]
T_{out}	°C	[28.0, 30.4]	[24.4, 33.6]
I_{sol}	W/m²	[213, 490]	[0, 905]
RH_{out}	%	[67.7, 81.4]	[49.6, 98.0]
DT	h	[10.8, 16.3]	[7.4, 21.4]
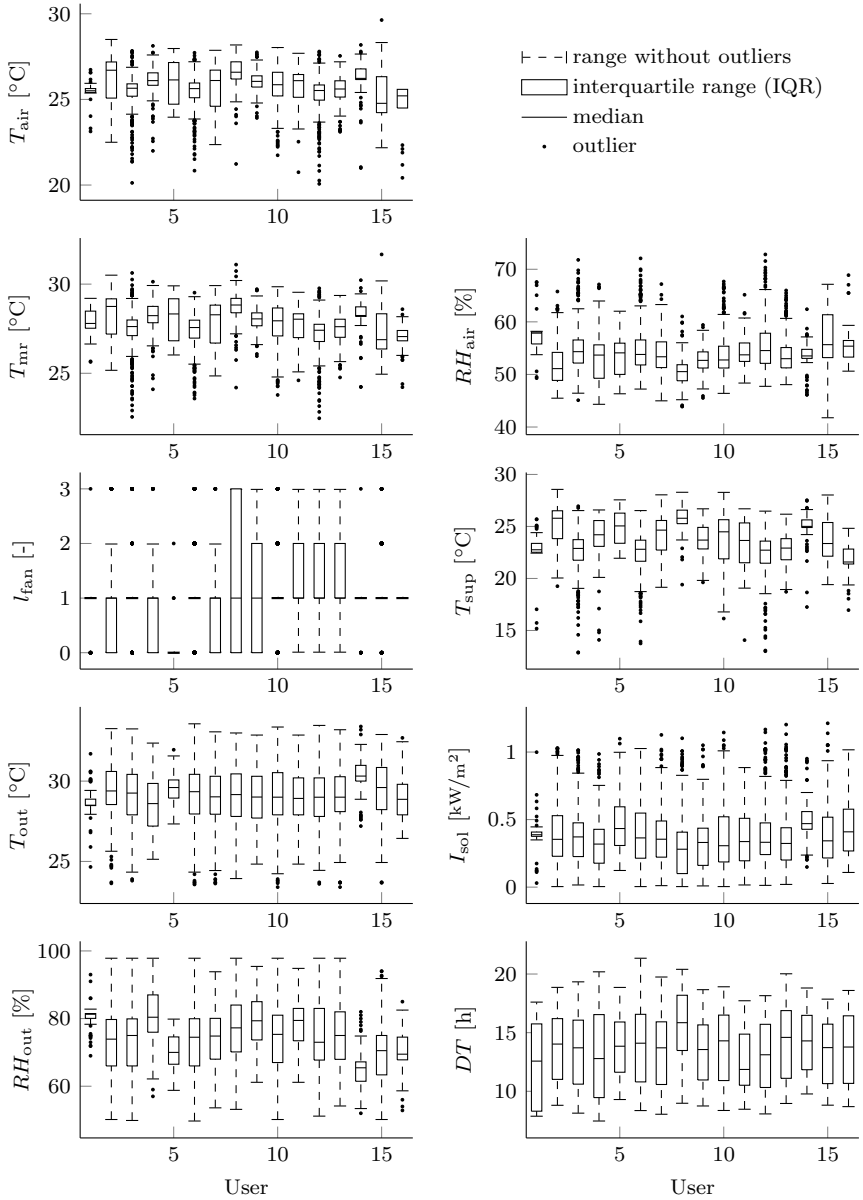
Figure B.1: Distribution of the collected voting data for the 16 considered users.

B.3 PMV Calculation

Fanger [30] considered the steady-state energy balance of the human body to derive an equation for the prediction of thermal comfort. He used comfort voting data and deduced empirical relations which represent comfortable conditions. As a consequence, the right hand side of (3.1), namely the required heat flow for a neutral sensation is evaluated such that the thermal load on the human body results in

$$
\begin{aligned}
L = M - W & \qquad \} \quad \text{actual heat flow} \\
& - f_{\mathrm{cl}} \left(3.96 \cdot 10^{-8} \left(\vartheta_{\mathrm{cl}}^4 - \vartheta_{\mathrm{mr}}^4 \right) + \alpha_{\mathrm{conv}} (T_{\mathrm{cl}} - T_{\mathrm{air}}) \right) \\
& - 3.05 \cdot 10^{-3} \left(5733 - 6.99(M - W) - p_{\mathrm{a}} \right) \\
& - 0.42 \left(M - W - 58.15 \right) - 1.73 \cdot 10^{-5} M (5867 - p_{\mathrm{a}}) \\
& - 0.0014 M (34 - T_{\mathrm{air}}).
\end{aligned}
$$

$$ \text{required heat flow} $$

(B.1)

All used symbols are explained in Table B.4 whereas [3] provides a more detailed description how the equations are obtained. The clothing temperature T_{cl} is found by solving

$$
T_{\mathrm{cl}} = 35.7 - 0.028(M - W) - I_{\mathrm{cl}} f_{\mathrm{cl}} \left(3.96 \cdot 10^{-8} \left(\vartheta_{\mathrm{cl}}^4 - \vartheta_{\mathrm{mr}}^4 \right) + \alpha_{\mathrm{conv}} (T_{\mathrm{cl}} - T_{\mathrm{air}}) \right)
$$

(B.2)

where the heat transfer coefficient α_{conv} and the clothing area factor f_{cl} are calculated by

$$
\alpha_{\mathrm{conv}} = \begin{cases} 2.38 \, ||T_{\mathrm{cl}} - T_{\mathrm{air}}||^{0.25} & \text{for} \quad 2.38 \, ||T_{\mathrm{cl}} - T_{\mathrm{air}}||^{0.25} > 12.1 \sqrt{v_{\mathrm{air}}} \\ 12.1 \sqrt{v_{\mathrm{air}}} & \text{for} \quad 2.38 \, ||T_{\mathrm{cl}} - T_{\mathrm{air}}||^{0.25} < 12.1 \sqrt{v_{\mathrm{air}}} \end{cases}
$$

(B.3)

$$
f_{\mathrm{cl}} = \begin{cases} 1.00 + 1.290 I_{\mathrm{cl}} & \text{for} \quad I_{\mathrm{cl}} \le 0.078 \\ 1.05 + 0.645 I_{\mathrm{cl}} & \text{for} \quad I_{\mathrm{cl}} > 0.078. \end{cases}
$$

(B.4)

The computation of the thermal load L consequently only depends on the parameters metabolism M, clothing insulation I_{cl}, air temperature T_{air}, radiation temperature T_{mr}, air velocity v_{air} and humidity RH_{air}. The mechanical work W is 0 for normal office activity and can be neglected for the performed analysis. The relation between L and thermal comfort prediction is then given by (3.2).

Table B.4: Nomenclature for PMV calculation.

Symbol	Description	Unit
M	Metabolic rate	W/m^2
W	Accomplished mechanical work	W/m^2
I_{cl}	Clothing insulation	$m^2 K/W$
f_{cl}	Clothing area factor	
$T_{air} \,\vert\, \vartheta_{air}$	Air temperature	$^{\circ}C \,\vert\, K$
$T_{mr} \,\vert\, \vartheta_{mr}$	Mean radiant temperature	$^{\circ}C \,\vert\, K$
$T_{cl} \,\vert\, \vartheta_{cl}$	Surface temperature of clothing	$^{\circ}C \,\vert\, K$
p_a	Partial water vapor pressure	Pa
α_{conv}	Convectional heat transfer coefficient	$W/m^2 K$

B.4 Mean Radiant Temperature in the Test-Bed

The calculation of mean radiant temperature usually requires detailed knowledge about the considered room. View factors, window and wall properties as well as sun position and orientation affect the radiation exchange. These properties are mainly unknown and thus, introduce a high complexity to the system when mean radiant temperature is needed for the comfort prediction. To reduce the complexity, a general relation is identified for the considered test-bed. Analyzing the measurement data reveals a strong relation between the mean radiant temperature T_{mr} and the air temperature T_{air}. Furthermore, solar influences are expected to affect T_{mr}. Therefore, all user-related observations described in Appendix B.2 as well as additional available environmental measurements within the office spaces are combined to a data base with over 4000 samples containing tuples of T_{air}, I_{sol} and T_{mr}. Figure B.2 shows the measured observation tuples as colored dots. Expressing the mean radiant temperature in terms of air temperature and solar radiation leads to the least square fit

$$T_{mr} = a_0 + a_1 T_{air} + a_1 I_{sol} = 2.38 + 0.98 T_{air} + 6.82 \cdot 10^{-5} I_{sol} \qquad (B.5)$$

which corresponds to the surface in Figure B.2. Consequently, $T_{mr} \propto T_{air}$ whereas I_{sol} does not influence the mean radiant temperature for the considered office space. Although the latter result is contrary to the natural intuition, it can be explained by the orientation and location of the regarded offices. Due to their location on the ground floor with plants in front of the windows and manually operated blinds, solar radiation rarely enters the offices directly. Consequently, the simplified assumption
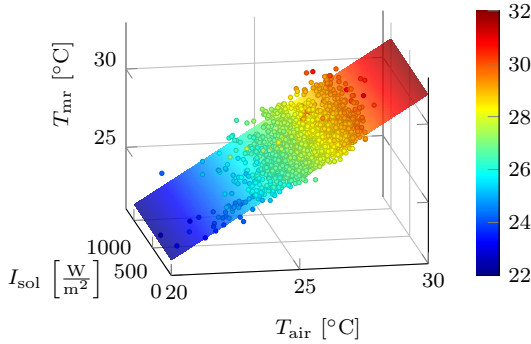
Figure B.2: Relation between mean radiant temperature, solar radiation and air temperature.

for the prediction of T_{mr} results in

$$T_{\mathrm{mr}} = 2.38 + 0.98 T_{\mathrm{air}}. \tag{B.6}$$

B.5 Cross-Correlation between Comfort Predictors

Computing cross-correlations between the considered comfort factors gives further insight on the reasons for the final feature selection or rather explains why specific features are neglected. Table B.5 lists the cross-correlation values calculated by (3.13).

The optimal feature selection in Table 3.3 revealed that T_{sup} and T_{out} have the lowest significance for predicting thermal comfort. The corresponding results in Table B.5 expose at least one or two strong cross-correlations to other parameters. The supply temperature T_{sup} is highly correlated with T_{air}, T_{mr} and RH_{air} such that its effects are already captured by other model components. Furthermore, the impact of T_{sup} on the room conditions and consequently on thermal comfort is expected to occur delayed due to the inertia of the room dynamics. The outside temperature T_{out}, on the other hand, exhibits a remarkable correlation with RH_{out} and I_{sol} what explains its substitution by other parameters.

Table B.5: Cross-correlation ϱ between the predictors of the linear feature vector ϕ_1.

	T_{air}	T_{mr}	RH_{air}	l_{fan}	T_{sup}	T_{out}	I_{sol}	RH_{out}	DT
T_{air}	1	0.95	-0.74	0.02	0.81	0.15	0.08	0.07	0.16
T_{mr}	-	1	-0.78	-0.01	0.79	0.19	0.09	0.05	0.21
RH_{air}	-	-	1	-0.03	-0.55	-0.30	-0.09	0.15	-0.49
l_{fan}	-	-	-	1	0.03	-0.08	-0.07	0.10	-0.01
T_{sup}	-	-	-	-	1	0.02	-0.01	0.18	0.07
T_{out}	-	-	-	-	-	1	0.56	-0.87	0.23
I_{sol}	-	-	-	-	-	-	1	-0.54	-0.15
RH_{out}	-	-	-	-	-	-	-	1	-0.17
DT	-	-	-	-	-	-	-	-	1

B.6 Combinatorics of Comfort Factors without Predefined Predictors

The evaluation in Section 3.4.5 is build on the control objective and thus includes the manipulated variables $\boldsymbol{u} = \begin{bmatrix} T_{\mathrm{air}} & l_{\mathrm{fan}} \end{bmatrix}^{\mathrm{T}}$ as fixed model components. However, the combinational analysis of the comfort factors returns slightly different results if no fixed basis is assumed. The corresponding validation errors and optimal feature combinations for the linear feature vector ϕ_1 are shown in Figure B.3 and Table B.6. The minimum MSE is achieved with the feature vector

$$\phi_1^* = \begin{bmatrix} 1 & T_{\mathrm{air}} & T_{\mathrm{mr}} & RH_{\mathrm{air}} & l_{\mathrm{fan}} & RH_{\mathrm{out}} & DT \end{bmatrix}^{\mathrm{T}}. \tag{B.7}$$

Since (B.7) contains the fixed input $\boldsymbol{u}$, it is identical to the combinational optimum (3.23) with predefined basis. According to Table B.6, only two combinations deviate from the approach in Section 3.4.5. The best single predictor is given by T_{sup}. This can be explained by the direct dependence between T_{sup} and T_{air}. Moreover, a low supply temperature causes local draught effects that impact the thermal comfort of the occupants sitting closer to the supplies. However, Figure B.3 also shows that the use of T_{air} leads to an almost identical model performance. The same is true for the substitution of T_{mr} by T_{air} for the best combination of 3 predictors. Although using the mean radiant temperature results in a slightly lower prediction error, replacing T_{mr} by the air temperature instead is a valid exchange regarding the associated MSE in Figure B.3.

The combinatorics for the quadratic shape function based on ϕ_2 leads to the optimal combination

$$\phi_2^* = \begin{bmatrix} 1 & T_{\mathrm{air}} & T_{\mathrm{air}}^2 & T_{\mathrm{mr}} & RH_{\mathrm{air}} & l_{\mathrm{fan}} & RH_{\mathrm{out}} & DT \end{bmatrix}^{\mathrm{T}}. \tag{B.8}$$
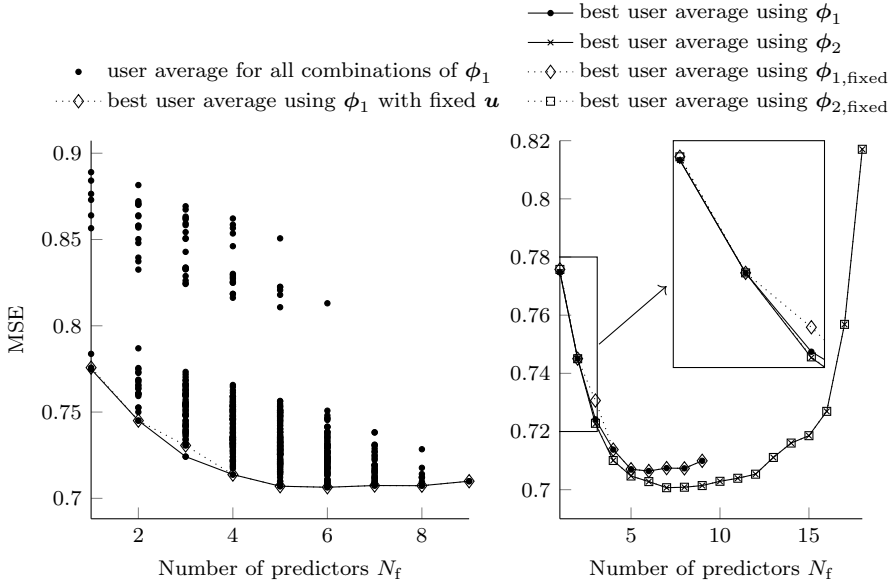
Figure B.3: Accumulated average and median 10-fold cross-validated prediction accuracy without fixed model basis.

Table B.6: Optimal feature selection for 1 to N_p predictors based on ϕ_1.

N_p	T_{air}	T_{mr}	RH_{air}	l_{fan}	T_{sup}	T_{out}	I_{sol}	RH_{out}	DT	MSE mean (median)
1				✓						0.775 (0.706)
2	✓			✓						0.745 (0.661)
3		✓	✓	✓						0.724 (0.676)
4	✓	✓	✓	✓						0.714 (0.617)
5	✓	✓	✓	✓			✓			0.707 (0.608)
6	✓	✓	✓	✓				✓	✓	0.706 (0.610)
7	✓	✓	✓	✓	✓		✓		✓	0.707 (0.617)
8	✓	✓	✓	✓		✓	✓	✓	✓	0.707 (0.604)
9	✓	✓	✓	✓	✓	✓	✓	✓	✓	0.710 (0.600)

Equivalently to Section 3.4.5, the only difference between (B.7) and (B.8) is the inclusion of the squared air temperature. In contrast to the small differences between results for ϕ_1 with and without fixed basis, the cross-validated MSE in Figure B.3 shows no visible deviations for ϕ_2.

In conclusion, the depicted prediction accuracy as well as the corresponding optimal input combinations of Table 3.3 and Table B.6 reveal that the predefined inclusion of $\boldsymbol{u}$ leads to almost identical results. Only feature vector dimensions < 4 substitute T_{air} by T_{sup} or T_{mr}. Nevertheless, the cross-validated MSE is comparable and supports the fixed usage of $\boldsymbol{u}$ as valid structural assumption. Moreover, the fixed basis reduces the risk of overfitting due to unskillfully selected features notably. Comparing the vertical range of the combinational results in Figure 3.10 and Figure B.3 shows that the fixed inclusion of $\boldsymbol{u}$ avoids the upper point cloud such that a reasonable model output is ensured for all possible linear combinations.

C Appendix - Adaptive Thermal Comfort Control

C.1 Effect of Rate Constraint for the Feedforward Control Algorithm

The trajectory generation based on disturbance-dependent comfort models entails discontinuities of the temperature command due to sudden changes of the disturbance values and even more pronounced steps originating from the discrete fan levels. While fan levels can be switched immediately, the room temperature has a slower dynamic. To avoid unrealizable temperature trajectories, a rate constraint

$$|T_{\mathrm{desired}}(t+t_{\mathrm{s}}) - T_{\mathrm{air}}(t)| \leq \Delta T_{\max} \tag{C.1}$$

can be added to (4.18), such that the increment of the temperature profile from time instant t to $t+t_{\mathrm{s}}$ is limited to feasible steps $\Delta T_{\max}$. Figure C.1 compares the unconstrained with a rate constrained optimization, where $\Delta T_{\max}$ is chosen to limit the temperature variation to $5\,^{\circ}\mathrm{C/h}$. The underlying personal comfort model is $\mathrm{PIV}_{\mathrm{gp}}$ (4.1d).

The additional limitation smoothens the temperature trajectory and uses the fans to balance the smaller temperature adjustments. The predicted voting is very similar to the unlimited optimization but outperforms the unlimited approach for some time periods. The resulting comfort level $\overline{\mathrm{PIV}}$ (4.24) is increased because the optimization incorporates more realistic dynamical assumptions such that the fan level can compensate for the delayed temperature change. Metaphorically, choosing the rate constraint according to the room dynamics is comparable to including the system dynamics in the trajectory planning, hence solving the MPC problem as done in Chapter 4.3. However, the control performance obviously depends on the right choice of $\Delta T_{\max}$ and can even worsen the result when it is chosen too conservatively, also visible in Figure C.1.
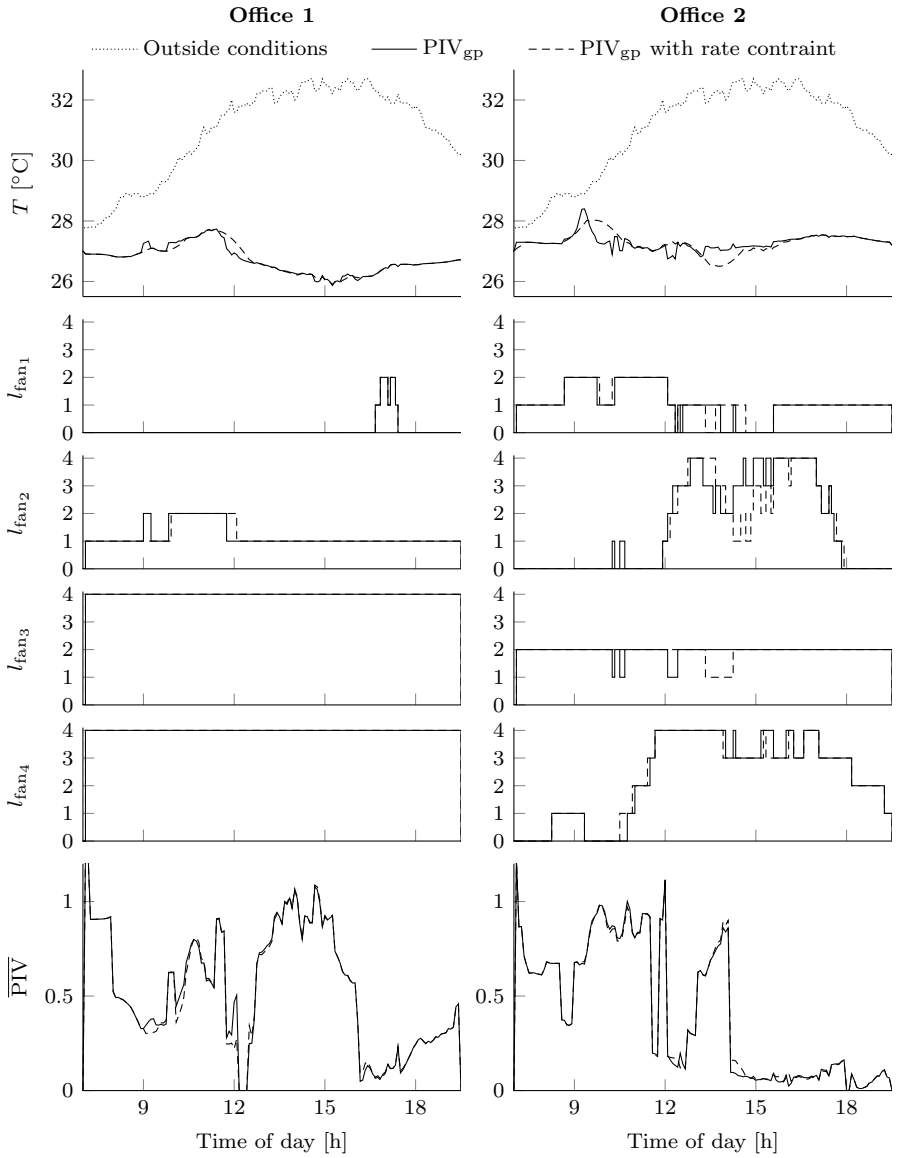
Figure C.1: Comparison of the trajectory generation with and without rate constraint.

Acronyms

*k*NN	*k*-Nearest Neighbors
AC	Air Conditioning
ACH	Air Changes per Hour
AHU	Air Handling Unit
ANN	Artificial Neural Network
ARMA	Autoregressive-Moving Average
CFD	Computational Fluid Dynamics
CV	Cross Validation
DE	Differential Evolution
ET^*	Effective Temperature
FCU	Fan Coil Unit
FEM	Finite Element Method
FVM	Finite Volume Method
GP	Gaussian Process
HVAC	Heating Ventilation and Air Conditioning
IoT	Internet of Things
IQR	Interquartile Range
LASSO	Least Absolute Shrinkage and Selection Operator
LMPC	Linear Model Predictive Control
MI	Mutual Information
MINLP	Mixed Integer Nonlinear Program
MIQP	Mixed Integer Quadratic Program
MISO	Multiple-Input-Single-Output
ML	Machine Learning

MPC	Model Predictive Control
MSE	Mean Squared Error
NLP	Nonlinear Program
NMPC	Nonlinear Model Predictive Control
OCP	Optimal Control Problem
OLSS	Ordinary Least Squares Solution
PCS	Personal Comfort System
PI	Proportional-Integral
PID	Proportional-Integral-Derivative
PIV	Predicted Individual Vote
PMV	Predicted Mean Vote
PPD	Predicted Percentage of Dissatisfied
QP	Quadratic Program
RANS	Reynolds-averaged Navier-Stokes
RC	Resistance-Capacitance
RF	Random Forest
RMSE	Root Mean Squared Error
SET*	Standard Effective Temperature
SVM	Support Vector Machine
VAC	Ventilation and Air Conditioning

List of Symbols

The following list contains all frequently used variables and parameters. Only locally used symbols are explained at their first occurrence. Bold symbols represent vectors and matrices.

Symbol	Description	Unit/Value
Operators		
$\lvert \cdot \rvert$	Absolute value of a scalar or determinat of a matrix	-
$(\cdot)$	Placeholder for arbitrary variable	-
$\cdot$	Dot product	-
$(\cdot)^{\circ k}$	k-th Hadamard (entrywise) product	-
$\lvert\lvert \cdot \rvert\rvert_1$	L_1-norm	-
$\lvert\lvert \cdot \rvert\rvert_2$	L_2-norm	-
∇	Nabla operator $\nabla = \begin{bmatrix} \frac{\partial}{\partial x_1} & \frac{\partial}{\partial x_2} & \frac{\partial}{\partial x_3} \end{bmatrix}^{\mathrm{T}}$	-
$\otimes$	Tensor product	-
Super- and Subscripts		
$*$	Result of optimization	-
adv	Advection	-
air	Air conditions	-
cond	Conduction	-
conv	Convection	-
core	Body core compartement	-
dist	Disturbance effects	-
eva	Evaporation	-
exh	Exhaust air conditions	-
ext	External	-
int	Internal	-
out	Outside conditions	-
pr	Primary air conditions	-
rad	Radiation effects	-
res	Respiration	-
sens	Sensor related variables	-
sk	Skin	-
sto	Heat storage	-

Symbol	Description	Unit/Value
sup	Supply air conditions	-
w	Wall	-
z	Zone	-

GREEK LETTERS

Symbol	Description	Unit/Value
α	Heat transfer coefficient	$\mathrm{W/m^2\,K}$
β	Regression coefficient	-
$\boldsymbol{\chi}$	Cartesian coordinates x_1, x_2 and x_3	-
δ	Distance between sensor location and actuator	m
ψ	Discharge coefficient	-
ϵ	Significance bound for common feature selection	-
η	Solar gain of the considered room/zone	$\mathrm{m^2}$
$\kappa(\boldsymbol{z}_i, \boldsymbol{z}_j)$	Covariance/kernel function	-
λ	Thermal conductivity	$\mathrm{W/m\,K}$
μ	Mean value of GP	-
ω	Binary variable	-
$\boldsymbol{\phi}$	Feature vector	-
ρ	Density of air	$\mathrm{kg/m^3}$
$\varrho, \varrho_{\mathrm{partial}}$	(Partial) Pearson corrleation coefficient	-
σ	Standard deviation	-
$\boldsymbol{\tau}$	Stress tensor	$\mathrm{N/m^2}$
$\boldsymbol{\theta}$	Hyperparameters of kernel function containing the characteristic length scale σ_l, the signal standard deviation σ_f and the scale-mixture parameter ζ	-
ν	Thermal comfort vote	-
ξ	Regularisation bound for LASSO regression	-

VARIABLES AND CONSTANTS

Symbol	Description	Unit/Value
A	Surface area	$\mathrm{m^2}$
$\boldsymbol{A}$	State/system matrix	-
$\boldsymbol{B}$	Input matrix	-
c_{fan}	Fan coefficient to define $v_{\mathrm{air}} \approx v_0 + c_{\mathrm{fan}} \cdot l_{\mathrm{fan}}$	-
c_p	Specific heat coefficient of air	$\mathrm{J/kg\,K}$
C	Heat capacity	$\mathrm{J/K}$
$\boldsymbol{C}$	Output matrix	-
$\boldsymbol{d}$	Vector of disturbances	-
$\mathcal{D}$	Observation data set	-
$\boldsymbol{D}$	Feedthrough matrix	-
DT	Time of day	h
e	Specific internal energy	$\mathrm{J/kg}$

Symbol	Description	Unit/Value
f_{cl}	Clothing area factor	-
$g, \boldsymbol{g}$	Gravitational acceleration (vector)	m/s^2
h	Specific enthalpy	J/kg
$\mathcal{H}$	Information entropy	nats
$\dot{H}$	Enthalpy flow	W
$\boldsymbol{I}$	Identity matrix	-
I_{cl}	Clothing insulation	$m^2/K\,W$
I_{op}	The time interval defined by the operating hours of the AC system over the examinded days	s
I_{sol}	Global solar radation	W/m^2
J	Objective/cost function	-
$\boldsymbol{K}$	Covariance/kernel matrix	-
l_{fan}	Fan level	-
L	Thermal load on the body	W/m^2
$\dot{m}$	Mass flow rate	kg/s
m_a	Mass of dry air	kg
$\dot{m}_{CO_2}$	CO_2 generation rate of an occupant	kg/s
$\dot{m}_{H_2O}$	Moisture generation of an occupant	kg/s
$\dot{m}_{infl}$	Infiltration rate of zone	kg/s
m_v	Mass of water vapor	kg
$\mathcal{M}$	N_m dimensional set of monitoring points	-
M	Metabolic rate	W/m^2
n	Number of observations/samples	-
$\mathcal{N}$	Normal/Gaussian distribution	-
N_{cfd}	Number of considered CFD simulations	18
N_f	Dimension of feature vector / number of predictors	-
N_m	Number of monitoring points / possible sensor locations	192
N_{occ}	Number of present occupants	-
N_p	Number of prediction steps for MPC	-
N_{sens}	Number of sensors	-
N_{sup}	Number of supplies	14
N_z	Dimension of input vector $\boldsymbol{z}$	-
p	Pressure	Pa
p_a	Partial water vapor pressure	Pa
p_{amb}	Ambient pressure	Pa
p_{sat}	Saturation vapor pressure	Pa
P	Probability density function	-
q	Heat flux	W/m^2
$\boldsymbol{Q}$	Weight matrix for the system states	-

Symbol	Description	Unit/Value
$\dot{Q}$	Heat flow rate	W
$\dot{Q}_{\mathrm{occ}}$	Heat gain of an occupant	W
R	Thermal resistance	K/W
$\boldsymbol{R}$	Weight matrix for the inputs	-
R_{a}	Specific gas constant of air	J/kg K
R_{v}	Specific gas constant of water vapor	J/kg K
RH	Relative humidity	-
$s, \boldsymbol{s}$	Sensor location and setup	-
$\mathcal{S}$	Set of sensor locations	-
t	Time	s
t_{op}	Accumulatd operationg time of the AC system over the examinded days	25 h
t_{p}	Prediction horizon for MPC	s
t_{s}	Sampling time for the control parametrization	s
T	Temperature	°C
T_{cl}	Surface temperature of clothing	°C
T_{desired}	Desired air temperature as a result of the thermal comfort optimization	°C
T_{dewpoint}	Dew point temperature	°C
T_{mr}	Mean radiant temperature	°C
$\bar{T}_{\mathrm{sens}}$	Average sensor temperature	°C
$\boldsymbol{u}$	Control input	-
$\mathcal{V}$	Validation data set	-
$\boldsymbol{v}$	Vector of velocities	m/s
V	Volume	m^3
W	Accomplished mechanical work	W/m²
$\boldsymbol{x}$	State vector	-
$X_{\mathrm{CO_2}}$	Carbon dioxide concentration of air	ppm
$X_{\mathrm{H_2O}}$	Specific humidity of air	kg/kg
$\boldsymbol{z}$	Model input vector	-
$\mathcal{Z}$	Set of potential comfort influencing factors	-
$\boldsymbol{Z}$	Matrix of observations	-

List of Figures

List of Tables

Bibliography

[1] A. Afram and F. Janabi-Sharifi. "Theory and applications of HVAC control systems – A review of model predictive control (MPC)". *Building and Environment* 72 (2014), pp. 343–355.

[2] American Society of Heating, Refrigeration and Air-Conditioning Engineers. *ANSI/ASHRAE Standard 55-2013: Thermal Environmental Conditions for Human Occupancy*. Atlanta, Georgia: ASHRAE, 2013.

[3] American Society of Heating, Refrigeration and Air-Conditioning Engineers. *2017 ASHRAE Handbook - Fundamentals*. SI-Edition. Atlanta, Georgia: ASHRAE, 2017.

[4] J. A. E. Andersson, J. Gillis, G. Horn, J. B. Rawlings, and M. Diehl. "CasADi – A software framework for nonlinear optimization and optimal control". *Mathematical Programming Computation* 11 (2019).

[5] ANSYS, Inc. *ANSYS Fluent Theory Guide*. Canonsburg, PA, 2016.

[6] E. Arens, H. Zhang, W. Pasut, Y. Zhai, T. Hoyt, and L. Huang. *Air movement as an energy efficient means toward occupant comfort*. Tech. rep. Berkeley: Center for the Built Environment, 2013.

[7] E. Atam and L. Helsen. "Control-Oriented Thermal Modeling of Multizone Buildings: Methods and Issues: Intelligent Control of a Building System". *IEEE Control Systems* 36 (2016), pp. 86–111.

[8] L. Bayer. "Bewertung der Zonendisparität einer bedarfsgesteuerten Zonenklimatisierung für kommerzielle Gebäude". MA thesis. University of Stuttgart, 2017.

[9] S. Bin and Y. Wenlai. "Application of Gaussian Process Regression to prediction of thermal comfort index". *2013 IEEE 11th International Conference on Electronic Measurement & Instruments*. IEEE, 2013, pp. 958–961.

[10] C. M. Bishop. *Pattern Recognition and Machine Learning*. 1st ed. New York: Springer Science+Business Media, LLC, 2006.

[11] Y. Boukhris, L. Gharbi, and N. Ghrab-Morcos. "Modeling coupled heat transfer and air flow in a partitioned building with a zonal model: Application to the winter thermal comfort". *Building Simulation* 2 (2009), pp. 67–74.

[12]   M. Buehren. *Differential Evolution.* MATLAB Central File Exchange. 2017. URL: https://de.mathworks.com/matlabcentral/fileexchange/18593-differential-evolution (visited on 03/18/2017).

[13]   Carrier International Sdn. Bhd. *Chilled Water Fan-Coil Units - 40LM Product Data Digest.* 40LM070. Data sheet. Selangor, Malaysia.

[14]   U. K. Chakraborty. *Advances in Differential Evolution.* Vol. 143. Studies in Computational Intelligence. Berlin, Heidelberg: Springer-Verlag, 2008.

[15]   K. E. Charles. *Fanger's Thermal Comfort and Draught Models.* Tech. rep. Ottawa: Institute for Research in Construction, National Research Council of Canada, 2003.

[16]   T. Chaudhuri, Y. C. Soh, H. Li, and L. Xie. "Machine learning based prediction of thermal comfort in buildings of equatorial Singapore". *2017 IEEE International Conference on Smart Grid and Smart Cities (ICSGSC).* IEEE, 2017, pp. 72–77.

[17]   W. Chen, S. Liu, Y. Gao, H. Zhang, E. Arens, L. Zhao, and J. Liu. "Experimental and numerical investigations of indoor air movement distribution with an office ceiling fan". *Building and Environment* 130 (2018), pp. 14–26.

[18]   B. Chenari, J. Dias Carrilho, and M. Gameiro Da Silva. "Towards sustainable, energy-efficient and healthy ventilation strategies in buildings: A review". *Renewable and Sustainable Energy Reviews* 59 (2016), pp. 1426–1447.

[19]   T. Chow, K. Fong, B. Givoni, Z. Lin, and A. Chan. "Thermal sensation of Hong Kong people with increased air speed, temperature and humidity in air-conditioned environment". *Building and Environment* 45 (2010), pp. 2177–2183.

[20]   T. M. Cover and J. A. Thomas. *Elements of Information Theory.* Ed. by D. L. Schilling. Wiley Series in Telecommunications. John Wiley & Sons, Inc., 1991.

[21]   L. Daniel, T. Williamson, V. Soebarto, and D. Chen. "A model for the cooling effect of air movement". *Living and Learning: Research for a Better Built Environment, 49th International Conference of the Architectural Science Association.* 2015, pp. 1077–1086.

[22]   Davis Instruments. *Wireless Vantage Pro2 ^{TM} & Vantage Pro2 ^{TM} Plus Stations.* Data sheet. 2015. URL: https://www.davisinstruments.com/product_documents/weather/spec_sheets/6152_62_53_63_SS.pdf (visited on 10/04/2018).

[23]   R. De Coninck and L. Helsen. "Practical implementation and evaluation of model predictive control for an office building in Brussels". *Energy and Buildings* 111 (2016), pp. 290–298.

[24]   R. J. de Dear, J. W. Ring, and P. O. Fanger. "Thermal Sensations Resulting From Sudden Ambient Temperature Changes". *Indoor air* 3 (1993), pp. 181–192.

[25]   R. J. de Dear, G. S. Brager, and D. Cooper. "Developing an adaptive model of thermal comfort and preference". *ASHRAE Transactions* 104 (Part 1) (1998), pp. 145–167.

[26]   Deutsches Institut für Normung e.V. (DIN EN ISO 7730). *Ergonomics of the thermal environment - Analytical determination and interpretation of thermal comfort using calculation of the PMV and PPD indices and local thermal comfort criteria (ISO 7730:2005).* 2006.

[27]   Deutsches Institut für Normung e.V. (DIN V ISO 18599-2). *Energy efficiency of buildings – Calculation of the net, final and primary energy demand for heating, cooling, ventilation, domestic hot water and lighting – Part 2: Net energy demand for heating and cooling of building zones.* 2018.

[28]   D. Enescu. "A review of thermal comfort models and indicators for indoor environments". *Renewable and Sustainable Energy Reviews* 79 (2017), pp. 1353–1379.

[29]   P. Erickson, M. Cline, N. Tirpankar, and T. Henderson. "Gaussian processes for multi-sensor environmental monitoring". *2015 IEEE International Conference on Multisensor Fusion and Integration for Intelligent Systems (MFI).* Vol. 2015-Octob. IEEE, 2015, pp. 208–213.

[30]   P. Fanger. *Thermal comfort: analysis and applications in environmental engineering.* New York: McGraw-Hill, 1970.

[31]   A. A. Farhan, K. Pattipati, B. Wang, and P. Luh. "Predicting individual thermal comfort using machine learning algorithms". *2015 IEEE International Conference on Automation Science and Engineering (CASE)* (2015), pp. 708–713.

[32]   D. Fay, L. O'Toole, and K. N. Brown. "Gaussian Process models for ubiquitous user comfort preference sampling; global priors, active sampling and outlier rejection". *Pervasive and Mobile Computing* 39 (2015), pp. 135–158.

[33]   D. Fiala. "Dynamic Simulation of Human Heat Transfer and Thermal Comfort". Ph.D. dissertation. Leicester, UK: DeMontfort University, 1998.

[34] M. Fiorentini, G. Serale, G. Kokogiannakis, A. Capozzoli, and P. Cooper. "Development and evaluation of a comfort-oriented control strategy for thermal management of mixed-mode ventilated buildings". *Energy and Buildings* 202 (2019), p. 109347.

[35] M. Fountain, F. Bauman, E. Arens, K. Miura, and R. de Dear. "Locally controlled air movement preferred in warm isothermal environments". *ASHRAE Transactions* 100 (1994), pp. 937–952.

[36] A. P. Gagge, J. A. J. Stolwijk, and Y. Nishi. "An Effective Temperature Scale Based on a Simple Model of Human Physiological Regulatiry Response". *ASHRAE Transactions* 77 (1971), pp. 247–262.

[37] J. Gao, Y. Wang, and P. Wargocki. "Comparative analysis of modified PMV models and SET models to predict human thermal sensation in naturally ventilated buildings". *Building and Environment* 92 (2015), pp. 200–208.

[38] M. N. Gibbs. "Bayesian Gaussian Processes for Regression and Classification". PhD thesis. University of Cambridge, 1997.

[39] S. I. U. H. Gilani, M. H. Khan, and W. Pao. "Thermal Comfort Analysis of PMV Model Prediction in Air Conditioned and Naturally Ventilated Buildings". *Energy Procedia* 75 (2015).

[40] B. Griffith and Q. Y. Chen. "A Momentum-Zonal Model for Predicting Zone Airflow and Temperature Distributions to Enhance Building Load and Energy Simulations". *HVAC&R Research* 9 (2003), pp. 309–325.

[41] J. Guenther and O. Sawodny. "Versatile Ventilation and Air Conditioning Operation: Gaussian Process Regression for Temperature Field Prediction". *2018 Annual American Control Conference (ACC)*. Vol. 2018-June. IEEE, 2018, pp. 5262–5267.

[42] J. Guenther and O. Sawodny. "Feature selection and Gaussian Process regression for personalized thermal comfort prediction". *Building and Environment* 148 (2019), pp. 448–458.

[43] J. Guenther and O. Sawodny. "Feature Selection for Thermal Comfort Modeling based on Constrained LASSO Regression". *8th IFAC Symposium on Mechatronic Systems MECHATRONICS 2019*. Vol. 52. IFAC-PapersOnLine 15. Elsevier, 2019, pp. 400–405.

[44] J. Guenther and O. Sawodny. "Optimal Sensor Placement based on Gaussian Process Regression for Shared Office Spaces under Various Ventilation Conditions". *2019 IEEE International Conference on Systems, Man and Cybernetics (SMC)*. IEEE, 2019, pp. 2869–2874.

[45] Gurobi Optimization, LLC. *Gurobi Optimizer Reference Manual*. 2020. URL: http://www.gurobi.com.

[46] F. Haghighat, Y. Li, and A. C. Megri. "Development and validation of a zonal model — POMA". *Building and Environment* 36 (2001), pp. 1039–1047.

[47] T. Hastie, R. Tibshirani, and J. Friedman. *The Elements of Statistical Learning*. Vol. 2. Springer Series in Statistics. New York: Springer New York, 2009.

[48] J. Hedderich and L. Sachs. *Angewandte Statistik*. 16th ed. Berlin, Heidelberg: Springer Spektrum, 2016.

[49] L. Huang, E. Arens, H. Zhang, and Y. Zhu. "Applicability of whole-body heat balance models for evaluating thermal sensation under non-uniform air movement in warm environments". *Building and Environment* 75 (2014), pp. 108–113.

[50] M. Humphreys. "Outdoor temperatures and comfort indoors". *Batiment International, Building Research and Practice* 6 (1978), pp. 92–92.

[51] M. A. Humphreys and J. Fergus Nicol. "The validity of ISO-PMV for predicting comfort votes in every-day thermal environments". *Energy and Buildings* 34 (2002), pp. 667–684.

[52] C. Inard, H. Bouia, and P. Dalicieux. "Prediction of air temperature distribution in buildings with a zonal model". *Energy and Buildings* 24 (1996), pp. 125–132.

[53] F. P. Incropera, D. P. DeWitt, T. L. Bergman, and A. S. Lavine. *Fundamentals of Heat and Mass Transfer*. Chichester, United Kingdom: John Wiley and Sons Ltd, 2010.

[54] International Energy Agency. *World Energy Outlook 2019*. World Energy Outlook. OECD, 2019.

[55] F. Jazizadeh, A. Ghahramani, B. Becerik-Gerber, T. Kichkaylo, and M. Orosz. "Human-Building Interaction Framework for Personalized Thermal Comfort-Driven Systems in Office Buildings". *Journal of Computing in Civil Engineering* 28 (2014), pp. 2–16.

[56] J. Jin, S. Shu, and F. Lin. "Personalized Control of Indoor Air Temperature Based on Deep Learning". *2019 Chinese Control And Decision Conference (CCDC)*. Vol. 31. 6. IEEE, 2019, pp. 1354–1359.

[57] W. Jung and F. Jazizadeh. "Comparative assessment of HVAC control strategies using personal thermal comfort and sensitivity models". *Building and Environment* 158 (2019), pp. 104–119.

[58] J. T. Kim, J. H. Lim, S. H. Cho, and G. Y. Yun. "Development of the adaptive PMV model for improving prediction performances". *Energy & Buildings* 98 (2015), pp. 100–105.

[59] J. Kim, F. Bauman, P. Raftery, E. Arens, H. Zhang, G. Fierro, M. Andersen, and D. Culler. "Occupant comfort and behavior: High-resolution data from a 6-month field study of personal comfort systems with 37 real office workers". *Building and Environment* 148 (2019), pp. 348–360.

[60] J. Kim, S. Schiavon, and G. Brager. "Personal comfort models – A new paradigm in thermal comfort for occupant-centric environmental control". *Building and Environment* 132 (2018), pp. 114–124.

[61] J. Kim, Y. Zhou, S. Schiavon, P. Raftery, and G. Brager. "Personal comfort models: Predicting individuals' thermal preference using occupant heating and cooling behavior and machine learning". *Building and Environment* 129 (2018), pp. 96–106.

[62] M. Klauco and M. Kvasnica. "Explicit MPC approach to PMV-based thermal comfort control". *53rd IEEE Conference on Decision and Control*. Vol. 53. Los Angeles: IEEE, 2014, pp. 4856–4861.

[63] N. E. Klepeis, W. C. Nelson, W. R. Ott, J. P. Robinson, A. M. Tsang, P. Switzer, J. V. Behar, S. C. Hern, and W. H. Engelmann. "The National Human Activity Pattern Survey (NHAPS): a resource for assessing exposure to environmental pollutants". *Journal of Exposure Science & Environmental Epidemiology* 11 (2001), pp. 231–252.

[64] B. Koelblen, A. Psikuta, A. Bogdan, S. Annaheim, and R. M. Rossi. "Thermal sensation models: Validation and sensitivity towards thermo-physiological parameters". *Building and Environment* 130 (2018), pp. 200–211.

[65] M. W. Kozusznik, L. P. Maricutoiu, J. M. Peiró, D. M. Vîrgă, A. Soriano, and C. Mateo-Cecilia. "Decoupling Office Energy Efficiency From Employees' Well-Being and Performance: A Systematic Review". *Frontiers in Psychology* 10 (2019).

[66] A. Krause. "Optimizing Sensing Theory and Applications". PhD thesis. Pittsburgh: Carnegie Mellon University, 2008.

[67] M. Kuß. "Gaussian Process Models for Robust Regression, Classification, and Reinforcement Learning". PhD thesis. Darmstadt: Technische Universität, 2006.

[68] Q. J. Kwong, N. M. Adam, and B. Sahari. "Thermal comfort assessment and potential for energy efficiency enhancement in modern tropical buildings: A review". *Energy and Buildings* 68 (2014), pp. 547–557.

[69] L. Lan, P. Wargocki, and Z. Lian. "Optimal thermal environment improves performance of office work". *REHVA Journal* 01 (2012), pp. 12–17.

[70] S. Lecheler. *Numerische Strömungsberechnung*. 4th ed. Wiesbaden: Springer Vieweg, 2018.

[71] W. Li, J. Zhang, and T. Zhao. "Indoor thermal environment optimal control for thermal comfort and energy saving based on online monitoring of thermal sensation". *Energy and Buildings* 197 (2019), pp. 57–67.

[72] Libelium Comunicaciones Distribuidas S.L. *Waspmote Datasheet v4.6*. Data sheet. 2014.

[73] A. Lipczynska, S. Schiavon, and L. T. Graham. "Thermal comfort and self-reported productivity in an office with ceiling fans in the tropics". *Building and Environment* 135 (2018), pp. 202–212.

[74] R. R. Madadi and C. Balaji. "Optimization of the location of multiple discrete heat sources in a ventilated cavity using artificial neural networks and micro genetic algorithm". *International Journal of Heat and Mass Transfer* 51 (2008), pp. 2299–2312.

[75] E. T. Maddalena, Y. Lian, and C. N. Jones. "Data-driven methods for building control – A review and promising future directions". *Control Engineering Practice* 95 (2020).

[76] K. Mařík, J. Rojíček, P. Stluka, and J. Vass. "Advanced HVAC Control: Theory vs. Reality". *18th IFAC World Congress*. Vol. 44. IFAC Proceedings Volumes 1. Elsevier, 2011, pp. 3108–3113.

[77] J. Mei and X. Xia. "Multi-Zone Building Temperature Control and Energy Efficiency Using Autonomous Hierarchical Control Strategy". *2018 IEEE 14th International Conference on Control and Automation (ICCA)*. Anchorage, AK, USA: IEEE, 2018, pp. 884–889.

[78] K. Mihara, B. Lasternas, Y. Takemasa, K. W. Tham, and C. Sekhar. "Indoor environment evaluation of a Dedicated Outdoor Air System with ceiling fans in the tropics – A thermal manikin study". *Building and Environment* 143 (2018), pp. 605–617.

[79] H. Mu, Z. Li, X. Wang, and S. Liu. "Temperature Distribution Measurement Using the Gaussian Process Regression Method". *Mathematical Problems in Engineering* 2017 (2017), pp. 1–12.

[80] M. Musy, E. Wurtz, F. Winkelmann, and F. Allard. "Generation of a zonal model to simulate natural convection in a room with a radiative/convective heater". *Building and Environment* 36 (2001), pp. 589–596.

[81] V. Norrefeldt. "VEPZO – Velocity Propagating Zonal Model". PhD thesis. Stuttgart: University of Stuttgart, 2013.

[82] N. A. Oseland. "Predicted and reported thermal sensation in climate chambers, offices and homes". *Energy and Buildings* 23 (1995), pp. 105–115.

[83] L. Pérez-Lombard, J. Ortiz, and C. Pout. "A review on buildings energy consumption information". *Energy and Buildings* 40 (2008), pp. 394–398.

[84] C. E. Rasmussen and C. K. I. Williams. *Gaussian Processes for Machine Learning*. Cambridge, Massachusetts: The MIT Press, 2006.

[85] H. Recknagel, E. Sprenger, and K.-J. Albers. *Taschenbuch für Heizung + Klimatechnik 2017/2018*. 78th ed. Munich: DIV Deutscher Industrieverlag GmbH, 2017.

[86] P. Riederer. "Thermal room modelling adapted to the test of hvac control systems". PhD thesis. École des Mines de Paris, 2002.

[87] S+S Regeltechnik GmbH. *Pendulum room temperature sensors with passive output - THERMASGARD® RPTF 2*. Data sheet. 2015. URL: https://spluss.de/fileadmin/assets/RPTF-2__GB-safe.pdf (visited on 10/04/2018).

[88] S. Schiavon, B. Yang, Y. Donner, V. Chang, and W. Nazaroff. "Thermal comfort, perceived air quality, and cognitive performance when personally controlled air movement is used by tropically acclimatized persons". *Indoor Air* 94 (2016), pp. 9–10.

[89] M. Schmidt. *Least squares optimization with L1-norm regularization*. Tech. rep. 2005.

[90] Sensirion AG. *Digital Humidity Sensor SHT7x (RH/T)*. Data sheet. URL: https://www.sensirion.com/en/environmental-sensors/humidity-sensors/pintype-digital-humidity-sensors/ (visited on 10/04/2018).

[91] A. Simone and B. W. Olesen. "Preferred air velocity and local cooling effect of desk fans in warm environments". *AIVC Conference*. Vol. 34. 2013.

[92] R. Storn and K. Price. *Differential Evolution- A Simple and Efficient Adaptive Scheme for Global Optimization over Continuous Spaces*. Tech. rep. Berkeley: International Computer Science Institute, 1995.

[93] D. Sturzenegger, D. Gyalistras, M. Morari, and R. S. Smith. "Model Predictive Climate Control of a Swiss Office Building: Implementation, Results, and Cost–Benefit Analysis". *IEEE Transactions on Control Systems Technology* 24 (2016), pp. 1–12.

[94] S. Tanabe and K. Kimura. "Effects of air temperature, humidity, and air movement on thermal comfort under hot and humid conditions". *ASHRAE Transactions* 100 (1994), pp. 953–969.

[95] R. Tibshirani. "Regression shrinkage and selection via the Lasso". *Journal of Royal Statistical Society* 58 (1996).

[96] U.S. Energy Information Administration. *International Energy Outlook 2016*. EIA, 2016.

[97] Verein Deutscher Ingenieure. *VDI-Wärmeatlas*. 11., bearb. VDI-Buch. Berlin, Heidelberg: Springer Vieweg, 2013.

[98] A. Wagner, E. Gossauer, C. Moosmann, T. Gropp, and R. Leonhart. "Thermal comfort and workplace occupant satisfaction—Results of field studies in German low energy office buildings". *Energy and Buildings* 39 (2007), pp. 758–769.

[99] J. T. Wen and S. Mishra. *Intelligent Building Control Systems*. Ed. by J. T. Wen and S. Mishra. Advances in Industrial Control. Cham: Springer International Publishing, 2018.

[100] H. P. Williams. *Model Building in Mathematical Programming*. 5th ed. John Wiley & Sons, Ltd., 2013.

[101] Y. Yau and B. Chew. "A review on predicted mean vote and adaptive thermal comfort models". *Building Services Engineering Research and Technology* 35 (2012), pp. 23–35.

[102] Y. Yu and A. C. Megri. "A Novel Pressurized Zonal Model using the Momentum Equation". *American Journal of Engineering and Applied Sciences* 7 (2014), pp. 77–87.

[103] Y. Zhai, E. Arens, K. Elsworth, and H. Zhang. "Selecting air speeds for cooling at sedentary and non-sedentary office activity levels". *Building and Environment* 122 (2017), pp. 247–257.

[104] Y. Zhai, Y. Zhang, H. Zhang, W. Pasut, E. Arens, and Q. Meng. "Human comfort and perceived air quality in warm and humid environments with ceiling fans". *Building and Environment* 90 (2015), pp. 178–185.

[105] Y. Zhou, X. Wang, Z. Xu, Y. Su, T. Liu, C. Shen, and X. Guan. "A Model-Driven Learning Approach for Predicting the Personalized Dynamic Thermal Comfort in Ordinary Office Environment". *2019 IEEE 15th International Conference on Automation Science and Engineering (CASE)*. IEEE, 2019, pp. 739–744.